INFORMATION TO USERS

This manuscript has been reproduced from the microfilm master. UMI films the text directly from the original or copy submitted. Thus, some thesis and dissertation copies are in typewriter face, while others may be from any type of computer printer.

The quality of this reproduction is dependent upon the quality of the copy submitted. Broken or indistinct print, colored or poor quality illustrations and photographs, print bleedthrough, substandard margins, and improper alignment can adversely affect reproduction.

In the unlikely event that the author did not send UMI a complete manuscript and there are missing pages, these will be noted. Also, if unauthorized copyright material had to be removed, a note will indicate the deletion.

Oversize materials (e.g., maps, drawings, charts) are reproduced by sectioning the original, beginning at the upper left-hand corner and continuing from left to right in equal sections with small overlaps. Each original is also photographed in one exposure and is included in reduced form at the back of the book.

Photographs included in the original manuscript have been reproduced xerographically in this copy. Higher quality 6" x 9" black and white photographic prints are available for any photographs or illustrations appearing in this copy for an additional charge. Contact UMI directly to order.

U·M·I

Order Number 9428167

Interfacial phenomena in welding: Vaporization and gas dissolution

Mundra, Kamlesh, Ph.D.

The Pennsylvania State University, 1994

U·M·I

300 N. Zeeb Rd.
Ann Arbor, MI 48106

The Pennsylvania State University

The Graduate School

Department of Materials Science and Engineering

INTERFACIAL PHENOMENA IN WELDING:

VAPORIZATION AND GAS DISSOLUTION

A Thesis in

Metals Science and Engineering

by

Kamlesh Mundra

Submitted in Partial Fulfillment
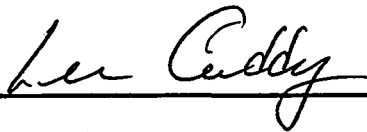of the Requirements
for the Degree of

Doctor of Philosophy

May 1994

We approve the thesis of Kamlesh Mundra.

Date of Signature

7 January 1994

Tarasankar DebRoy
Professor of Materials Science and Engineering
Thesis Advisor
Chair of Committee

10 January 1994

Lee Cuddy
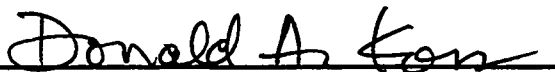**Associate Professor of Metallurgy**

11 January '94

Peter A. Thrower
Professor of Materials Science

January 10, 1994

Robert C. Voigt
Associate Professor of Industrial Engineering

Jan 10, 1994

Donald A. Koss
Professor of Metallurgy
In Charge of Graduate Programs in
**   Metals Science and Engineering**

ABSTRACT

During welding of many important engineering alloys, appreciable changes in the composition and properties of weld metal can occur due to pronounced vaporization of alloying elements from the weld pool. A theoretical model was developed to predict rates of vaporization and composition changes occurring during high density beam welding processes. The model takes into account the kinetics of vapor condensation. The effect of plasma on vaporization rates was taken into account based on the results of previous investigations and work done as part of this investigation. The velocity distribution functions of gas molecules at various locations above the weld pool surface and the heat transfer and fluid flow phenomena in the pool were coupled to model the rates of vaporization of various elements during conduction mode laser beam welding of iron, titanium, AISI 201 and 202 stainless steels for low and high powers. Computed values of the rates of vaporization of elements, the vapor composition and the weld metal composition change were found to be in good agreement with the corresponding experimental values reported in literature. The synthesis of the principles of gas dynamics and weld pool transport phenomena can serve as a basis for weld metal composition control.

The role of plasma in influencing the vaporization rates was studied. Controlled physical modeling of vaporization from the weld pool surface was conducted with ultra-purity iron samples in the presence and absence of plasma under various conditions. The plasma was characterized using optical emission spectroscopy and plasma parameters such as electron temperature and electron energy were determined from the spectral data. The rates of vaporization in the presence of plasma were found to be considerably lower than when no plasma was present. In the absence of plasma, the decrease in vaporization rates with

pressure was consistent with decreasing mass transfer rates. In the presence of plasma, the increase in vaporization rate with pressure was explained on the basis of changes in the relative magnitudes of the space charge effect.

Similar to the vaporization of alloying elements, the partitioning of gases such as hydrogen, nitrogen and oxygen between the weld pool and its environment can significantly affect the microstructure and properties of the weld. During welding the gas concentration in the weld metal is considerably higher than that calculated by Sieverts' law. This is due to the dissociation of diatomic gas molecules to atomic and ionic species in the presence of plasma. In order to seek a better understanding of the dissolution process, a two-temperature model was developed. The model was verified against the experimental data reported in literature by various researchers. Based on results of the model, the enhanced solubility in the presence of plasma could be explained on the basis of monatomic species present in the plasma environment.

TABLE OF CONTENTS

LIST OF FIGURES

LIST OF TABLES

ACKNOWLEDGMENTS

I would first like to offer my deep gratitude to my thesis advisor, Dr. Tarasankar DebRoy for all his guidance, encouragement and valuable suggestions throughout the course of this investigation. I also wish to thank Dr. L. Cuddy, Dr. P. A. Thrower and Dr. R. C. Voigt for serving on my thesis committee and giving their valuable time to read and comment on this thesis. I also wish to thank the faculty, staff and fellow students for their valuable help and guidance. I offer special thanks to Mr. Kanishka Tankala for friendly advice, encouragement and helpful discussions.

I am extremely grateful to my parents for their love and guidance throughout my life. My special thanks go to my wife, Deepika, for her love, encouragement and patience during the course of this investigation. I greatly appreciate the much needed laughter and relaxation provided by my son, Abhishek, in between the long hours of work.

Finally I extend my appreciation to the Department of Energy whose financial grant made this work possible.

Chapter 1

INTRODUCTION

1.1 General Introduction

Welding is one of the most important and versatile means of material fabrication available in industry. It is used to join hundreds of different commercial alloys of many different shapes and sizes. Welding technology is used extensively in the fabrication of automobiles and aircrafts, pressure vessels and boilers, buildings and bridges, integrated circuit connections and hundreds of other items. Welding is of great economic importance because it is one of the most important tools available to the engineer in his efforts to reduce production and fabrication costs.

During the last few years, both the increasing demand for advanced and complex fabrication of new engineering materials and the availability of high power sources have simulated considerable interest in welding research. This has led to a phenomenal growth of welding science and technology. Welding science has now evolved as an interdisciplinary activity requiring integration of knowledge from various fields and incorporating the most advanced tools of various basic and applied sciences [1]. However, technological progress and continuing interdisciplinary research on welding have brought new issues and problems to the surface. Resolution of these issues and problems would significantly contribute towards improved understanding and control of welding processes and welded materials. Furthermore, the progress made can also

enhance the understanding and development of several other materials-processing operations, especially those requiring application of high energy density processes [1].

1.2 Physical Processes during Welding

Some of the important physical processes occurring during welding can be understood with the help of Fig. 1.1. The interaction of the material and the heat source leads to rapid heating and melting of the material. For example, during laser welding, the energy absorbed by the specimen results in a rise in temperature of the solid. The energy, in turn, is conducted away to the bulk of the sample. On continued irradiation of the beam the temperature rises rapidly and a molten pool is formed.

In the weld pool, the metal undergoes vigorous recirculatory motion driven primarily by buoyancy, electromagnetic and surface tension forces. Buoyancy effects originate from the spatial variation of the liquid metal density mainly because of the temperature variations in the pool. Since large variations in temperature are present in the weld pool, the corresponding density gradients produce convective flow of the liquid. Electromagnetic forces are important when large electric current passes through the molten weld pool. It results from the interaction between the divergent path of current and the magnetic field it generates. The spatial variation of the surface tension owing to the temperature and concentration gradients at the weld pool surface often provides the main driving force for the convective flow, known as the Marangoni flow. Depending on how the various driving forces interact, the convective flow can be simple recirculation or a complex pattern with several convective cells operating [2-4]. Fluid flow and heat

Plasma

Heat Source

Liquid

Liquid + Solid

Solid
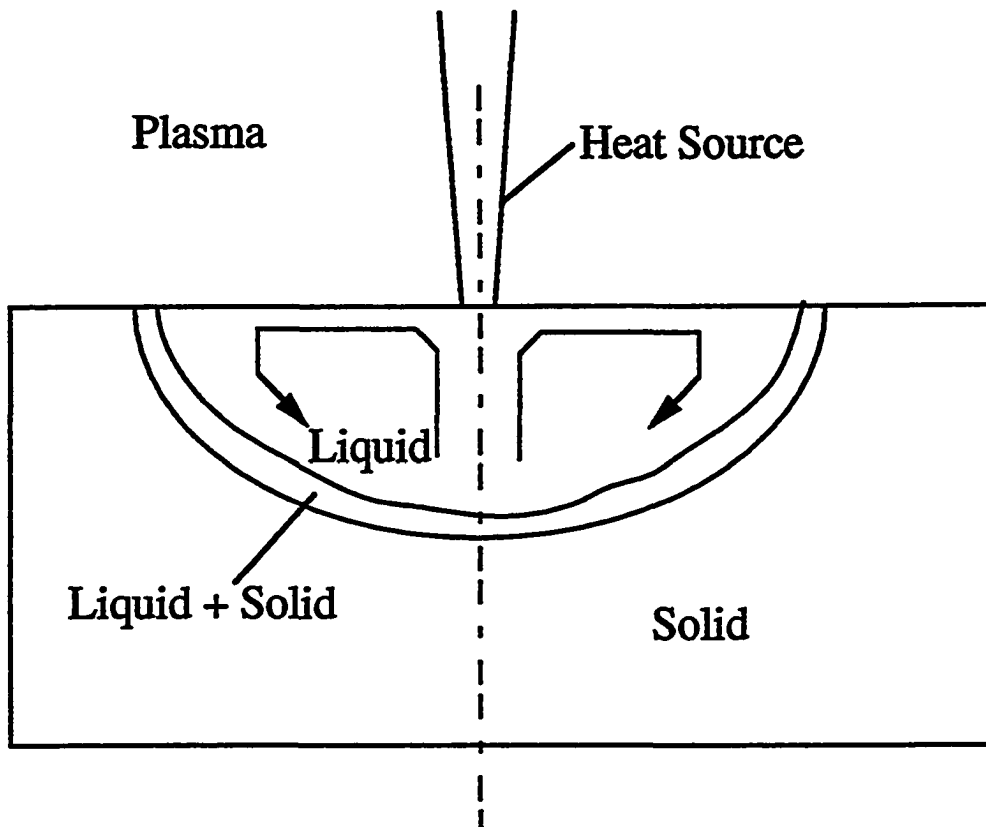
Fig. 1.1   Schematic diagram showing interaction between the heat source and the base metal.

transfer are important in determining the size and shape of the weld pool and the weld macro- and microstructures [5-9].

The high temperatures established at the weld pool surface in welding leads to occurrence of several important physical processes at the liquid vapor interface. The weld quality is significantly affected by these interfacial processes [10-12]. Fig. 1.2 shows examples of important interfacial phenomena during welding. With the growing awareness of the importance of these processes in welding, several important issues have become apparent. Two very important problems that affect the weld quality are the vaporization of the alloying elements and the dissolution of the gases such hydrogen, nitrogen and oxygen at the weld pool surface.

The weld pool surface temperatures during welding are much higher than the melting point of the weld metal. As a consequence, pronounced vaporization of the alloying elements takes place from the weld pool surface. Such losses often result in changes in the composition of the weld metal, affect weld structure and properties, and are a serious problem in the welding of many important engineering alloys. For example, selective vaporization of a volatile alloying element is known to result in welds of low tensile strength and unacceptable porosity during welding [13]. During arc welding, presence of alloying elements in the vapor phase affects the temperature of the arc [14]. The vaporized material also influences the plasma composition and this in turn affects the heat transfer from the laser beam to the work-piece [15] and, therefore, the weld properties. The presence of plasma in turn influences the rate of vaporization of the alloying elements [16]. In the last few years significant progress has been made in understanding the phenomena of vaporization. However, there is currently no comprehensive theoretical model to predict vaporization rates of alloying elements and

Partition of Alloying
Elements between Flux
and Weld Metal

Liquid Metal
Transport

Droplet Transfer

Ejection of Weld Metal

Vaporization of
Alloying Elements

Interfacial
Processes

Dissolution of
Gaseous Species

Nitrogen, Oxygen
and Hydrogen

Plasma-Material
Interaction

Heat Exchange
between Weld Pool
and Surrounding
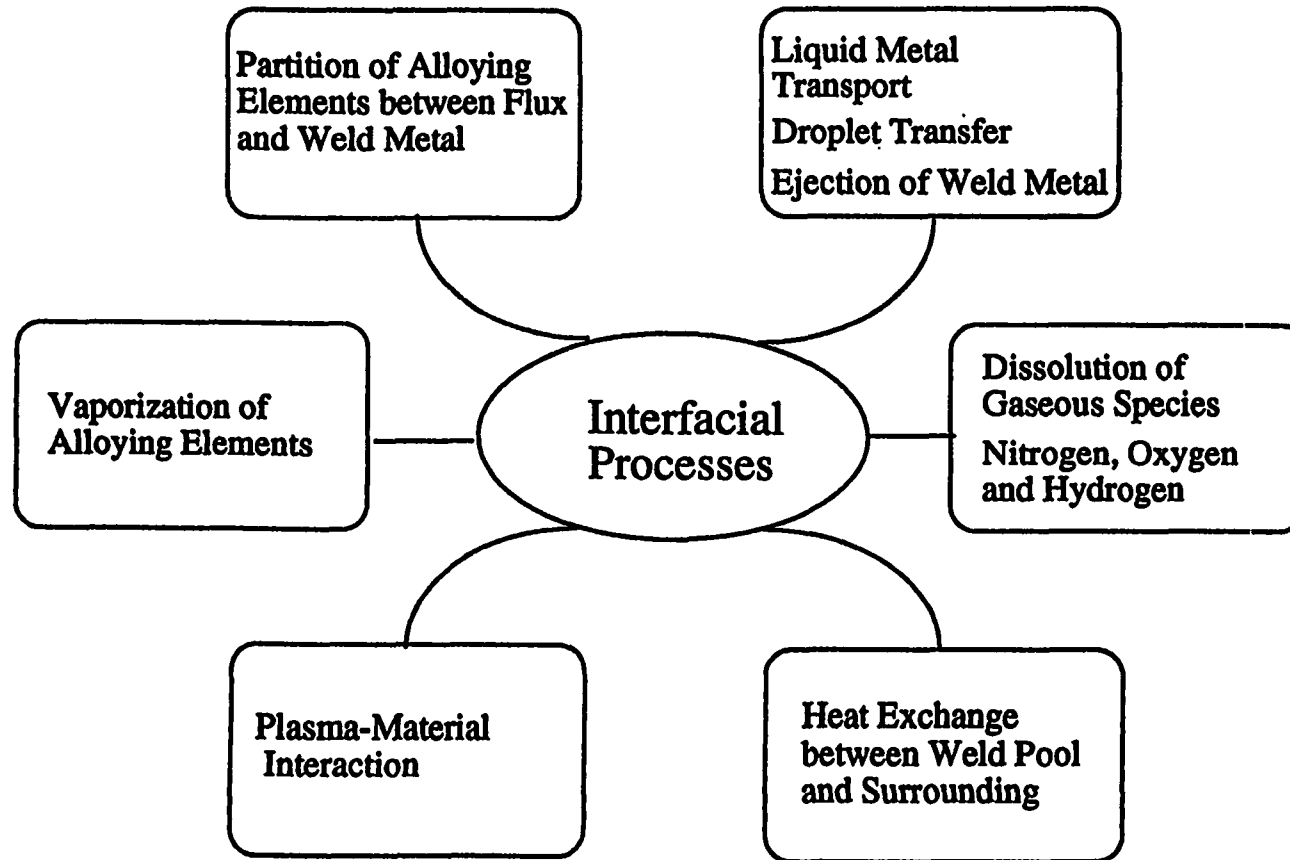
Fig. 1.2   Various examples of interfacial processes in welding.

the resulting weld pool composition changes. Apart from providing a basis for predicting weld pool composition change, development of a comprehensive model on vaporization would provide a means to control the process parameters to get a desired weld composition.

Similarly, the extent of partition of gases such as hydrogen, nitrogen and oxygen between the weld pool and its environment can affect the weld microstructure and properties significantly. The gases may dissolve in the weld metal or combine with elements in the alloy to form inclusions. Under certain conditions, the gases may reach a saturation limit and escape to form pinholes or bubbles. In the welding of steels, hydrogen induces cracking, nitrogen increases yield strength and the tensile strength but reduces ductility, and oxygen promotes inclusion formation [17]. When a metal is exposed to a pure diatomic gas such as nitrogen, the concentration of the species in the metal is proportional to the square root of its partial pressure at any given temperature and the amount of gaseous species can be predicted by Sieverts' Law [18]. However, in most welding processes, there is a strong plasma present near the weld pool surface. The plasma consists of, beside common diatomic molecules, excited molecules, atoms and ions along with electrons. The presence of these species leads to enhanced solubility of gases in the weld metal. As a result, the gas concentrations in the weld metal [19-21] are significantly higher than those calculated by Sieverts' Law. However, a general understanding of the phenomena of the partitioning of gases between the weld pool and its environment remains to be developed. A better understanding of this phenomena of partitioning of gases between the weld pool and its environment will provide means of controlling the dissolution of gases.

1.3 Statement of Objectives

The objective of this investigation is to understand and model the two important interfacial phenomena in welding that affect the weld metal structure and properties significantly: alloying element vaporization and dissolution of gases. More specifically, the goals are:

(1)   To better understand the physics of the vaporization process during welding,

(2)   To develop a comprehensive theoretical model for the prediction of vaporization rates and the composition change during welding with high energy density beam processes,

(3)   To compare the predictions of the mathematical model with experimental observations,

(4)   To develop an understanding of the principles of dissolution of gases in the weld metal,

(5)   To develop a mathematical model to identify the reasons for enhanced solubility of gases in the welding environment, and

(6)   To verify the predictions of the model with the available results of various well designed experiments.

1.4 Layout of the Thesis

The thesis is divided into five chapters. Chapter 1 is the introduction. In this chapter the physical phenomena occurring during welding are briefly described and the objectives of the present study are stated. Finally, the thesis layout is presented. A critical review of the

literature relevant to vaporization of elements and gas dissolution during welding is presented in Chapter 2. Chapter 3 is devoted to the description of the theoretical and experimental procedures used in this study. It also includes a brief description of the experiments of the various investigators from where data have been used to verify the predictions of the models. The theoretical predictions and the experimental verification of the models are presented in Chapter 4. Finally the conclusions of the investigations are presented in Chapter 5. Furthermore, suggestions for future work are also documented in this chapter.

1.5 References

1.   S. A . David and T. DebRoy, Science **257**, 487 (1992)

2.   T. Zacharia, S. A. David, J. M. Vitek and T. DebRoy, Welding Journal **68**, 499 (1989).

3.   T. Zacharia, S. A. David, J. M. Vitek and T. DebRoy, Welding Journal **68**, 510 (1989).

4.   T. Zacharia, S. A. David, J. M. Vitek and H. G. Kraus, Metall. Trans. **22B**, 243 (1991).

5.   A. Paul and T. DebRoy, Metall. Trans. **19B**, 851 (1988).

6.   J. Szekely, Advances in Welding Science and Technology, S. A. David, Ed. (ASM International, Materials Park, OH, 1987), p. 3.

7.   S. Kou and Y. Le, Metall. Trans. **14A**, 2243 (1983).

8   C. Chan, J. Mazumder and M. M. Chen, Metall. Trans. **15A**, 2175 (1984).

9.   A. Mutsunawa, International Trends in Welding Science and Technology, S. A. David and J. M. Vitek, Eds., (ASM International, Materials Park, OH, 1987), p. 3.

10.   T. DebRoy, International Trends in Welding Science and Technology, S. A. David and J. M. Vitek, Eds., (ASM International, Materials Park, OH, 1987), p. 17.

11. T. DebRoy, Mathematical Modeling of Weld Phenomena, K. E. Easterling and H. Cerjak, Eds. (Institute of Metals, London, 1992), p. 24.

12. T. DebRoy, to be published in the Proceedings of the Second International Seminar on Numerical Analysis of Weldability, H. Cerjak, Ed., 10-11 May 1993, Graz-Seggau, Austria.

13 A. Blake and J. Mazumder, J. Ind. Eng. 107, 275 (1985).

14. S. S. Glickstein, Welding Journal 55, 222 (1976).

15. R. Miller and T. DebRoy, J. Appl. Phys. 68, 2045 (1990).

16. P. Sahoo, M. M. Collur and T. DebRoy, Metall. Trans. 19B, 967 (1988).

17. S. Kou, Welding Metallurgy (John Wiley and Sons, New York, NY, 1987), p. 61.

18. A. Sieverts, Z. Phys. Chem 60, 129 (1907).

19. S. Ohno and M. Uda, Trans. Nat. Res. Inst. Met. 23, 243 (1981).

20. G. Den Ouden and O. Griebling, Recent Trends in Welding Science and Technology, S. A. David and J. M. Vitek, Eds., (ASM International, Metals Park, OH, 1990) p. 431.

21. S. A. Gedeon and T. W. Eagar, Welding Journal 69, 264 (1990).

Chapter 2

BACKGROUND AND PREVIOUS WORK

In this chapter, a critical review of the literature on vaporization and gas dissolution that takes place during welding is presented. Since heat transfer and fluid flow inside the molten pool affect the temperature distribution on the weld pool surface, and consequently, the vaporization rates and the resulting composition change, this subject is also reviewed.

2.1 Vaporization of Alloying Elements

2.1.1 Effects of Vaporization of Alloying Elements

2.1.1.1 Composition Change

The change in composition of the weld metal during welding of various materials containing one or more volatile components is well documented in the literature. A 10 % depletion in magnesium content of the weld zone was reported by Hettche et al. [1] for laser welding of Al-Mg and Al-Mg-Zn alloys. Blake and Mazumder [2,3] reported loss of magnesium during laser welding of aluminum alloy 5083 and made an attempt to reduce this loss. The effects of the independent laser processing parameters were correlated with as-welded alloy chemistry. It was concluded that magnesium loss could be reduced by a specialized jet design for the delivery of the shielding gas. No attempt was made to study the mechanism of vaporization or the factors affecting the vaporization rates. Moon and

Metzbower [4] found that approximately 20 % of the magnesium was lost during welding of aluminum alloy 5456. Cieslak and Fuerscbach [5] observed substantial magnesium vaporization during laser welding of aluminum alloys 6061, 5446 and 5086.

Several studies have also been carried out to investigate the vaporization loss from various grades of stainless steels. Kokora et al. [6,7] and Uglov et al. [8] have reported changes in the concentration of alloying elements in the laser welded regions of X12M steels. Redistribution of manganese, chromium and nickel in 12X18H9T stainless steels has been observed by Krishtal et al. [9] and Rikman et al. [10]. Rykalin et al. [11] reported that the concentration of chromium and silicon in the laser welded stainless steel remains unchanged. Khan and DebRoy [12] and Collur and DebRoy [13] have reported manganese losses from the laser welded region of AISI 201 and 202 steels. The extent of loss of manganese due to laser welding of various grades of high manganese stainless steels can be observed from Fig. 2.1 [14] where the concentration of manganese in the base metal and the weld zone, determined by electron probe microanalysis (EPMA), is plotted as a function of distance. The severe depletion of manganese in the weld metal is clearly evident. Khan, David and DebRoy [15] showed that the composition change was most pronounced for welding of thin plates at low laser power because of small size of the weld pool. Khan and DebRoy [12], by analyzing the vapor condensed in a quartz tube, and Collur and DebRoy [13], Miller and DebRoy [16] and Dunn et al. [17], by in-situ monitoring of the alloying elements in the vapor phase by optical emission spectroscopy, found that during welding of stainless steels the vapor consisted primarily of iron, manganese, chromium and nickel. A typical emission spectrum of the plasma [13] produced during laser welding of AISI 201 stainless steels using helium gas for shielding is shown in Fig. 2.2. The spectra shows that iron and manganese are the most dominant metal vapors in the welding of AISI 201 stainless steel, followed by chromium. Nickel was
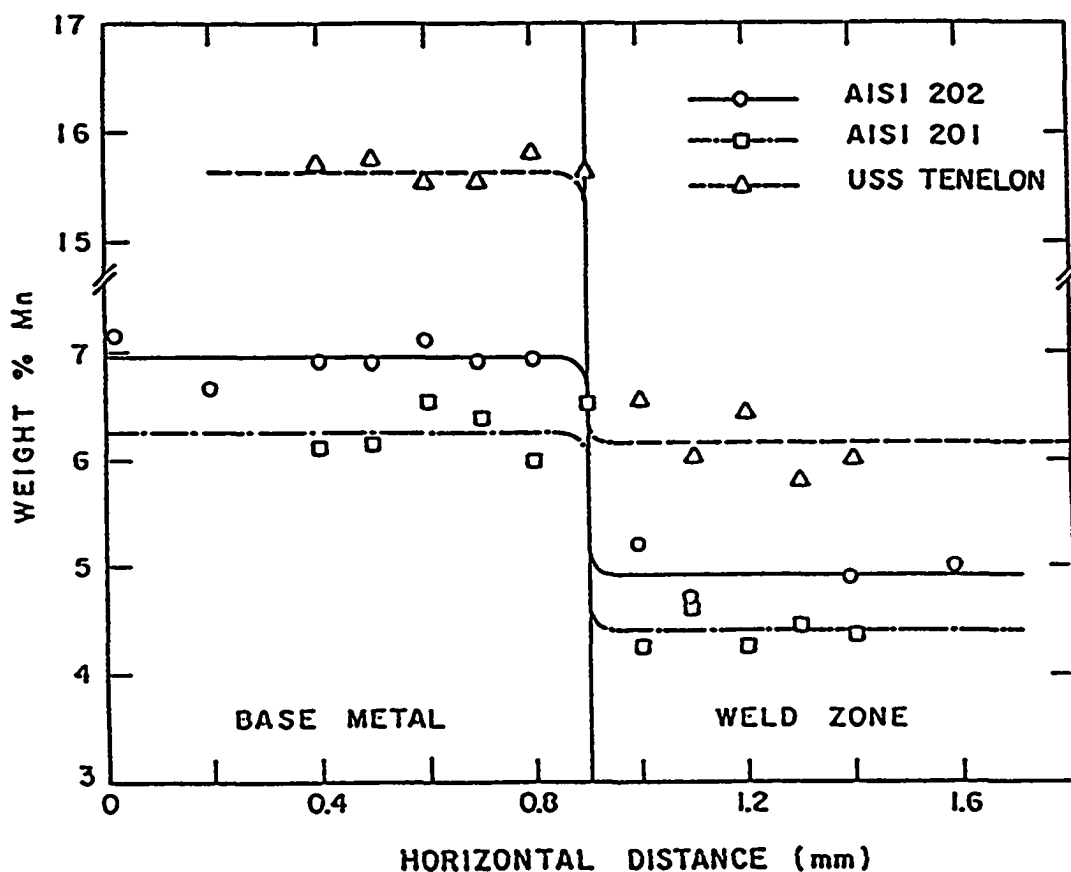
Fig. 2.1   A concentration profile of manganese in the weld zone and the base metal for laser welding of AISI 201, AISI 202 and USS Tenelon stainless steels [14]. Laser power: 560 Watts, welding speed: 3.5×10^{-3} m/s, shielding gas flow rate: 1×10^{-4} m^3/s.
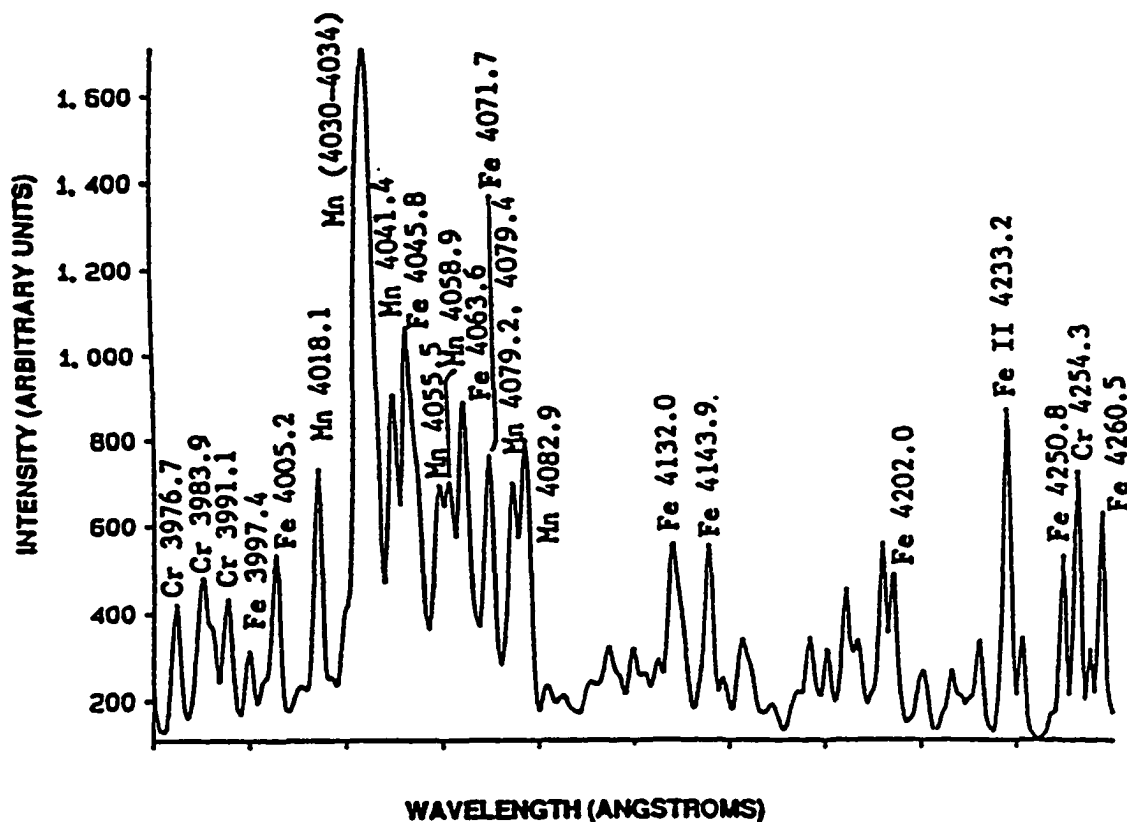
Fig. 2.2 A typical spectrum of the plasma produced during laser welding of AISI 201 stainless steel using helium gas for shielding atmosphere [13]. Gas flow rate: 3.33×10^{-5} m^3/s, welding speed: 0.005 m/s, current: 35 mA, pulse length: 0.0035, frequency: 100 Hz.

present in very low concentration. Block-Bolten and Eagar [18,19] presented the first formal treatment of the loss of alloying elements from the weld pools of stainless steels and aluminum alloys during arc welding. They used the Langmuir equation [20,21] to predict the most prominent species in the vapor phase during welding of stainless steels and aluminum alloys. The Langmuir equation is of the form:

$$J_i = \frac{P_i}{\sqrt{2\pi M_i RT}} \qquad (2.1)$$

where J_i is the vaporization flux of element i, P_i is the partial pressure of the element i on the molten pool, M_i is the molecular weight of the element i, R is the gas constant and T is the absolute temperature. The results based on the Langmuir equation showed that zinc was the most dominant vapor species in the welding of 7075 aluminum alloy and magnesium was the more dominant vapor species in the welding of 5083 and 5456 aluminum alloys. In the welding of stainless steels, iron and manganese were shown to be the prominent species. These findings were consistent with the experimental observations [18,19]. However, the rates calculated by Langmuir equation are generally significantly higher than the actual experimental rates [22].

2.1.1.2   Mechanical Properties

It is fairly well documented that the changes in the composition of the weld metal due to vaporization of alloying elements can significantly effect the weld structure and properties and are a serious problem in the welding of many important engineering alloys. A series of tests conducted by the Aluminum Association [23] on Al-Mg alloys indicated that a

decrease in magnesium from 6 % to 3 % decreased the tensile strength from 32 Kg/mm^2 to 20 Kg/mm^2. Magnesium loss during welding of Al-Mg alloys results in welds of low tensile strength and unacceptable porosity [24]. Magnesium, due to its high vapor pressure, is easily lost during welding. Moon and Metzbower [4,25] butt welded 12.7 mm thick plates of aluminum alloy 5456 using a high power CO_2 laser. Their aim was to correlate the mechanical properties with the vaporization of magnesium from the weld metal. They found a slight increase in the yield strength and a reduction in ductility and ultimate tensile strength (UTS) of the laser welded Al-Mg alloys due to vaporization of magnesium precipitates. The fractured surface was found to have visible porosity. The reasons for the formation of the pores in the laser welded Al-Mg alloys are not well understood. It may be either due to drastic change in the solubility of hydrogen because of the decrease in temperature during solidification [25] or it may be due to the vaporization of magnesium. Blake and Mazumder [3] also found that the loss of magnesium during CO_2 laser welding of aluminum alloy 5083 can result in reduced tensile strength. Similarly Cieslak and Fuerscbach [5] attributed the reduction in hardness of both the precipitation hardened and solid solution strengthened aluminum alloys after welding and subsequent heat treatment to the loss of magnesium during welding. In the case of 5456 and 5086 alloys, the loss of strength was attributed to the reduction in the solid solution strengthening caused by the vaporization of magnesium. In the case of 6061 alloy, a reduced capability of the material to precipitation harden due to lower magnesium concentration resulted in reduced weld metal hardness.

Denny and Metzbower [26] investigated the effect of laser welding on the mechanical properties of high strength low alloy steels (HSLA) A710/736. They found that there was a decrease in the yield strength and the percent elongation in the welded specimens. Much of the strength and toughness of the A710/736 was a result of precipitates formed during

solidification. Since these steels contain about 1.25 % manganese, laser welding could cause loss of manganese and thus the reduction in precipitation hardening and degradation of properties.

2.1.2 Factors Affecting Vaporization Rates

2.1.2.1 Weld Pool Temperature Distribution

Since partial pressures of vaporizing elements have a strong temperature dependence, the rates of vaporization of various alloying elements from the weld pool are strongly dependent on the temperature distribution at the weld pool surface.. A slight variation in temperature can change the pressure and the vaporization rates significantly. Although the knowledge of weld pool temperature is a crucial factor in determining vaporization rates, its determination during welding is not straightforward. This is due to the fact that the weld pools are small in size and are often covered by an intense plasma [13,16,17] which interferes with most non-contact temperature measurement techniques. Khan and DebRoy [12] have utilized the selective vaporization of alloying elements from a high manganese stainless steel and have shown that the rates of vaporization of any two elements can serve as an indicator of the effective weld pool temperature during welding. They reported that the effective weld pool temperature during laser welding of high manganese stainless steel is close to the boiling point of iron.

It has been suggested that the weld pool peak temperature is limited by the vaporization of elements from the weld pool. Block-Bolten and Eagar [19] derived the following equation by considering the energy balance to determine the maximum temperature of the weld pool.

. $$W(L_e - \Delta H) = x P \qquad\qquad (2.2)$$

where W is the temperature dependent vaporization rate, L_e is the enthalpy of vaporization, ΔH is the enthalpy of mixing, P is the power density and x is the fraction of the input power used for vaporization. Their calculations indicated the peak temperature in the arc welding to be about 2773 K. Furthermore, they found that the peak temperature in high energy density processes, such as the laser and electron beam processes, can be as high as 4273 - 5273 K. It should be noted that the relation between the vaporization rate W and temperature significantly affects the value of the temperature calculated from equation (2.2). In fact, the temperature versus vaporization rate relation used by Block-Bolten and Eagar [19], i.e. the Langmuir equation, grossly over predicts the vaporization rate at any given temperature, or for a given vaporization rate, grossly under predicts the temperature. In fact Kraus [27] has shown that the peak temperature in the GTA stainless steel weld pool, measured by the laser reflectance method, could reach as high as 2950 K. The temperature distribution obtained by Kraus [27] is shown in Fig. 2.3. It is observed that the peak temperature value is higher than the limit calculated by Block-Bolten and Eagar [19], assuming Langmuir relation between the vaporization rates and temperature.

It is also evident from Fig. 2.3 that the temperature at the center of the pool is highest whereas, at its periphery, i.e. at the solid/liquid interface away from the center of the pool, the temperature is of the order of the melting point of the alloy. A strong temperature gradient, therefore, exists at the surface of the pool. Since measurement of temperature fields in the weld pool during laser welding is a rather difficult task, a recourse has been to simulate the temperature fields by mathematical modeling of the heat transfer and fluid flow in the weld pool taking into account the essential physical features of the welding process.
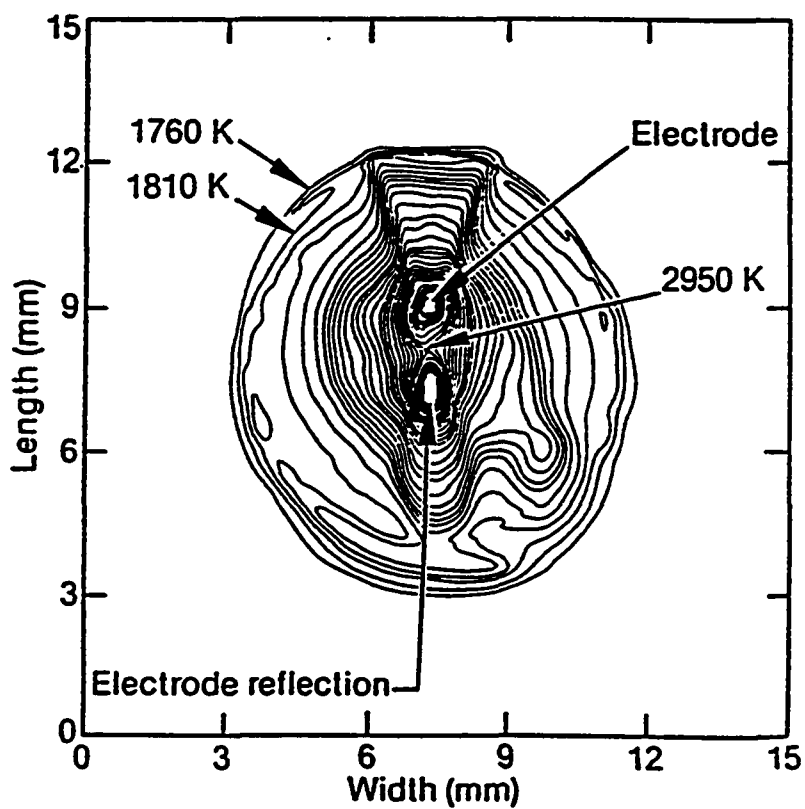
Fig. 2.3 Weld pool surface isothermal temperature counters for GTA welding of 8630 steel [27]. Current: 150 A, Voltage: 15.5 V.

Since considerable amount of research effort has been devoted to this aspect in the last decade, the subject is reviewed later in this chapter.

2.1.2.2 Role of Plasma

During laser welding, a plasma plume is always present near the weld pool. The effect of plasma in influencing vaporization rates of metal drops was determined by Sahoo et al. [22,28] by conducting appropriate physical modeling experiments. Fig. 2.4 shows the results of isothermal vaporization rates of iron, copper and several binary systems both in the presence and the absence of plasma. It is observed from the data that the presence of plasma lowers the vaporization rate significantly. In the plasma both excited neutral and ionized metal and shielding gas species are present along with free electrons. In view of the high mobility of the electrons among the various charged species in the system, the flux of the electrons to the liquid metal surface is far higher than the flux of the heavier species in the plasma. As a result, the liquid metal surface acquires negative charge and the vapor near the surface becomes densely populated with positively charged ions as shown in Fig. 2.5. The attraction between the positively charged metal ions and the negatively charged evaporating surface leads to enhanced condensation of metallic species, resulting in lower vaporization rates.

2.1.2.3 Role of Surface Active Elements

The presence of surface-active elements such as oxygen and sulfur can influence the rate of vaporization. These elements can potentially occupy the sites at the surface of the molten pool and influence the vaporization rates [14]. They can also alter the temperature
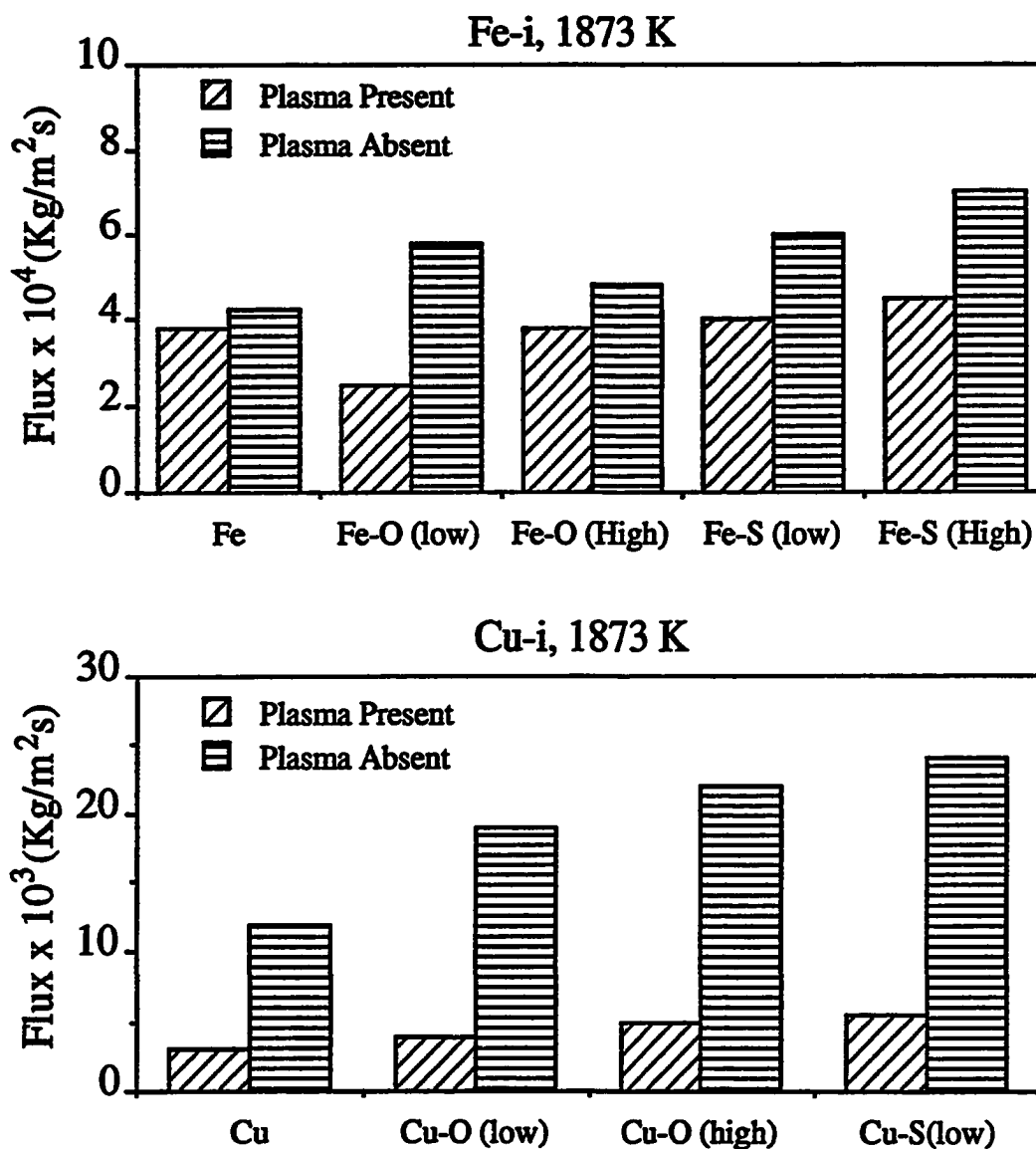
Fig. 2.4 Vaporization flux both in the presence and absence of plasma [28] for (a) iron-solute systems and where 'low' and 'high' denote initial solute concentration of roughly 0.03 and 0.25 % respectively, and (b) copper-solute system where 'low' and 'high' denote initial solute concentration of 0.1 and 0.5 % respectively. Chamber pressure were 0.3 and 1.0 mm of Hg for iron and copper systems respectively.
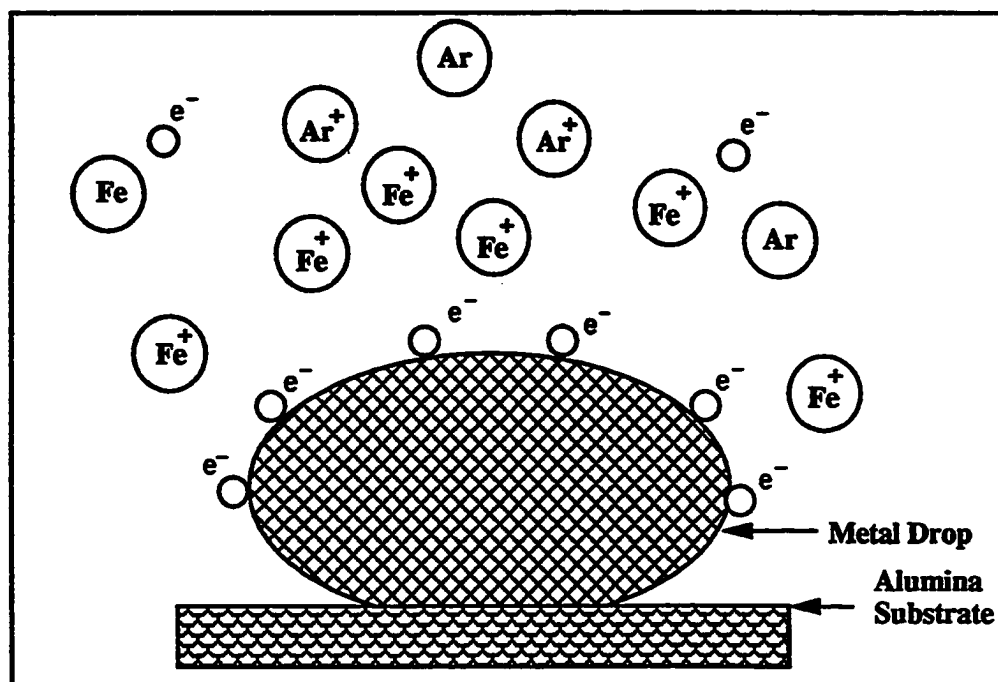
Fig. 2.5 Schematic representation of the plasma near the interface [28].

coefficient of surface tension [29-33] and thus affect the weld pool surface area and the temperature distribution [34,35] which in turn strongly influence the vaporization rates. Thus, from the welding data, it is difficult to determine if an observed change in the vaporization rate is attributable to changes in the weld pool size and surface area or is contributed by interfacial effects such as the blockage of a portion of surface sites by the surface active element. In either case, during welding, the primary interfacial effect of sulfur cannot be easily separated from its secondary effects manifested in surface area and temperature distribution changes. To determine the effects of oxygen and sulfur on the metal vaporization rate, Sahoo et al. [22,28] vaporized iron and copper drops doped with oxygen or sulfur isothermally both in the presence and in the absence of a low pressure argon plasma. Fig. 2.4 shows the results of isothermal vaporization rates of iron, copper and several binary systems both in the presence and absence of a plasma.

Since surface active agents such as sulfur and oxygen are preferentially absorbed at the surface, their presence can influence the nature of the interface. Based on conventional thermodynamic treatment, one would expect that the presence of these elements would lead to a reduction of the number of surface sites for vaporization. As a result, based on adsorption considerations, a reduction in the vaporization rate would be expected when these elements are present. However, it is observed from Fig. 2.4 that for both iron and copper systems the metal vaporization rates are somewhat enhanced by the presence of these elements. These findings are consistent with the independent results of metal vaporization during welding of various iron base alloys. For example, increase in the intensity of the iron peaks in the emission spectra was observed when sulfur was present in the weld pool [17,36]. Although such apparent anomaly has been observed [28] to be consistent with the interfacial turbulence effects [37], the role of surface active agents on vaporization is not well understood.

2.1.2.4   Welding Parameters

The most important laser welding parameters which influence the rate of vaporization are the factors which control the heat input. The temperature and the surface area of the molten pool depend on the energy input and its distribution, which in turn are influenced by the laser power, beam radius and welding speed. Therefore, laser power and its distribution and welding speed are important process parameters which control the rate of vaporization. Experiments conducted on the laser welding of various types of steels [38-40] and aluminum alloys [41] have demonstrated that laser power and welding speed can influence the alloying element loss. Another important process parameter is the type and flow rate of the shielding gas. Seaman [42] and Rein et al. [43] found that both composition and flow rate of shielding gas influence the depth of penetration. Seaman [42] suggested the use of a mixture of light and heavy gases (10 % Ar and 90 % He) for optimum penetration. Collur et al. [14] conducted laser welding experiments with different flow rates and nature of the shielding gas with AISI 202 stainless steel. The data indicated that the vaporization rate was independent of the nature and the flow rate of the shielding gas. Besides above mentioned factors, variables such as specimen thickness and surface finish can affect the extent of vaporization [44].

2.1.3   Heat Transfer and Fluid Flow

An important factor in the study of alloying elements vaporization is the fluid flow and heat transfer inside the weld pool. The fluid flow and heat transfer affect the weld pool temperature distribution and is important in the development of weld pool geometry. As a consequence, understanding of fluid flow and heat transfer is very important for the calculation of the vaporization rates and the resultant composition change. Since

measurement of temperature distribution in the weld pool is difficult, an alternative approach is to model the essential features of the welding process mathematically. Indeed, the modeling of heat transfer and fluid flow has provided detailed insight into the welding processes that could not have been obtained otherwise.

Much of the earlier mathematical models of welding process involved conductive heat transfer only. Myers et al. [45] reviewed several theoretical techniques for calculating the thermal history associated with welding. Mazumder [46] has compiled a table summarizing some of the analytical solutions of the heat conduction equation for a moving heat source. Among the numerous solutions of the heat conduction equation, the most widely used appears to be that involving the equation developed by Rosenthal [47]. The thermal analysis for laser heating and melting reported by Cline and Anthony [48] seems to be the most realistic analytical conduction model reported so far.

The analytical solution of the heat conduction equation mentioned above ignored the latent heat associated with the phase change. In addition no allowance is made for convective heat transfer effects. The solutions are valid for calculations of temperature profiles far away from the molten pool and cannot be used to predict the temperature distribution within the molten pool.

In the last decade, significant effort has gone into developing mathematical models which take into account the convective heat transfer effects, as driven by a combination of buoyancy, electromagnetic and surface tension forces. Quantitative studies on fluid flow in stationary GTA welds have been carried out by Sozou et al. [49], Andrews et al. [50] and Atthey [51]. The weld pool was considered hemispherical and the electromagnetic force alone was considered as the driving force for the fluid flow. Orper et al. [52,53] studied

fluid flow in stationary GTA weld pool. They considered the effect of combination of buoyancy, electromagnetic and surface tension forces on fluid flow. The weld pool shape was not calculated, but treated as known in the fluid flow model. Chan et al. [54] developed a two dimensional fluid flow model for surface melting due to rectangular laser beam. The heat of fusion was neglected. Kou and Sun [55] simulated fluid flow and heat transfer in stationary arc welds by considering the buoyancy, electromagnetic and surface tension effects for fluid flow. The weld pool boundary was unknown and was determined by solving the temperature and velocity fields. Recently Zacharia et al. [56,57] developed a three dimensional transient model for simulating fluid flow and heat transfer conditions associated with GTA welding process.

Apart from understanding the role of the various forces on fluid flow and heat transfer during welding, significant effort has also gone into incorporating the complex physics of the welding process in the mathematical models. Work by Heiple and Roger [29,30] and Heiple et al. [31] have demonstrated that minor surface active elements such as sulfur, oxygen, cerium, selenium and tellurium influence the weld penetration by their effect on weld pool fluid flow and heat transfer. Presence of surface active elements can significantly alter the temperature coefficient of surface tension ($d\gamma/dT$) at the weld pool surface. Furthermore, these elements often change the temperature dependence of surface tension from a negative value for pure liquid to a positive value for liquid metal with surface active elements. It was demonstrated by Sahoo et al. [32] and McNallan and DebRoy [33] that the interfacial tension can be expressed as a function of temperature and the composition of the surface active elements satisfactorily by a formalism based on the combination of Gibbs and Langmuir adsorption isotherms. The interfacial tension for Fe-O alloy, based on the formalism developed by Sahoo et al. [32], as a function of temperature and activity of oxygen is presented in Fig. 2.6 [58]. The results show that the surface tension is a strong
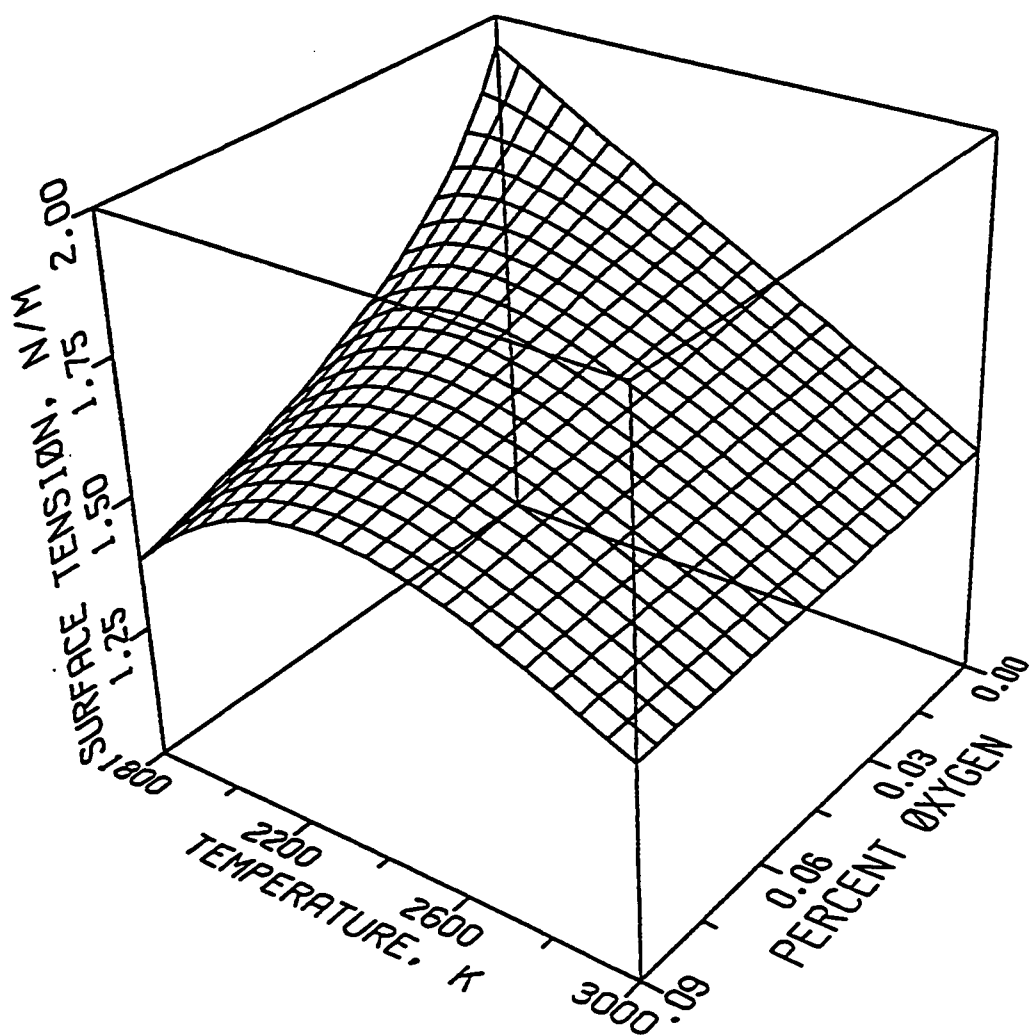
Fig. 2.6   Surface tension of iron-oxygen alloy as a function of temperature and oxygen concentration [58].

function of the concentration of the surface active elements and the temperature of the weld pool surface. The importance of considering composition and temperature dependent surface tension, $d\gamma/dT$, was illustrated by Zacharia et al. [34,35]. They found that when constant $d\gamma/dT$ is used, the weld pool geometry predicted is significantly different from the experimentally observed geometry. However, when $d\gamma/dT$ was calculated using the formalism of Sahoo, DebRoy and McNallan [32], the resulting weld pool shape agreed well with the corresponding experimental geometry. In the manner the choice of $d\gamma/dT$ affects the output of the mathematical models, Mundra et al. [59] and Zacharia et al. [60] have demonstrated that the choice of thermophysical properties can significantly influence the output of the fluid flow and heat transfer model.

It has been shown [18,19] that the evaporative heat loss from the weld pool surface results in an important cooling effect on the weld pool surface temperature. To a limited extent Thompson and Szekely [61] have incorporated the effect of vaporization by prescribing a vaporization temperature and not allowing the free surface temperature to exceed the boiling point of the metal. Choo and Szekely [62] also incorporated the affect of evaporative cooling in their fluid flow and heat transfer model for the calculation of free surface temperature distribution. Zacharia et al. [60] has demonstrated that the evaporative heat loss can significantly influence the development of the weld pool and must be included in the numerical and physical models that describe welding.

Recently, numerical models have been developed to consider the affect of fluid flow and heat transfer on the free surface topography. Paul and DebRoy [63] studied the deformation of the laser weld pool surface due to Marongoni convection. Zacharia et al. [56,57,64] have also relaxed the assumption of rigid free surface. Tsai and Kou [65,66] and Choo et

al. [62] have also developed heat transfer and fluid flow models that take into account the free surface of the weld pool.

It is evident from the literature that in the past few years significant progress has been made to understand the weld pool development through mathematical modeling. Various complexities of the welding processes can now be incorporated in the models. The modeling of fluid flow and heat transfer has provided a detailed insight into the various aspects of the welding processes which could not have been obtained otherwise.

2.1.4 Calculation of Vaporization Rates

Much of the previous work on calculation of the vaporization rates during welding was based on the Langmuir equation [20,21]. Dushman [67] suggested a relation based on Langmuir equation for the calculation of vaporization rates at different temperatures. Block-Bolten and Eagar [18,19] used Langmuir equation to calculate vaporization rates of alloying elements during arc welding of aluminum alloys and Fe-Cr, Fe-Mn and AISI 304 stainless steel. Harris and Davenport [68] also suggested that vaporization rates of an element can be calculated using Langmuir equation. Khan and DebRoy [12] measured the effective temperature on the weld pool surface from the ratio of the vaporization rates calculated from the Langmuir equation. Zacharia et al. [60] used Dushmans equation and the data reported by Kim [69] for the calculation of evaporative heat loss during welding of stainless steel. Although the rates calculated from the Langmuir equation are useful for obtaining relative vaporization rates of various alloying elements, the calculated vaporization rates are significantly higher than the actual vaporization rates under commonly used welding conditions. Even at low pressures, of the order of 200 micrometers of Hg, the vaporization

rates of pure metal drops were found [22] to be about an order of magnitude lower than the values calculated from the Langmuir equation.

The main difficulties in the calculation of the alloying element vaporization rate using Langmuir equation can be attributed to two factors. First, the equation is valid only at low pressure since it does not consider condensation of the vaporized molecules. Second, the effect of plasma [22,28] in the suppression of the vaporization rate is not taken into account. When a metal is irradiated with a very high power density laser beam, a significant amount of vapor condensation can take place and the kinetics of vapor condensation must be taken into account in the calculation of the net vaporization rate. Anisimov [70] and Knight [71] derived the equations for the calculation of the vapor condensation rates for pure metals by solving the equations of conservation of mass, momentum and energy in a thin layer adjacent to the liquid-vapor interface, known as the Knudsen layer. Chan and Majumdar [72] used Knight's results to calculate laser induced material vaporization rates from molten aluminum, titanium and a superalloy. In the works of Anisimov [70], Knight [71] and Chan and Majumdar [72] the temperature calculations were performed in one dimension. Furthermore, in their studies, the emphasis was on the calculation of the net vaporization rate taking into account the condensation of vapor. Also no comparison between the theoretical predictions and the experimental results was undertaken for the irradiation of either pure metals or alloys. In addition, in all the previous works, the effect of plasma [22,28] was not taken into account and no predictions of weld pool composition changes were attempted.

2.2 Dissolution of Gases

2.2.1 Dissolution under Non-Welding Conditions

It is now fairly well established that the solubility of a diatomic gas, e.g. nitrogen, is proportional to the square root of the pressure of nitrogen which is in equilibrium with the melt. This relationship, known as the Sieverts' law [73], follows directly from the consideration of the reaction

$$1/2 \, N_2 = 2 \, \underline{N} \tag{2.3}$$

where the equilibrium constant, K, may be expressed as

$$K = \frac{a_N}{\sqrt{P_{N_2}}} \tag{2.4}$$

where a_N is the activity of dissolved nitrogen and P_{N_2} is the pressure of diatomic nitrogen. If the concentration of nitrogen is sufficiently small so that nitrogen obeys Henry's law [74], the equilibrium constant for the solution of nitrogen can be expressed as follows:

$$K = \frac{[N]}{\sqrt{P_{N_2}}} \tag{2.5}$$

where [N] is the weight percent of dissolved nitrogen in metal. Diatomic gases, such as O_2 and H_2 also obey this law when their concentration in solution is sufficiently small.

There are numerous examples cited in literature which demonstrate that the solubility of a diatomic gas can be predicted by the Sieverts' law. For example, Pehlke and Elliot [75]

showed that the dissolution of nitrogen in liquid iron adhered to Sieverts' law. Similarly, the dissolution of hydrogen [76,77] and oxygen [78,79] from diatomic gas in liquid iron could be explained on the basis of Sieverts' law.

2.2.2 Dissolution under Welding Conditions

During welding a plasma plume is always present near the weld pool surface. The transformation of ordinary molecular species to excited neutral atoms, molecules and/or ions in the gas phase in the presence of plasma results in enhanced dissolution of gaseous species in the weld metal. Oxygen and nitrogen contents as high as 0.7 and 0.2 wt % respectively have been measured in the weld metal [80]. Ohno and Uda [81] conducted arc welding experiments with nickel to study the nitrogen dissolution during welding. The results are presented in Fig. 2.7. It is evident from the figure that the solubility of nitrogen in the weld metal is considerably higher than the solubility predicted by Sieverts' law. Uda et al. [82] have also demonstrated that the concentration of nitrogen in liquid iron during arc melting is significantly higher than the corresponding equilibrium solubility when the metals are exposed to diatomic nitrogen molecules under non-arc melting conditions. Katz and King [83] and Ouden and Griebling [84] observed that, in the presence of an arc discharge, the concentration of nitrogen in liquid iron is significantly higher than the value predicted by Sieverts' Law. Bandopadhyay et al. [85] studied the plasma enhanced nitrogen solubility in pure tantalum and niobium at 2243 K. Their data showed a much greater nitrogen solubility for the metal concerned in the presence of plasma than without the plasma. Some of the previous work on gas solubility in metals has been summarized in Table 2.1. All these studies show that it would be inappropriate to calculate nitrogen solubility in the weld metal by any straightforward application of the Sieverts' law.
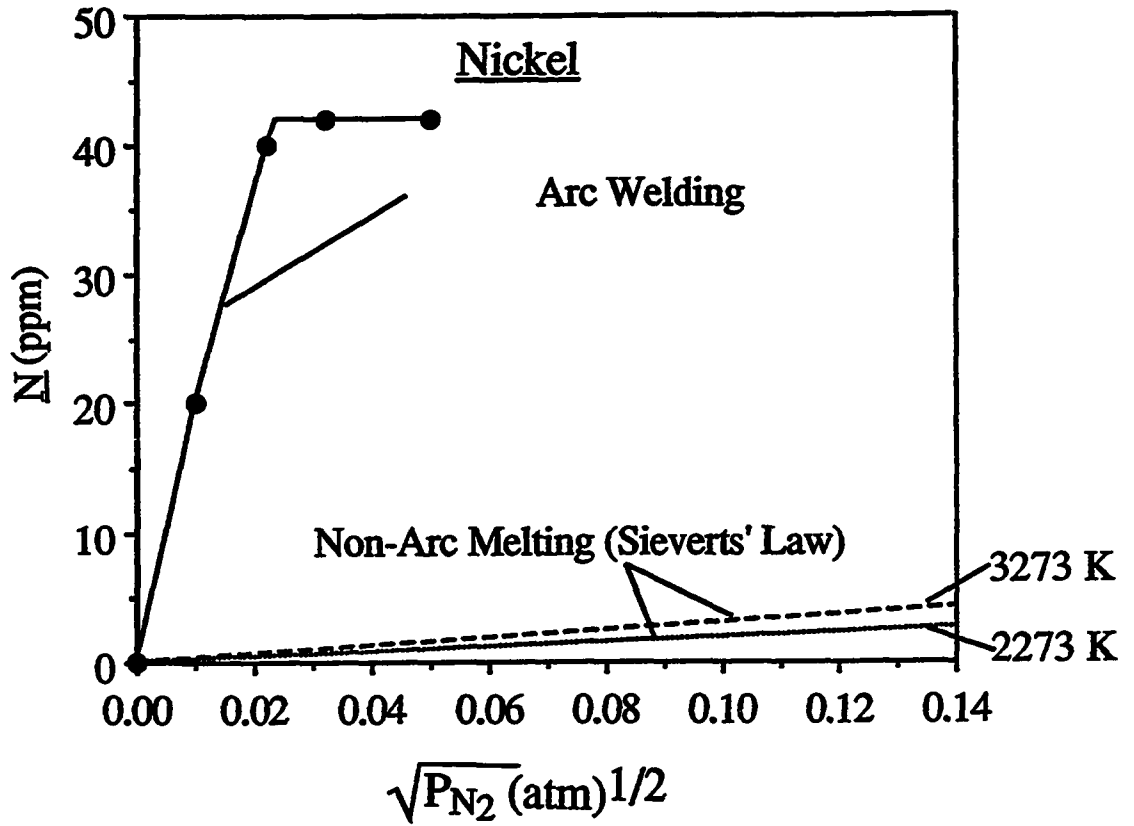
Fig. 2.7   Nitrogen content of nickel welded metal plotted as a function of $\sqrt{P_{N_2}}$ [81].

Table 2.1: Plasma-enhanced gas solubility in metals.

Experimental Conditions*	Type of Enhanced Excitation**	Enhanced Solubility ***	Reference
5g,170A,-,2373K	A	20	82
10kg,200A,2.5cm,1873K	A	2-3	83
10g,100A,2mm,1873K	A	2-10	84
0.3g,2.1A,-,1873K	B	5	86
0.62-0.81g,-,-,2243K	B	3	85
0.5g, -,-,600 K	C	25	95

* sample weight, arc current, arc distance and metal temperature.

** A,B and C indicates electric arc, glow discharge and microwave discharge, respectively.

*** ratio of gas concentrations in the metal in the presence of plasma and diatomic gas.

2.2.3 Effect of Enhanced Dissolution on Weld Properties

The dissolution of nitrogen, oxygen and hydrogen in the weld pool affects weldment properties. The gases may dissolve interstitially in the weld metal, whereupon they escape to form pinholes or bubbles, or combine with elements in the alloy to form inclusions. In the welding of steels, nitrogen increases the yield strength and the tensile strength but reduces the ductility [87], oxygen promotes inclusion formation and decreases the strength, toughness, and ductility [87], and hydrogen induces cracking [88]. For aluminum and magnesium alloys, the formation of insoluble oxide films on the weld pool surface during welding can even cause incomplete fusion of the weld [80]. Hydrogen porosity is often observed in aluminum alloys [89]. Excessive hydrogen porosity in aluminum welds results in reduced ductility and strength [90] and lower fatigue resistance [91]. Hydrogen can also cause microfissuring in the heat affected zone of the copper weld [80].

2.2.4 Mechanism of Gas Dissolution

The enhanced solubility of gases in the weld metal has been attributed to the presence of one or more different gaseous species present in the gas phase. Bandopadhyay et al. [85] characterized the plasma by optical emission spectroscopy during their nitrogen solubility experiments with tantalum and niobium samples. The nitrogen species that were identified in the plasma are N^*, N ions, N_2^*, and N_2^+. They attributed the enhanced solubility to the presence of these excited neutral atoms and ions. Mitra [92] suggested that the N_2^+ ions present in the plasma act as precursors in the formation of the nitrogen atoms. The formation of N_2^+ involves collision of nitrogen molecules with energetic electrons according to the following reaction:

$$N_2^* + e_f^- = N_2^+ + 2e^-$$

<div align="right">(2.6)</div>
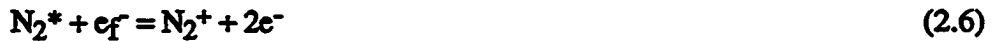
where e_f^- denotes a fast electron with at least 15.6 eV energy which is much higher than the average kinetic energy of the electrons and, therefore, possessed by only a small population of electrons in the plasma. Then N_2^+ ions collide with electrons to form excited nitrogen atoms.

$$N_2^+ + e_f^- = 2N^*$$

<div align="right">(2.7)</div>

If single nitrogen atoms are formed, i.e., N(g), these species will be directly adsorbed at selected sites on the surface of the molten iron sample according to the reaction N(g) + Site = N(ads) after which the dissolution of nitrogen will occur by the reaction N(ads) = N(%) + Site. The overall reaction for this process is N(g) = N(%). As compared to the Sieverts' law case, in this situation, the amount of nitrogen dissolved is proportional to the first power of nitrogen pressure. Lakomsky and Torkhov [93] attributed the enhanced solubility of nitrogen in metals, in the presence of plasma, to excited nitrogen molecules, N_2^*. Their hypothesis involves adsorption of nitrogen molecules with excess vibrational energy, N_2^*(g), provided by the electric field. The overall mechanism of nitrogen solution is as follows:

$$N_2^* + Site = N_2^*(ads)$$

<div align="right">(2.8)</div>

$$N_2^*(ads) + Site = 2N\ (ads)$$

<div align="right">(2.9)</div>

$$2N(ads) = 2N(\%) + 2Sites$$

<div align="right">(2.10)</div>
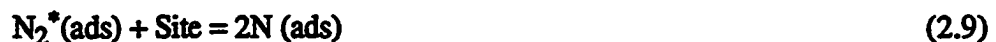
to yield an overall reaction $N_2^*(g) = 2N(\%)$. However, Katz and King [83] argued that it is difficult to see how an adsorbed molecule could have excess vibrational energy. Katz and King [83] postulated that the increased solubility in the presence of plasma is due to the presence of monatomic nitrogen. Similarly, Gedeon and Eagar [94] attributed the increased hydrogen solubility in the weld metal to the presence of monatomic hydrogen. Currently, the enhanced solubility has been attributed to the various species such as N_2^*, N_2^+, N^* and N present in the plasma. Further work needs to be done to identify the dominant species responsible for the enhanced dissolution.

2.3 Summary

During high energy density beam welding of many important engineering alloys pronounced vaporization of alloying elements takes place from the weld pool surface. As a consequence, the composition of the solidified weld pool may differ significantly from that of the alloy being welded. Apart from the characterization of the chemical composition and the properties of the final fabricated product to evaluate the direct effects of vaporization, much of the previous experimental work was based on in-situ monitoring of the alloying element vaporization by optical emission spectroscopy. Theoretically, Langmuir equation has been used to calculate the rates of vaporization during welding. However, the rates predicted are significantly higher than the actual vaporization rates under commonly used welding conditions. Although significant effort has been made towards understanding various aspects of vaporization during welding, a comprehensive theoretical model to predict, from fundamental principles, alloying element vaporization rates and the resulting weld pool composition change is still lacking. A comprehensive theoretical model would

allow calculation of acceptable limits of operating parameters and would be useful for weld metal composition control.

Another important interfacial phenomenon that affects weldment properties is the dissolution of gases in the weld metal. Although it is now well recognized that the solubility of gases under welding conditions is significantly higher than those predicted by the Sieverts' law, a general understanding of the partition of interstitial gases between the weld pool and its environment remains to be developed. The enhanced solubility of gases in the weld metal under welding conditions has been attributed to the presence of one or more different gaseous species present in the gas phase. Identifying the species responsible for enhanced dissolution, through experimental and theoretical work, will provide improved fundamental understanding of the dissolution process. Furthermore, such an understanding will be useful for control of weld metal composition and properties.

2.4   References

1.   L. R. Hettche, E. A. Metzbower, J. D. Ayers and P. G. Moore, Naval Research Reviews 28, 4 (1981).

2.   A. Blake and J. Mazumder, ICALEO 31, 33 (1982).

3.   A. Blake and J. Mazumder, J. Eng. Transactions of AIME 107, 275 (1985).

4.   D. W. Moon and E. A. Metzbower, Welding Journal 62, 53 (1983).

5.   M. J. Cieslak and P. W. Fuerschbach, Metall. Trans. 19B, 319 (1988).

6.   A. N. Kokora and E. P. Rikman, Fizikai Khimiya Obrabotki Materialov 1, 11 (1968), as quoted in reference in 11.

7.   A. N. Kokora, A. A. Zhukov and V. A. Shalashov, Laser Machining of Steels 2, 41 (1977), as quoted in reference 11.

8.   A. A. Uglov, A. N. Kokora and M. A. Krishtal, Fizikai Khimiya Obrabotki Materialov 4, 3 (1973), as quoted in reference in 11..

9. M. A. Krishtal, A. A. Zhokov and A. N. Kokora, Metallurgiya, Moscow, (1973), as quoted in reference 11.

10. E. P. Rikman, A. N. Kokora and A. A. Zhukov, Vaprosy Metallovedeniya Prochnosti Metallovi Splavov, Priokskiz, 182 (1968), as quoted in reference 11.

11. N. Rykalin, A. Uglov and A. Kokora, Laser Machining and Welding, (Mir Publishers, Moscow, 1978), p. 226.

12. P. A. A. Khan and T. DebRoy, Metall. Trans. 15B, 641 (1984).

13. M. M. Collur and T. DebRoy, Metall. Trans. 20B, 277 (1989).

14. M. M. Collur, A. Paul and T. DebRoy, Metall. Trans. 18B, 773 (1987).

15. P. A. A. Khan, T. DebRoy and S. A. David, Welding Journal 67, 1 (1988).

16. R. Miller and T. DebRoy, J. Appl. Phys. 68, 2045 (1990).

17. G. J. Dunn, C. D. Allemand, and T. W. Eager, Metall. Trans. 17A, 1851 (1986).

18. A. Block-Bolten and T. W. Eager, Metall. Trans. 15B, 461 (1984).

19. A. Block-Bolten and T. W. Eagar, Trends in Welding Research in the U. S., S. A. David, Ed., (ASM, Metals Park, OH, 1982), p. 53.

20. I. Langmuir, Phys. Rev. 2, 329 (1913).

21. R. D. Phelke, Unit Processes in Extractive Metallurgy, (Elsevier North Holland Publishing Co., Inc., New York, NY, 1982).

22. P. Sahoo, M. M. Collur and T. DebRoy, Metall. Trans. 19B, 967 (1988).

23. L. F. Mondolfo, Aluminum Alloys, (Butterworth and Co. Ltd, London, 1976), p. 315.

24. D. B. Snow and E. M. Breinan, United Technologies Research Center, Connecticut, ONR Report # R78-911989-14, July 1978.

25. E. A. Metzbower, Naval Engineers Journal 93, 49 (1981).

26. P. E. Denny and E. A. Metzbower, ICALEO 38, 80 (1983).

27. H. G. Kraus, Welding Journal 68, 269 (1989).

28. P. Sahoo and T. DebRoy, Materials Letters 6, 406 (1988).

29. C. R. Heiple and J. R. Roger, Trends in Welding Research in U. S., S. A. David, Ed., (ASM, Metals Park, OH, 1982), p. 489.

30. C. R. Heiple and J. R. Roger, Welding Journal 61, 97 (1982).

31. C. R. Heiple, J. R. Roger, R. T. Stagner and R. J. Aden, Welding Journal 62, 72 (1983).

32. P. Sahoo, T. DebRoy and M. J. McNallan, Metall. Trans. 19B, 483 (1988).

33. T. DebRoy and M. J. McNallan, Metall. Trans. 22B, 557 (1991).

34. T. Zacharia, S. A. David, J. M. Vitek and T. DebRoy, Welding Journal 68, 499 (1989).

35. T. Zacharia, S. A. David, J. M. Vitek and T. DebRoy, Welding Journal 68, 510 (1989).

36. M. M. Savitskii and G. I. Leskov, Automatic Welding 33, 11 (1980).

37. F. D. Richardson, Physical Chemistry of Melts in Metallurgy 2, (Academic Press, New York, 1974) p. 452.

38. J. Mazumder, Journal of Metals 34, 16 (1982).

39. P. A. A. Khan and T. DebRoy, Laser Processing of Materials, K Mukerjee and J. Mazumder, Eds., (The Metallurgical Society of AIME, Warrendale, PA, 1985), p. 71.

40. F. L. Beardson and R. E. Bisaro, Welding Journal 52, 227 (1973).

41. T. Marsico, Unpublished Research, The Pennsylvania State University, 1987 (as quoted in reference 44).

42. F. D. Seaman, quoted in I. Miyamoto et al., ICALEO 44, 68 (1984).

43. R. M. Rein et al., Pat # 1448740, The U. K. Patent Office, 1972.

44. P. A. A. Khan, Ph. D. Thesis, The Pennsylvania State University, 1987.

45. P. S. Myers, O. A. Uyehara and G. L. Borman, Weld. Res. Conc. Bull. 1, no. 123 (1967).

46. J. Mazumder, Laser Materials Processing, M. Bass, Ed. (North Holland Publishing Co., NY, 1983), p. 112.

47. D. Rosenthal, Trans. ASME 48, 848 (1946).

48. H. E. Cline and T. R. Anthony, J. Appl. Phys. 48, 3895 (1977).

49. C. Sozou and W. M. Pickering, J. Fluid Mech. 73, 641 (1976).

50. J. G. Andrews and R. E. Cline, J. Fluid Mech. 84, 281 (1978).

51. D. R. Atthey, J. Fluid Mech. **98**, 787 (1980).

52. G. M. Oreper, T. W. Eagar and J. Szekely, Welding Journal **62**, 307 (1983).

53. G. M. Oreper and J. Szekely, J. Fluid Mech. **147**, 53 (1984).

54. C. Chan, J. Mazumder and M. M. Chen, Metall. Trans. **15A**, 2175 (1984).

55. S. Kou and D. K. Sun, Metall. Trans. **16A**, 203 (1985).

56. T. Zacharia, A. H. Eraslan and D. K. Aidun, Welding Journal **67**, 18 (1988).

57. T. Zacharia, A. H. Eraslan and D. K. Aidun, Welding Journal **67**, 53 (1988).

58. T. DebRoy, to be published in the Proceedings of the Second International Seminar on Numerical Analysis of Weldability, H. Cerjak, Ed., 10-11 May 1993, Graz-Seggau, Austria.

59. K. Mundra, T. DebRoy, T. Zacharia and S. A. David, Welding Journal **71**, 313 (1992).

60. T. Zacharia, S. A. David and J. M. Vitek, Metall. Trans. **22B**, 233 (1991).

61. M. E. Thompson and J. Szekely, Int. J. Heat Mass Transfer **32**, 007 (1989).

62. R. T. C. Choo and J. Szekely, Welding Journal **70**, 223 (1991).

63. A. Paul and T. DebRoy, Metall. Trans. **19B**, 851 (1988).

64. T. Zacharia, S. A. David, J. M. Vitek and H. G. Kraus, Metall. Trans. **22B**, 243 (1991).

65. M. C. Tsai and S. Kou, Int. J. Num. Meth. in Fluids **9**, 1503 (1989).

66. M. C. Tsai and S. Kou, Welding Journal **69**, 241 (1991).

67. S. Dushman, Scientific Foundations of Vacuum Techniques, (John Wiley and Sons, Inc., New York, NY, 1949), p. 18.

68. R. Harris and W. G. Davenport, Metall. Trans. **13B**, 581 (1982).

69. C. S. Kim, Thermophysical Properties of Stainless Steels, (Argonne National Laboratory, Argonne, IL, 1975), Report No. ANL-75-55.

70. S. I. Anisimov and A. Kh. Rakhmatulina, Soviet Physics - JETP **37**, 441 (1973).

71. C. J. Knight, AIAA Journal **17**, 519 (1979).

72. C. L. Chan and J. Mazumder, J. Appl. Phys. **62**, 4579 (1987).

73. A. Sieverts, Z. Phys. Chem **60**, **129** (1907).

74. D. R. Gaskell, Introduction to Metallurgical Thermodynamics, (Scripta Publishing Co., Washington, D. C., 1973), p. 296.

75. R. Pehlke and J. F. Elliott, Trans. Met. Soc. AIME **218**, 1088 (1960).

76. Von W. Geller and T. Sun, Arch. Eisenhuttenw. **21**, 423 (1950), as quoted from reference 77.

77. The Making, Shaping and Treating of Steel, H. E. McGannon, Ed., (United States Steel, Pittsburgh, PA, 1970), p. 326.

78. J. Chipman and K. L. Fetters, Trans. ASM **29**, 953 (1941).

79. C. R. Taylor and J. Chipman, Trans. AIME **154**, 228 (1953).

80. S. Kou, Welding Metallurgy (John Wiley and Sons, New York, NY, 1987), p. 61.

81. S. Ohno and M. Uda, Trans. Nat. Res. Inst. Met. **23**, 243 (1981).

82. M. Uda and S. Ohno, Trans. Nat. Res. Inst. Met. **20**, 16 (1978).

83. J. D. Katz and T. B. King, Metall. Trans. **20B**, 175 (1989).

84. G. Den Ouden and O. Griebling, Recent Trends in Welding Science and Technology, S. A. David and J. M. Vitek, Eds., (ASM International, Metals Park, OH, 1990) p. 431..

85. A. Bandopadhyay, A. Banerjee and T. DebRoy, Metall. Trans. **23B**, 207 (1992).

86. Q. Gang, M. Small and T. DebRoy, Unpublished Research, The Pennsylvania State University, PA, 1991.

87. D. Seferian, The Metallurgy of Welding, (Wiley, New York, NY, 1962).

88. W. F. Savage, E. F. Nippes and E. S. Szekeres, Welding Journal **55**, 276 (1976).

89. J. H. Devletian and W. E. Wood, Weld. Res. Council Bull. **290**, (1983).

90. R. J. Shore, MS Thesis, The Ohio State University, Columbus, OH, 1968.

91. A. W. Pense and R. D. Stout, Weld. Res. Council Bull. **152**, (1970).

92. S. K. Mitra, Phys. Rev. **90**, 516 (1953).

93. V. I. Lakomsky and G. F. Torkhov, Soviet Physics **13**, 1159 (1969).

94. S. A. Gedeon and T. W. Eagar, Welding Journal **69**, 264 (1990).

95. D. Madey and T. DebRoy, Unpublished Research, The Pennsylvania State University, PA, 1993.

Chapter 3

PROCEDURES

3.1 Determination of Vaporization Rate

3.1.1 Experimental Procedures

During the course of this investigation, experimental results of previous investigations carried out at Penn State were used for the validation of the mathematical model for the calculation of vaporization rates and the weld metal composition changes. Since the details of the experimental procedure and the experimental data are presented in previous publications [1-5], only a brief summary is presented here. Samples of iron and titanium [4,5], AISI 201 [1,3] and AISI 202 [1,2] steels were irradiated by carbon dioxide lasers. An electrically operated table capable of moving along two orthogonal directions, by using electrical signals from a microprocessor based controller, was used to position the sample. The experiments were carried out in an inert atmosphere of helium or argon inside a plexiglass chamber. The weight of the samples before and after the exposure to the laser irradiation were recorded and the difference gave the total amount of the material lost due to vaporization. The total rate of alloying element vaporization was determined from the measured values of the loss in sample weight and the laser material interaction time. The interaction time was recorded by an electronic chronometer suitably connected to a movable specimen table to obtain automatic clock start and stop features. Khan et al. [1-3], in their vaporization experiments with stainless steels, collected a portion of the vaporized material as condensate on the inner surface of a hollow, cylindrical, open ended quartz tube which

was held stationary and co-axial with the laser beam. They determined the composition of the condensate by atomic absorption spectroscopy (AA) and electron probe microanalysis (EPMA) techniques [1]. Furthermore, they used EPMA to determine the chemical composition of the base metal and the fabricated weld. The rates of vaporization of the individual alloying elements were determined from the total vaporization rate and the composition of the condensate [1-3].

3.1.2   Theoretical Investigations

3.1.2.1   Heat Transfer and Fluid Flow in Molten Pool

The change in the composition of a weld pool is a strong function of the rate of vaporization of the alloying elements and the volume of the molten metal. The rates of vaporization of the various alloying elements from the weld pool are largely dependent on the temperature distribution at the pool surface. Direct reliable measurements of temperature profile at pool surface is difficult since the weld pool is small in size and is often covered by an intense plasma [6-9] which interferes with most noncontact temperature measurement procedures. Procedures based on the selective vaporization of alloying elements [1,2] do not provide any spatial resolution of the temperature at the pool surface. A recourse is to simulate temperature fields by mathematical modeling of the essential physical features of the process. The task involves numerical solution of the Navier-Stokes equation and the equation of conservation of energy. This approach has been adopted in this work. The equations and the appropriate boundary conditions are described in the following section.

3.1.2.1.1 Governing Equations and Boundary Conditions

The steady state heat transfer and fluid flow phenomena in an axisymmetric weld pool are represented by the following equations [10] of mass, momentum and enthalpy:

Conservation of Mass:

$$\frac{1}{r}\frac{\partial}{\partial r}(rv) + \frac{\partial u}{\partial x} = 0 \tag{3.1}$$

Conservation of Momentum:

Radial Direction:

$$\rho v\frac{\partial v}{\partial r} + \rho u\frac{\partial v}{\partial x} = -\frac{\partial p}{\partial r} + \mu\left(\frac{\partial^2 v}{\partial r^2} + \frac{\partial^2 v}{\partial x^2} + (\frac{1}{r}\frac{\partial v}{\partial x} - \frac{v}{r^2})\right) + S(r) \tag{3.2}$$

Axial Direction:

$$\rho v\frac{\partial u}{\partial r} + \rho u\frac{\partial u}{\partial x} = -\frac{\partial p}{\partial x} + \mu\left(\frac{\partial^2 u}{\partial r^2} + \frac{\partial^2 u}{\partial x^2} + \frac{1}{r}\frac{\partial u}{\partial r}\right) + \rho g_x + S(x) \tag{3.3}$$

Conservation of Enthalpy:

$$\frac{\partial}{\partial x}(\rho u\phi) + \frac{1}{r}\frac{\partial}{\partial r}(\rho v\phi r) = \frac{\partial}{\partial x}\left\{\frac{k}{C_p}\left(\frac{\partial\phi}{\partial x}\right)\right\} + \frac{1}{r}\frac{\partial}{\partial r}\left\{\frac{k}{C_p}\left(r\frac{\partial\phi}{\partial x}\right)\right\} + S_\phi(r) \tag{3.4}$$

where u and v are the axial and radial velocity, respectively, r and x are the radial and axial direction indicators, respectively, ρ is the density, μ is the viscosity, p is the pressure, C_p is the specific heat, k is the thermal conductivity, ϕ is the enthalpy, g_x is the acceleration due to gravity, S(x) and S(r) are the source term for momentum equations and represents body force, and $S_\phi(r)$ is the source of enthalpy and represents the net absorption of energy at the pool surface. For gas tungsten arc (GTA) welding, the electric currents and the induced magnetic field influence fluid flow and heat transfer by way of the electromagnetic force. Therefore, for GTA welding, the body force, S, can be expressed as:

$$S = J \times B \tag{3.5}$$

where J is current density vector and B is the magnetic flux vector. The electromagnetic force $J \times B$ can be expressed as follows:

$$J \times B = B_\theta (J_r x - J_x r) \tag{3.6}$$

where x and r are the unit vectors in axial and radial direction, respectively. J_r is the radial component of J, J_x is the axial component of J, and B_θ is the θ component of B, where θ is the third independent variable in cylindrical coordinate system. $B_\theta J_r$ represents the source term S(x) and $B_\theta J_x$ represents the source term S(r). J_r, J_x and B_θ can be derived from steady state version of Maxwell's equations for the electromagnetic field [11]. For semi-infinite thickness of the workpeice, J_r, J_x and B_θ are given as follows [11]:

$$J_x = \frac{I}{2\pi} \int_0^\infty \lambda J_0(\lambda r) \exp(-\lambda x - \lambda^2 r_b^2/12) \, d\lambda \tag{3.7}$$

$$J_r = \frac{I}{2\pi} \int_0^\infty \lambda J_1(\lambda r) \, \exp\left(-\lambda x - \lambda^2 r_b^2/12\right) d\lambda \tag{3.8}$$

$$B_\theta = \frac{\mu_m I}{2\pi} \int_0^\infty \lambda J_1(\lambda r) \, \exp\left(-\lambda x - \lambda^2 r_b^2/12\right) d\lambda \tag{3.9}$$

where μ_m is the magnetic permeability, I is the welding current, r_b is the arc radius, J_0 and J_1 are the Bessel functions of the first kind and of zero and first order, respectively. The equations for evaluating Bessel functions are available in standard mathematical tables in handbooks [12]. With the use of equations of Bessel functions, J_r, J_x and B_θ can be evaluated to obtain S(x) and S(r).

Special features of the computational scheme that have been taken into account include the convective and radiative heat loss from the surface of the pool, and the evaporative heat loss due to vaporization of alloying elements. The local heat flux at the pool surface, J_h, in J/m^2-s is given by:

$$J_h(r) = \frac{3Q\eta}{\pi r_b^2} e^{(-3r^2/r_b^2)} - h(T_l - T_g) - \varepsilon\sigma(T_l^4 - T_g^4) - \sum_{i=1}^n J_i \Delta H_i \tag{3.10}$$

where Q is the power input, η is the absorption coefficient, r_b is the beam radius, T_l is the local weld pool surface temperature, T_g is the ambient temperature, ε is the emissivity, σ is the Stefan-Boltzmann constant, J_i is the vaporization flux of i in kg/m^2-s, ΔH_i is the enthalpy of vaporization of the element i in J/kg, n is the number of alloying elements and h is the heat transfer coefficient in J/m^2-s-K. The procedure for calculating vaporization flux, J_i, is presented in sections 3.1.2.2 and 3.1.2.3. The first term on the right hand side of

equation (3.10) represents heat absorbed from the power source, the second term represents the heat loss to the shielding gas, third term takes into account the radiative heat loss and the last term accounts for the heat loss due to vaporization. The power density distribution of the source is assumed to be Gaussian in nature. The convective heat transfer coefficient in J/m^2-s-K for a gas jet impinging on a surface was derived from the graphical results of Schlunder and Gniclinski [13] and is given by the following relation:

$$ h = \frac{2Pr^{0.42}Re^{0.5}k}{d}\left(1+\frac{Re^{0.55}}{200}\right)^{0.5}\left[0.483 - 0.108\frac{r}{d} + 7.71 \times 10^{-3}\left\{\frac{r}{d}\right\}^2\right] \quad (3.11) $$

where d is the diameter of the nozzle in meters, r is the radial distance on the pool surface in meters, k is the thermal conductivity of shielding gas in J/m-s-K at temperature T_{av}, which is the arithmetic average of T_l and T_g, Re is the Reynolds number at the nozzle exit and Pr is the Prandtl number. The Reynolds number and Prandtl number are given by the following relations:

$$ Re = \frac{\rho u d}{\mu} = \frac{4}{\pi}\frac{\rho}{\mu}\frac{Q_0}{d} \quad (3.12) $$

$$ Pr = Cp\frac{\mu}{k} \quad (3.13) $$

where ρ, μ and Cp are the density, viscosity and specific heat of the shielding gas, respectively, u is the velocity of the shielding gas at nozzle exit and Q_0 is the flow rate of the shielding gas. The procedure for calculating the thermophysical properties of a gas is presented in Appendix A.

The calculations were performed for two-dimensional, steady, incompressible, laminar flow. Fig. 3.1 shows the regions of interest of the weld pool and the boundary conditions used in the calculations. The boundary conditions included the prescription of the heat exchange between the surface of the sample and the laser beam by equation (3.10). At the bottom and the sides of the plate, the temperature was equated to the ambient temperature. At the solid-liquid interface, the curved boundary was approximated by a series of steps and the velocities were prescribed to be zero. At the axis of symmetry the radial velocity, the gradients of axial velocity in the radial direction and temperature were taken to be zero. At the surface of the weld pool, the Marongoni effect was incorporated by equating the shear stress, τ, to the spatial gradient of the surface tension. The shear stress or the Marongoni stress, τ, is given by the following relation:

$$\tau = -\mu\frac{dv}{dx} = \frac{d\gamma}{dT}\frac{dT}{dr} \tag{3.14}$$

where $d\gamma/dT$ is the temperature coefficient of surface tension. For pure metal, $d\gamma/dT$ is constant. For alloys containing surface active elements, $d\gamma/dT$ is a function of composition of the element and temperature at the pool surface and can be calculated based on the formalism developed by Sahoo, DebRoy and McNallan [14].

$$\frac{d\gamma}{dT} = -A - R\Gamma s \ln\left(1 + Ka_i\right) - \frac{Ka_i}{1 + Ka_i}\Gamma s\frac{\Delta H^o}{T} \tag{3.15}$$

where

$$K = k_i\, e^{-\frac{\Delta H^o}{RT}} \tag{3.16}$$

r,v

u,x

$J_h(r)$

r_b

Laser Beam

$\tau = -\mu\dfrac{dv}{dx} = \dfrac{d\gamma}{dT}\dfrac{dT}{dr}$

u = 0

Molten Pool

S(r), S(x)

$T = T_{m.p.}$

Solid/Liquid
Interface

$\dfrac{dT}{dr} = 0, \dfrac{du}{dr} = 0, v = 0$

u = 0
v = 0

Solid

$T = T_{amb}$

$T = T_{amb}$

Axis of Symmetry
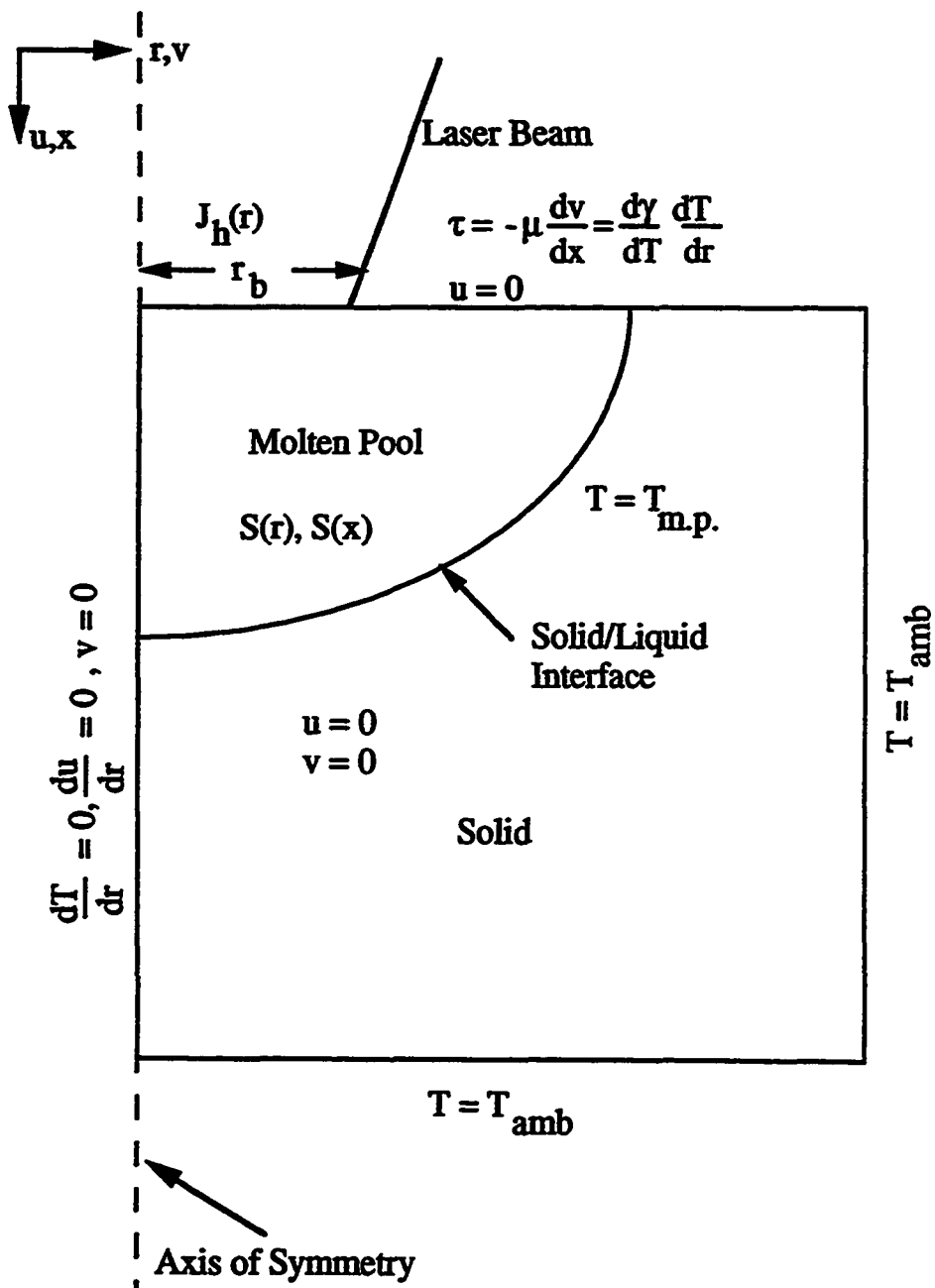
Fig. 3.1   A schematic diagram of the region of interest for the fluid flow and heat transfer calculations along with the boundary conditions.

where A is temperature coefficient of surface tension for pure metal, R is the gas constant, Γs is the surface excess at saturation, k_1 is entropy factor, ΔH^o is the standard heat of absorption and a$_1$ is the activity of the surface active elements.

The governing conservation equations were represented in a finite difference form and solved iteratively on a line-by-line basis utilizing a Tri-Diagonal Matrix Algorithm (TDMA). The Semi-Implicit Method for Pressure-Linked Equations (SIMPLE) algorithm was employed for the discretization of the equations. The details of the procedure are described elsewhere[15]. The adaptation part of the computational program, developed to simulate the welding processes and generate the fluid flow and the temperature fields, along with certain representative test cases are documented elsewhere [16].

3.1.2.2 Vaporization due to Pressure Gradient

In laser processing of metals and alloys, the temperatures reached at the surface of the material often exceed the boiling point [17,18]. For example, von Allmen [19] determined molten pool temperatures in excess of boiling point for laser treatment of copper. Batanov et al. [20] indicated that temperatures on the surface of the laser irradiated material can be higher than the normal boiling point. Paul and DebRoy [21] and Zacharia et al.[22] have reported temperatures close to the boiling point for laser welding. Khan and DebRoy [2] measured the liquid pool surface temperatures close to the boiling point from the ratio of the rates of vaporization of alloying elements. Chan and Majumdar [23] have also reported temperatures greater than boiling point for the laser irradiation of aluminum, titanium and a superalloy. Theoretical calculations of the vaporization rates by Anisimov [24] and Knight

[25] are based on the premise that the liquid pool surface temperatures are higher than the boiling point.

At temperatures greater than the boiling point, the pressures at the pool surface are higher than the ambient pressure and the excess pressure provides a driving force for the vapor to move away from the surface. The velocity distribution functions of the vapor molecules, f_1, f_2 and f_3, escaping from the weld pool surface at various locations are shown schematically in Fig. 3.2. Near the weld pool surface, the molecules cannot travel in the negative direction i.e. towards the pool surface and, as a consequence, the distribution function is half-Maxwellian. Close to the weld pool surface, there exists a space of several mean free paths length, known as the Knudsen layer, at the outer edge of which the velocity distribution reaches the equilibrium distribution. Here, the vapor molecule velocity, ξ, can vary from $-\infty$ to $+\infty$, as observed in Fig. 3.2. A portion of the vaporized material condenses on the liquid surface.

The temperature T_v, density ρ_v, pressure P_v and the mean velocity of the vapor, u, at the edge of the Knudsen layer can be related to temperature, T_l, pressure, P_l, and the density, ρ_l, of the vapor at the liquid surface by treating the Knudsen layer as a gasdynamic discontinuity. Anisimov [24] and Knight [25] derived expressions for the changes in the vapor density, temperature, velocity and the extent of condensation by using the velocity distribution functions presented in Fig. 3.2 and solving the equations of conservation of mass, momentum, and translational kinetic energy across the Knudsen layer. Since the details of the procedure are available in their papers and the equations are derived in Appendix B, only a summary of the results, commonly referred to as the jump conditions, are presented in equations (3.17) through (3.19).

$$f_3 = \sqrt{\frac{1}{2\pi R T_v}} \exp\left(-\frac{(\xi-u)^2}{2RT_v}\right)$$

Shielding Gas $\quad \rho_g, P_g, T_g$ Pressure
Wavefront

Shielding Gas $\quad \rho_2, P_2, T_2$ Contact
Discontinuity

f_3

ξ

Vapor $\quad \rho_v, P_v, T_v$

f_1

Knudsen Layer

f_2

ρ_l, P_l, T_l

ξ

$+y$

0

$-y$

ξ

$f_2 = \beta f_3$

Liquid

$$f_1 = \sqrt{\frac{1}{2\pi R T_l}} \exp\left(-\frac{\xi^2}{2RT_l}\right)$$

Solid
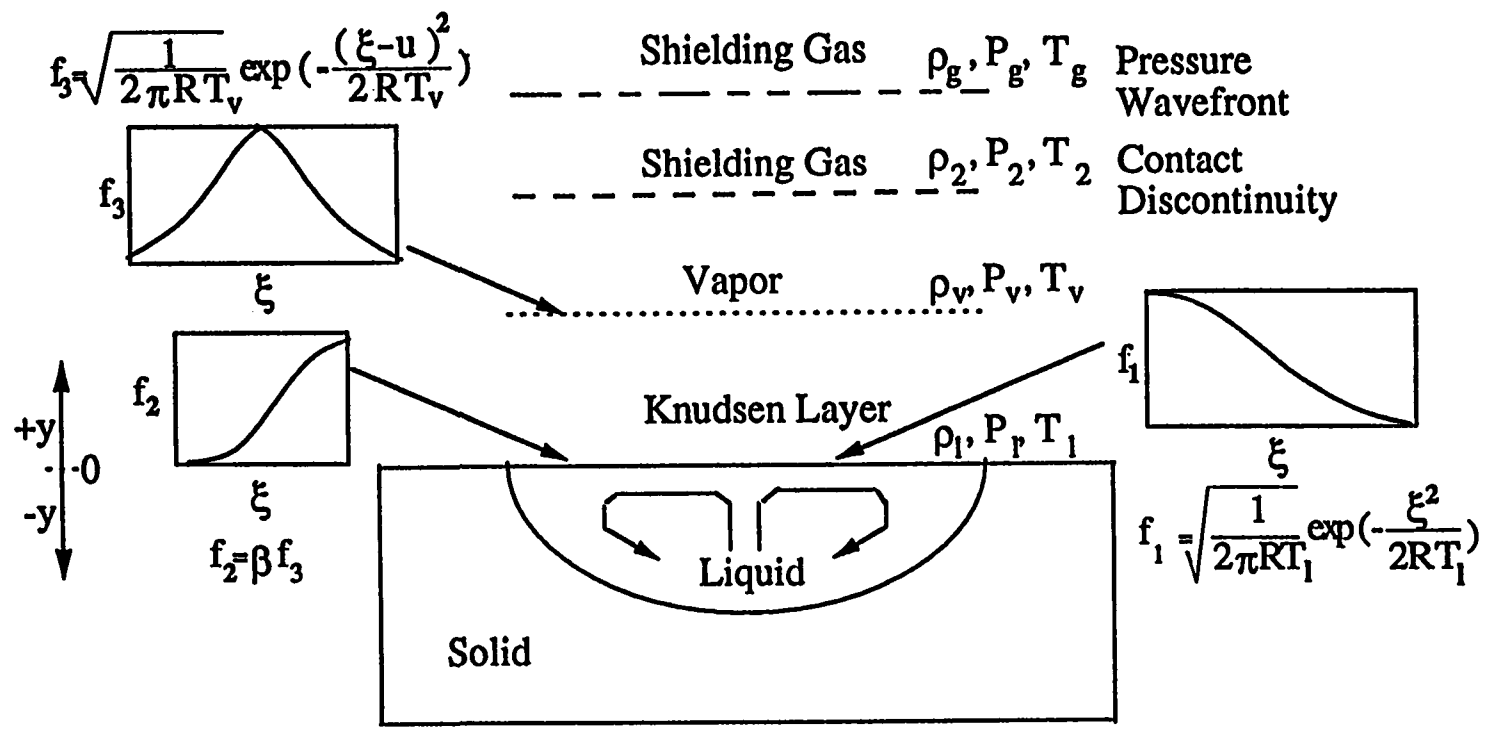
Fig. 3.2   A schematic diagram of the velocity distribution functions in the Knudsen layer
and the adjacent regions.

52

$$\frac{T_v}{T_1} = \left(\sqrt{1 + \pi \left(\frac{\gamma_v - 1}{\gamma_v + 1} \frac{m}{2} \right)^2} - \sqrt{\pi} \frac{\gamma_v - 1}{\gamma_v + 1} \frac{m}{2} \right)^2 \qquad (3.17)$$

where $m = u/\sqrt{2 R_v T_v}$, $R_v = R/M_v$, γ_v is the ratio of specific heats of the vapor which is treated as a monatomic gas and M_v is the average molecular weight of the vapor in kg/mole.

$$\frac{\rho_v}{\rho_1} = \sqrt{\frac{T_1}{T_v}} \left((m^2 + \frac{1}{2}) e^{m^2} \mathrm{erfc}(m) - \frac{m}{\sqrt{\pi}} \right) + \frac{1}{2} \frac{T_1}{T_v} \left(1 - \sqrt{p}\, m e^{m^2} \mathrm{erfc}(m) \right) \qquad (3.18)$$

where erfc is the complimentary error function.

The condensation factor, β, is given by:

$$\beta = \left((2m^2 + 1) - m \sqrt{\pi \frac{T_1}{T_v}} \right) e^{m^2} \frac{\rho_1}{\rho_v} \sqrt{\frac{T_1}{T_v}} \qquad (3.19)$$

The density, ρ_1, can be computed from P_1 and T_1 assuming that the vapor behaves like an ideal gas. The equilibrium vapor pressure, P_1, at the pool surface is obtained from the equilibrium vapor pressure-temperature relationships of the various alloying elements.

$$\frac{P_1}{P_g} = \sum_{i=1}^{n} a_i \frac{P_i^0}{P_g} \qquad (3.20)$$

where P_g is the ambient pressure, a_i is the activity of the alloying element i and P_i^0 is the equilibrium vapor pressure of the pure element i at T_1 and n is the number of alloying

elements. For pure metals n is equal to one, a_i is equal to unity and equation (3.20) reduces to $P_1 = P_i^0$. The Knudsen layer extends only a few molecular mean free path in thickness and it is filled with metal vapor. Therefore, the total pressure is determined by adding the equilibrium vapor pressures of the individual components. The shielding gas is not present in this layer. Since the temperatures at the weld pool surface are very high, the activities were taken to be equal to the corresponding mole fractions. The average molecular weight of the vapor, M_v, in the Knudsen layer is given by:

$$M_v = \sum_{i=1}^{n} M_i \frac{a_i P_i^0}{P_1} \tag{3.21}$$

where M_i is the molecular weight of species i, a_i is the activity of species i in the liquid metal, and P_i^0 and P_1 are the equilibrium vapor pressures of the pure element i and total equilibrium vapor pressure at the pool surface, respectively at T_1. For pure metals equation (3.21) reduces to $M_v = M_i$. Since there are four unknowns in equation (3.17) through (3.19), viz. T_v, ρ_1, β and m, it is necessary to have an additional equation to have unique values of these variables. The necessary equation is obtained by relating the pressure at the edge of the Knudsen layer to the ambient conditions. Across the Knudsen layer the vapor wavefront moves into the shielding gas, as shown in Fig. 3.2. The moving interface between the vapor and the shielding gas is a contact discontinuity. Across this interface, the pressures are the same, i.e., $P_2 = P_v$. However, there are discontinuities in temperature and the density [26]. The pressure rise at the liquid-vapor interface propagates as a pressure wave as shown in Fig. 3.2. The wavefront may be treated as a pressure discontinuity, and the pressure change across the wavefront may be obtained by applying the Rankine-Hugoniot relationship [27]:

$$\frac{P_1}{P_g}\frac{P_2}{P_1} = 1 + \gamma_v M\Gamma \left(\frac{\gamma_v + 1}{4} M\Gamma + \sqrt{1 + (\frac{\gamma_v + 1}{4} M\Gamma)^2}\right) \qquad (3.22)$$

where P_g and P_2 are the pressures in front of and behind the wavefront respectively, γ_v is the ratio of specific heats for shielding gas and $\Gamma = \sqrt{\gamma_v P_v T_v} / \sqrt{\gamma_g P_g T_g}$. The Mach number, M is related to m according to the equation:

$$m = M \sqrt{\frac{\gamma_v}{2}} \qquad (3.23)$$

In equation (3.22), P_1/P_g can be computed from equation (3.20) for a given local surface temperature and, since $P_2 = P_v$, for an ideal gas, P_2/P_1 can be expressed as a function of m with the help of equations (3.17) and (3.18). Thus, equation (3.22) is effectively reduced to a nonlinear equation in m and can be solved iteratively or graphically to obtain m and the Mach number for a given local weld pool surface temperature. The values of T_v, ρ_v and β, corresponding to a local temperature T_l can be determined from equations (3.17) through (3.19) by using the computed value of m. The procedure for the calculation of temperature, pressure and density at various locations in the gas phase is summarized in Appendix C. The computer program developed to calculate the Mach number and density of vapor at the edge of Knudsen layer for pure metal and AISI 201 steel is presented in Appendix D.

The Mach number and the density ρ_v can be used to calculate the vaporization flux, J_p, in kg/m^2-s, due to pressure gradient at the pool surface corresponding to a local surface temperature T_l.

$$J_p = \rho_v M S \qquad (3.24)$$

where S is the speed of sound in vapor at temperature T_v. Since the rate of vaporization of an alloying element is proportional to its partial pressure over the pool, its flux, $J_{p,i}$ is given by:

$$J_{p,i} = a_i \frac{P_i^o}{P_l} \frac{M_i}{M_v} J_p \tag{3.25}$$

The total condensation flux, J_{cond}, in kg/m²-s, due to the excess pressure at surface temperature T_l is given by [24]:

$$J_{cond} = \beta \rho_v \sqrt{\frac{R_v T_v}{2\pi}} \left(e^{-m^2} - m\sqrt{\pi} \, \text{erfc}(m) \right) \tag{3.26}$$

where β is the condensation factor defined by equation (3.19).

3.1.2.3 Vaporization due to Concentration Gradient

At the pool surface, the concentrations of the alloying elements in the vapor is considerably higher than their respective concentrations in the bulk shielding gas. The vaporization flux of an element i due to concentration gradient, $J_{c,i}$, in kg/m²-s, is then defined as:

$$J_{c,i} = K_{g,i} \left(M_i \frac{a_i P_i^o}{RT_l} - C_i^b \right) \tag{3.27}$$

where P_i^o is equilibrium vapor-pressure of the element i over pure liquid in atmosphere, M_i is the molecular weight of the element i in kg/kg-mole, R is the gas constant in m³ atm/kg-mole K, $K_{g,i}$ is the mass transfer coefficient of the element i in m/s and C_i^b is the

concentration of the element i in kg/m^3 in the bulk shielding gas. The concentration of element i in the bulk of the gas, C_i^b, will be significantly lower than at the surface and therefore can be neglected. The mass transfer coefficient was derived form the graphical results of Schlunder and Gniclinski [13] and is given by:

$$K_{g,i} = \frac{2Sc^{0.42}Re^{0.5}D}{d}\left(1+\frac{Re^{0.55}}{200}\right)^{0.5}\left[0.483-0.108\frac{r}{d}+7.71\times10^{-3}\left(\frac{r}{d}\right)^2\right] \qquad (3.28)$$

where d is the diameter of the nozzle in meters, r is the radial distance on the pool surface in meters, D is the diffusivity of the element in the shielding gas in m^2/s at temperature T_{av}, Re is the Reynolds number at the nozzle exit and Sc is the Schmidt number of the element at average temperature T_{av}. The total vaporization flux, J_i for an element i is then given by:

$$J_i = J_{c,i} + J_{p,i} \qquad (3.29)$$

3.1.2.4   Composition Change in the Weld Pool

If the total rate of vaporization and the rates of vaporization of the alloying elements are known, the composition of the weld metal can be predicted by simple mass balance. The final weight percent of an element i, $(wt\%i)_f$ is given by:

$$(wt\%i)_f = \frac{vA\rho(wt\%i)_i - 100\,P\int_0^r 2\pi J_i r\,dr}{vA\rho - P\int_0^r 2\pi J r\,dr} \qquad (3.30)$$

where v is the scanning speed in m/s, ρ is the density of the weld metal in kg/m^3, (wt%i)$_i$ is the initial weight percent of an element i in the weld metal, $\int_0^r 2\pi J_i r\, dr$ and $\int_0^r 2\pi J r\, dr$ are the rates of vaporization of an element i and the total rate of vaporization, respectively, in kg/s, where $\int_0^r 2\pi r\, dr$ represents the top surface of the weld pool from where the vaporization is taking place, A is the area of the vertical cross-section perpendicular to the scanning direction in m^2, and P is the fraction (<1) that takes into account the effect of plasma on the vaporization rate. The role of plasma in influencing the vaporization rates was discussed in Chapter 2, section 2.1.2.2. During the course of this investigation, experiments were conducted to correlate the plasma characteristics to the vaporization rate. The experimental procedure is discussed in the next section. The areas of interest in the calculation of the composition change are shown in Fig. 3.3. For low laser beam velocities, the weld pool top surface is assumed to be circular. The composition change is then by

$$(\Delta wt\%i) = (wt\%i)_f - wt\%i)_i \qquad (3.31)$$

The listing of the Fortran program developed to calculate the vaporization rates and the composition change of the various alloying elements is given in Appendix E.

3.2 Effect of Plasma on Vaporization Rates

3.2.1 Experimental Procedures

In most welding processes a strong plasma is always present near the weld pool surface. It has been suggested in the literature [28,29] that plasma affects vaporization rates.
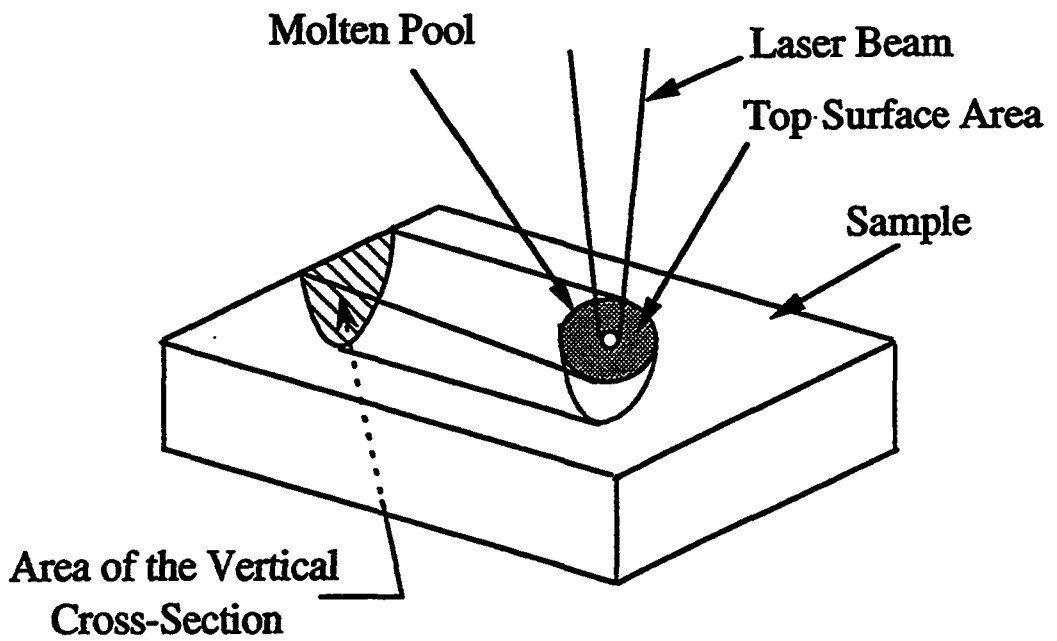
Fig. 3.3 A schematic diagram of the areas of interest in the calculation of weld metal composition change.

However, very little information on the effect of plasma on vaporization rates can be obtained from the welding experiments. This is due to the fact that designing two sets of welding experiments such that in one set plasma is formed and in the other set plasma is absent, and at the same time maintaining identical temperature conditions on the pool surface, is extremely difficult. To overcome this difficulty, physical modeling experiments were conducted. Fig. 3.4 shows a schematic diagram of the experimental set-up employed in the isothermal vaporization experiments. A radio frequency (RF) induction furnace capable of supplying up to 10 KW of power at 450 KHz was used as the power source. The rf power was supplied through a copper coil wound on a quartz tube. For the experiments in the presence of plasma, copper coil with twelve turns and a total length of 7 cm was used. Thin, circular, disc-shaped samples of ultra pure iron with 1.6 ± 0.3 mm thickness and 5.0 mm diameter were placed on a tantalum wire specimen holder. To start the experiment, the system was evacuated and filled with helium gas. Helium was passed at a flow rate of 200 cc/sec. The gas flow was monitored using MKS mass flow controller. The sample was then heated to a temperature of 1573 K by adjusting the rf power. A two-color pyrometer with an internal calibration standard of 2273 K was used for the temperature measurements. The experiments were carried out at different pressures. The pressure in the chamber was monitored and controlled with an MKS Baratron pressure gauge and an electrically operated throttle value. The duration of the experiments was counted after the adjustment of temperature, which took less than two minutes. The experiments were conducted for 45 minutes. The rate of vaporization was determined from the weight change of the sample, the exposure time and the surface area of the sample.

To correlate the plasma characteristics with the rates of vaporization, an emission spectroscope was used to characterize the plasma. The light emission data is useful to identify the various species present in the plasma and to determine important plasma
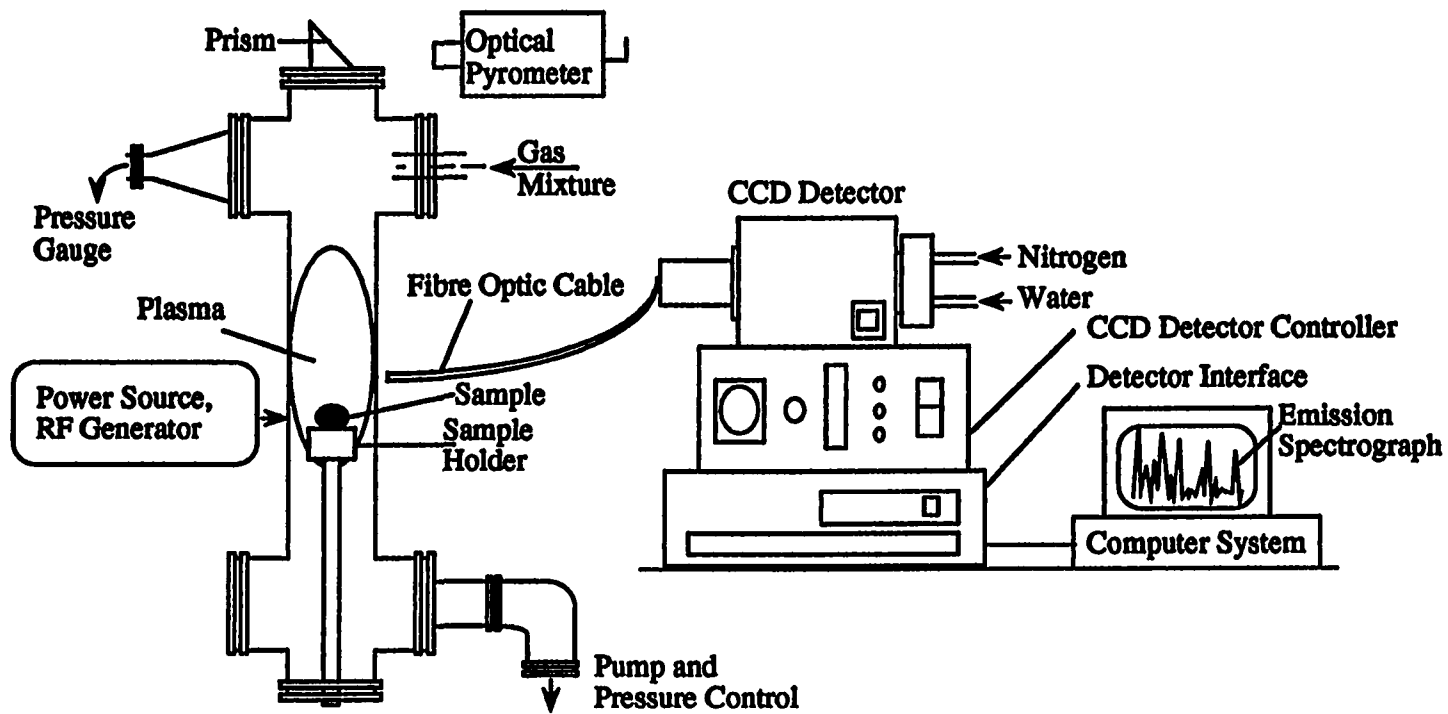
Fig. 3.4   A schematic diagram of the experimental set-up used for isothermal vaporization experiments.

parameters such as electron density and electron temperature. The emission spectroscope system, model 1461 OMA (optical multichannel analyzer) of Princeton Applied Research Corporation, was used along with a host computer system and OMA 2000 software for acquisition and analysis of the data. The light emissions were transmitted to the spectrograph using optical fibers. Diffraction gratings with 1200 lines/mm was used for data scanning and acquisition. Wavelength calibration was achieved using argon, neon and mercury calibration lamps.

A set of vaporization experiments at different pressures was carried out in the absence of plasma to compare the rates of vaporization in the presence and the absence of plasma. The formation of plasma was avoided by using a short copper coil with fewer turns around the quartz tube. Four turns in a length of 3 cm was used. A small amount of hydrogen was added to helium in the experiments since hydrogen makes the formation of plasma difficult. The difference in diffusivity of iron vapor in helium and hydrogen at 1573 K and 10 torr pressure is less than 7 percent (960 cm^2/s for helium and 1025 cm^2/s for hydrogen). Therefore, the addition of a small amount of hydrogen to helium would not change the mass transfer rate of iron vapor through helium in any significant way.

3.3 Gas Dissolution and Two Temperature Model

Most of the previous works on the solubility of gaseous species in metals exposed to plasma were conducted using electric arcs and relatively large quantities of metals [30-32]. In these investigations, the metal in contact with the plasma jet was exposed to a strong temperature gradient, with the maximum temperature established at the jet axis. It is known from recent studies [11, 21, 22] that when a liquid metal is heated by an electric arc, the

propagation of strong convection currents due to Marangoni, densimetric, and electromagnetic effects is insufficient to eliminate the commonly present strong temperature gradient within the liquid metal. Therefore, the local gas dissolution rate changes in a manner commensurate with the temperature profile on the liquid metal surface. Although, a steady state concentration of dissolved gas for such systems can be determined experimentally, the inevitable existence of a large temperature gradient precludes straightforward interpretation of the experimental data. As a consequence, such data provide very little information about the physics of the dissolution process. The difficulties encountered in the analysis of the results can be overcome by conducting controlled experiments with metal drops held isothermally in a well defined environment. For example, Ouden and Griebling [33] exposed ultra-pure iron samples to a mixture of nitrogen and argon in the presence of an electric arc. Similarly, Bandopadhyay et al. [34] separately exposed high purity niobium and tantalum samples to well characterized helium and nitrogen plasma at a constant temperature and determined the nitrogen content of the samples. Such carefully controlled physical modeling experiments can provide valuable insight into the physics of the dissolution process and, at the same time, the data obtained can be used for verification of any model developed to predict the solubility of gases in metals.

As stated above, in the physical modeling experiments with pure metal drops maintained at a constant temperature, the complexity of temperature gradient on the surface of the drop is eliminated. This makes the task of modeling of the dissolution processes relatively easy. Furthermore, since the samples are quenched quickly after the plasma is switched off, all the gas dissolved is retained in the drop and this gives a true measure of the gas dissolved in the drop. A schematic representation of the mathematical model is given in Fig. 3.5. It is assumed that the gas near the metal drop consist primarily of neutral diatomic and
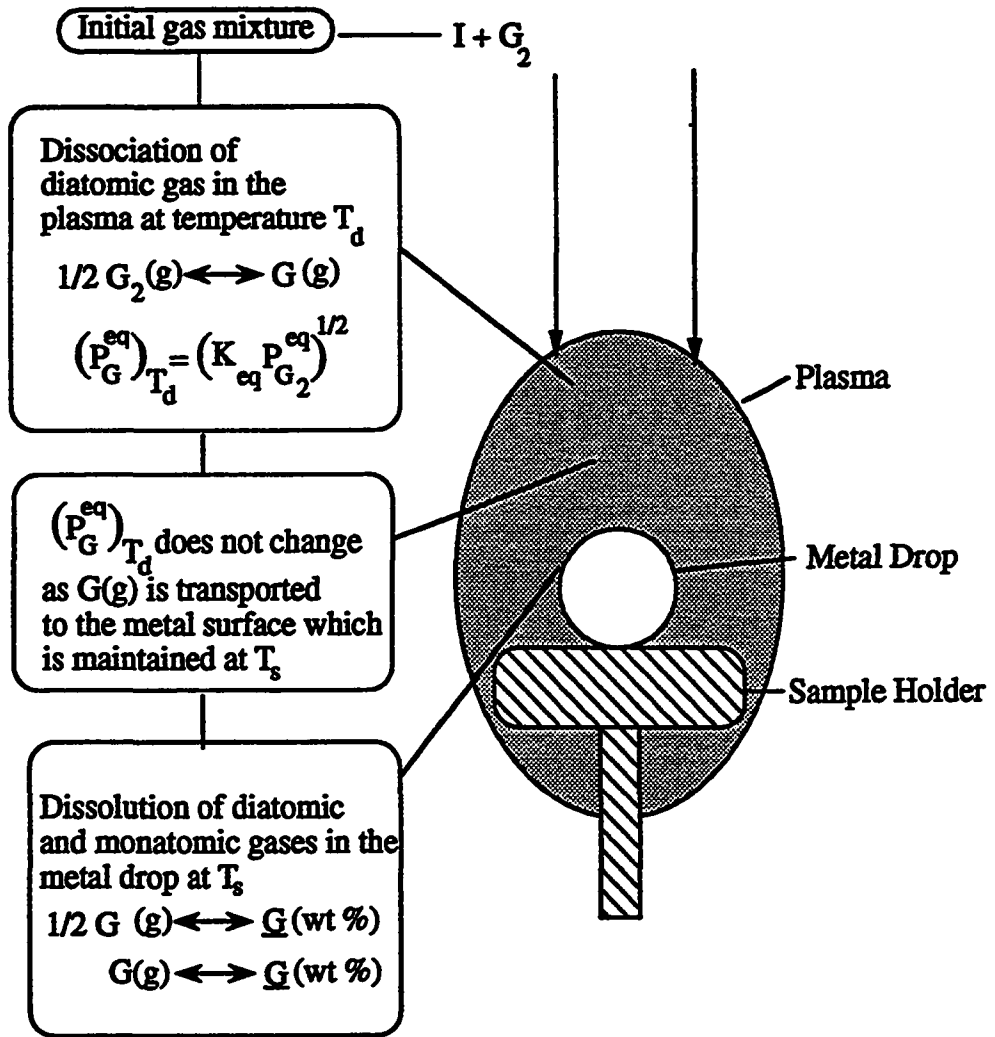
Fig. 3.5 A schematic diagram of the two temperature model for gas dissolution.

monatomic species of the source gas, in addition to the inert gas present in the initial mixture. In the model, it is postulated that the diatomic gas dissociates in the presence of an arc or any other plasma generating source. It is also assumed that the dissociation temperature, T_d, is different from the sample temperature, T_s. Furthermore, it is assumed that after the dissociation of the diatomic gas takes place at T_d, there is no change in the partial pressures of diatomic and monatomic gas and subsequently the gas dissolves in the sample at temperature T_s. The reactions that are of interest, in the dissolution of gas G, are

$$\frac{1}{2} G_2 \text{ (g)} = G\text{(g)} \qquad\qquad \Delta G_1^o \qquad\qquad (3.32)$$

$$\frac{1}{2} G_2 \text{ (g)} = \underline{G}^d \text{ (wt \%)} \qquad\qquad \Delta G_2^o \qquad\qquad (3.33)$$

$$G\text{(g)} = \underline{G}^m \text{(wt \%)} \qquad\qquad \Delta G_3^o \qquad\qquad (3.34)$$

where ΔG^{o}'s are the standard free energies of the reactions. From equations (3.33) and (3.34) the solubilities of the gas in the sample, maintained at temperature T_s, due to diatomic and monatomic species are given by

$$\underline{\text{Diatomic:}} \qquad \underline{G}^d \text{ (wt \%)} = \sqrt{P_{G_2}} \; e^{- \frac{\Delta G_2^o}{RT_s}} \qquad\qquad (3.35)$$

$$\underline{\text{Monatomic:}} \quad \underline{G}^m \text{(wt \%)} = P_G \, e^{- \frac{\Delta G_3^o}{RT_s}} \qquad\qquad (3.36)$$

Thus, in order to calculate the solubility in samples we need to know the values of P_{G_2} and P_G. If the initial gas mixture consists of y % diatomic gas in an inert gas I, and x % of the diatomic gas dissociates at temperature T_d, then from equation (3.32) we can write

$$P_G = (P_{G_2})^{1/2} e^{-\frac{\Delta G^o_1}{RT_d}}$$ (3.39)

From gas composition we can also write

$$\frac{P_{G_2}}{P_G} = \frac{(100\text{-}x)}{2x}$$ (3.40)

If the total chamber pressure is P_T, we have

$$P_I = \frac{(100\text{-}y)P_T}{(100+yx/100)}$$ (3.41)

and

$$P_I + P_{G_2} + P_G = P_T$$ (3.42)

where P_I is the pressure of the inert gas. In equations (3.39) through (3.42), for an assumed temperature of dissociation T_d, we have four unknowns, viz. P_G, P_{G_2}, P_I and x. Therefore, they can be solved iteratively or graphically to get unique values of these variables. The values of P_{G_2} and P_G can be used to predict the solubility due to diatomic and monatomic species from equations (3.35) and (3.36), respectively, for an assumed temperature of dissociation. Since the presence of diatomic species alone cannot explain the enhanced solubility, it is anticipated that the presence of monatomic species in the gas phase would help explain the increased solubility.

3.4 References

1. P. A. A. Khan, Ph. D. Thesis, The Pennsylvania State University, 1987.

2. P. A. A. Khan and T. DebRoy, Metall. Trans. **15B**, 641 (1984).

3. P. A. A. Khan, T. DebRoy and S. A. David, Welding Journal **67**, 1 (1988).

4. S. Basu, M. S. Thesis, The Pennsylvania State University, 1992.

5. T. DebRoy, S. Basu and K. Mundra, J. Appl. Phys. **70**, 1313 (1991)

6. R. Miller and T. DebRoy, J. Appl. Phys. **68**, 2045 (1990).

7. G. J. Dunn, C. D. Allemand, and T. W. Eagar, Metall. Trans. **17A**, 1851 (1986).

8. M. M. Collur and T. DebRoy, Metall. Trans. **20B**, 277 (1989).

9. M. M. Collur, Ph. D. Thesis, The Pennsylvania State University, 1988.

10. R. B. Bird, W. E. Stewart and E. N. Lightfoot, Transport Phenomena (John Wiley and Sons, New York, NY, 1960).

11. S. Kou and D. K. Sun, Metall. Trans. **16A**, 203 (1985).

12. CRC Standard Mathematical Tables, 28th Edition, W. H. Beyer, Ed. (CRC Press, Inc., Florida, 1987).

13. E. U. Schlunder and V. Gniclinski, Chem. -Ing. -Tech. **39**, 578 (1967).

14. P. Sahoo, T. DebRoy and M. J. McNallan, Metall. Trans. **19B**, 483 (1988).

15. S. V. Patankar, Numerical Heat Transfer and Fluid Flow (McGraw-Hill, New York, NY, 1980).

16. K. Mundra and T. DebRoy, Unpublished Research, The Pennsylvania State University, 1993.

17. S. I. Anisimov, A. M. Bonch-Bruevich, M. A. El'yashevich, Ya A. Imas, N. A. Pavlenko and G. S. Romanvov, Soviet Phys.-Tech. Phys. **11**, 945 (1967).

18. F. W. Dabby and U. Paek, IEEE Journal of Quantam Phys. **QE-8**, 106 (1972).

19. M. von Allmen, Laser Beam Interactions with Materials (Springer- Verlag, Berlin, 1987), p. 161.

20. V. A. Batanov, F. V. Bunkin, A. M. Prokhorov and V. B. Fedorov, Soviet Physics - JETP **36**, 311 (1973).

21. A. Paul and T. DebRoy, Metall. Trans. **19B**, 851 (1988).

22. T. Zacharia, S. A. David, J. M. Vitek and T. DebRoy, Welding Journal **68**, 499 (1989).

23. C. L. Chan and J. Mazumder, J. Appl. Phys. **62**, 4579 (1987).

24. S. I. Anisimov and A. Kh. Rakhmatulina, Soviet Physics - JETP **37**, 441 (1973).

25. C. J. Knight, AIAA Journal **17**, 519 (1979).

26. G. Emanuel, Gasdynamics: Theory and Application (AIAA Education Series, New York, NY, 1986).

27. W. Vincenti and C. Kruger, Introduction to Physical Gas Dynamics (Wiley, New York, NY, 1965).

28. P. Sahoo, M. M. Collur and T. DebRoy, Metall. Trans. **19B**, 967 (1988).

29. P. Sahoo and T. DebRoy, Materials Letters **6**, 406 (1988).

30. S. Ohno and M. Uda, Trans. Nat. Res. Inst. Met. **23**, 243 (1981).

31 M. Uda, S. Ohno and T. Wada, J. Jpn. Weld Soc. **38**, 382 (1969).

32. J. D. Katz and T. B. King, Metall. Trans. **20B**, 175 (1989).

33. G. Den Ouden and O. Griebling, Recent Trends in Welding Science and Technology, S. A. David and J. M. Vitek, Eds., (ASM International, Metals Park, OH, 1990) p. 431.

34. A. Bandopadhyay, A. Banerjee and T. DebRoy, Metall. Trans. **23B**, 207 (1992).

Chapter 4

RESULTS AND DISCUSSION

4.1 Vaporization from Weld Pool Surface

4.1.1 Role of Thermophysical Properties in Weld Pool Fluid Flow and Heat Transfer Modeling

The rate of vaporization of alloying elements from the weld pool surface is influenced by the temperature distribution at the pool surface. During this investigation the temperature fields on the weld pool surface were simulated by numerical solution of the Navier-Stokes equation and the equation of conservation of energy. The details of the equations, boundary conditions and the solution procedure are outlined in Chapter 3.

Values of several important thermophysical properties are necessary to solve Navier-Stokes equation and the equation of conservation of energy for simulating heat transfer and fluid flow in the weld pool. Our existing database of high-temperature materials processing was developed, to a large extent, to understand the manufacture and the subsequent processing or use of metals and alloys [1,2]. Unlike welding, these operations are seldom carried out at temperature much above the melting point of metals or alloys. Furthermore, in most thermochemical processing, the processing environment does not contain plasma [1,2]. In contrast in many welding operations, the peak temperature in the weld pool can be very high and the weld metal is surrounded by plasma [3-5]. Thermophysical data for such high-temperatures are scarce, if not available. Therefore, it is important to examine the

impact of the choice of thermophysical properties on the results of fluid flow and heat transfer in a weld pool [2].

For the solution of the equations of conservation of mass and momentum, equations (3.1) to (3.3), density, ρ, and viscosity, μ, data are required. Similarly, values of thermal conductivity, k, specific heat, Cp, and density, ρ, are necessary for the solution of the equation of conservation of enthalpy. However, in equation (3.4), the thermal conductivity and the specific heat appear as a single variable, k/Cp. The value of energy absorption coefficient and the laser beam power density distribution are needed to define the energy influx at the surface. Furthermore, one needs to know the temperature dependence of surface tension, dγ/dT, to calculate the shear stress at the weld pool surface in accordance with equation (3.14). Thus, for a constant material density and given laser beam power density distribution, the important properties required for the calculations are the absorption coefficient, the temperature coefficient of surface tension, viscosity of the molten metal and the ratio of thermal conductivity and the specific heat for both the solid and the liquid phases. The plots of specific heat, Cp, thermal conductivity, k, and their ratio, k/Cp for pure iron [6,7] as functions of temperature are presented in Fig. 4.1. It is observed from Fig. 4.1, that for solid iron, the values of k/Cp vary from 0.24 gm/cm-sec to 1.8 gm/cm-sec. Similar variations in the values of other thermophysical properties are common in literature. Since temperature independent constant values of thermophysical properties have been frequently used in the literature, it is important to understand the consequences of such practice.

Fig. 4.2 shows the steady state velocity and temperature fields, for laser welding of iron with a laser power of 500 W, obtained using four different combinations of thermophysical properties. Specific variations are given in the figure caption. The enthalpy field obtained
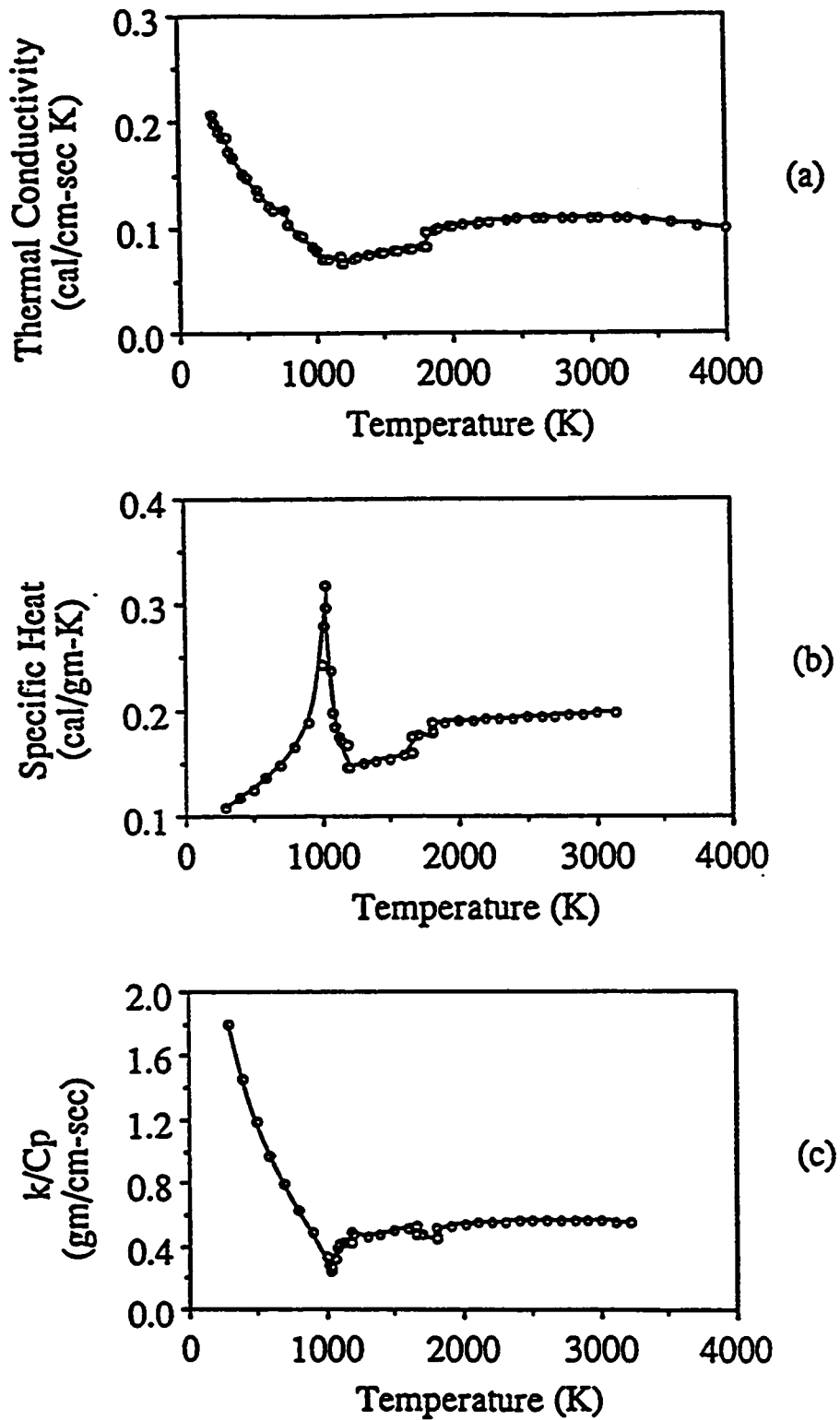
Fig. 4.1   Variation of thermal conductivity, k, specific heat, Cp, and k/Cp as a function of temperature for iron.

Velocity Fields

Temperature Fields
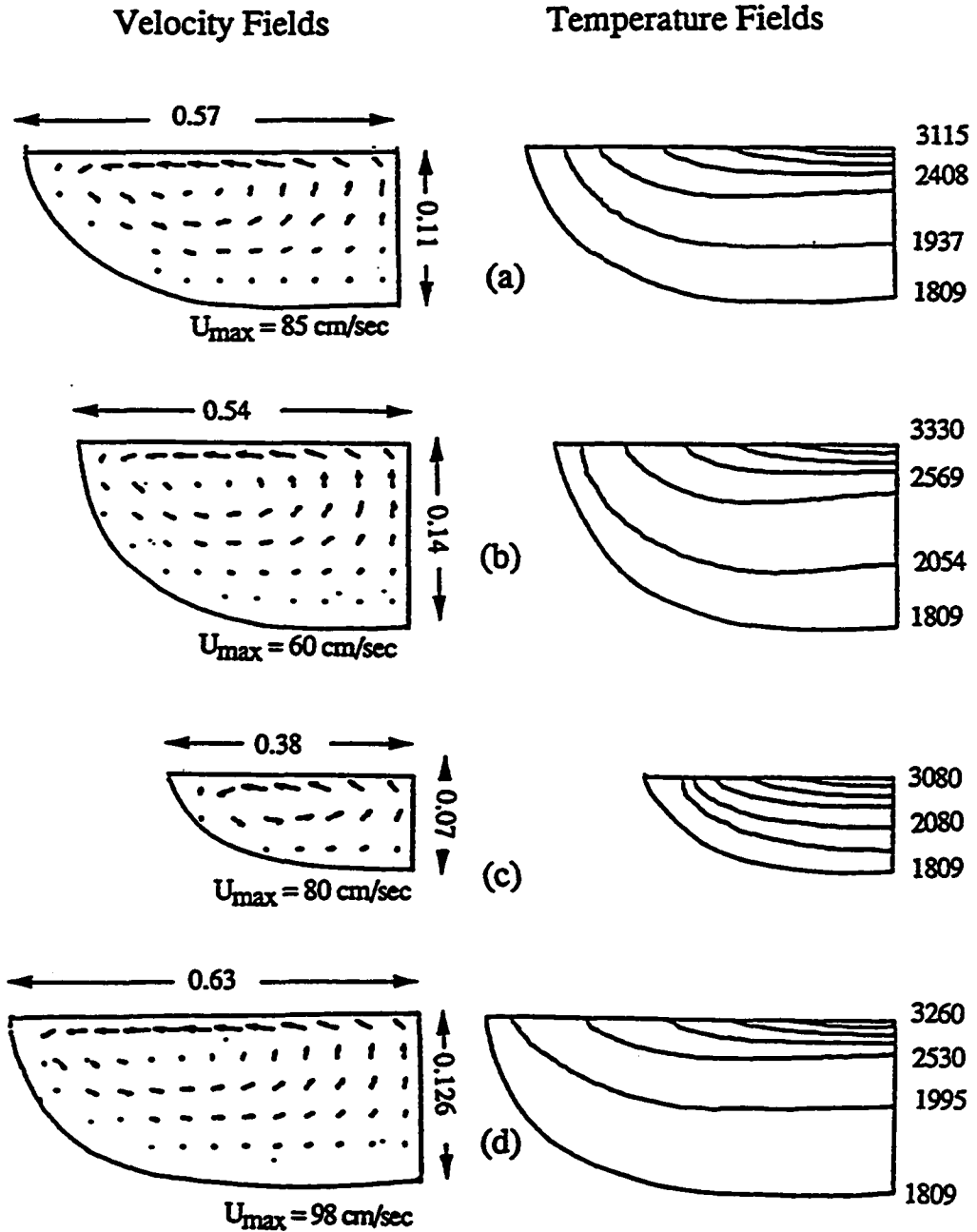
Fig. 4.2 Velocity and temperature fields for four different cases. a) data used as in the table, b) viscosity used is 1.0 gm/cm-sec, c) k/Cp of solid used is 0.48 gm/cm-sec and d) absorption coefficient used 0.18. All dimensions are in mm and temperatures are in K.

through the solution of equations of conservation of mass, momentum and energy was converted to temperature field using data presented in Fig. 4.3 [7]. The values of the thermophysical properties used for the calculations are indicated in Table 4.1. It is observed from the computed results that depending on the values of the thermophysical properties used, the pool geometry and the temperature and the velocity fields can vary significantly. Since a detailed discussion of the impact of various thermophysical properties on fluid flow and heat transfer in a weld pool is given elsewhere [2], it is not presented here. The results indicate that accurate values of thermophysical properties are necessary for realistic simulation of weld pool behavior.

4.1.2 Vaporization of Pure Metal

4.1.2.1 Velocity and Temperature Fields

When a laser beam strikes the surface of the sample, melting occurs almost instantaneously. For a high power density laser beam, the time required to reach the steady state is very small. Zacharia et al. [8] noted that in laser welding "quasi-steady" state is achieved very quickly as the energy supplied to the weld pool is rapidly conducted away by the base metal. Mehrabian et al. [9] showed that the time required to reach the maximum melt depth in iron for a laser power of 2×10^5 watts/cm^2 is of the order of 1 msec. Thus, for much of the duration of a large laser pulse of several milliseconds span, the molten pool is in a steady state. The steady state temperature and velocity fields for iron and titanium welded with a laser power of 500 W in an argon atmosphere, calculated from the solution of Navier-Stokes equation and the equations of conservation of mass and energy, are shown in Fig. 4.4. The calculation takes into consideration the heat loss to the argon
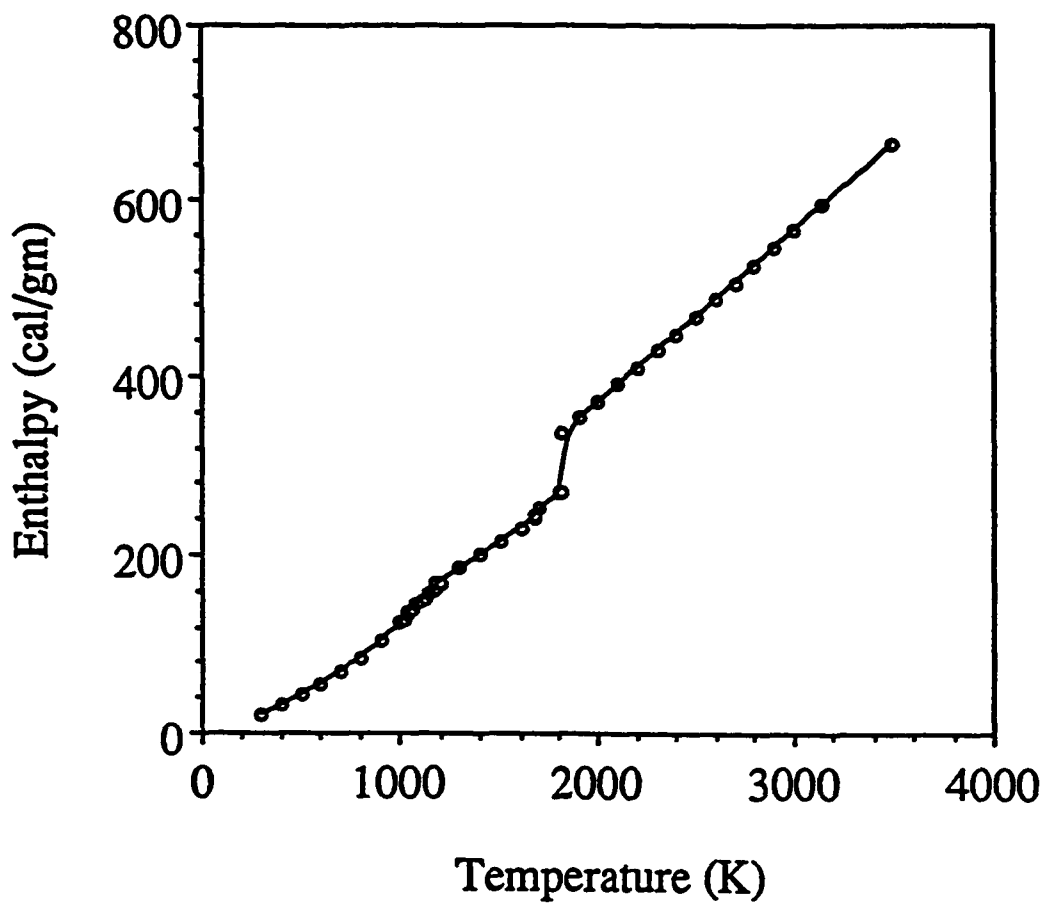
Fig. 4.3   Enthalpy vs. temperature curve for iron.

Table 4.1 Data used for the calculation of velocity and temperature fields presented in Fig. 4.2.

Property/Parameter	Value
Density (gms/cm^3)	7.80
Melting Point (K)	1809.0
Laser Power (Watts)	500.0
Radius of the Beam (cm)	0.20
Viscosity (gm/cm-sec)	0.40
k/Cp of Solid (gm/cm-sec)	0.24
k/Cp of Liquid (gm/cm-sec)	0.54
Absorption Coefficient	0.15
Temperature Coefficient of Surface Tension (dyne/cm-K)	-0.50

Velocity Field

0.034 cm   0.016 cm

0.039 cm   0.019 cm

Vector Scale —— 100 cm/sec.

Temperature Field

3300 K
2301 K
1927 K
1811 K

3744 K
2775 K
2221 K
1941 K

a)

b)

Fig. 4.4   Velocity and temperature Fields for a) iron and b) titanium for a laser power of 500 W and argon flow rate of 1 liter/min.

shielding gas in accordance with equation (3.10). The data used for the calculations are presented in Table 4.2. The details of the calculations of thermal diffusivity and viscosity of the shielding gas used in the calculations are described in Appendix A. The laser beam absorption coefficient for iron was taken from the data of Khan and DebRoy [10], and the absorption coefficient value for titanium was calculated using Bramson's empirical relation [11]. Both iron and titanium have negative temperature coefficients of surface tension, $d\gamma/dT$. Therefore, the velocities at the surface are radially outwards resulting in a relatively shallow pool. The maximum radial velocities are of the order of 60 cm/sec which is close to the value reported by Zacharia et al. [8]. The temperature profiles indicate that there is a strong temperature gradient on the surface of the pool consistent with the absorption of a significant amount of energy in a small localized area near the laser beam axis. The experimentally determined weld pool diameter and depth are compared with the corresponding theoretically predicted values in Table 4.3. It is observed that there is good agreement between the experimental and the calculated values. For the same power, the larger liquid pool size of titanium is consistent with its higher laser beam absorption coefficient.

4.1.2.2 Vaporization Rates

The calculated values of the radial distribution of temperature in the liquid pool for iron and titanium are presented in Fig. 4.5. From the data it is evident that in each case, very high temperatures are reached on the pool surface and there is a region on the surface where the temperatures are greater than the boiling point. Liquid pool surface temperatures in excess of boiling point have been reported by several authors [12-16].

Table 4.2   Data used for the calculation of velocity and temperature fields presented in Fig. 4.4.

Property	Iron	Titanium
Molecular weight (gm/mole)	55.85	47.9
Density (gm/cm^3)	7.8	4.54
Melting point (K)	1811.0	1941.0
Boiling point (K)	3135.0	3533.0
dγ/dT (dyne/cm-K)	-0.5	-0.26
Latent heat of vaporization (cal/gm)	1514.02	2110.08
Latent heat of melting (cal/gm)	70.0	96.298
Thermal conductivity (cal/cm-sec-K)	0.075	0.049
Specific heat of solid (cal/gm-K)	0.168	0.177
Specific heat of liquid (cal/gm-K)	0.197	0.187
Effective viscosity(gm/sec-cm)	0.5	0.5
Power (Watts)	500	500
Absorption coefficient	0.15	0.2
Radius of the Beam (cm)	0.02	0.02
Diameter of the nozzle (cm)	0.5	0.5
Helium flow rate (l/min)	1.0	1.0
Ratio of specific heats of Vapor (γ_v)	1.667	1.667

Table 4.3: Experimental and theoretical depth and diameter of the laser melted pool for titanium and iron for a laser power of 500 W and argon flow rate of 1 liter/min.

Element	Iron		Titanium	
Depth/ diameter	Experimental	Theoretical	Experimental	Theoretical
Depth (cm)	7.0×10^{-2}	6.8×10^{-2}	8.0×10^{-2}	7.8×10^{-2}
Diameter (cm)	1.7×10^{-2}	1.6×10^{-2}	2.0×10^{-2}	1.9×10^{-2}
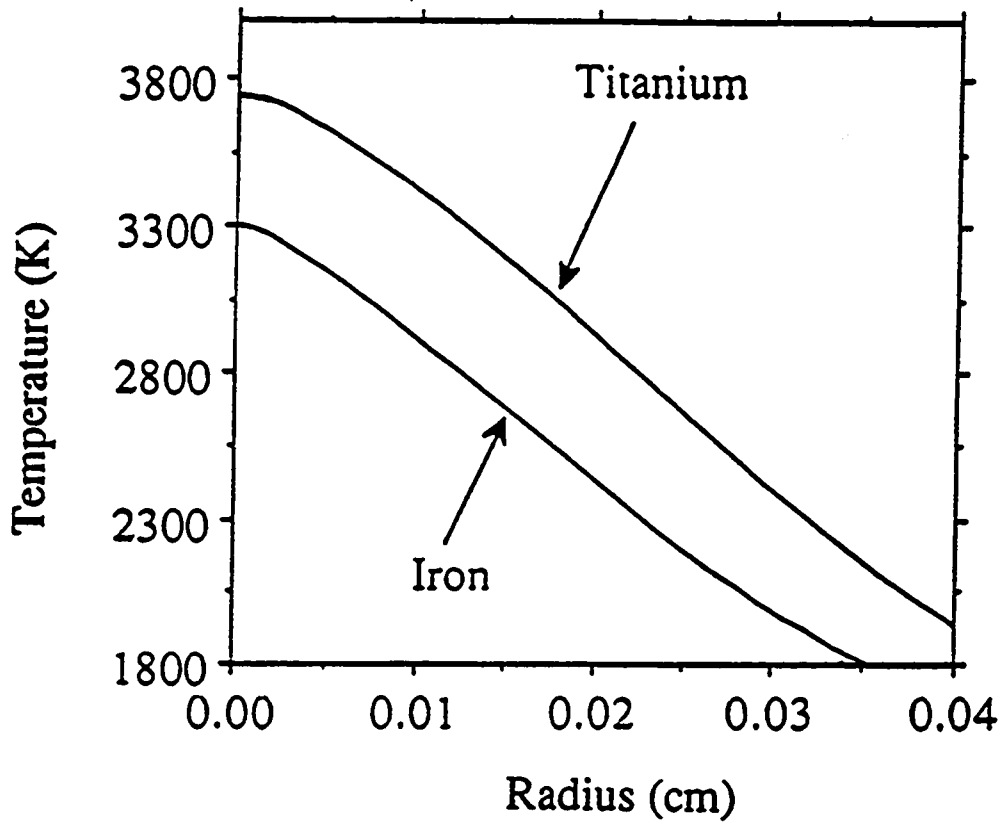
Fig. 4.5   Computed liquid pool surface temperatures for iron and titanium at a laser power of 500 W and gas flow rate of 1 liter/minute.

When the local surface temperature is higher than the boiling point of the metal, the pressure at the weld pool surface is greater than the ambient pressure. The excess pressure provides the driving force for the vapor to move away from the surface. Furthermore, at temperatures in excess of the boiling point, the high vapor density near the surface of the pool leads to significant condensation of the vapor on the surface and the vaporization rate is determined by the conditions across the Knudsen layer. In such a case, the relations among the temperature, pressure and the Mach number for a material can be represented on a plot of temperature vs. pressure for the various values of Mach number. The plot, commonly referred to as the flow state diagram, obtained from the solution of equations (3.17) to (3.23) for iron is shown in Fig. 4.6. The Mach number of the vapor across the Knudsen layer is then uniquely defined and is given by the Mach number of the line that intersects the equilibrium vapor pressure curve at that temperature. The density of the vapor across the Knudsen layer is then calculated by making use of equation (3.18). The calculated values of the Mach number and the density of the vapor across the Knudsen layer as a function of surface temperature are presented in Figs. 4.7 and 4.8 for iron and titanium, respectively. When the relative vaporization behavior of iron and titanium are compared from Figs. 4.7 and 4.8, it is evident that at any given temperature iron has higher Mach number. This is due to the fact that iron has a lower boiling point as compared to titanium.

At temperatures lower than the boiling point, the rate of vaporization due to concentration gradient is computed from mass transport considerations which takes into account the gas flow conditions and the nature of the shielding gas in accordance with equation (3.28). In order to determine the mass transfer coefficient, the viscosity and the diffusivity of iron and titanium in the shielding gas were determined by making use of the Chapman-Enskog theory [17]. The details of the estimation procedure are given in Appendix A. The partial
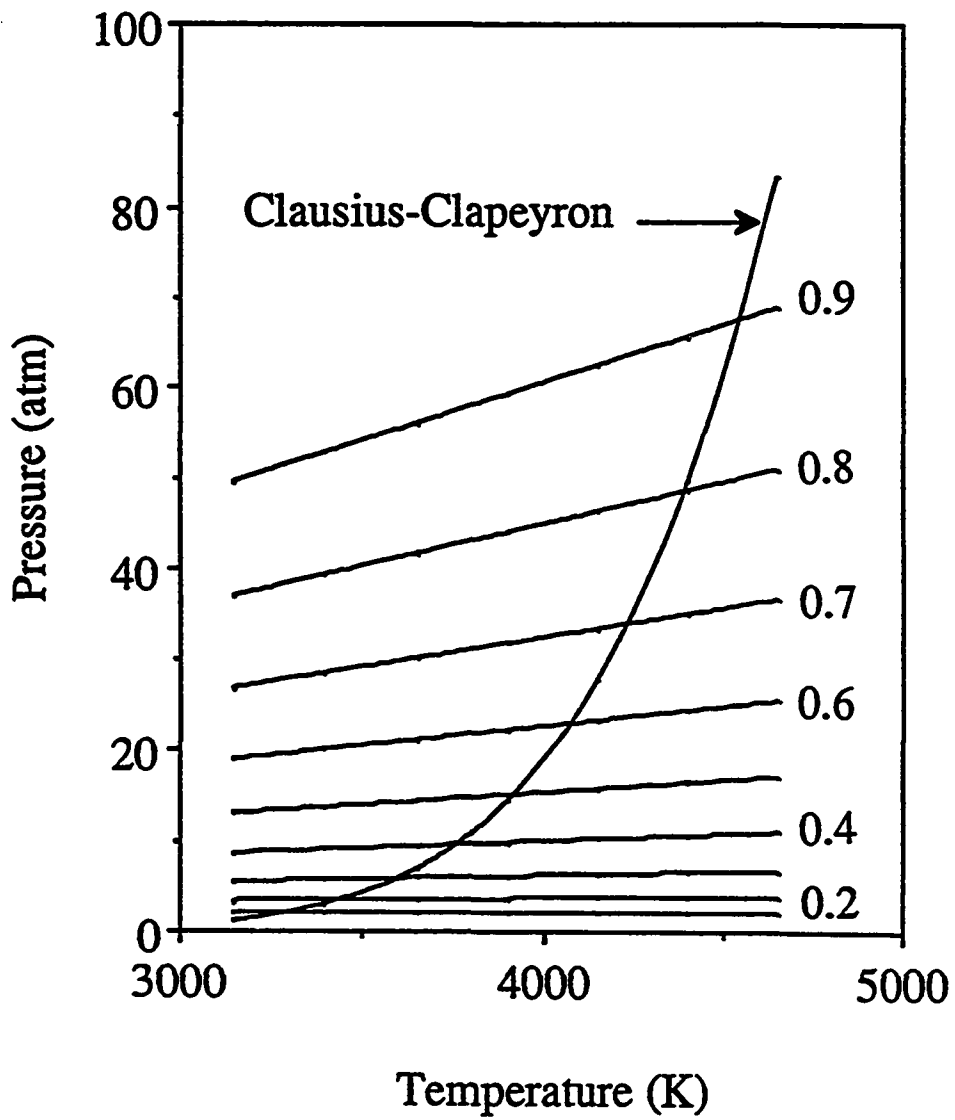
Fig. 4.6   Flow state diagram for iron.
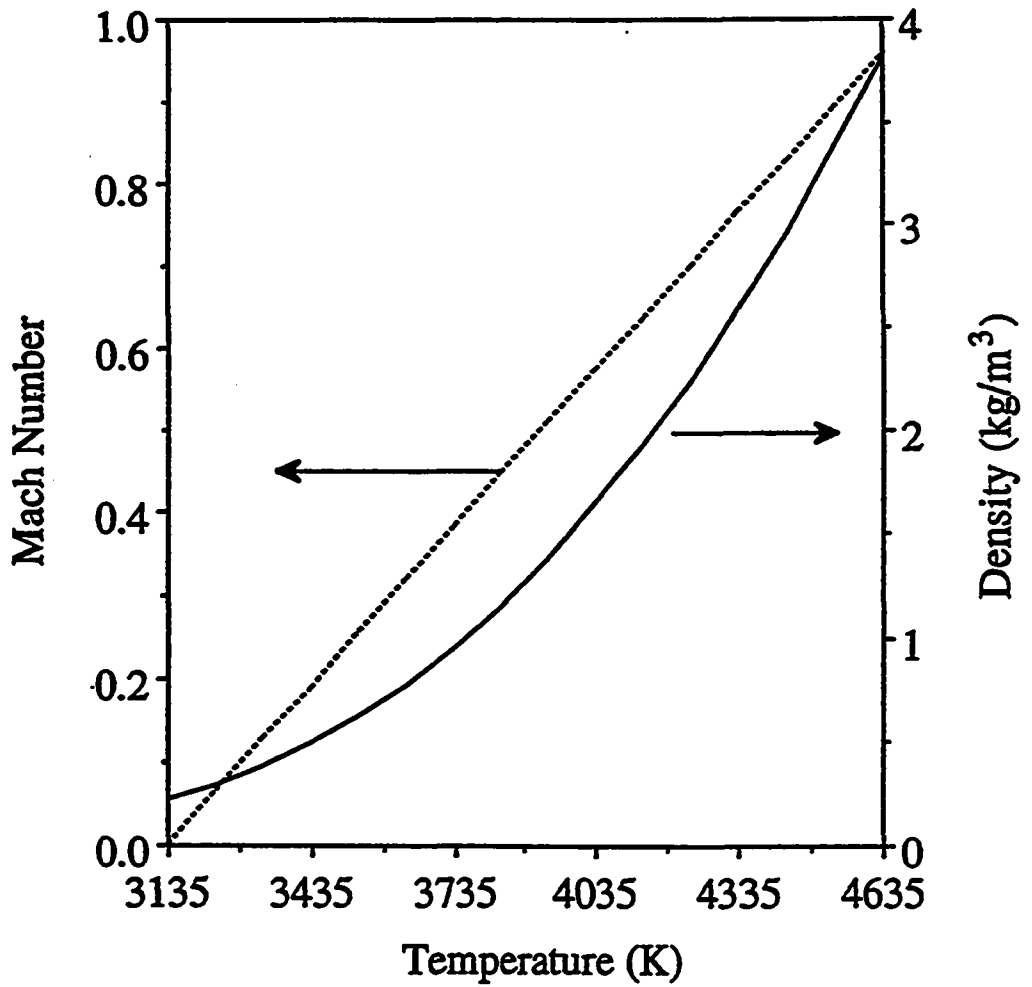
Fig. 4.7 Mach number and density for iron at the edge of Knudsen layer for different liquid pool surface temperatures.
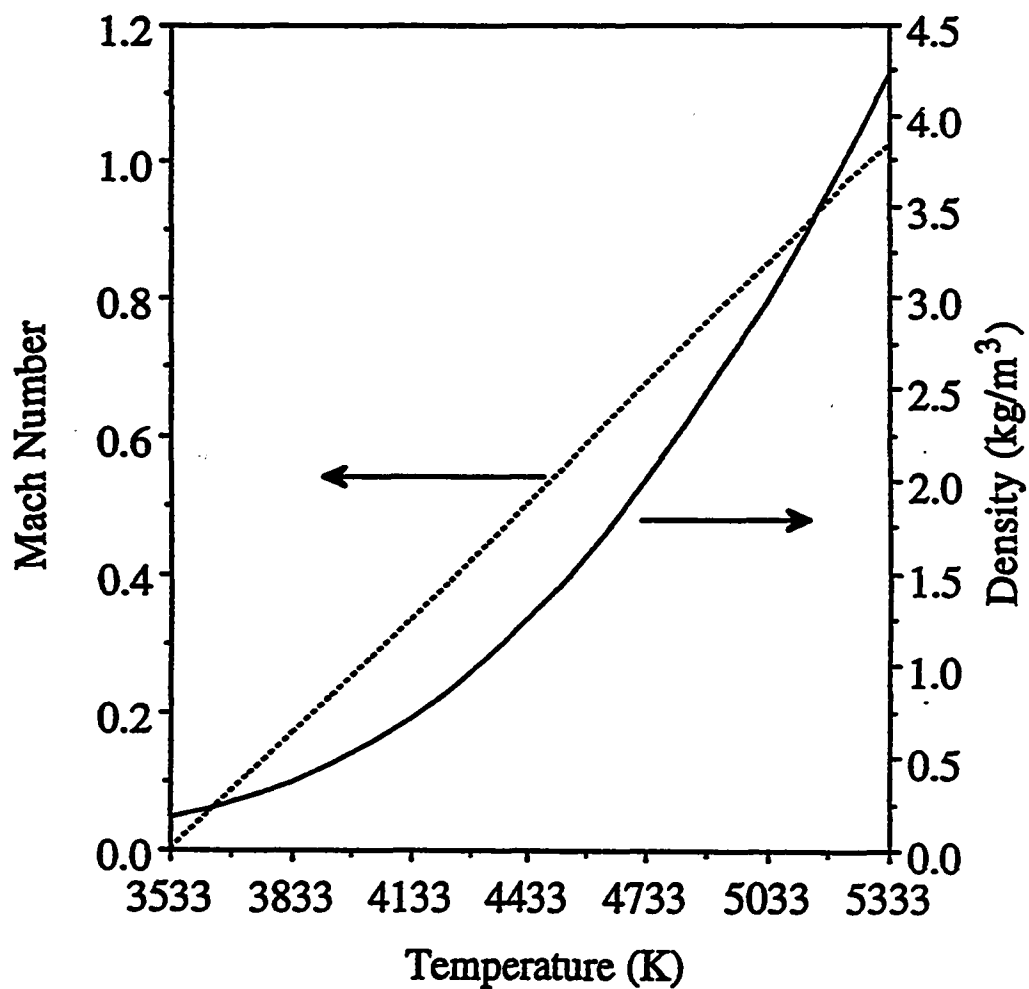
Fig. 4.8   Mach number and density for titanium at the edge of Knudsen layer for different liquid pool surface temperatures.

pressures of the metal vapors in the bulk gas stream away from the weld pool surface are negligible as compared to their values at the gas-liquid interface. The radial distributions of the vaporization flux calculated from equation (3.29) and from the Langmuir equation are plotted in Figs. 4.9 and 4.10 for iron and titanium, respectively. It is observed that the rates predicted by the Langmuir equation are always higher than the actual rates. The total vaporization rate obtained from the integration of the local flux over the entire pool surface, the integrated local Langmuir fluxes and the experimentally determined rate are plotted in Fig. 4.11 for both titanium and iron. It is observed that the rates predicted by the present work are in good agreement with the corresponding experimental data. Furthermore, the vaporization rates predicted by the Langmuir equation are much higher than the experimentally determined rates.

4.1.3 Vaporization from Stainless Steels

The results of modeling of laser induced vaporization rates of pure metals from the principles of gasdynamics and weld pool transport phenomena were found to be in good agreement with the corresponding experimental values. In order to further examine the predictive capabilities of the model on vaporization, two different sets of modeling were carried out. The first set consisted of modeling of vaporization rates of alloying elements from AISI 202 stainless steel for low laser powers. The modeling results were compared with the experimental data reported in the literature [18]. The second set included calculation of weld metal composition change in high power conduction mode laser welded AISI 201 stainless steel. The modeling results were verified against the experimental observation of Khan et al. [19]. These are discussed in the following sections.
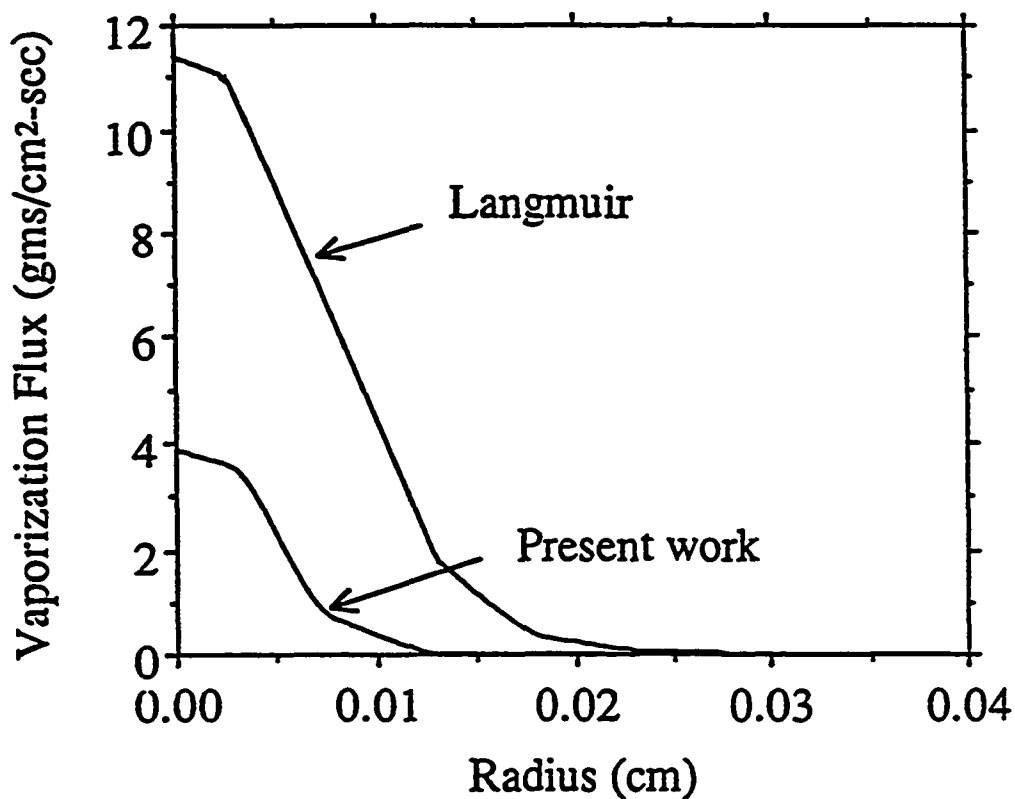
Fig. 4.9   Vaporization flux of iron calculated from Langmuir equation and from the model presented in this work for a laser power of 500 W and gas flow rate of 1 liter/minute.
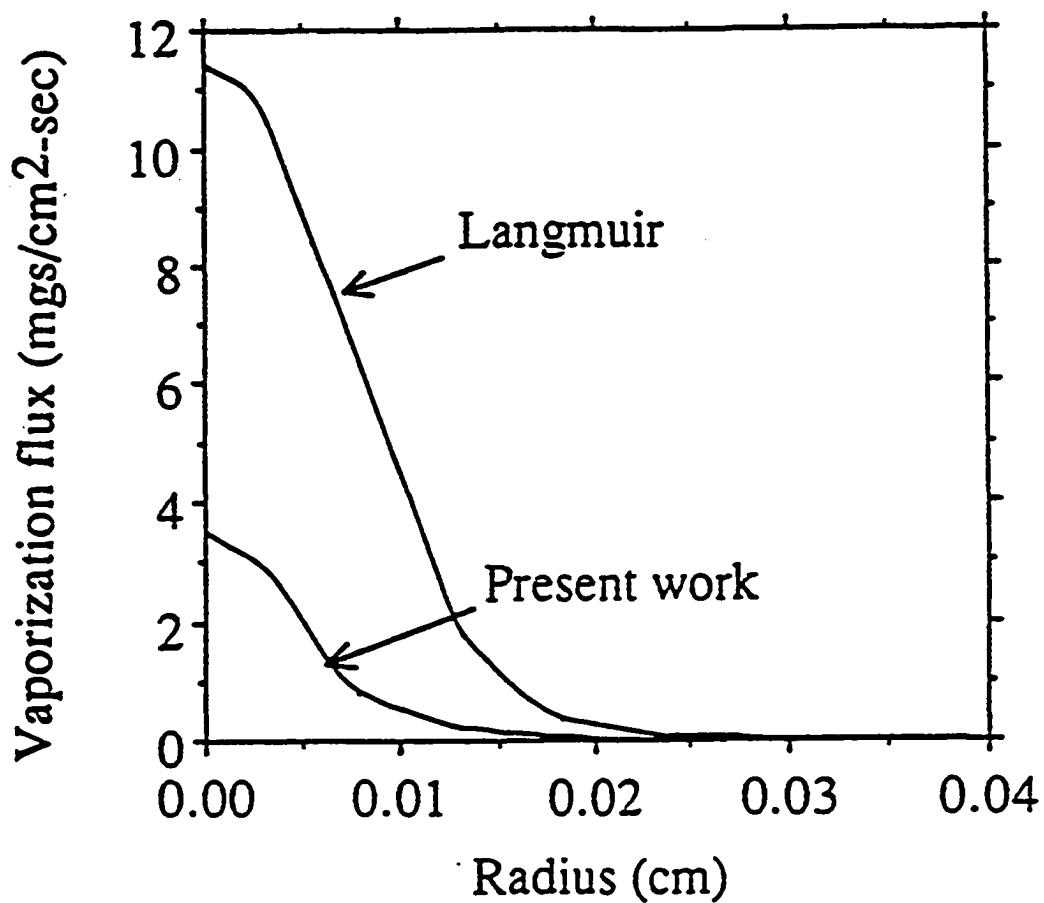
Fig. 4.10 Vaporization flux of titanium calculated from the Langmuir equation and from the model presented in this work for a laser power of 500 W and gas flow rate of 1 liter/minute.
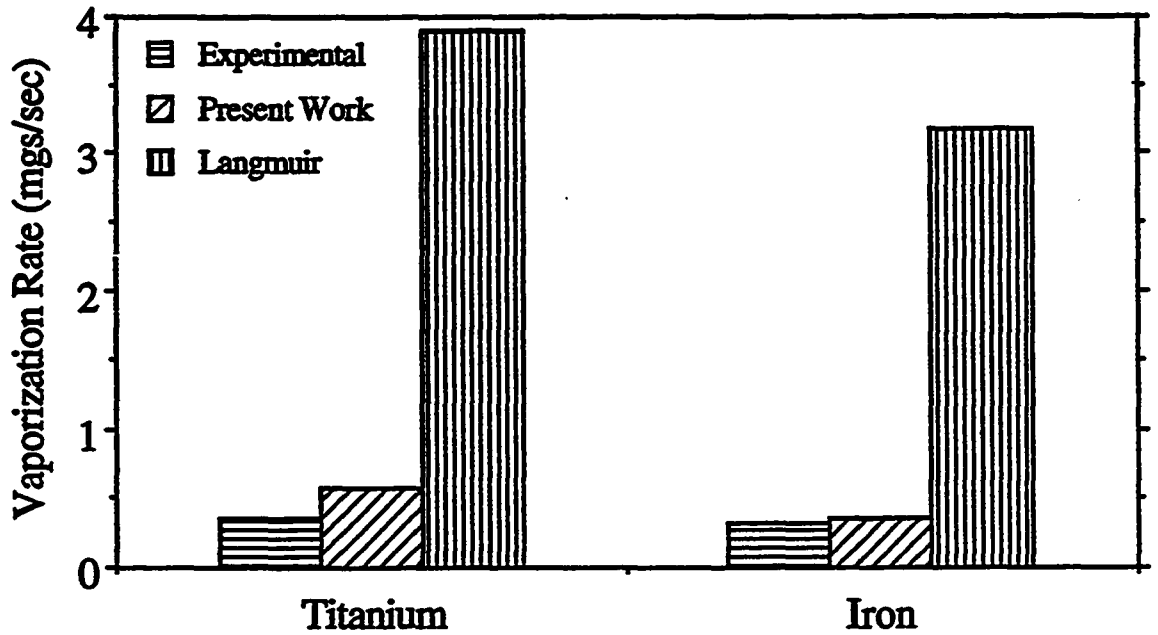
Fig. 4.11 Comparison of the experimental vaporization rate with the rates calculated from the Langmuir equation and from the model presented in this work for a laser power of 500 W and gas flow rate of 1 liter/minute.

4.1.3.1 Vaporization from AISI 202 Stainless Steels, Low Laser Powers

4.1.3.1.1 Velocity and Temperature Fields

The steady state temperature and velocity fields, obtained from the solution of Navier-Stokes equations and the equations of conservation of mass and energy, for laser welding of AISI 202 stainless steel with a laser power of 560 W in helium atmosphere, are shown in Fig. 4.12. The calculation takes into consideration the convective heat loss to the shielding gas and the evaporative heat loss at the pool surface in accordance with the equation (3.10). The data used for the calculations are presented in Tables 4.4 and 4.5. The details of the calculations of thermal diffusivity and viscosity of the shielding gas, for calculation of convective heat loss at the pool surface, are presented in Appendix A. For low concentration of surface active elements, the temperature coefficient of surface tension is negative [20,21]. Therefore, the velocities at the weld pool surface, shown in Fig. 4.12, are radially outwards resulting in a relatively shallow pool. The velocity and temperature field are similar in nature to the velocity and temperature field for pure metals presented in Fig. 4.4. The maximum radial velocity is of the order of 0.7 m/s which is close to the value reported by Zacharia et al [8]. An order of magnitude calculation of radial velocity at the surface can also be done from equation (3.14) [22]. Writing the equation in finite difference form we have:

$$-\mu\left(\frac{v_1 - v_2}{x_1 - x_2}\right) = \frac{d\gamma}{dt}\left(\frac{T_1 - T_2}{r_1 - r_2}\right) \tag{4.1}$$

where T_1 is the maximum temperature at the pool surface, T_2 is the melting point, (r_1 -r_2) is the radius of the pool, $d\gamma/dT$ is the temperature coefficient of surface tension, μ is the

Table 4.4 Data used for the calculations in the welding of AISI 202 stainless steel.

Property/Parameter	Value
Density (kg/m^3)	7200.0
Melting point (K)	1811.0
Laser power (Watts)	560.0
Radius of the beam (m)	2.0×10^{-4}
Effective viscosity (kg/m-s)	0.05
Thermal diffusivity of solid (m^2/s)	3.3×10^{-5}
Thermal diffusivity of liquid (m^2/s)	7.5×10^{-5}
Specific heat of solid (J/kg-K)	710.6
Specific heat of liquid (J/kg-K)	836.0
Absorption coefficient	0.17
Temperature coefficient of surface tension (N/m-s)	-5.3×10^{-4}
Ratio of specific heats of vapor (γ_v)	1.667
Diameter of the nozzle (m)	5×10^{-3}

Table 4.5 Enthalpies of vaporization of the alloying elements [29].

Element	Enthalpy (kJ/kg)
Iron	6087
Manganese	4005
Chromium	6577
Nickel	6388

Velocity Field

$$\longleftarrow 3.9 \times 10^{-4}\,\text{m} \longrightarrow$$

$$2.0 \times 10^{-4}\,\text{m}$$

$$U_{max} = 0.7\ \text{m/s}$$

Temperature Field

3182 K

2311 K

2062 K
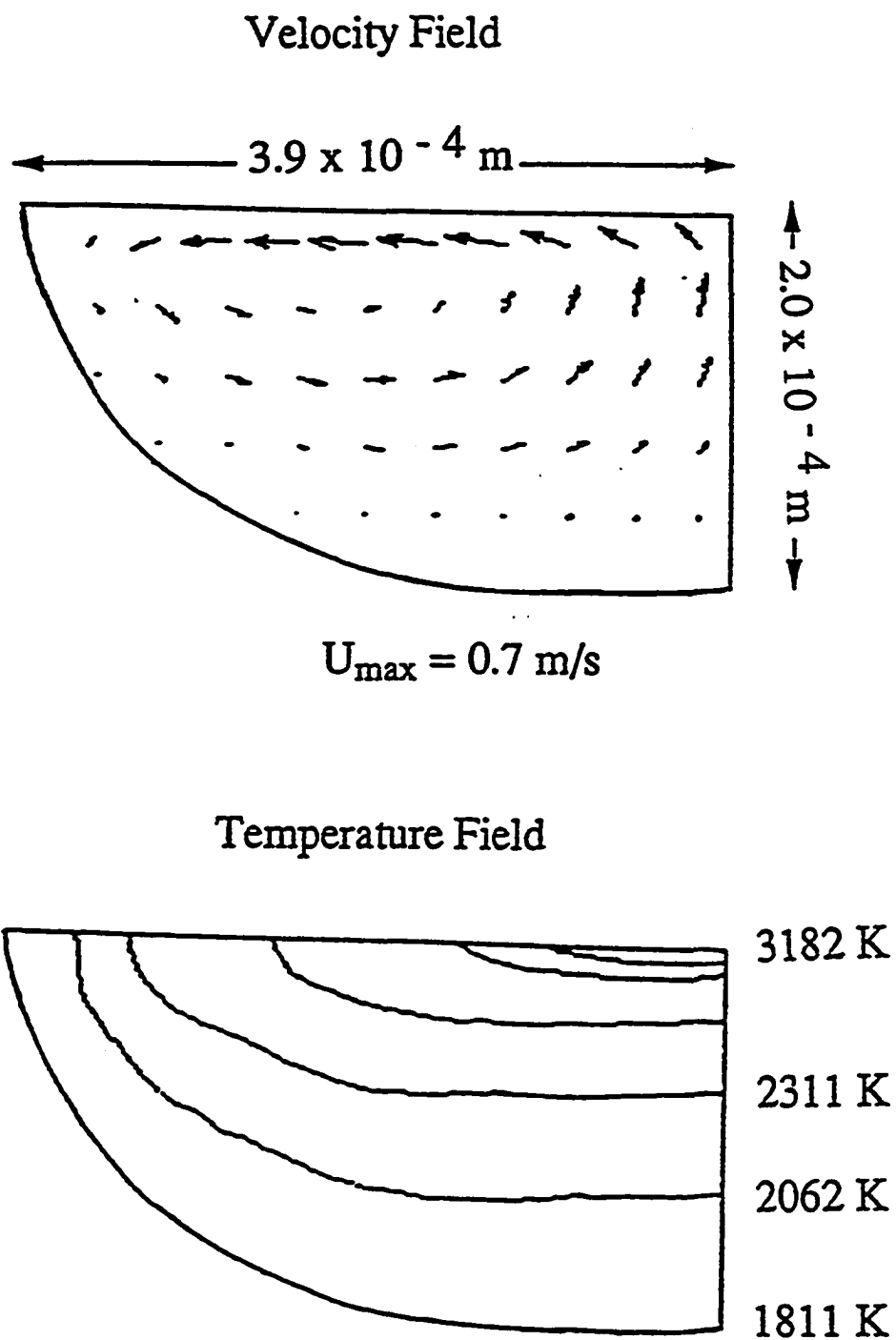
1811 K

Fig. 4.12 Velocity and temperature fields for a laser power of 560 W and helium gas flow rate of 6 liters/minute.

viscosity, v_1 is the velocity at the surface, x_1, and v_2 is the velocity at x_2. From Fig. 4.12 we have $T_1 = 3182$ K, $T_2 = 1811$ K, ($r_1 - r_2$) $= 3.9 \times 10^{-4}$ m, and from Table 4.4 we have $\mu = 0.05$ kg/m-s and $d\gamma/dT = 5.3 \times 10^{-4}$ N/m-K. The radial velocity becomes zero very close to the surface of the pool. From Fig. 4.12 approximating the distance x_2 where radial velocity v_2 becomes zero as depth/6 and substituting the values of the terms in equation (4.1), we get v_1 approximately equal to 1.2 m/s. The value of the velocity is of the same order of magnitude as the velocity obtained from the solution of equations of conservation of mass, momentum and energy in the weld pool. The slightly higher value of velocity obtained from equation (4.1) can be understood from the fact that the velocity profile is approximated linearly between x_1 and x_2. The theoretically predicted pool diameter and depth, presented in Table 4.6, are in good agreement with the experimentally observed values [18,23]. Furthermore, the theoretically predicted peak temperature indicated in Table 4.6 was found to be in good agreement with the temperature experimentally determined by Khan and DebRoy [18].

The computed results also demonstrate the importance of weld pool evaporative heat flux in the calculation of the peak temperature. For a gas flow rate of 6 liters/minute of helium, the peak temperature was found to be 3222 K when the evaporative heat loss was not considered whereas when the heat loss was considered, the peak temperature dropped to 3182 K. These results are consistent with the observations of Zacharia et el. [24] who reported a significant drop in the calculated temperatures when evaporative heat loss from the pool surface was considered.

Table 4.6: Comparison of predicted values of weld pool geometry and peak temperatures with experimental data for the welding of AISI 202 stainless steel [18,23].

Parameter	Experimental	Model Prediction
Weld Pool Width (m)	8.2×10^{-4}	7.8×10^{-4}
Weld Pool Depth (m)	2.3×10^{-4}	2.0×10^{-4}
Peak Temperatures (K)	3093 ± 44	3182

4.1.3.1.2 Vaporization Rates for 202 Stainless Steels, Low Laser Power

From the temperature field in Fig. 4.12, it is evident that the temperatures reached at the weld pool surface are high and the temperature at the center of the pool is greater than the boiling point of pure iron. The temperature at which the pressure on the surface is equal to 1 atmosphere was calculated to be 2952 K from the equilibrium vapor pressure-temperature relationship for the various alloying elements given in Appendix F and the composition of the AISI 202 stainless steel indicated in Table 4.7. The flow state diagram for AISI 202 stainless steel, obtained from the solution of equations (3.17) to (3.23), is shown in Fig. 4.13. The Mach number of the vapor across the Knudsen layer is uniquely defined and is given by the Mach number of the line that intersects the equilibrium vapor pressure curve at a given temperature. For example, the Mach number of the vapor across the Kundsen layer at weld pool surface temperature of 3200 K is 0.3 and the equilibrium vapor pressure at the pool surface is 2.5 atmosphere. The values of the Mach number and the density of the vapor across the Knudsen layer, calculated from equation (3.18), for various surface temperatures are presented in Fig. 4.14. The computed values of both the Mach number and the vapor density indicate their strong dependence on the surface temperature mainly due mainly to the strong correlation between the vapor pressure and temperature. From the values of the Mach number and the density, total vaporization flux and the flux of the individual alloying elements due to pressure gradient are calculated from equation (3.24). The vaporization rate due to concentration gradient is calculated from mass transport considerations which take into account the gas flow conditions and the nature of the shielding gas in accordance with equation (3.27).

Table 4.7:   Composition of AISI 202 stainless steel.

Elements	Composition (wt. %)	Activity (mole fraction)
Manganese	6.58	0.066
Chromium	17.80	0.190
Nickel	4.77	0.045
Iron	70.14	0.698
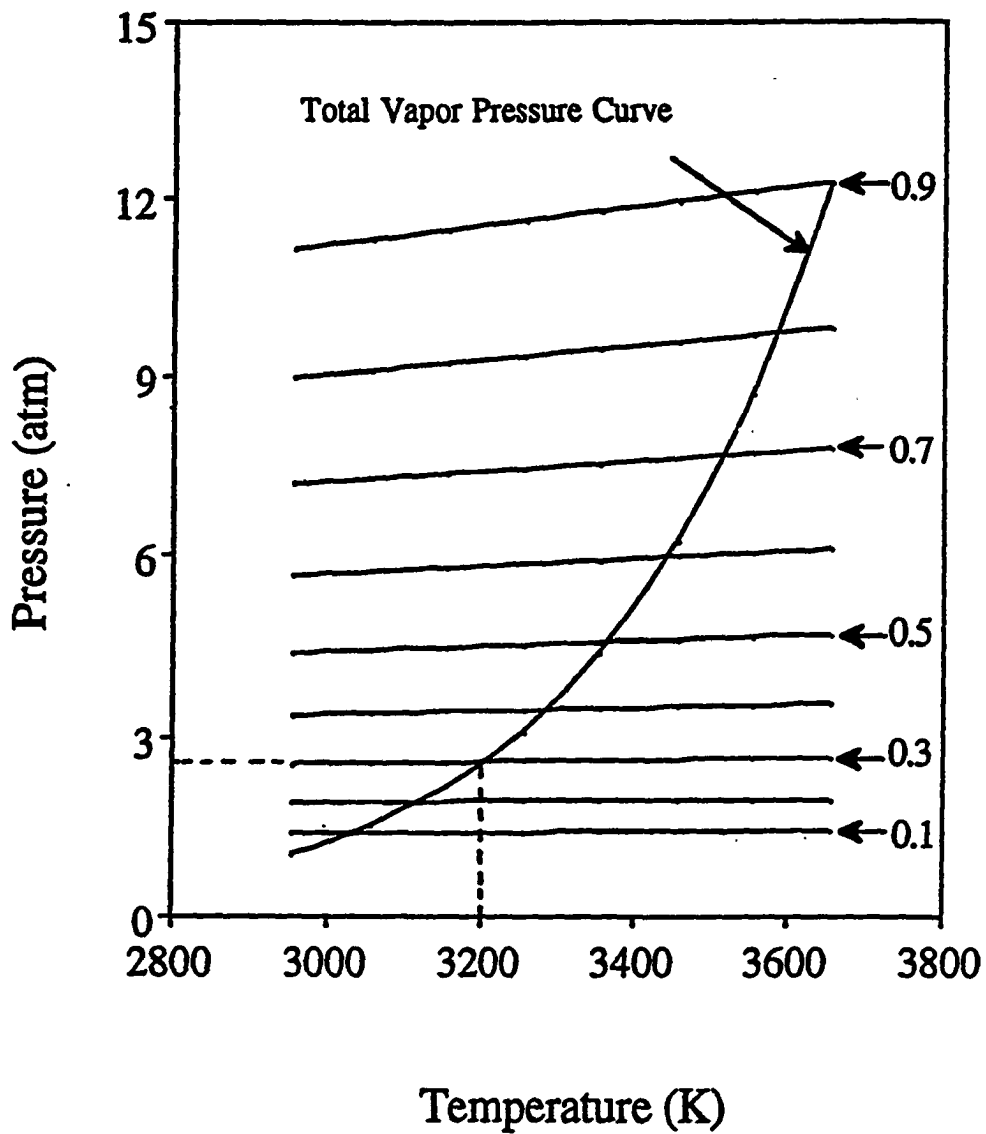
Fig. 4.13 Flow state diagram for AISI 202 stainless steel in helium atmosphere. The Mach number for various lines are indicated in the figure.
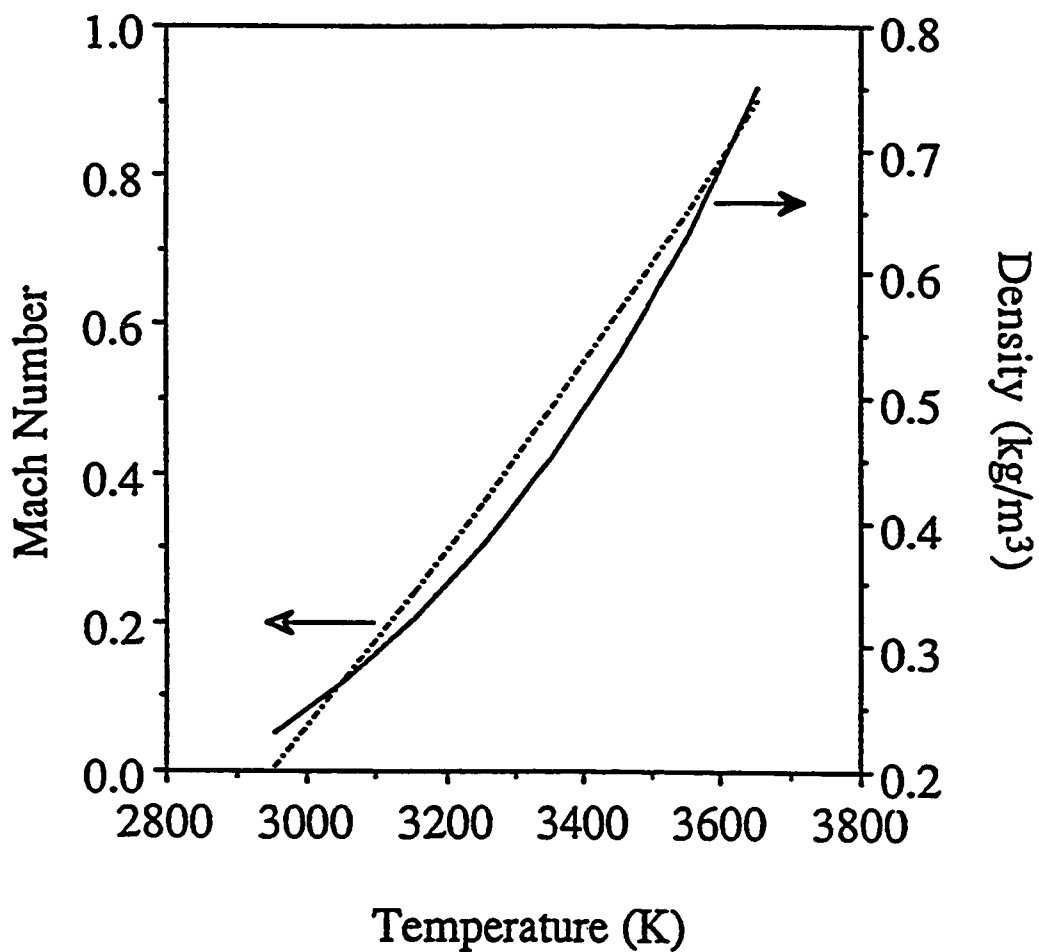
Fig. 4.14 Mach number and density for AISI 202 stainless steel for various temperatures at the edge of Knudsen layer in helium atmosphere.

The radial distribution of the vaporization flux of the alloying elements and the total flux due to the combined effects of total pressure and concentration gradients are plotted in Fig. 4.15. Similarly, the radial distribution of the vaporization flux of the individual alloying elements and the total flux calculated from the Langmuir equation are plotted in Fig. 4.16. Comparison of the results in Fig. 4.15 and Fig. 4.16 indicates that the flux of the alloying elements predicted from Langmuir equation is much higher than the corresponding value predicted from the present work. Furthermore, it is evident from Figs. 4.15 and 4.16 that much of the vaporization takes place at the center of the pool where the temperatures are the highest. At a short distance away from the center of the pool the vaporization flux drops sharply. This can be understood from Fig. 4.17 where the equilibrium vapor pressures of iron, manganese, chromium and nickel are plotted as a function of temperature. It is evident from the figure that the equilibrium vapor pressures are strong function of temperature and drop sharply as the temperature drops. This results in low vaporization flux at low temperatures. In Fig. 4.18, the experimentally determined vaporization rates for the AISI 202 stainless steel are compared with the rates computed from the model and the values calculated from the Langmuir equation for the same steel. It is observed that the experimentally determined vaporization rates are closer to the values predicted by the present model than the rates calculated from the Langmuir equation. Furthermore, the predicted ratios of the vaporization rates of the alloying elements are in good agreement with the corresponding experimentally determined values as observed from Table 4.8.

The effects of the nature and the flow rate of the shielding gas on the weld pool temperature are observed from the results in Fig. 4.19 where the calculated peak temperatures in helium and argon are indicated. The observed temperature difference in the two cases is about 35K. At a peak temperature of about 3200K, this difference would be difficult to determine experimentally. For a given shielding gas, the calculations indicate that with the increase in
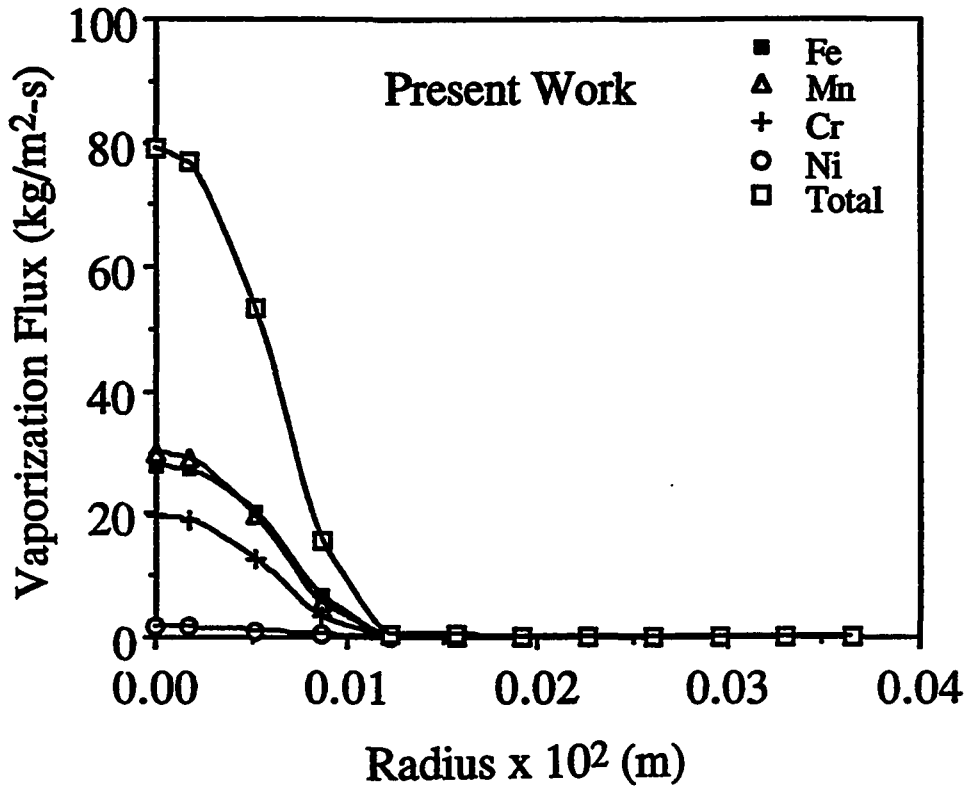
Fig. 4.15 Vaporization flux for various alloying elements and the total flux from the present work.
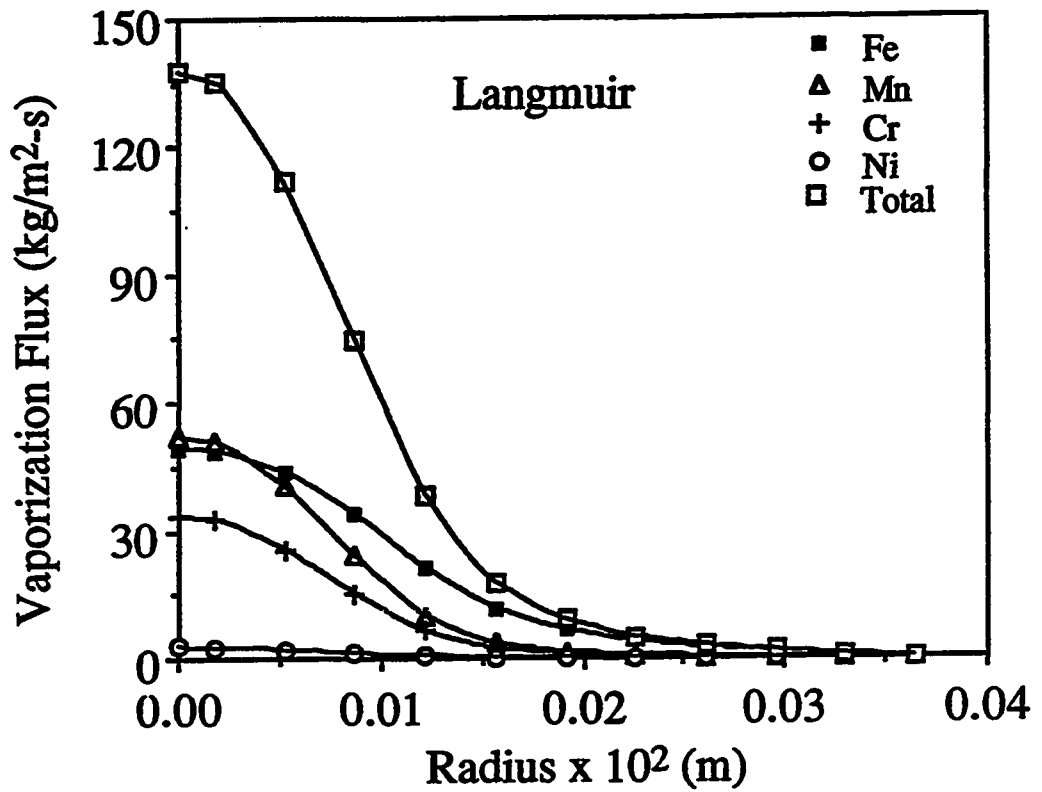
Fig. 4.16 Vaporization flux for various alloying elements and the total flux computed using Langmuir equation.
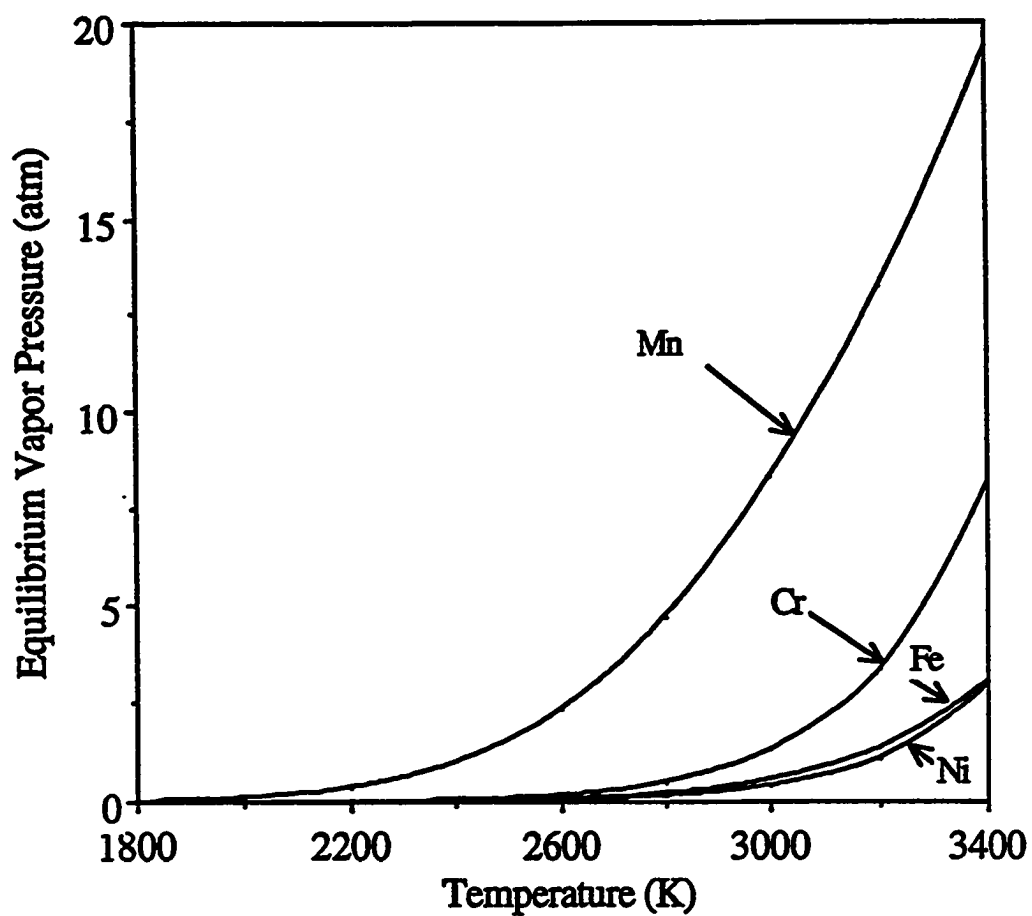
Fig. 4.17 Equilibrium vapor pressure-temperature curves for iron, manganese, chromium and nickel.
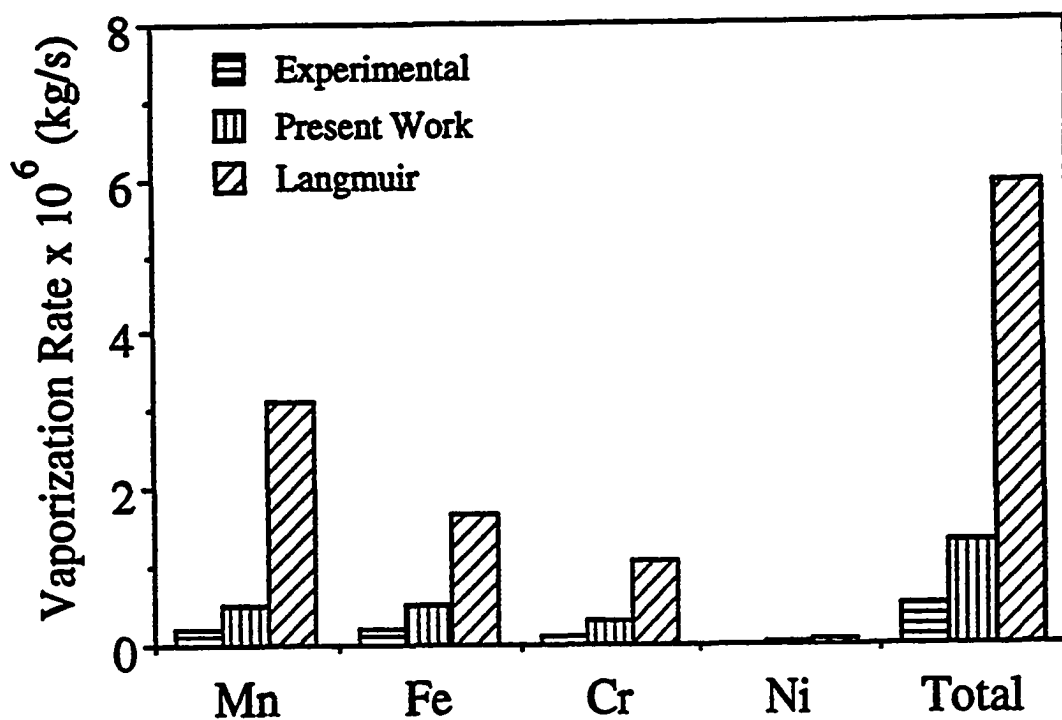
Fig. 4.18 Comparison of the experimental vaporization rates with the rates calculated from the Langmuir equation and from the present work.

Table 4.8. Comparison of the predicted vapor composition with the experimentally determined values [18] for the welding of AISI 202 stainless steel. Laser power: 560 Watts.

Composition Ratio (Moles of i/Moles of j)	Experimental	Present Work
J_{Fe}/J_{Mn}	1.08±0.07	1.00
J_{Cr}/J_{Mn}	0.56±0.08	0.65
J_{Ni}/J_{Mn}	0.05±0.01	0.05
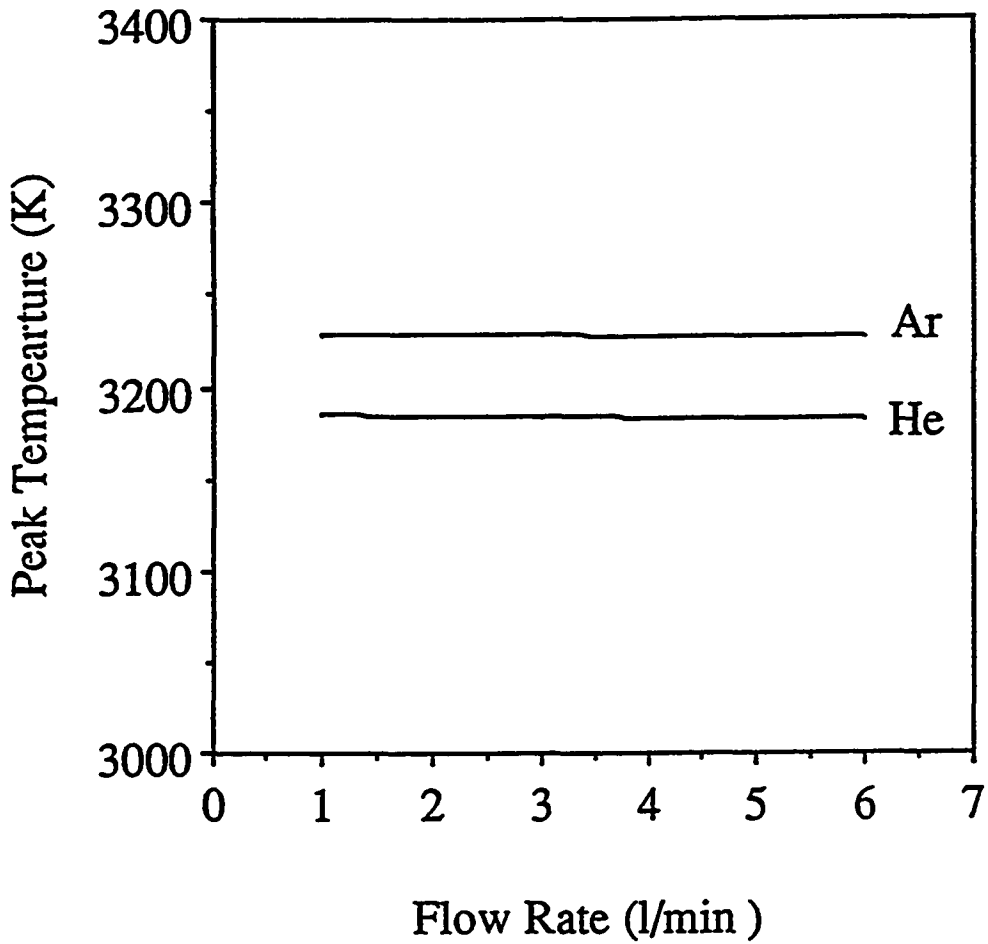
Fig. 4.19 Peak temperatures calculated as a function of gas flow rate and the type of the shielding gas used.

the gas flow rate, the peak temperature on the pool surface does not change significantly as can be observed from Fig. 4.19.

To understand the effect of the type of the shielding gas, let us consider isothermal evaporation in helium and argon driven by the pressure gradient alone, since the pressure gradient driven mass transfer rate is significantly higher than the concentration gradient driven rate. In such a case, at a given temperature, the computed results in Fig. 4.20 indicate a higher vaporization rate of AISI 202 stainless steel in helium than that in argon. This is due to the fact that condensation of vapor molecules is more pronounced in argon than in helium due to the differences in the physical properties of the two gases, particularly their densities. The convective heat loss to the shielding gas is considerably smaller than the laser beam energy absorbed by the weld pool. Therefore, if the evaporative cooling were ignored, and the computed weld pool surface temperature distributions were identical in helium and in argon, the computed vaporization rate would have been much higher in helium than that in argon as can be observed from Fig. 4.21. In the absence of evaporative heat loss, the radial distribution of the net energy absorption is shown by the uppermost curve in Fig. 4.22. However, when the evaporative heat loss is considered, the net absorbed energy in argon atmosphere is slightly higher than that in helium as can be observed in Fig. 4.22. The difference in the net energy absorption in argon and helium results in about 35K lower peak temperature in helium atmosphere as has been discussed earlier. The lower temperature in helium compensates the difference in vaporization rates when evaporative heat loss is considered. The resulting vaporization rate is about 15% higher in helium than in argon. The calculated results are consistent with the observations of Collur et al. [25] who measured vaporization rates during laser welding of AISI 201 stainless steel in different shielding gases at various shielding gas flow rates. The experiments were conducted with helium, argon and nitrogen and the gas flow rate was in
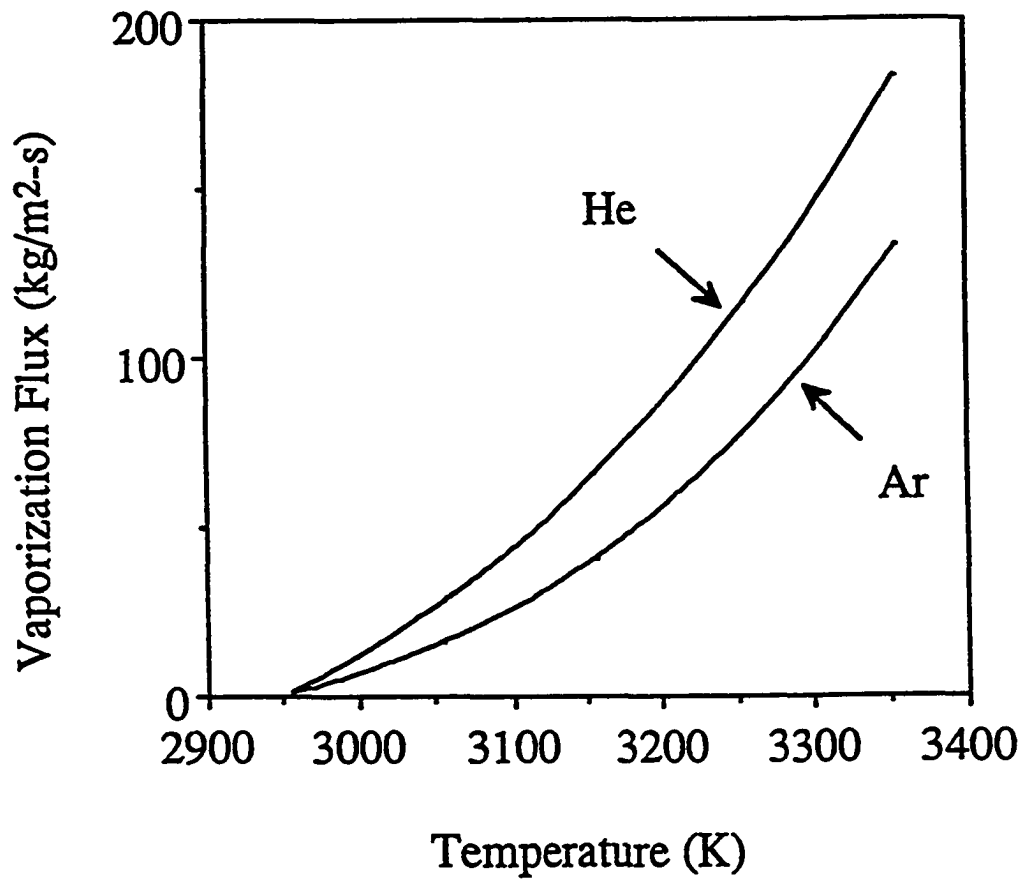
Fig. 4.20 Pressure gradient driven vaporization flux as function of temperature in helium and argon.
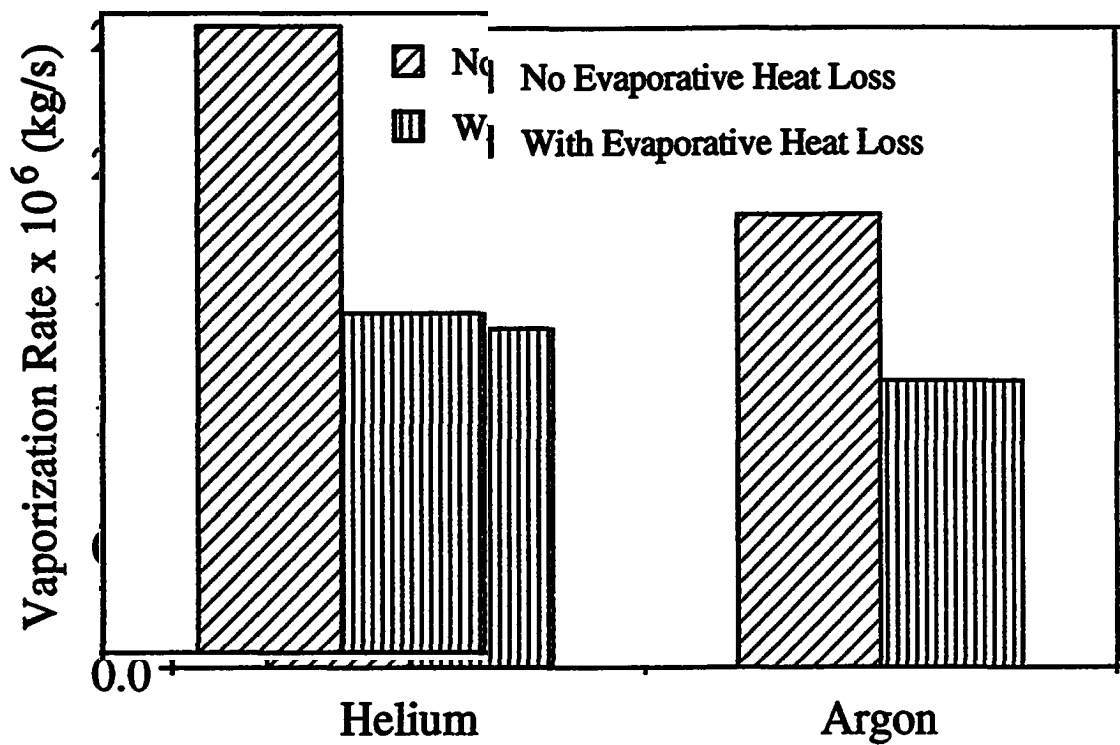
Fig. 4.21 Comparison of vaporization rate in helium and argon for a flow rate of 6 liters/minute with or without consideration of evaporative heat loss.
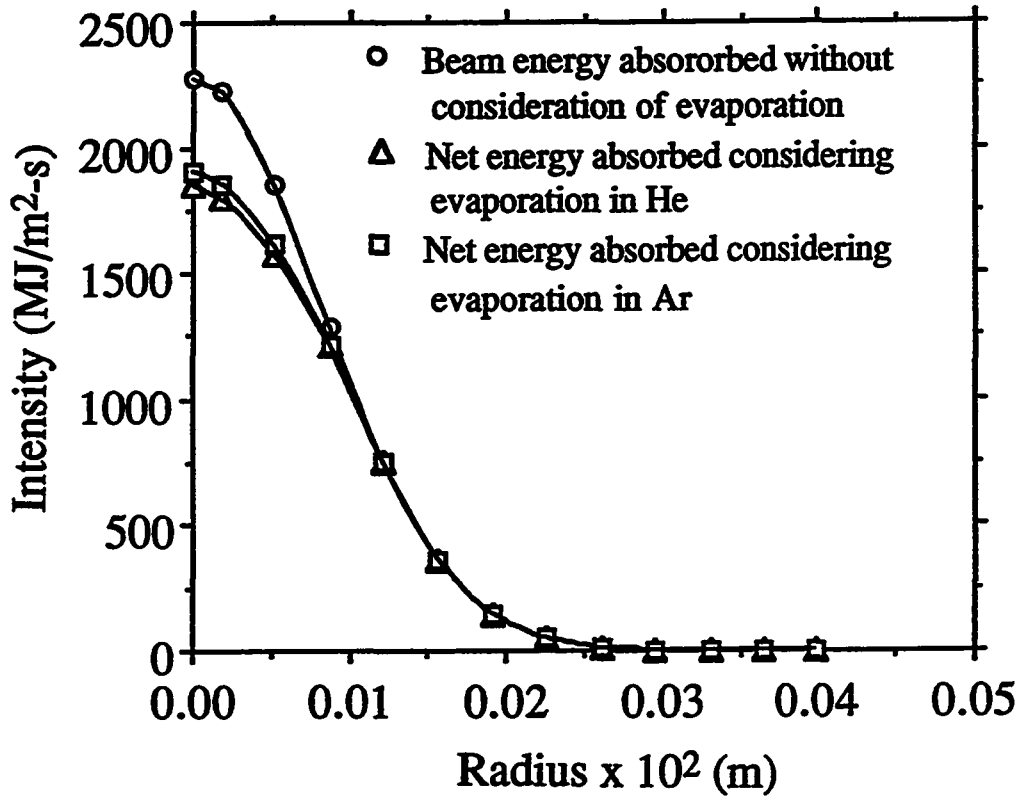
Fig. 4.22 Energy absorbed vs. radius with and without consideration of evaporative heat loss.

the range of 2 to 12 l/min. They found that the vaporization rate did not change significantly with either the shielding gas flow rate or with the type of the gas as shown in Fig. 4.23. The rates predicted by the model are in fair agreement with the experimental data. Furthermore, the vaporization rates predicted by the Langmuir equation is significantly higher than the corresponding experimental values.

4.1.3.2   Vaporization from AISI 201 Stainless Steels, High Laser Powers

4.1.3.2.1 Velocity and Temperature Fields

The steady state temperature and velocity fields, for AISI 201 stainless steel for a laser power of 3000 W, obtained from the solution of Navier-Stokes equations and the equations of conservation of mass and energy are shown in Fig. 4.24. The calculation takes into consideration the convective heat loss to the shielding gas and the radiative and evaporative heat losses at the pool surface. A sample calculation of the various heat losses for a laser power of 3000 W are given in Table 4.9. The calculations indicate that the convective and radiative heat losses are less than one percent of the evaporative heat loss. The average thermophysical properties and other data used for the calculations are presented in Tables 4.10 (a) and (b). The enthalpies of vaporization of the alloying elements used in the calculations are given in Table 4.5. The velocities at the weld pool surface, shown in Fig. 4.24, are radially outwards resulting in a relatively shallow pool. The maximum radial velocity is of the order of 0.9 m/s which is close to the value reported by Zacharia et al. [8] and Paul and DebRoy [26]. Using equation (4.1) and carrying out calculations similar to the calculations presented in section 4.1.3.1.1, the radial   velocity at the surface is
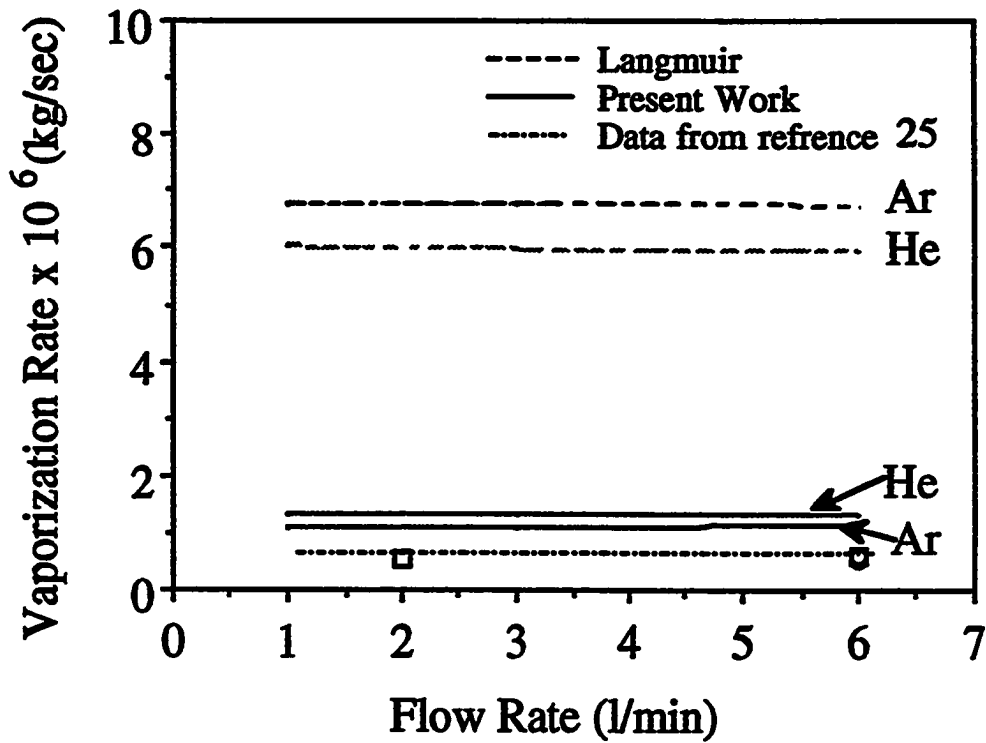
Fig. 4.23 Vaporization rate predicted from the model and from the Langmuir equation for different types of the shielding gas at various flow rates. Experimental vaporization rates are taken from reference 25.

Velocity Field

$$\longleftarrow 2.1 \times 10^{-3} \text{ m} \longrightarrow$$

$$1.4 \times 10^{-3} \text{ m}$$

$$U_{max} = 0.9 \text{ m/s}$$

Temperature Field

3208 K

2237 K

1987 K

1811 K
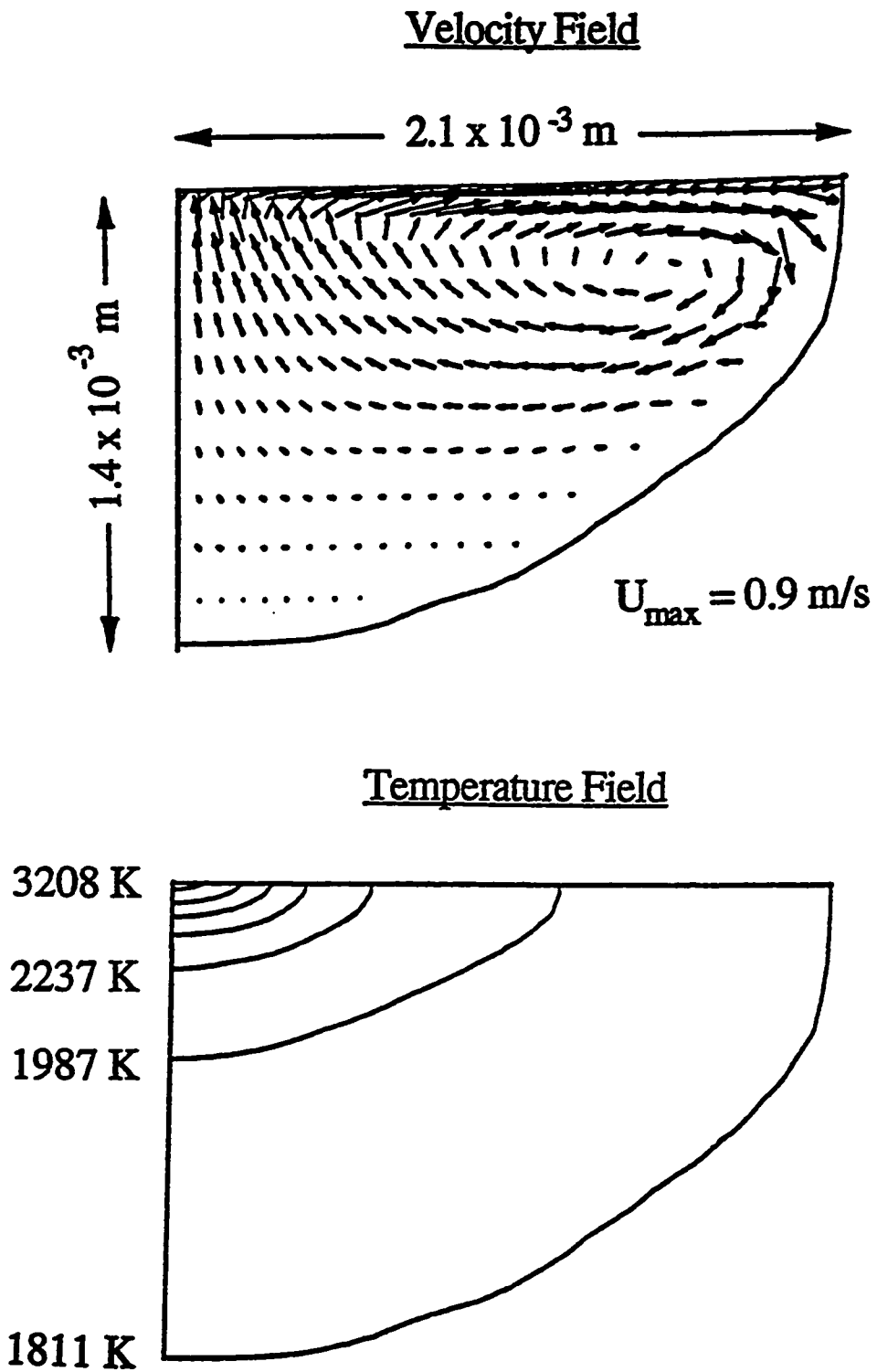
Fig. 4.24   Velocity and temperature fields for a laser power of 3000 W.

Table 4.9 Comparison of the various heat losses at the pool surface.

Parameter	Value
Laser power (Watts)	3000
Peak temperature (K)	3208
Peak intensity (J/m^2-s)	1.058×10^{10}
Absorbed peak intensity (J/m^2-s)	2.116×10^9
Evaporative heat loss (J/m^2-s)	5.098×10^8
Convective heat loss (J/m^2-s)	3.427×10^6
Radiative heat loss (J/m^2-s)	5.98×10^5

Table 4.10(a). Data used for calculations of AISI 201 stainless steel.

Property/Parameter	Value
Density (kg/m^3)	7200.0
Melting point (K)	1811.0
Effective viscosity (kg/m-s)	3.0×10^{-2}
Thermal diffusivity of solid (m^2/s)	3.8×10^{-6}
Thermal diffusivity of liquid (m^2/s)	3.5×10^{-5}
Specific heat of solid (J/kg-K)	710.6
Specific heat of liquid (J/kg-K)	836.0
Temperature coefficient of surface tension (N/m-s)	-4.3×10^{-4}
Ratio of specific heats of vapor (g_v)	1.667
Helium flow rate (m^3/s)	5.5×10^{-4}
Scanning speed of the laser (m/s)	15.24×10^{-3}
Emissivity of the pool surface	0.1

Table 4.10 (b). Beam radius and absorption coefficients values used
for calculations.

Power (Watts)	Radius of the Beam (m)	Absorption Coefficient
1000	1.5×10^{-4}	0.16
2000	3.1×10^{-4}	0.19
2500	3.9×10^{-4}	0.19
3000	5.2×10^{-4}	0.20
4000	7.7×10^{-4}	0.21

approximately equal to 1.42 m/s. The value of the velocity is of the same order of magnitude as the velocity obtained from the solution of equations of conservation of mass, momentum and energy in the weld pool. The slightly higher value of velocity obtained from equation (4.1) can be understood from the fact that in equation (4.1) the velocity profile is approximated linearly between x_1 and x_2. It is observed from Fig. 4.25 that the calculated values of the area of cross-section of the weld pool for different laser powers are in good agreement with the corresponding experimental values. As indicated in Table 4.10 (b) the expansion of the laser beam radius with power was taken into account. In the range of laser powers investigated, slight adjustment of the absorption coefficient values, within $\pm$ 15 %, was necessary to obtain good agreement between the experimental and the calculated cross sectional areas.

The peak temperatures decreased slightly with power as can be observed from Fig. 4.26 (a) mainly because of the difference in the focusing optics and the resulting changes in beam characteristics at high laser powers. The computed results also demonstrate the importance of evaporative heat loss in the calculation of the peak temperature for different laser powers. It is observed from Fig. 4.26 (a) that the evaporative heat loss significantly reduces the peak temperature and substantial errors in the calculated temperatures result if the heat loss is ignored. Similar observations were made in the modeling of fluid flow and heat transfer in the welding of AISI 202 stainless steel with low laser power. It is observed from Figs. 4.25 and 4.26 (b) that both the surface area and the area of cross-section of the pool increases with power. Because of the pronounced increase in the surface area, the rate of vaporization and consequently, the heat loss due to vaporization increases significantly with power.
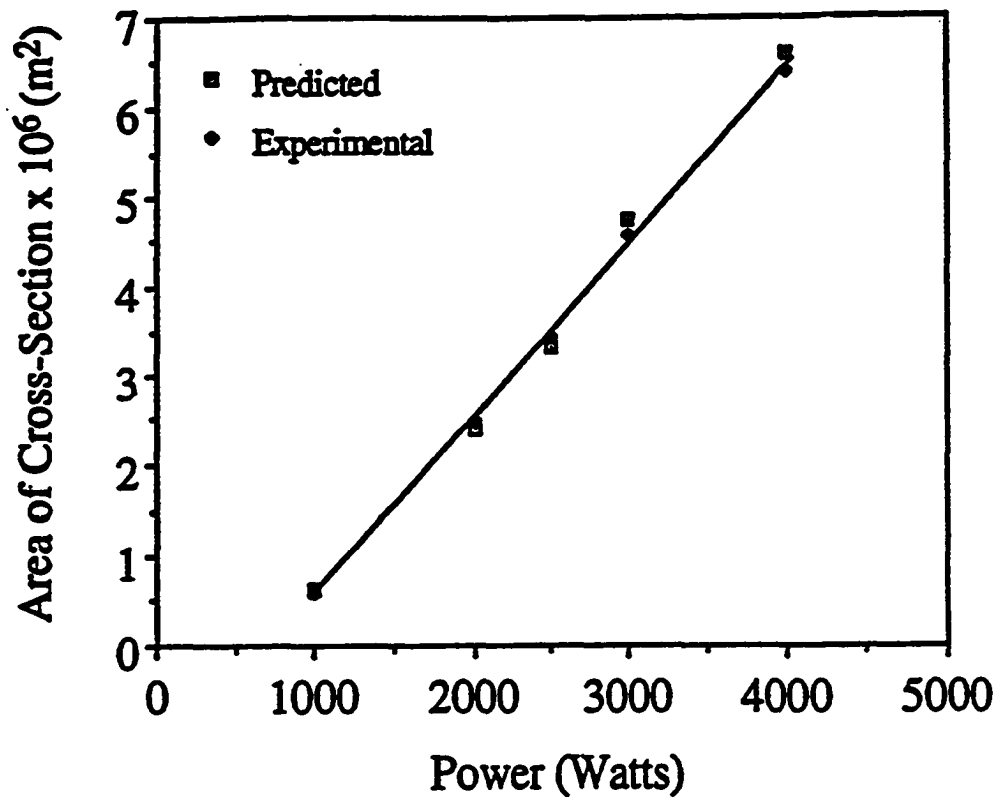
Fig. 4.25 Comparison of the experimental and the predicted areas of cross-section.
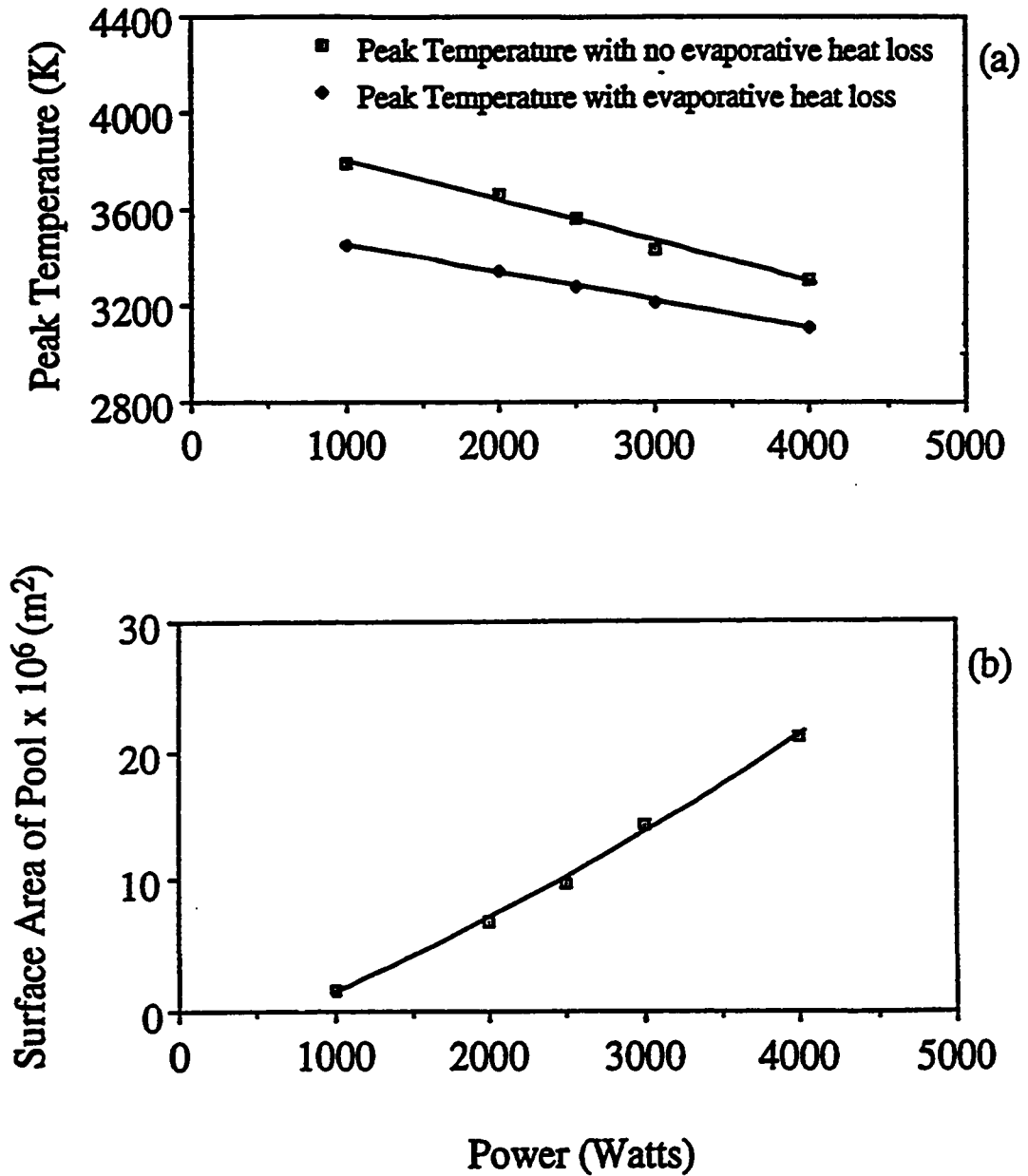
Fig. 4.26 (a) Peak temperatures with and without the evaporative heat loss vs. power, and (b) surface area of the pool vs. power.

4.1.3.2.2 Vaporization Rates for 201 Stainless Steels, High Laser Powers

From the peak temperatures plotted in Fig. 4.26 (a) it is observed that the temperatures reached at the center of the pool are greater than the boiling point of pure iron. The temperature at which the pressure on the surface is equal to 1 atmosphere was calculated to be 2953 K from the equilibrium vapor pressure-temperature relationship for the various alloying elements presented in Appendix F and the composition of the AISI 201 stainless steel indicated in Table 4.11. The flow state diagram for the AISI 201 stainless steel is shown in Fig. 4.27. For a given surface temperature, the Mach number of the vapor across the Knudsen layer is uniquely defined and is given by the line that intersects the equilibrium vapor pressure curve at that temperature. For example, at 3200 K the value of the Mach number is 0.29. The calculated variations of temperature, pressure and density at various location in the gas phase, for a weld pool surface temperature of 3200 K, are presented in Fig. 4.28. The details of the calculation procedure are summarized in Appendix C. The values of the Mach number and the density of the vapor across the Knudsen layer are presented in Fig. 4.29 for various surface temperatures. From the values of the Mach number and the density, total vaporization flux and the flux of the individual alloying elements due to pressure gradient are calculated from equations (3.24) and (3.25). The vaporization rate due to concentration gradient is calculated from mass transport considerations. The procedure takes into account the gas flow conditions and the nature of the shielding gas in accordance with equation (3.27).

The radial distribution of the total flux and the vaporization flux of the various alloying elements due to the combined effects of total pressure and concentration gradients are plotted in Fig. 4.30. Similarly, the radial distribution of the vaporization flux of the individual alloying elements and the total flux calculated from the Langmuir equation are

Table 4.11:   Initial and final compositions of AISI 201 stainless steel after welding. Laser power: 3000 Watts, Welding speed: 15.24×10^{-3} m/s.

Elements	Initial Composition (wt. %)	Activity (mole fraction)	Final Expected Composition (wt. %)	Expected Change (wt. %)
Manganese	6.50	0.066	6.16	-0.34
Chromium	17.00	0.180	16.93	-0.07
Nickel	4.25	0.041	4.28	+0.03
Iron	70.94	0.710	71.30	+0.36
Remainder	1.31	-	1.33	+0.02
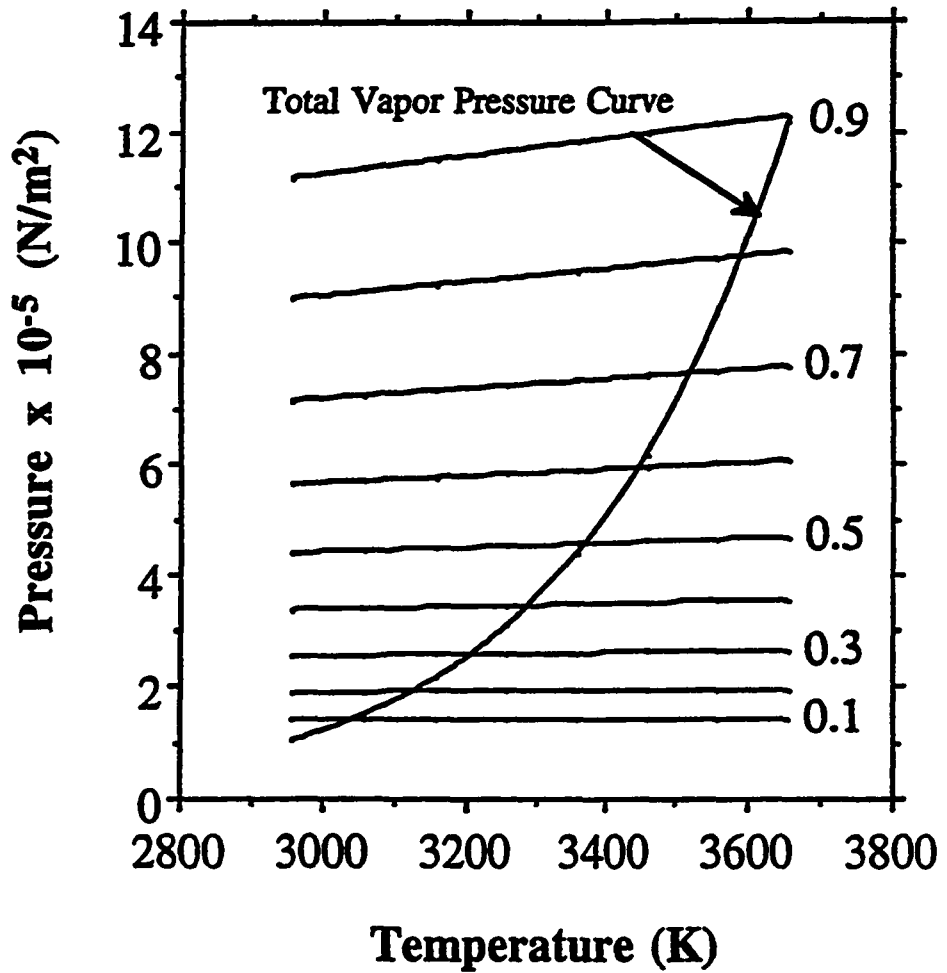
Fig. 4.27 Flow state diagram for AISI 201 stainless steel in helium atmosphere. The Mach number for various lines are indicated in the figure.
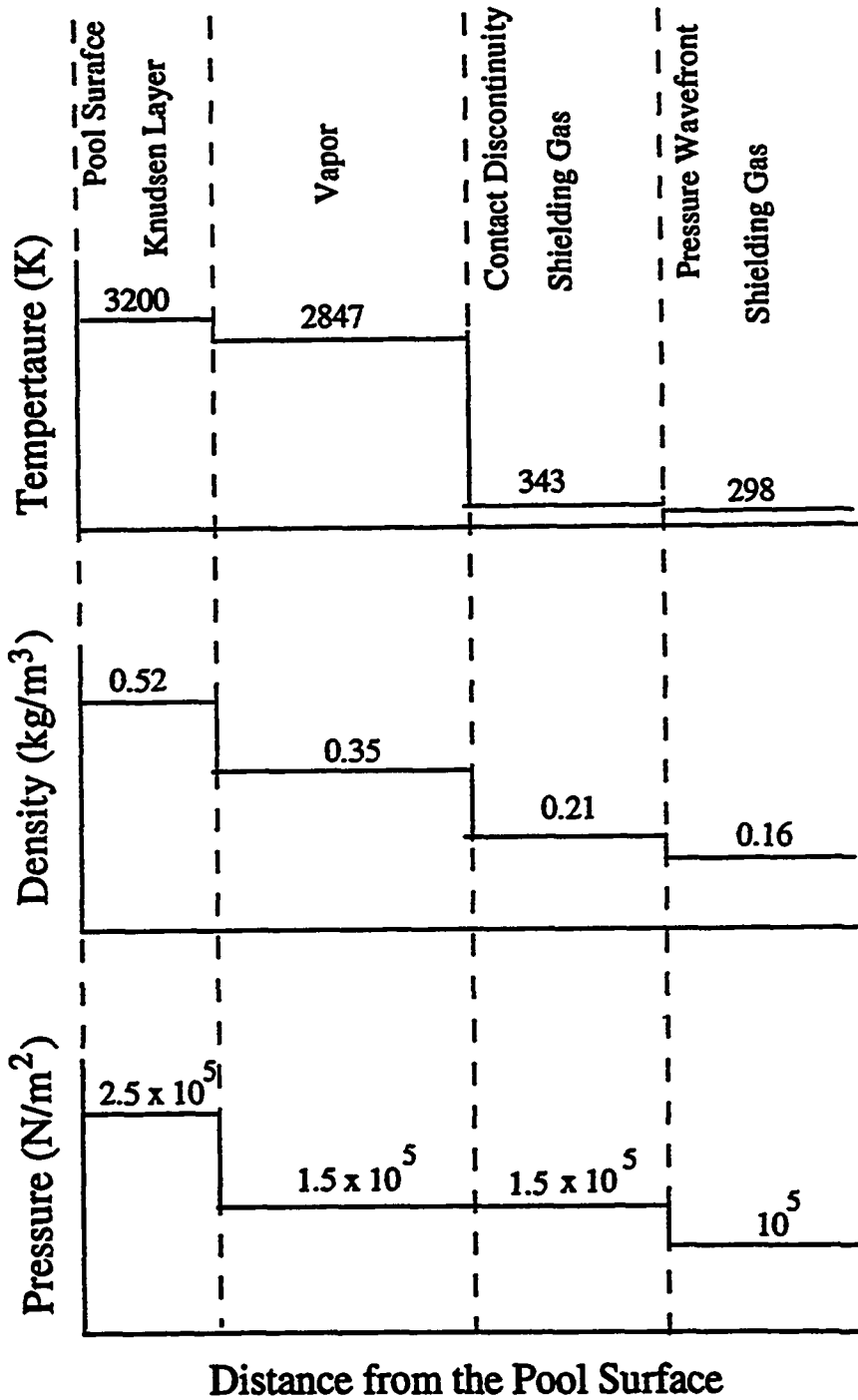
Fig. 4.28 Values of temperature, pressure and density at various locations in the gas phase for pool surface temperature of 3200 K.
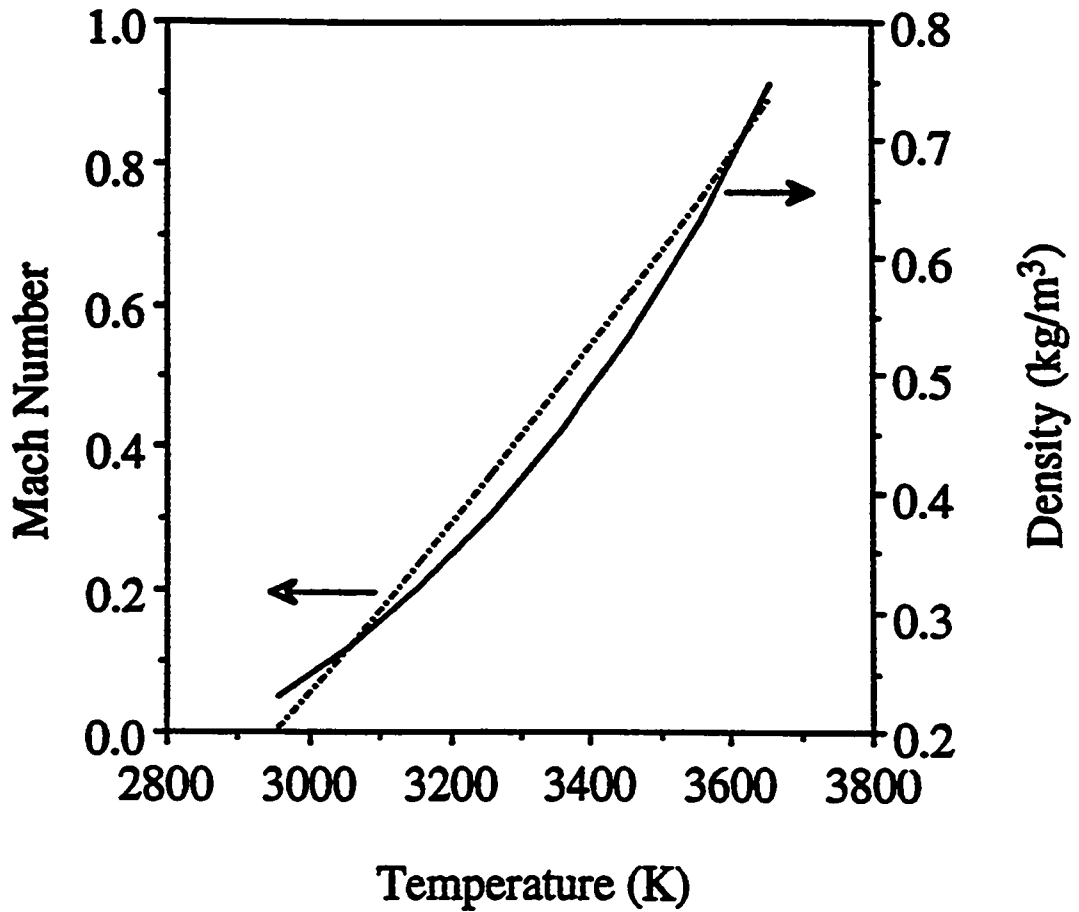
Fig. 4.29 Mach number and density for AISI 201 stainless steel for various temperatures at the edge of Knudsen layer in helium atmosphere.
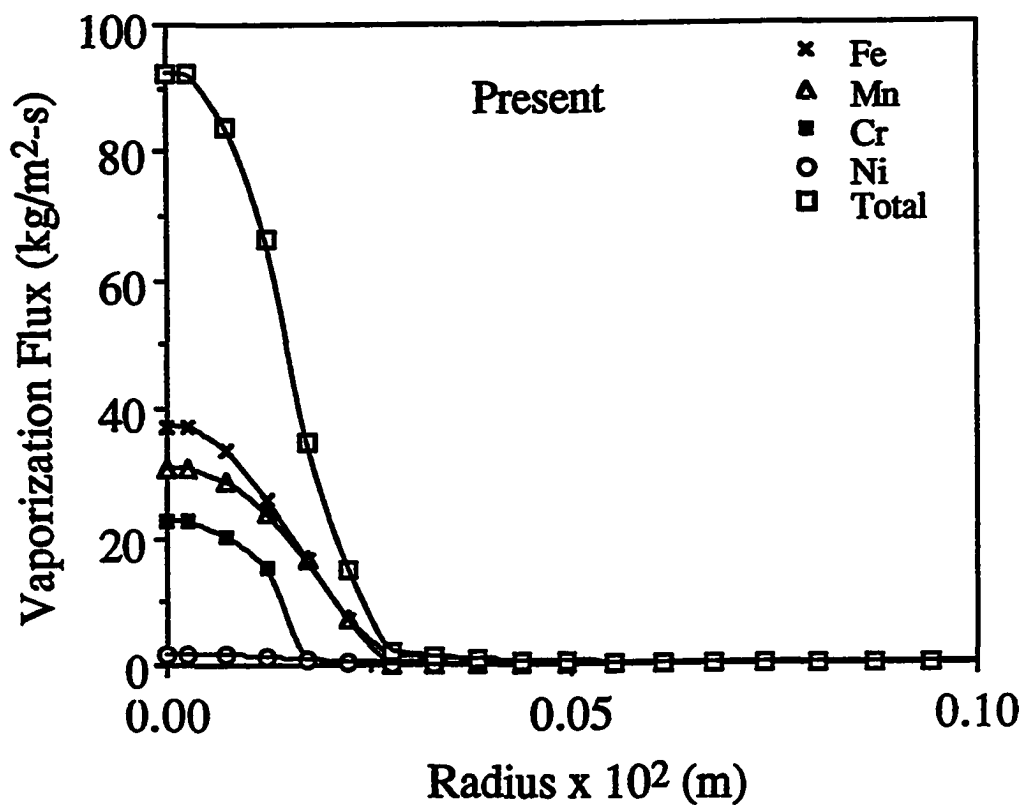
Fig. 4.30 Total vaporization flux and flux of various alloying elements calculated from the present model for a laser power of 3000 Watts.

plotted in Fig. 4.31. In figures 4.30 and 4.31 vaporization fluxes are plotted only in the region close to the center of the pool where vaporization is significant. At a very short distance away from the center of the pool the vaporization flux drops sharply. This is due to the fact vapor pressures of the alloying elements are strong functions of temperature and drops sharply as temperature drops. This can be observed from Fig. 4.17 where the equilibrium vapor pressure of the alloying elements are presented as a function of temperature. Comparison of the results in Figs. 4.30 and 4.31 indicates that the flux of the alloying elements predicted from the Langmuir equation is much higher than the corresponding value calculated in the present work.

4.1.3.2.3 Effect of Plasma on Vaporization Rates

A brief description of the role of plasma in influencing the vaporization rates was discussed in Chapter 2, section 2.1.2.2. Sahoo et al. [27,28] observed in their physical modeling experiments with metal drops that the presence of plasma lowers the vaporization rate. During the course of this investigation, experiments were conducted to correlate the plasma characteristics to the vaporization rate of ultra-pure iron. These results are discussed in more detail later in this chapter. Based on the results of the experiments of Sahoo et al. [27,28] and the present work it was observed that for iron, the vaporization rate in the presence of plasma varied from 30 to 90 pct of the vaporization rate when no plasma was present. The results of the controlled physical modeling experiments were used to incorporate the effect of the plasma on the vaporization rate. An average of one-third of the vaporized material was assumed to recondense on the surface of the material due to the space charge effect.
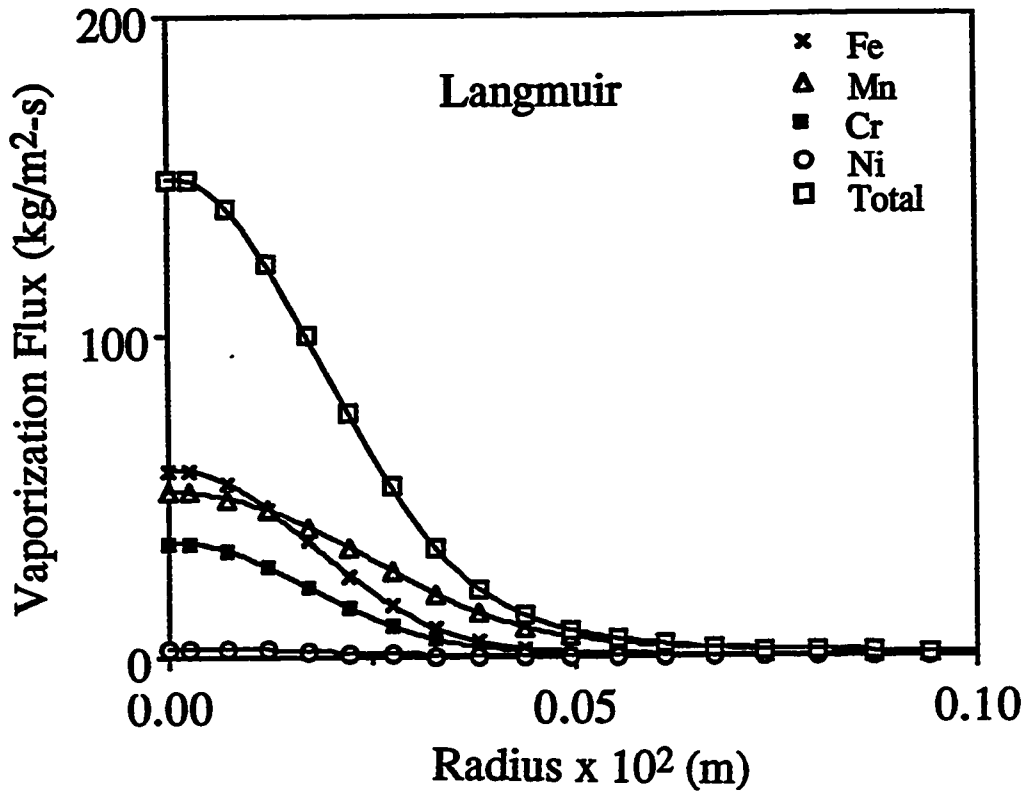
Fig. 4.31 Vaporization flux for various alloying elements and the total flux computed using the Langmuir equation for a laser power of 3000 Watts.

4.1.3.2.4 Composition Change

In Fig. 4.32 the total vaporization rate computed from the model and the value calculated from the Langmuir equation are compared with the experimentally determined rate for a laser power of 3000 Watts. It is observed that the computed value of the vaporization rate is in good agreement with the experimental data. The rate calculated from the Langmuir equation was significantly higher than the experimental value. Similarly, the experimentally determined rates of vaporization of Mn and Fe agreed well with the corresponding calculated results. For various laser powers, the changes in the manganese concentrations calculated from its rates of vaporization and the corresponding weld geometries are presented in Fig. 4.33. It can be observed that the calculated changes in manganese concentrations are in good agreement with the experimentally observed composition changes. Furthermore, the values predicted by the Langmuir equation are significantly higher than the corresponding experimental values. Although the rate of vaporization of manganese increases with power, the change in the concentration of manganese in the weld pool becomes less pronounced at high laser powers. This is because at high powers, the increase in vaporization rate is also accompanied by an increase in the volume of the weld pool. The volume increase outweighs the effect of increased vaporization rate. The expected changes in the concentrations of iron, chromium and nickel for a laser power of 3000 Watts are presented in Table 4.11. It is observed from the computed results that the concentrations of manganese and chromium decreased and those of iron and nickel slightly increased due to welding. Although both iron and nickel are lost from the weld pool, the net increase in the weight percents of iron and nickel is due to the concentration balance. The results are consistent with the experimental data of Khan and DebRoy [18] who found increased weight percentages of iron and nickel and decreased weight percentages of manganese and chromium in the laser welded 202 stainless steel.
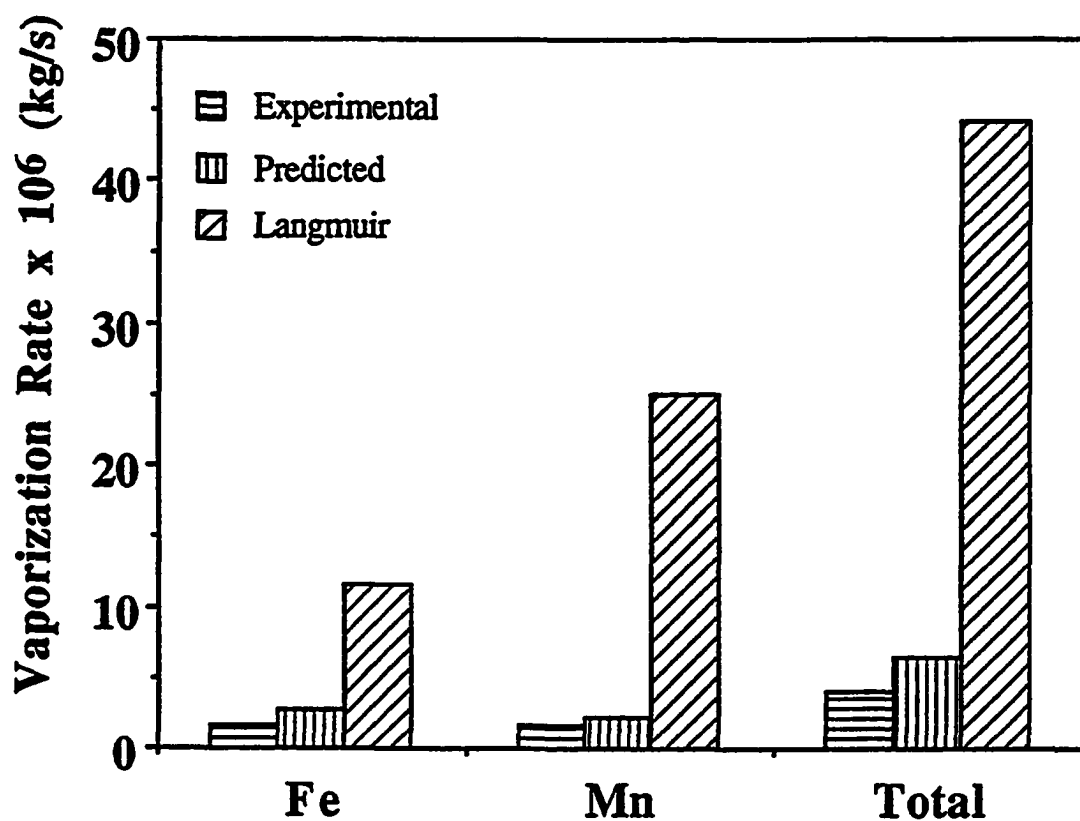
Fig. 4.32 Comparison of the vaporization rates calculated from the Langmuir equation and from the present model with experimentally determined values for a laser power of 3000 Watts.
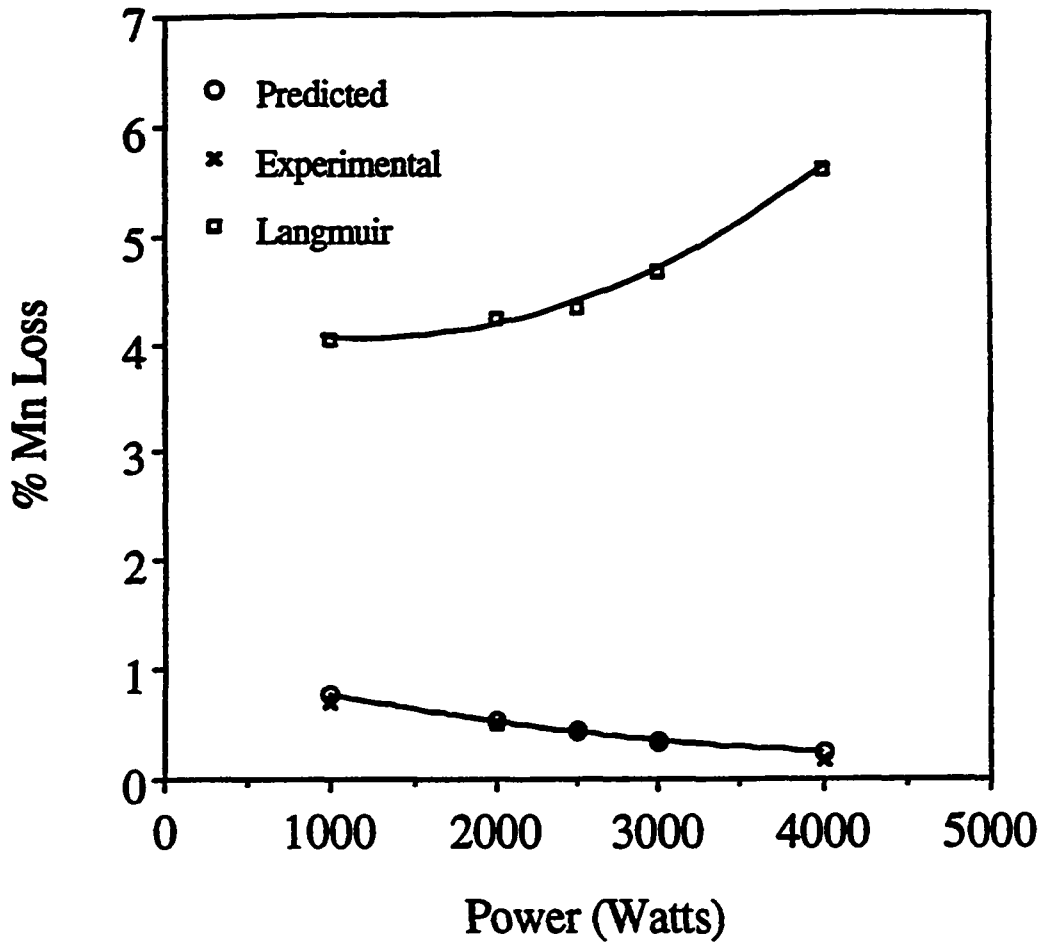
Fig. 4.33 Calculated and experimental changes in the manganese concentration in the weld pool.

4.2 Effect of Plasma on Vaporization Rates

The experimental vaporization rates of iron samples, maintained at 1573 K in helium atmosphere and at 10 Torr pressure, with and without the presence of plasma are compared in Fig. 4.34. Also presented on the bar graph is the vaporization rate predicted by the Langmuir equation [30]. The Langmuir equation [30] is given by:

$$J = 0.0583 \, P^O \sqrt{\frac{M}{T}}$$

(4.2)

where J is rate of vaporization in gm/cm^2-s, P^O is the equilibrium vapor pressure in Torr at temperature T in K and M is the molecular weight in gms/gm-mole. There is a considerable scatter in the equilibrium vapor pressure-temperature data reported in literature for solid iron. This is evident from Fig. 4.35 [31] where the data from several sources are compiled. At 1573 K the equilibrium vapor pressure for iron from the solid line in Fig. 4.35 can be approximated to be equal to 0.0012 Torr (mm Hg). From the data reported in Smithels Metals Reference Book [32] the equilibrium vapor pressure of iron at 1573 is 0.000446 Torr. The equilibrium vapor pressure-temperature relationship from Smithels book [32] is given in Appendix F. In the calculation of vaporization rate from Langmuir equation, the equilibrium vapor pressure data presented in Fig. 4.35 was used. It is observed from Fig. 4.34 that the vaporization rate in the presence of plasma is significantly lower than the vaporization rate in the absence of plasma. The results are consistent with the observations of Sahoo et al. [27,28], presented in Fig. 2.4, who reported a significant drop in vaporization rates of iron, copper and several binary systems in the presence of plasma. They attributed the lowering of the vaporization rates in the presence of plasma to the space charge effect, discussed in Chapter 2, section 2.1.2.2. Furthermore, the rate of
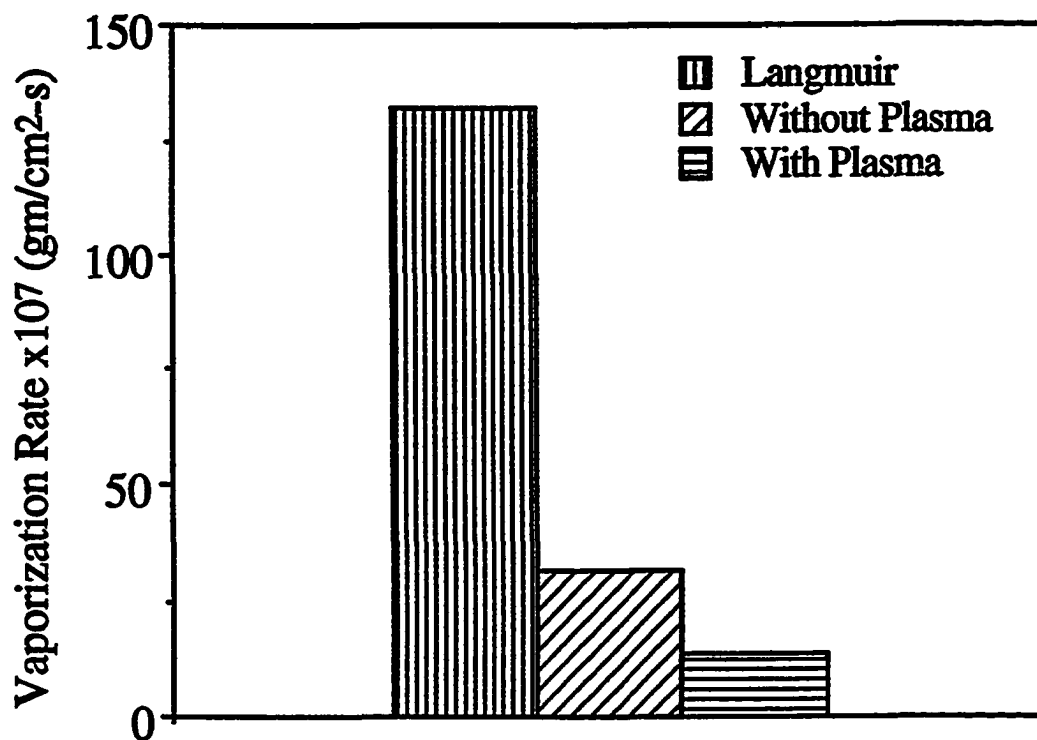
Fig. 4.34 Comparison of vaporization rates of iron, in the presence and absence of plasma, maintained at 1573 K in helium atmosphere at 10 Torr pressure. The vaporization predicted by Langmuir equation is also shown.
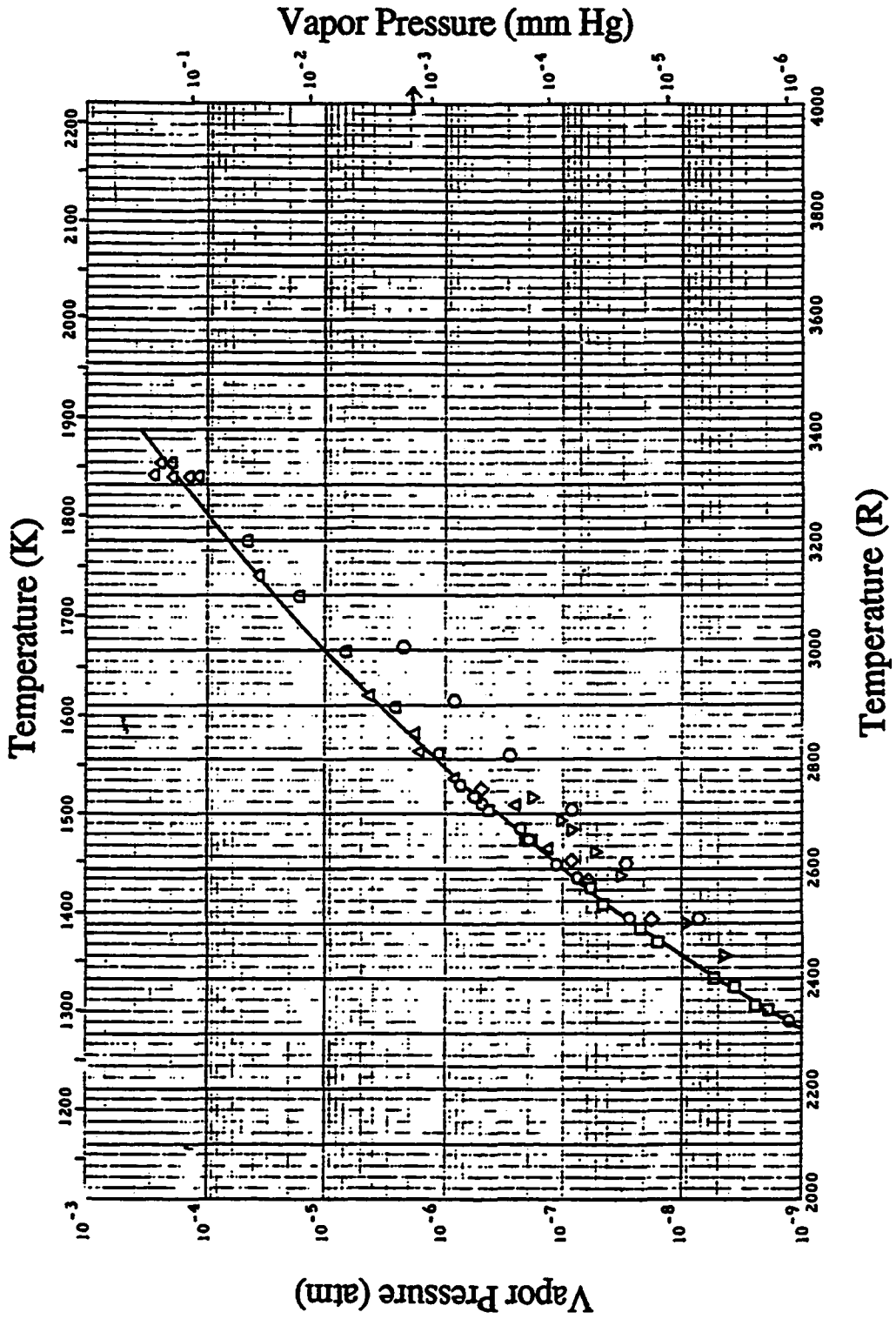
Fig. 4.35 Equilibrium vapor pressure-temperature data for iron [31].

vaporization predicted by Langmuir equation is significantly higher than the experimental vaporization rates both in the presence and absence of plasma. This can be attributed to the fact that Langmuir equation is valid in vacuum or at very low pressures and it does not consider mass transfer of the vaporized molecules through the gas phase. The Langmuir equation has been used by various researchers [33-36] for the calculation of vaporization rates at atmospheric pressure for welding problems. This can result in considerable overprediction of vaporization rates.

4.2.1 Effect of Pressure on Vaporization Rates

The rates of vaporization of iron, maintained at 1573 K, for different pressures in the presence and the absence of plasma are presented in Fig. 4.36. Except at 10 Torr, the experiments with and without plasma were done at different pressures. This was due to the fact that obtaining experimental conditions without generating the plasma at low pressures was extremely difficult. It is observed from Fig. 4.36 and the Langmuir rate presented in Fig. 4.34 that, under all conditions of experiments, the rates of vaporization of iron was lower than the rates predicted by the Langmuir equation, which is independent of the chamber pressure used in the experiments. Furthermore, significant difference in the variation of vaporization rates with pressure, with and without plasma, can be observed from Fig. 4.36. It is observed that in the absence of plasma the rate of vaporization decreases with increase in pressure. When plasma is present the rate of vaporization increases with pressure. The reasons for the different behavior of the vaporization rates in the presence and the absence of plasma are discussed below.
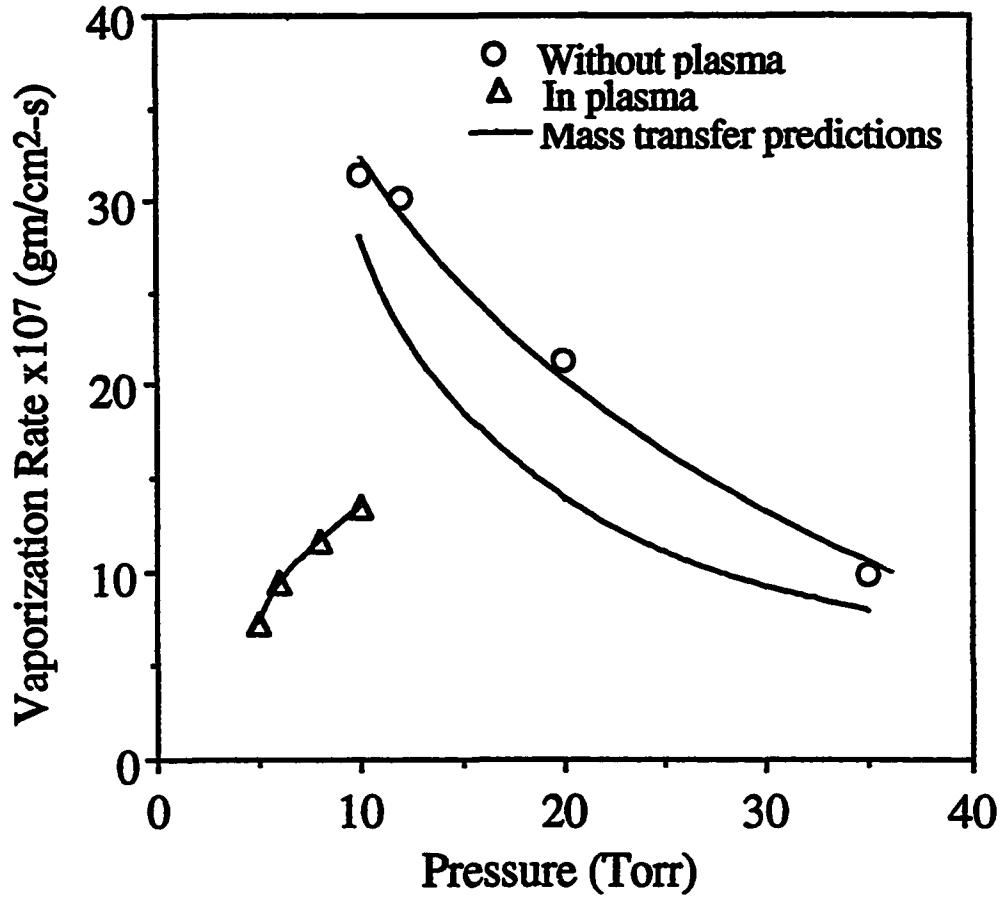
Fig. 4.36 Variation of vaporization rate of iron with pressure in the absence and presence of plasma. The mass transfer predictions of vaporization rates are also shown.

4.2.2 Vaporization in the Absence of Plasma

At the surface of the sample the concentration of iron vapor is considerably higher than its concentration in the bulk atmosphere. The vaporization flux of iron, J_{Fe}, due to mass transfer, owing to the concentration gradient, is defined as:

$$J_{Fe} = (P^0_{Fe} - P_b) \frac{K_g}{RT} \qquad (4.3)$$

where P^0_{Fe} and P_b are the vapor pressure of iron at the surface of the sample and in the bulk gas, respectively, K_g is the mass transfer coefficient, T is the temperature and R is the gas constant. The vapor pressure of iron in the bulk of the gas will be significantly lower than at the surface and therefore can be neglected. Since, under all experimental conditions, the temperature of the sample was maintained at 1573, in equation (4.3) the only variable is K_g. The mass transfer coefficient, K_g, is given by:

$$K_g = \frac{D_{A/B} \, Sh}{L} \qquad (4.4)$$

where $D_{A/B}$ is the binary diffusivity of A/B pair, Sh is the Sherwood number and L is a characteristic length. The binary molecular diffusivity, $D_{A/B}$, of a gas pair A and B, at absolute temperature T is given by:

$$D_{A/B} = \frac{1.8583 \times 10^{-3}}{p \sigma_{A/B}^2 \Omega_D(T^*)} \sqrt{\left[\frac{1}{M_A} + \frac{1}{M_B}\right] T^3} \qquad (4.5)$$

The symbols and their definitions are given in Appendix A. The Sherwood number is a function of Reynolds' number, Re, and Schmidt number, Sc.

$$Sh = f(Re, Sc) \tag{4.6}$$

The Schmidt number is given by $\mu/\rho D_{A/B}$ where μ and ρ are the viscosity and the density of the surrounding fluid, respectively. The Schmidt number of fluid does not change with pressure. This is due to the fact that density of the fluid is directly proportional to the pressure, $D_{A/B}$ is inversely proportional to the pressure and viscosity does not depend on pressure. As a result, the increase in density of the gas with pressure is compensated by the decrease in the diffusivity with pressure. The Reynolds' number, Re, is given by $\rho u L/\mu$ where μ and ρ are the viscosity and the density of the surrounding fluid, respectively, u is the velocity of the fluid and L is a characteristic length. For a given system, L is a constant. Also viscosity, μ, does not change with pressure and, for a given flow rate of the gas, ρu is constant. Thus Reynolds' number does not change with pressure. Thus, in equation (4.4) the only variable that changes with pressure is $D_{A/B}$. The plot of diffusivity of iron vapor in helium as a function of pressure is given in Fig. 4.37. It is observed that the diffusivity decreases with pressure. The decrease in diffusivity results in decrease in mass transfer coefficient, K_g, which can result in lower vaporization rates at higher pressures in the absence of plasma.

In order to further examine the variation of vaporization rates with pressure in the absence of the plasma, rates of vaporization at different pressures were predicted using the following mass transfer correlation [37]:

$$K_g = \frac{D_{A/B}}{L} [2.0 + 0.6\,(Re)^{1/2}(Sc)^{1/3}] \tag{4.7}$$
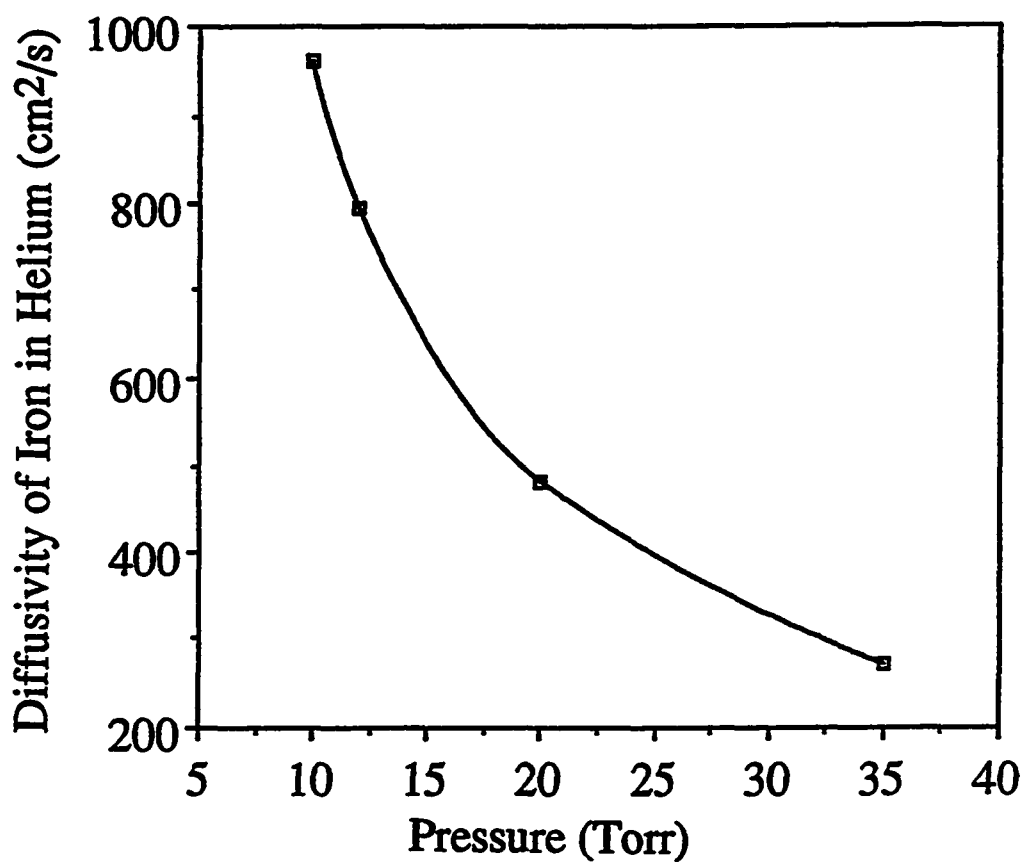
Fig. 4.37   Variation of diffusivity of iron in helium with pressure at 1573 K.

This equation gives the mass transfer coefficient for a sphere immersed in a flowing fluid. Although cylindrical discs were used in the experiments, due to lack of availability of a better correlation in literature, equation (4.7) was used. The rates of vaporization predicted from equation (4.3), using the values of K_g calculated from equation (4.7), at different pressures are plotted in Fig. 4.36. A sample calculation is presented in Table 4. 12. In the calculations the equilibrium vapor pressure data from Handbook of Thermophysical Properties of Solid Materials [31] was used. It is observed from Fig. 4.36 that the predicted rates are somewhat lower than the experimentally observed rates. However, the predicted vaporization rates follows the trend that is observed in the experimental data. Thus, the mass transfer predictions of vaporization rates is consistent with the experimental observations. The lower predicted rates could be due to the fact that only an approximate mass transfer correlation was used.

4.2.3 Vaporization in the Presence of Plasma

Sahoo et al [27,28] attributed the decrease in vaporization rates in the presence of plasma to the space charge effect. The space charge effect is a consequence of the high mobility of the electrons which results in the surface of the metal drop to acquire a negative charge and the vapor near the surface becomes populated with positively charged ions. The attraction between the positively charged metal ions and the negatively charged surface leads to condensation of metallic species, resulting in lower vaporization rates. Sahoo et al. [27,28] argued that electron mobility and density are two important factors that will influence the decrease in the vaporization rate in the presence of plasma. Optical emission spectroscopy was used to investigate these two parameters at various pressure.

Table 4.12   Data used for the calculation of mass transfer rates.
The calculations are done for 10 Torr pressure.

Parameter/Property	Value
Temperature (K)	1573
Pressure (Torr)	10
Viscosity of helium (gm/cm-s)	5.72×10^{-4}
Density of helium (gm/cm^3)	4.03×10^{-7}
Flow rate of helium (cm^3)	200.0
Diameter of the tube (cm)	4.8
Diamter of the sample (cm)	0.5
Average velocity in the tube (cm/s)	74.68
Diffusivity of iron in helium (cm^2/s)	960.29
Schmidt number	1.48
Reynolds' number	0.0263
Sherwood number	2.11
Mass transfer coefficeint (cm/s)	4052.42
Equilibrium vapor pressure (Torr)	0.0012
Vaporization rate (gm/cm^2-s)	28×10^{-7}

A typical spectrum, in the 390 to 430 nm wavelength range, of helium plasma with iron sample kept in the chamber, at 6 Torr pressure, is given in Fig. 4.38 (a). Also presented in Fig. 4.38 (b) is a typical spectrum of pure helium plasma. Each spectral line corresponds to a particular energy emission. In Table 4.13, the theoretically possible emissions from helium and iron in the range of 360 to 400 nm are presented [38,39]. It is evident from the table that there are many common wavelengths where both helium and iron emissions are expected. As a consequence of this, the characterization of the plasma becomes difficult. To avoid the difficulty, optical spectra of helium plasma were taken in the absence of the iron sample. In this way the variation of electron density and electron temperature with pressure could be investigated.

4.2.4 Electron Temperature and Electron Density

The average kinetic energy of the electrons, expressed as the electron temperature, was determined from the intensity vs. wavelength data obtained from the emission spectroscopy. The calculation procedure is outlined in standard textbooks [40]. Therefore, only a brief outline of the procedure is presented here. The combination of the equation for absolute intensity of an atomic line with an expression for the Boltzmann distribution of energy populations yields an expression of the following form:

$$\ln\left(\frac{I}{gA\nu}\right) = \ln C - \frac{E_q}{kT}$$

(4.8)

where I is the integrated intensity in s^{-2}, g is the degeneracy of the upper level q, A is the transition probability for the transition from the upper energy state q to the lower energy level in s^{-1}, ν is the frequency in s^{-1}, E_q is the energy associated with level q in $cm^{-1}K^{-1}$, k
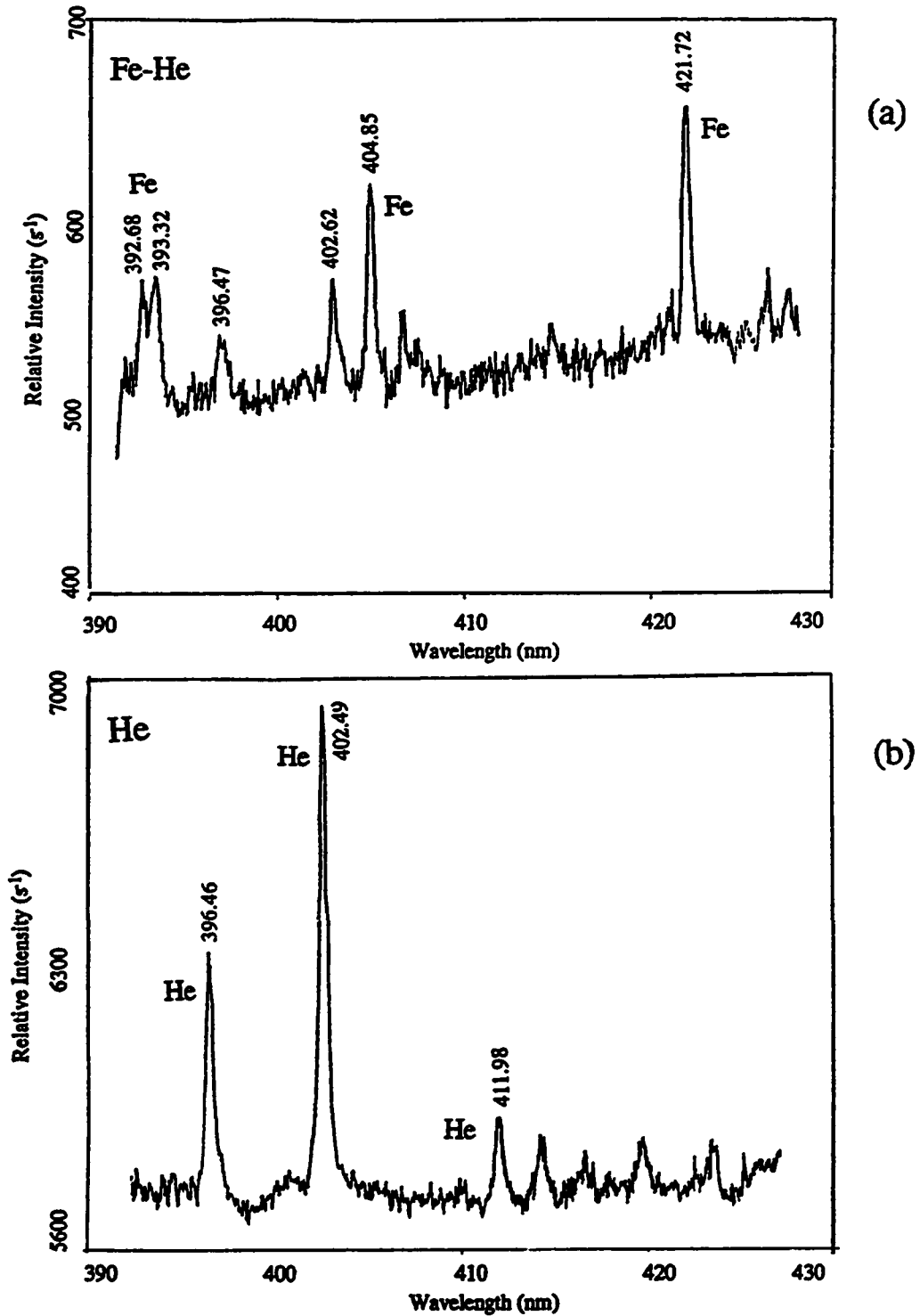
Fig. 4.38 Typical spectra in the 390 to 430 nm wavelength range of (a) iron-helium plasma and (b) helium plasma. The peaks unique to iron and helium emissions are identified.

Table 4.13 Iron (Fe I) and helium (He I) allowed transitions in the 360 to 400 nm range.

Iron (Fe I) Peaks (nm)	360.20, 360.32, 360.36, 360.38, 360.54, 360.66, 360.88, 361.01, 361.07, 361.20, 361.31, 361.34, 361.47, 361.51, 361.56, 361.61, 361.63, 361.77, 361.87, 362.02, 362.14, 362.20, 362.31, 362.40, 362.43, 362.70, 362.80, 362.88, 363.03, 363.14, 363.20, 363.25, 363.38, 363.51, 363.69, 363.72, 363.78, 363.83, 364.03, 364.14, 364.45, 364.48, 364.58, 364.78, 364.95, 365.00, 365.14, 365.37, 365.46, 365.54, 365.71, 365.78, 365.85, 365.95, 366.13, 366.45, 366.46, 366.94, 366.69, 366.72, 366.82, 366.88, 366.91, 366.95, 367.00, 367.08, 367.26, 367.47, 367.63, 367.68, 367.73, 367.76, 367.88, 367.99, 368.16, 368.22, 368.30, 368.41, 368.60, 368.62, 368.71, 368.74, 368.84, 368.88, 368.90, 368.99, 369.07, 369.40, 369.40, 369.74, 369.86, 369.91, 370.10, 372.02, 370.36, 370.38, 370.40, 370.44, 370.55, 370.78, 370.92, 371.12, 371.14, 371.59, 371.84, 371.99, 372.25, 372.43, 372.54, 372.69, 372.70, 372.76, 372.86, 373.03, 373.09, 373.13, 373.24, 373.33, 373.48, 373.53, 373.71, 373.83, 373.91, 373.93, 374.02, 374.26, 374.33, 374.41, 374.55, 374.59, 374.64, 374.69, 374.82, 374.94, 375.10, 375.18, 375.31, 375.36, 375.45, 375.60, 375.69, 375.74, 375.82, 376.00, 376.05, 376.14, 376.22, 376.37, 376.55, 376.60, 376.66, 376.71, 376.80, 377.03, 377.15, 377.33, 377.37, 377.48, 377.58, 377.64, 377.70, 377.74, 377.83, 377.85, 377.87, 378.11, 378.19, 378.24, 378.26, 378.57, 378.59, 378.61, 378.66, 378.71, 378.78, 378.91, 378.98, 379.00, 379.15, 379.17, 379.21, 379.28, 379.38, 379.43, 379.50, 379.79, 379.85, 379.95, 380.16, 380.20, 380.22, 380.40, 380.53, 380.62, 380.67, 380.75, 380.82, 380.87, 380.90, 381.07, 381.18, 381.36, 381.38, 381.45, 381.58, 381.63, 381.76, 381.95, 382.04, 382.11, 382.18, 382.44, 382.58, 382.68, 382.78, 382.91, 382.97, 383.33, 383.42, 383.63, 383.71, 383.92, 383.96, 384.04, 384.10, 384.32, 384.51, 384.56, 384.60, 384.64, 384.68, 384.82, 384.99, 385.08, 385.25, 385.34, 385.63, 385.92, 385.99, 386.37, 386.55, 386.72, 386.79, 387.17, 387.25, 387.29, 387.37, 387.60, 387.80, 387.85, 388.32, 388.43, 388.51, 388.55, 388.62, 388.70, 388.85, 388.88, 389.03, 389.08, 389.19, 389.33, 389.56, 389.74, 389.90, 389.97, 390.05, 390.29, 390.39, 390.64, 390.67, 390.74, 390.79, 390.96, 390.98, 391.08, 391.10, 391.36, 391.42, 391.67, 391.71, 391.90, 392.02, 392.08, 392.29, 392.52, 392.79, 393.03, 393.11, 393.53, 393.73, 394.12, 394.24, 394.33, 394.47, 394.48, 394.51, 394.69, 394.87, 394.91, 394.99, 395.11, 395.26, 395.31, 395.38, 395.53, 395.59, 395.64, 395.70, 396.02, 396.11, 396.23, 396.31, 396.45, 396.60, 396.74, 396.79, 396.92, 396.96, 397.03, 397.13, 397.36, 397.44, 397.47, 397.52, 397.58, 397.66, 397.77, 397.96, 398.06, 398.11, 398.17, 398.39, 398.53, 398.98, 399.03, 399.41, 399.52, 399.59, 399.69, 399.73, 399.80, 400.02, 400.04
Helium (He I) Peaks (nm)	361.36, 363.42, 365.20, 370.50, 381.96, 383.35, 386.75, 387.17, 388.86, 392.65, 393.59, 393.59, 396.47, 400.92

is the Boltzmann constant, and C is a constant. The electron temperature can be obtained from the slope of a plot of $\ln(I/gA\nu)$ vs. E_q.

The electron density, n_e, was evaluated from the Stark broadening of the peaks. The electron density [41] can be related to the full Stark width, $\Delta\lambda_s$, as

$$n_e = C(n_e,T)\Delta\lambda_s^{3/2} \tag{4.9}$$

where $C(n_e,T)$ is a weak function of electron density and temperature.

The Bolzmann plot for helium plasma maintained at 10 Torr is presented in Fig. 4.39. The data used for the calculations are presented in Table 4.14. The variation of electron temperature with pressure is presented in Fig. 4.40. It is evident from the figure that the electron temperature decreases with pressure. The results are consistent with the data of Madey [42], who calculated electron temperature in oxygen plasma formed with microwave power for different pressures, and Banerjee et al. [43,44], who investigated electron temperature variation with pressure in the plasma enhanced chemical vapor deposition (PECVD) of silicon oxide for silane, nitrous oxide and argon mixture.

The electron density variation with pressure, n_e/n_{eo}, calculated from equation (4.9) for three different peaks of helium emissions, is presented in Fig. 4.41. The symbol n_{eo} represents the electron density at 8.0 Torr pressure. The Stark broadening at a wavelength of 446.48 nm for the three different pressures is presented in Fig. 4.42. It is evident from Fig. 4.41 that there is no significant variation in electron density with pressure.

Table 4.14: Data used for the calculation of electron temperatures [38].

λ (nm)	g	A (s^{-1}) x 10^8	Eq (cm^{-1})
396.47	3	0.0717	191493
402.62	15	0.117	193917
447.15	15	0.215	191445
471.32	3	0.106	190298
492.19	5	0.202	191447
501.57	3	0.1338	186210
504.77	3	0.0655	190940
667.81	5	0.638	186105
706.57	3	0.278	183237
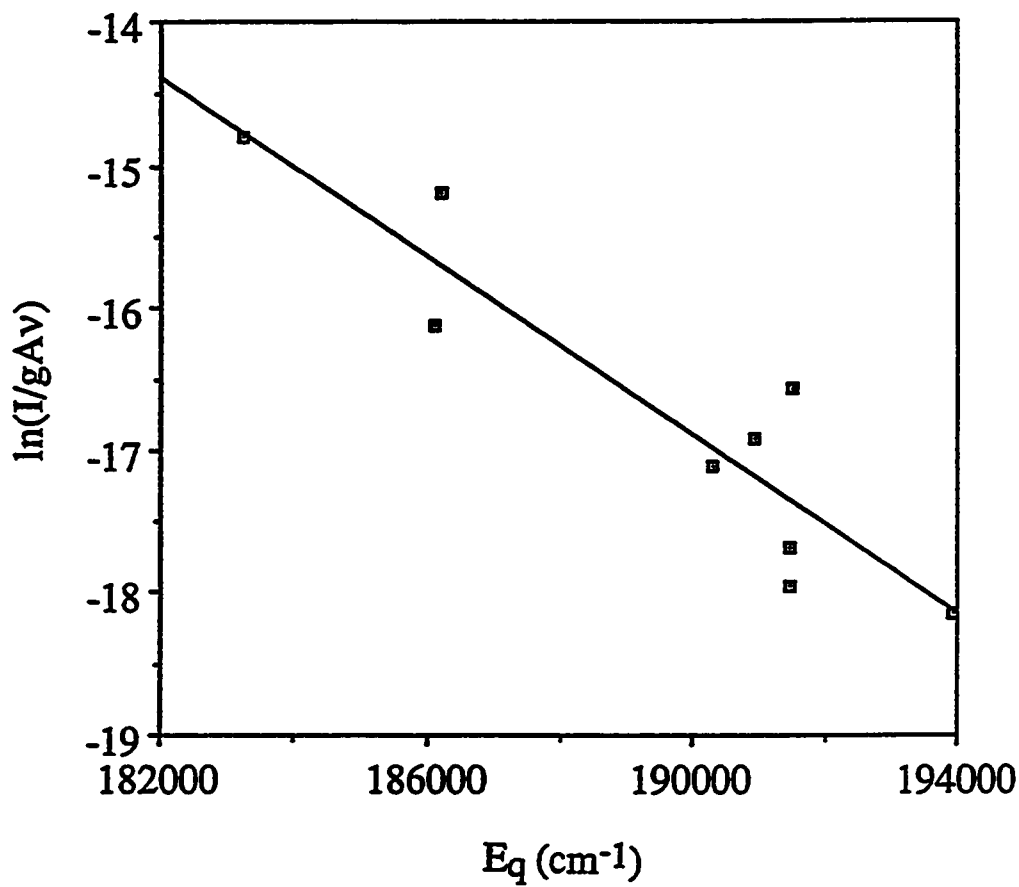
Fig. 4.39 Bolzmann plot for helium plasma maintained at 10 Torr.
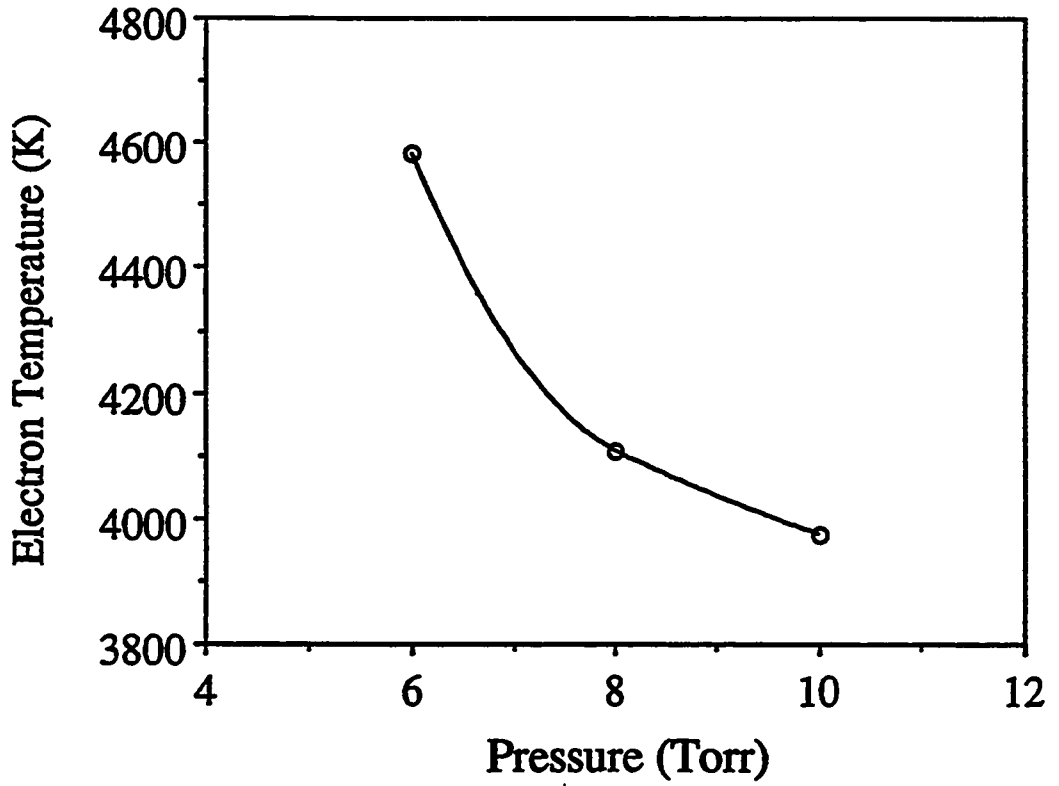
Fig. 4.40 Variation of electron temperature with pressure of helium plasma.
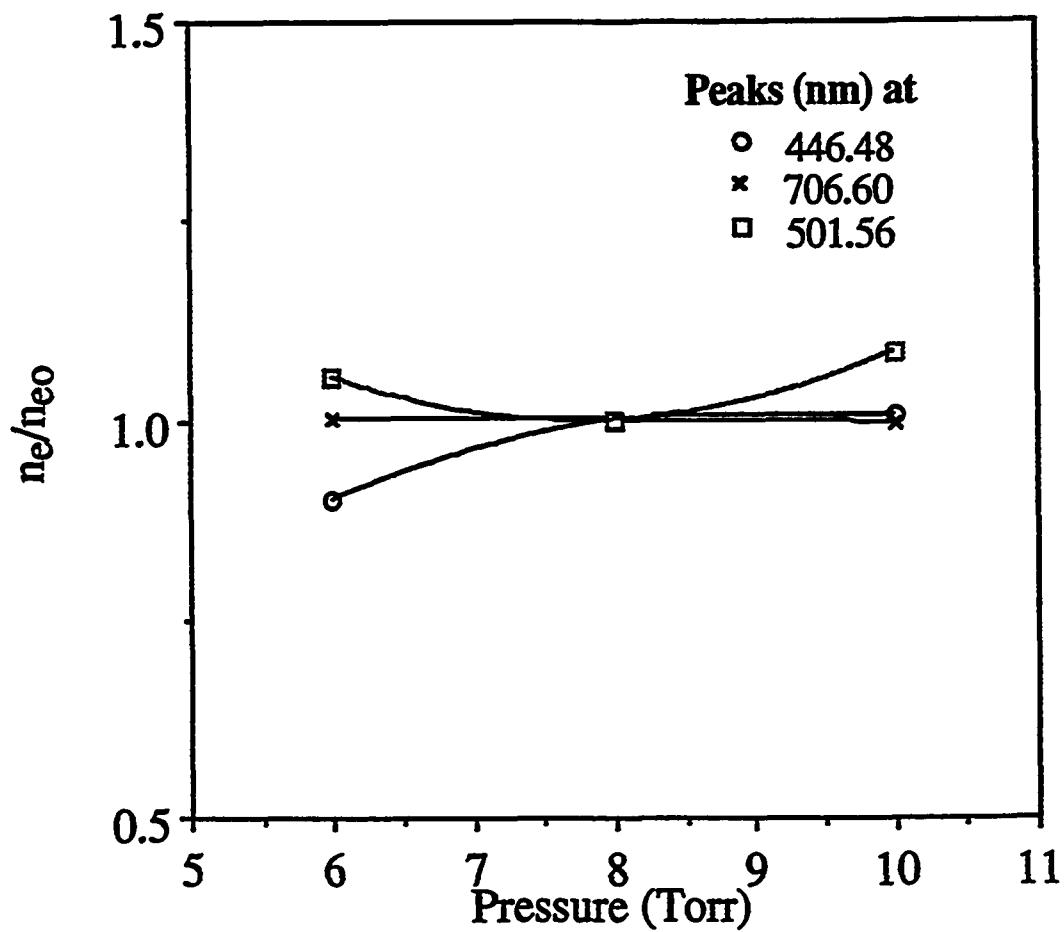
Fig. 4.41 Variation of electron density of helium plasma with pressure. The calculations are done with Stark broadening of three different peaks.
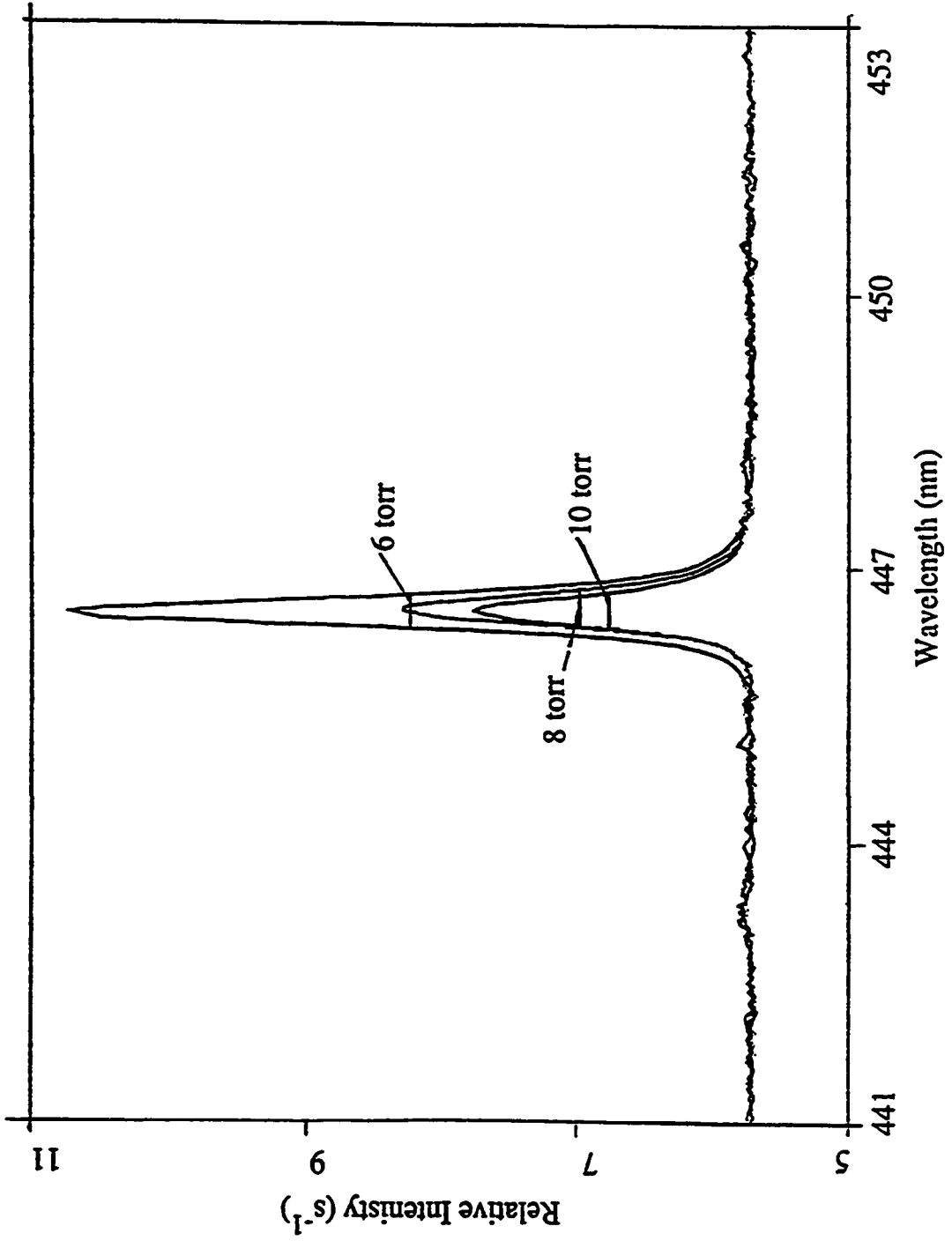
Fig. 4.42 Stark broadening of a helium emission at a wavelength of 446.48 nm for three different pressures.

The calculation of electron temperature and electron density with pressure indicates that electron temperature changes with pressure. This variation in electron temperature can explain the increase in vaporization rate with pressure. The flux of electrons, j_e, and ions, j_i, when the plasma is initiated is given by [45]

$$j_e = \frac{e n_e v_e}{4}$$ (4.10)

and $$j_i = \frac{e n_i v_i}{4}$$ (4.11)

where n_e and n_i are the electron and ion density, respectively, and v_e and v_i are the mean velocities of electrons and ions, respectively. Since plasma is electrically neutral, $n_e = n_i$. Furthermore, since $v_e \gg v_i$, therefore $j_e \gg j_i$. Therefore, as soon as the plasma is initiated the sample immediately starts to build a negative charge and acquires negative potential with respect to the plasma. Since the sample acquires a negative charge, electrons are repelled and ions are attracted. This results in a decrease in the electron flux and an increase in the ion flux. The sample continues to acquire negative charge until the electron flux is balanced by the ion flux. Now consider two separate cases where the mean velocities of the electrons in the first case, $(v_e)_1$, is greater than the mean velocities of the electrons in the second case, $(v_e)_2$. Since $(v_e)_1 > (v_e)_2$ the flux of electrons at the sample surface in the first case just when the plasma is initiated, given by equation (4.10), is higher than in the second case. As a result, the build-up of the negative charge in the first case is higher and more ion flux is required to balance the electron flux. This would lead to more condensation of ions on the sample surface, and hence lower vaporization rates, in the first case. As the pressure decreases the electron temperature increases as is observed from Fig. 4.40. As a consequence, v_e is higher at low pressures. This results in higher build-up of negative

charge on the sample surface and higher ion flux on the sample surface is required to balance electron flux. This results in lower vaporization rates at lower pressure due to increased condensation of positively charged metallic ions on the sample surface.

4.3 Gas Dissolution at theWeld Pool Surface

4.3.1 Identification of the Species

The two temperature model on gas dissolution, presented in Chapter 3, section 3.3, assumed that the gas near the metal drop consists primarily of monatomic and diatomic species. However, the plasma itself consists of excited neutral atoms, molecules and ions. A schematic diagram of the plasma near a metal drop is shown in Fig. 4.43. In the figure the gaseous species are represented by N, metal species by M, inert gas species by I and electrons by e. Any excited neutral molecule cannot contribute to enhanced solubility since it will loose its excess vibrational energy when adsorbed [46]. In the plasma, the flux of the highly mobile electrons to the liquid surface is far greater than the flux of the heavier species. As a result, the liquid metal surface is surrounded by negative charge. Hence, the adsorption of negatively charged species such as N^- is highly improbable and they would not contribute towards enhanced solubility. Furthermore, positively charged species such as N^+ and N_2^+ will be attracted towards the surface where they will absorb electrons near the surface and will effectively be N and N_2. Thus, any species near the metal drop is more likely to be neutral atoms or molecules like N and N_2. Although, the presence of excited, neutral atoms and ions can lead to enhanced adsorption, Katz and King [46] showed that nitrogen dissolution is limited by mass transfer in the melt. Thus, enhanced dissolution
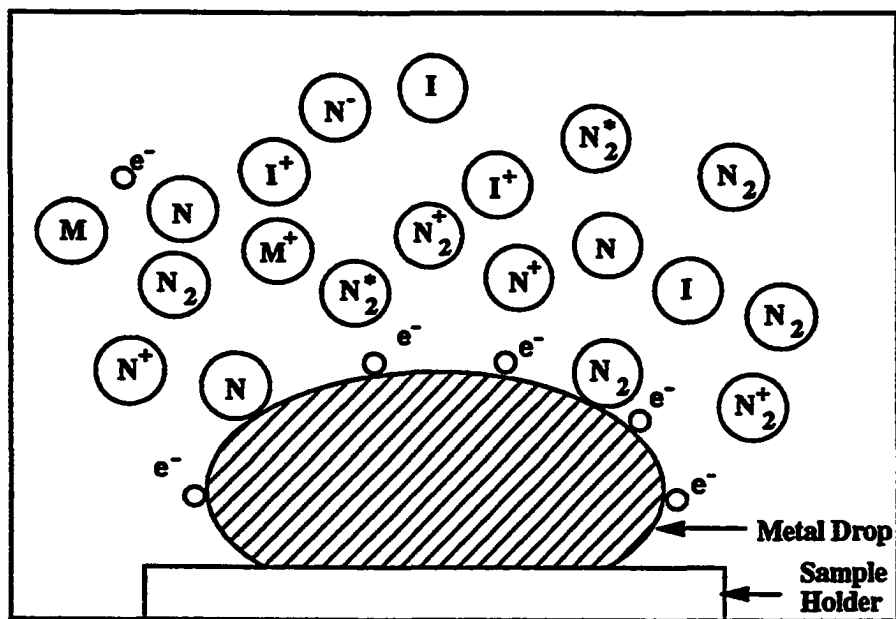
Fig. 4.43 A schematic diagram of the gaseous species near a metal drop.

cannot be explained by enhanced adsorption alone. Therefore, the increased solubility is more likely due to the presence of the monatomic nitrogen in the gas phase.

4.3.2 Two Temperature Model

It was qualitatively shown in the previous section that the enhanced solubility in the presence of plasma is likely due to the presence of monatomic gaseous species present in the gas phase. However, it is important that this assumption is verified further with the help of experimental observations. The two temperature model presented in Chapter 3 along with the experimental observations of different researchers are discussed below to further validate the model and the hypothesis.

Bandopadhyay et al. [47] conducted nitrogen dissolution experiments with two different metals under identical conditions. In these experiments, samples of ultra-pure tantalum and niobium were separately exposed to a well characterized helium and nitrogen containing glow discharge plasma at 2243 K and the amount of nitrogen in these metals were determined. The total pressure in the chamber was maintained at 1.45×10^{-3} atmosphere and the partial pressure of N_2 was 1.11×10^{-5} atmosphere. The steady state nitrogen content determined in niobium and tantalum samples were 0.5 and 1.0 weight percent, respectively.

The experiments of Bandopadhyay et al. [47] with two different metals can provide significant insight into the physics of dissolution process. In the two temperature model presented in Chapter 3 it was shown through equations (3.39) to (3.42) that the solubility

due to monatomic species in the samples can be determined uniquely for an assumed dissociation temperature, T_d. Combining equations (3.39) to (3.42) we have

$$\left[\frac{z(100-x)}{2x}\right]^2 + z^2\frac{(100-x)}{2x} + \frac{(100-y)P_T}{(100+yx/100)} = P_T \tag{4.12}$$

where $z = e^{(-\Delta G_2^0/RT_d)}$, y is the percent of diatomic gas in the inert gas, x is the % of the diatomic gas that dissociates at dissociation temperature, T_d, P_T is the total pressure in the reaction chamber and ΔG_2^0 is the standard free energy for dissolution reaction from diatomic gas. Equation (4.12) gives a relationship between the degree of dissociation and dissociation temperature T_d. For the experimental conditions of Bandopadhyay et al. [47] the degree of dissociation is plotted as a function of dissociation temperature in Fig. 4.44. The free energy data required for the calculations are given in Table 4.15. It is be observed from the figure that the degree of dissociation increases with dissociation temperature. The computed solubilities in tantalum sample due to diatomic and monatomic nitrogen obtained from equations (3.35) and (3.36) are plotted in Fig. 4.45 (a) for various dissociation temperatures. The experimental result of Bandopadhyay et al. [47] for tantalum is also superimposed on the graph. From the perusal of the data we can make two important conclusions. First, the solubility due to diatomic species is significantly lower than the experimentally observed solubility. Furthermore, to attribute the enhanced solubility to the presence of monatomic nitrogen, the dissociation temperature in the plasma should be approximately 2390 K. The conditions in the experiments of Bandopadhyay et al.[47] were such that the metal sample did not effect the properties of the plasma. Since the dissociation temperature is a concept representing a characteristic of the plasma, it should not change with the change of sample in the chamber for the same experimental conditions. Thus, for the hypothesis that the enhanced solubility is due to the presence of monatomic nitrogen to

The plot shows Degree of Dissociation, x (y-axis from 0.0 to 1.2) versus Temperature of Dissociation, T_d (K) (x-axis from 2200 to 2500).

Text within plot:
Total Pressure = 0.00145 atm.
Partial Pressure of Diatomic
Nitrogen in the Initial Mixture = 0.0000111 atm.
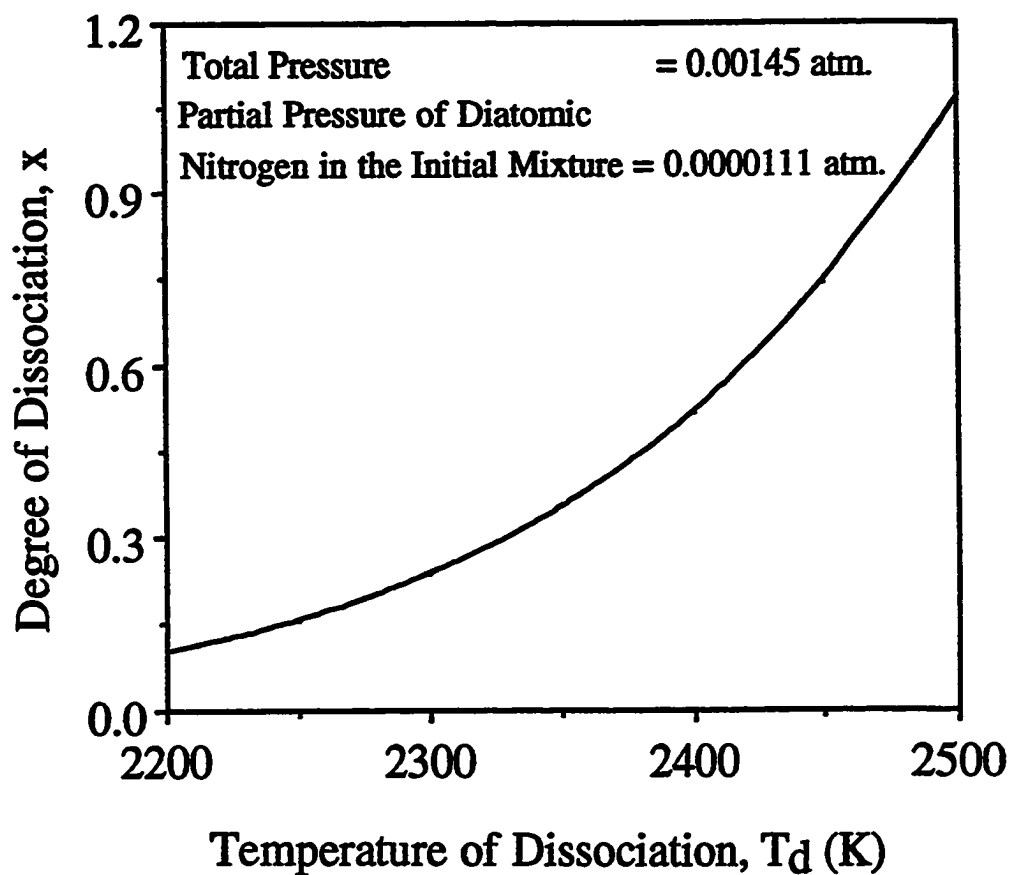
Fig. 4.44 Plot of dissociation temperature vs. percent nitogen dissociated for the experimental conditions of Bandopadhaya et al. [47].
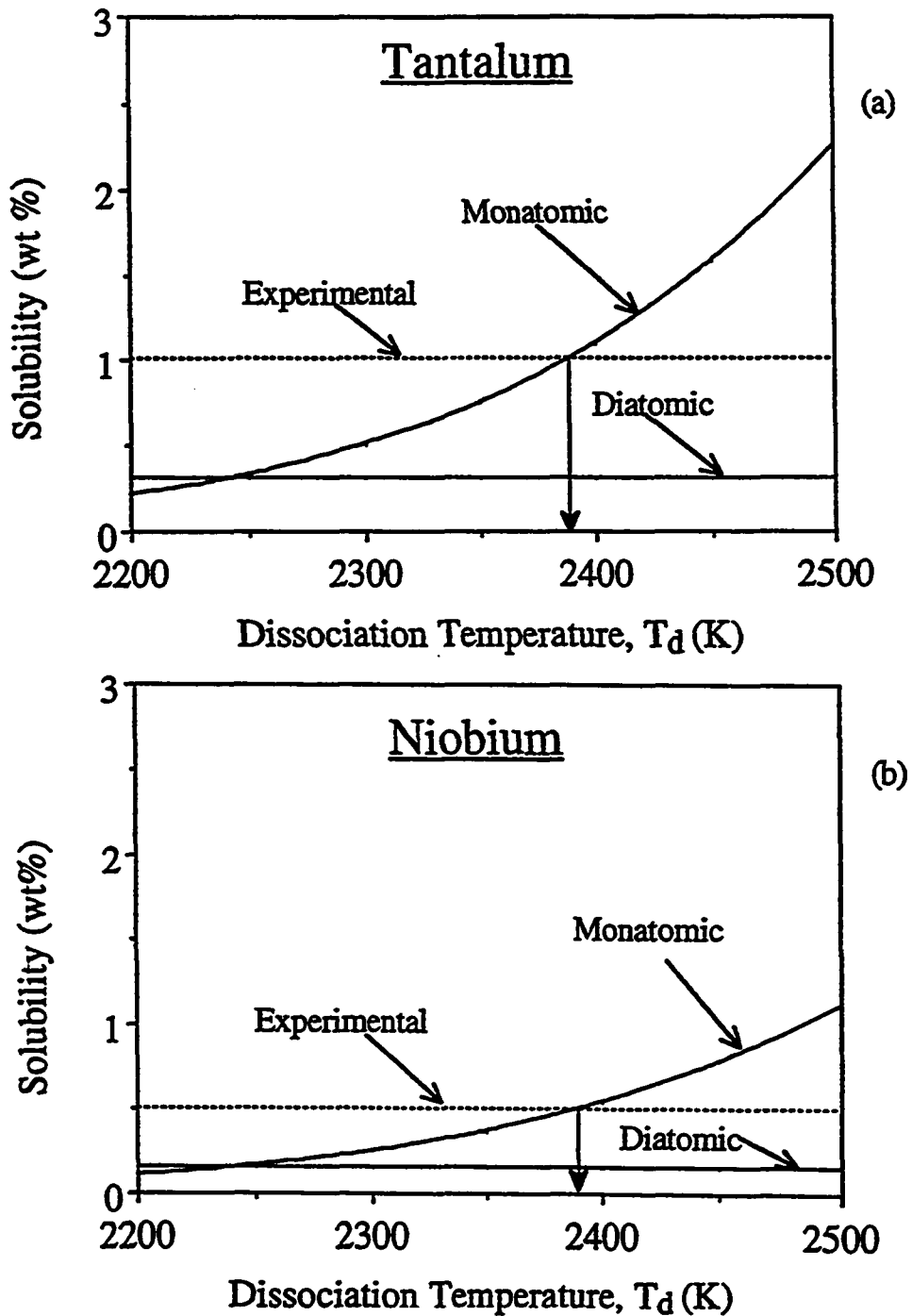
Fig. 4.45 Computed solubility of nitrogen due to diatomic and monatomic nitrogen as a function of dissociation temperature in (a) tantalum and (b) niobium for the experimental conditions of Bandopadhaya et al. [47]. The observed experimental solubilities are also presented.

Table 4.15 Free energy temperature relationship for nitrogen dissociation and dissolution in tantalum, niobium and liquid iron. Free energy data is in cal/gm-mole.

Metal	Reaction	Free Energy Temperature Relationship	Reference Number
-	$\frac{1}{2} N_2\,(g) = N\,(g)$	86596.0 - 15.659 T	51
Tantalum	$\frac{1}{2} N_2\,(g) = \underline{N}\,(wt\ \%,\ s)$	-43483.519 + 10.394 T	52
	$N\,(g) = \underline{N}\,(wt\ \%,\ s)$	-130,079.518 + 26.053 T	
Niobium	$\frac{1}{2} N_2\,(g) = \underline{N}\,(wt\ \%,\ s)$	-42512.625 + 11.357 T	52
	$N\,(g) = \underline{N}\,(wt\ \%,\ s)$	-129,108.629 + 27.016 T	
Liquid Iron	$\frac{1}{2} N_2\,(g) = \underline{N}\,(wt\ \%,\ l)$	860.0 + 5.71 T	53
	$N\,(g) = \underline{N}\,(wt\ \%,\ l)$	-85736.0 + 21.405 T	

be correct, the experimental solubility data for niobium should predict a dissociation temperature of 2390 K. The solubility vs. dissociation temperature for niobium sample is given in Fig. 4.45 (b). Also presented on the graph is the result of Bandopadhyay et al. [47]. It is observed that the experimental data is consistent with an assumed dissociation temperature of 2390 K. The dissociation temperature for tantalum-nitrogen sample was also found to be 2390 K for the experimental conditions Bandopadhyay et al.[47]. Thus, independent of the nature of the sample kept in the chamber, the dissociation temperature is observed to be 2390 K. Thus the experimental data of Bandopadhyay et al.[47] are consistent with two temperature model with a dissociation temperature independent of the nature of the sample.

To further verify the assumption that the enhanced solubility is due to the presence of monatomic nitrogen, we have tested the two temperature model against the experimental observations of Ouden et al. [48]. In their experiments, ultra-pure iron drops were exposed to a nitrogen and argon containing arc plasma. The nitrogen content in the feed gas mixture was varied from 0 % to 25 %. The total pressure in the chamber was maintained at 1 atmosphere and the samples were kept at 1873 K. The experimental results are given in Fig. 4.46. It is observed that for a partial pressure of nitrogen of 0.01 atmosphere, the solubility of gas in the iron drop is 0.021 wt %. It is observed from the solubility vs. dissociation temperature curve, presented in Fig. 4.47, that for the solubility to be 0.021 wt% under the conditions of the experiments, the dissociation temperature should be close to 2010 K. If we assume that the dissociation temperature does not change significantly with the change in the composition of the gas, we can plot the solubility as a function of percentage nitrogen in the gas for the dissociation temperature of 2010 K. The results are superimposed on the experimental observations in Fig. 4.46. It is observed that at low partial pressures of nitrogen, the predictions are in good agreement with the
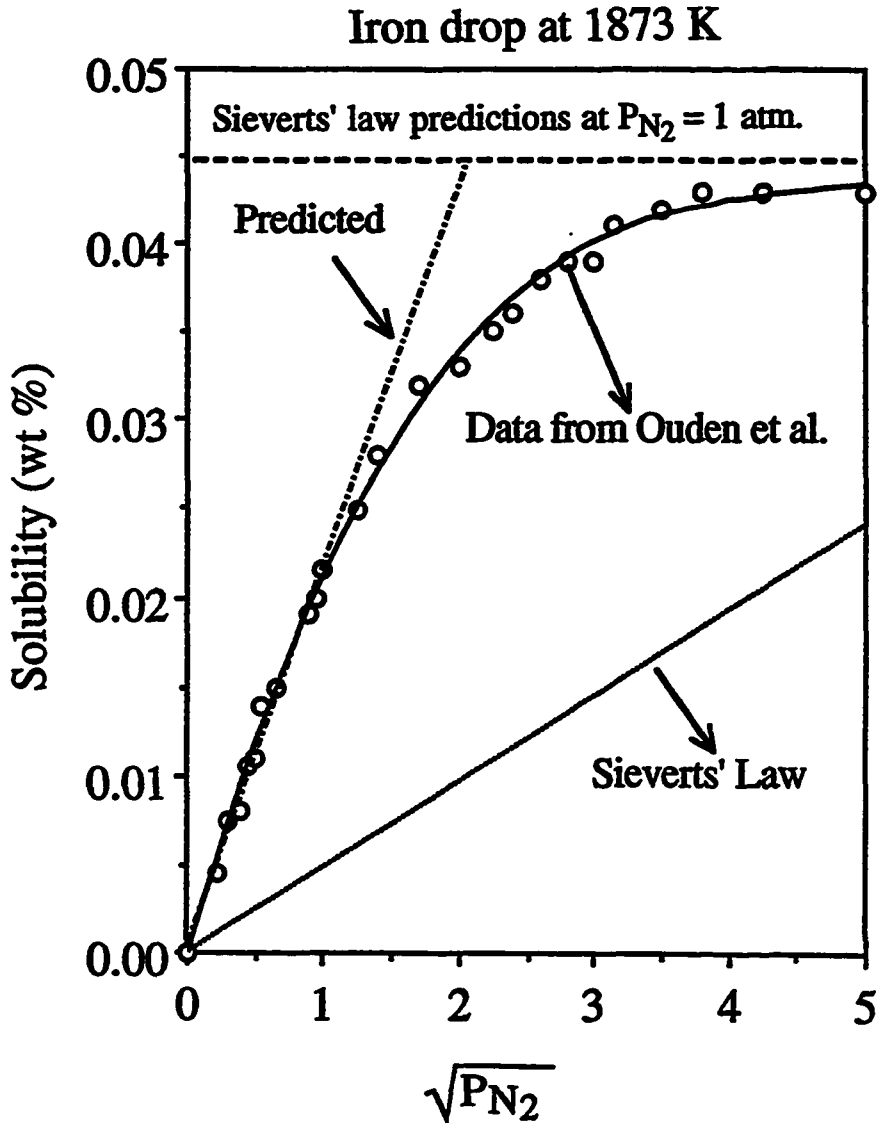
Fig. 4.46 Experimental results of nitrogen solubility in iron for the experimental conditions of Ouden et al. [48]. Sieverts' law nitrogen solubility predictions are also presented. The solubility predicted at low partial pressures of nitrogen by assuming a temperature of dissociation of 2010 K is also superimposed.
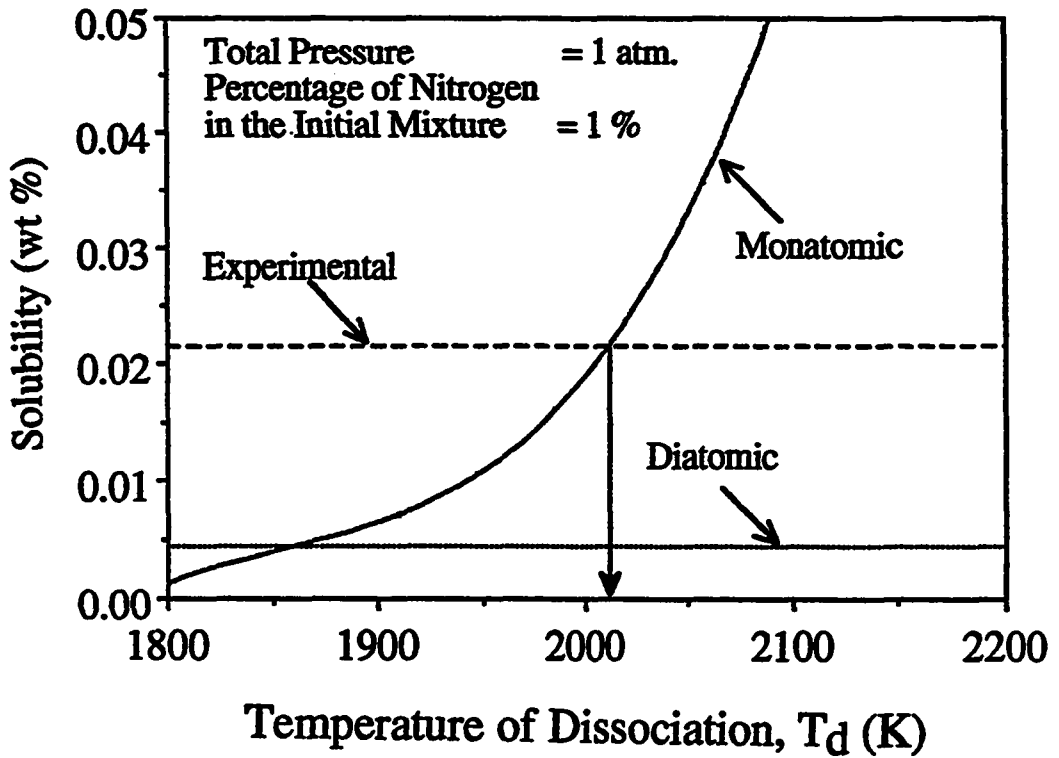
Fig. 4.47 Plot of solubility vs. dissociation temperature for the experimental conditions of Ouden et al. [48] and for nitrogen partial pressure of 0.01 atm.

experimental observations. The deviations at higher pressure of nitrogen can be attributed to the fact that the assumed temperature of dissociation of 2010 K may not be valid in the entire pressure range. Furthermore gas bubble formation was observed beyond a nitrogen content of 16 percent in the nitrogen-argon gas mixture and no further increase in solubility was noticed. The formation of gas bubbles during the dissolution process is discussed in the next section. The solubility data at low pressures indicates that nitrogen dissolution is proportional to the square root of partial pressure of nitrogen. This behavior is similar to the one that is predicted by Sieverts' Law. This Sieverts' Law type nature of the solubility curve be explained from equation (4.13) derived below. Substituting for P_G from equation (3.39) in equation (3.36), we have

$$\underline{C}^m \text{ (wt \%)} = \sqrt{P_{G_2}}\, e^{-\left\{ \frac{\Delta G_1^0}{RT_d} + \frac{\Delta G_3^0}{RT_s} \right\}} \tag{4.13}$$

or $\quad \underline{C}^m \text{ (wt \%)} = K_{en}\sqrt{P_{G_2}} \tag{4.14}$

where K_{en} is the enhanced equilibrium constant and is given by:

$$K_{en} = e^{-\left\{ \frac{\Delta G_1^0}{RT_d} + \frac{\Delta G_3^0}{RT_s} \right\}} \tag{4.15}$$

Equation (4.14) shows that the solubility due to monatomic nitrogen is proportional to the square root of partial pressure of nitrogen. However, the proportionality constant, K_{en}, is enhanced due to the presence of monatomic nitrogen.

Katz and King [46] observed in their experiments with iron, that for the same conditions in the plasma, the nitrogen concentration in the metal increased with decrease in the temperature of the liquid iron. Their data are presented in Fig. 4.48. In Fig. 4.48, θ_T is the measure of the fraction of total sites occupied by surface active elements such as sulfur or oxygen. The nitrogen solubility curves as a function of partial pressure and temperature for diatomic and monatomic species are presented in Figs. 4.49 and 4.50, respectively. The free energy data required are given in Table 4.15. It is observed from Fig. 4.49 that at a given partial pressure of diatomic nitrogen in the gas phase, the equilibrium nitrogen concentration increases slightly with temperature. Thus, the variation of nitrogen concentration with temperature observed by Katz and King [46] cannot be explained by the equilibrium calculations involving diatomic nitrogen in the gas phase. In contrast, the trend in their data on the decrease in the concentration of nitrogen in the melt with increase in temperature is consistent with the calculated equilibrium concentrations at various temperatures presented in Fig. 4.50 involving monatomic nitrogen.

4.3.3 Formation of Gas Bubbles During Gas Dissolution

During weld solidification, formation of gas bubbles and pin holes is a common occurrence. However, under certain conditions of experiments gas bubbles can be formed during the dissolution processes. Ouden et al. [48] observed formation of gas bubbles in their experiments with iron drops exposed to nitrogen-argon plasma when the solubility of nitrogen in iron was close to 0.043 weight percent. Similarly, Ohno and Uda [49] observed formation of bubbles in nickel during their arc welding experiments. Similar observations were made by Uda and Ohno [50] in their arc melting experiments with iron. In all these experiments, the solubility of nitrogen did not increase with nitrogen partial pressure in the
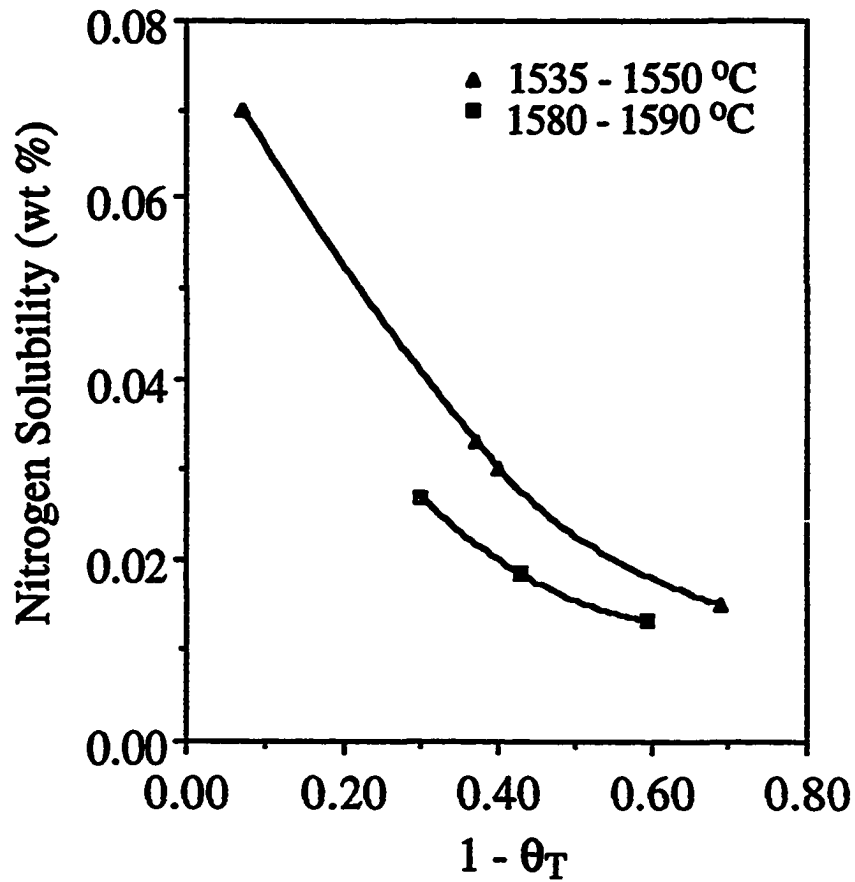
Fig. 4.48 Steady state nitrogen content vs. surface availability at two different temperatures for ARMCO iron [46]. Experiments were conducted with Ar-5% N_2 plasma.
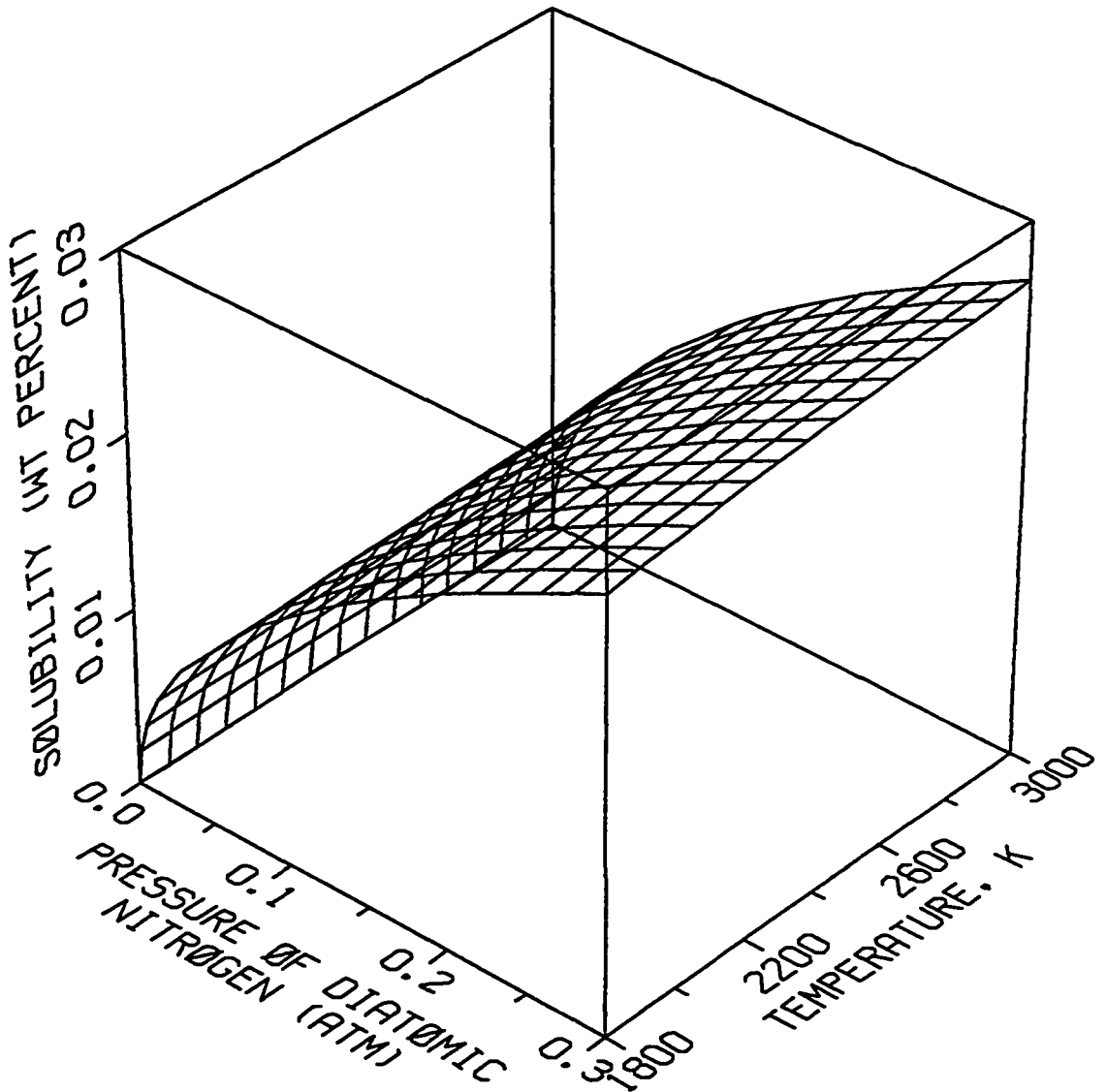
Fig. 4.49 Equilibrium solubility in iron, calculated using equation (3.35), due to diatomic nitrogen as a function of temperature and partial pressure of diatomic nitrogen. The data used are given in Table 4.15.
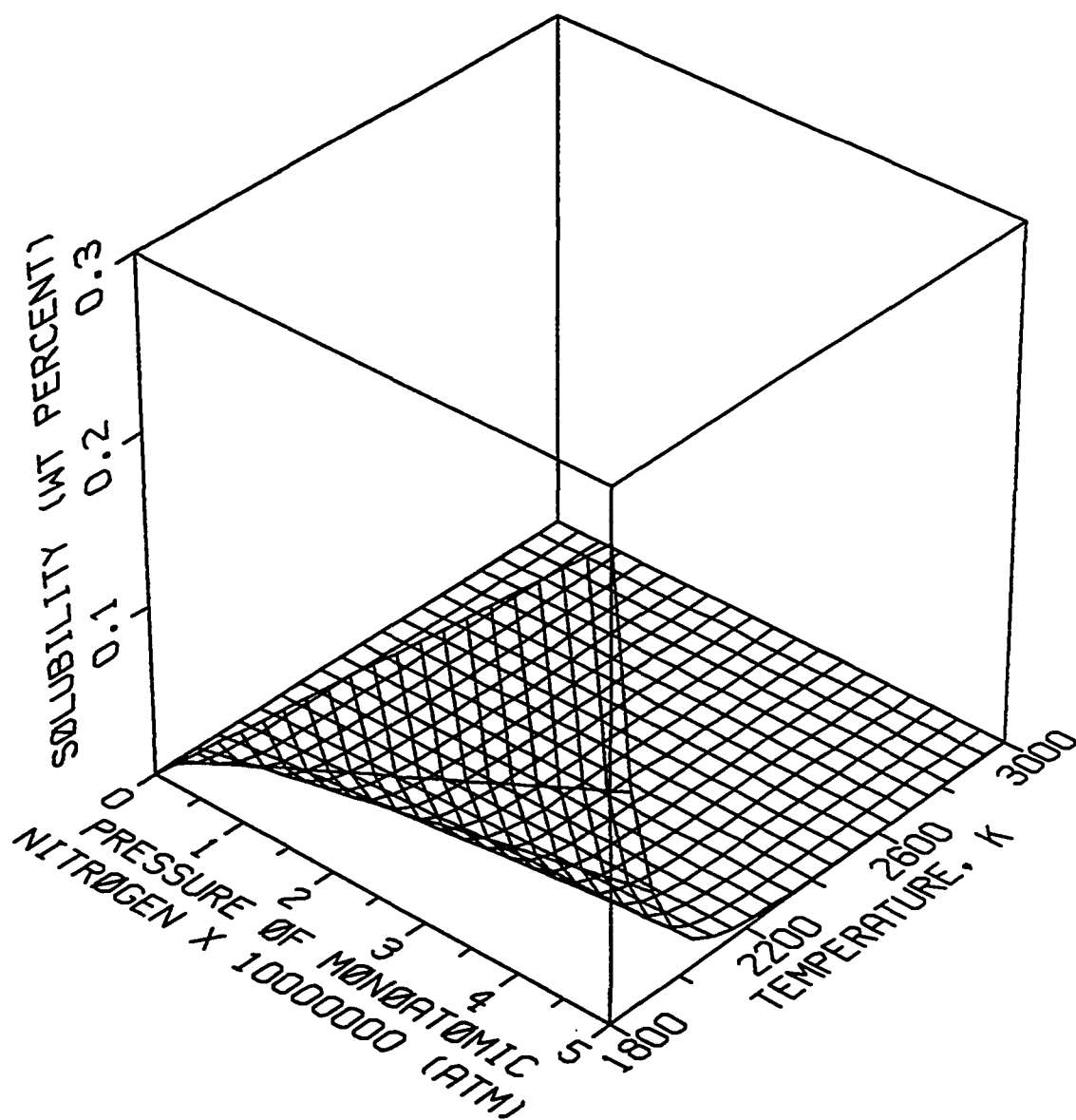
Fig. 4.50 Equilibrium solubility in iron, calculated using equation (3.36), due to monatomic nitrogen as a function of temperature and partial pressure of monatomic nitrogen. The data used are given in Table 4.15.

gas mixture once the bubble formation began. All these experiments of gas dissolution were carried out at a total pressure of 1 atmosphere pressure. However, the partial pressures of nitrogen were much less than 1 atmosphere pressure. In all the experiments, the bubble formation were observed when the experimental solubility was close to the solubility predicted by Sieverts' law under nitrogen pressure of 1 atmosphere. However, the equilibrium concentrations of nitrogen in the metal predicted by Sieverts's law from the partial pressures of nitrogen were much lower than the experimentally observed concentrations. The presence of monatomic nitrogen in the plasma enhances the dissolution and the solubility's are reached close to Sieverts's law predictions at much lower partial pressure of nitrogen than 1 atmosphere. Once the Sieverts' law solubility is reached, the following reaction in the liquid metal also becomes important.

$$2\underline{N} \text{ (l)} \rightarrow N_2 \text{ (g)} \qquad\qquad (4.14)$$

The formation of N_2 can lead to nucleation of bubbles in the melt at various heterogeneous sites and once the pressure in the bubbles on the melt surface is close to the ambient pressure (1 atmosphere in these experiments) they are expelled out and thus limit the solubility.

4.4 References

1.   S. A . David and T. DebRoy, Science 257, 487 (1992).

2.   K. Mundra, T. DebRoy, T. Zacharia and S. A. David, Welding Journal 71, 313 (1992).

3.   R. Miller and T. DebRoy, J. Appl. Phys. 68, 2045 (1990).

4.   G. J. Dunn, C. D. Allemand, and T. W. Eager, Metall. Trans. 17A, 1851 (1986).

5   M. M. Collur and T. DebRoy, Metall. Trans. 20B, 277(1989).

6. C. Y. Ho, R. W. Powell and P. E. Liley, J. Phys. Chem. Ref. Data 3(1), I-368 (1974).

7. M. W. Chase, J. Phys. Chem. Ref. Data 14(1), 1174 (1985).

8. T. Zacharia, S. A. David, J. M. Vitek and T. DebRoy, Welding Journal 68, 499 (1989).

9. R. Mehrabian, S. Kou, S. C. Hsu and A. Munitz, AIP Conference Proceedings (MRS, Boston, 1978).

10. P. A. A. Khan and T. DebRoy, Metall. Trans. 16B, 853 (1985).

11. M. Bramson, Infrared Radiation: A Handbook for Applications, (Plenum, New York, 1968), p.127.

12. S. I. Anisimov and A. Kh. Rakhmatulina, Soviet Physics - JETP 37, 441 (1973).

13. C. J. Knight, AIAA Journal 17, 519 (1979).

14. C. L. Chan and J. Mazumder, J. Appl. Phys. 62, 4579 (1987).

15. M. von Allmen, Laser Beam Interactions with Materials, (Springer, 1987), p. 161.

16. F. W. Dabby and U. Paek, IEEE Journal of Quantum Electronics QE-8, 106 (1972).

17. J. O. Hirschfelder, C. F. Curtiss, and R. B. Bird, Molecular Theory of Gases and Liquids, (John Wiley and Sons, Inc., New York, NY, 1954).

18. P. A. A. Khan and T. DebRoy, Metall. Trans. 15B, 641 (1984).

19. P. A. A. Khan, T. DebRoy and S. A. David, Welding Journal 67, 1 (1988).

20. P. Sahoo, T. DebRoy and M. J. McNallan, Metall. Trans. 19B, 483 (1988).

21. T. DebRoy and M. J. McNallan, Metall. Trans. 22B, 557 (1991).

22 S. A. David, T. DebRoy and J. M. Vitek, Accepted for publication in Materials Research Society (MRS) Bulletin.

23. P. A. A. Khan, Ph. D. Thesis, The Pennsylvania State University, 1987.

24. T. Zacharia, S. A. David and J. M. Vitek, Metall. Trans. 22B, 233 (1991).

25. M. M. Collur, A. Paul and T. DebRoy, Metall. Trans. 18B, 773 (1987).

26. A. Paul and T. DebRoy, Metall. Trans. 19B, 851 (1988).

27. P. Sahoo, M. M. Collur and T. DebRoy, Metall. Trans. 19B, 967 (1988).

28. P. Sahoo and T. DebRoy, Materials Letters 6, 406 (1988).

29. T. Iida and R. L. Guthrie, The Physical Properties of Liquid Metals, (Oxford Science Publication), 1988.

30. R. D. Phelke, Unit Processes in Extractive Metallurgy, (Elsevier North Holland Publishing Co., Inc., NY, 1982).

31. A. Goldsmith, T. E. Waterman and H. J. Hirchhorn, Handbook of Thermo-physical Properties of Solid Materials, (The MacMillan Co., NY, 1961), p. 371.

32. Smithells Metals Reference Book, 6th Edition, Ed. E. A. Brandes, (Butterworths and Co. , London, 1983).

33. T. Zacharia, S. A. David and J. M. Vitek, Metall. Trans. 22B, 233 (1991).

34. E. A. Metzbower, Metall. Trans. 24B, 875 (1993).

35. A. Block-Bolten and T. W. Eager, Metall. Trans. 15B, 461 (1984).

36. A. Block-Bolten and T. W. Eagar, Trends in Welding Research in the U. S., S. A. David, Ed., (ASM, Metals Park, OH, 1982), p. 53.

37. R. B. Bird, W. E. Stewart and E. N. Lightfoot, Transport Phenomena, (John Wiley and Sons, NY, 1960), p. 409.

38. W. L. Wiese, M. W. Smith, and B. M. Glennon, Atomic Transition Probabilities, vol. 1, National Bureau of Standards, Gaithersburg, 1966, pp. 48-76.

39. F. R. Fuhr, G. A. Martin and W.L. Wiese, Atomic Transition Probabilities Iron Through Nickel, J. Phys. Chem Ref. Data, vol. 17, suppl. 4, 1988.

40. P. W. J. M. Boumans, Theory of Spectrochemical Excitation, (Hilger and Watts, London, 1966), pp. 103-106.

41. H. R. Griem, Plasma Spectroscopy, (McGraw-Hill, New York, NY, 1964), pp. 303-312, 450-51, and 539.

42. D. Madey, Unpublished Research, The Pennsylvania State University, University Park, PA.

43. A. Banerjee and T. DebRoy, Accepted for publication in J. Am. Cer. Soc.

44. A. Banerjee, M.S. Thesis, The Pennsylvania State University, University Park, PA, 1992.

45. B. Chapman, Glow Discharge Plasma, (John Wiley and Sons, New York, NY, 1980), pp. 51-53.

46. J. D. Katz and T. B. King, Metall. Trans. 20B, 175 (1989).

47. A. Bandopadhyay, A. Banerjee and T. DebRoy, Metall. Trans. **23B**, 207 (1992).

48. G. Den Ouden and O. Griebling, Recent Trends in Welding Science and Technology, S. A. David and J. M. Vitek, Eds., (ASM International, Metals Park, OH, 1990), p. 431.

49. S. Ohno and M. Uda, Trans. Nat. Res. Inst. Met. **23**, 243 (1981).

50. M. Uda and S. Ohno, Trans. Nat. Res. Inst. Met. **20**, 16 (1978).

51. J. F. Elliot, M. Gleiser and V. Ramakrishna, Thermochemistry for Steelmaking I (Addison-Wesley Publishing Co., MA, 1963), p.75.

52. E. Fromm and H. Jehn, Metall. Trans. **3**, 1685 (1972).

53. J. F. Elliot and M. Gleiser, Thermochemistry for Steelmaking II (Addison-Wesley Publishing Co., MA, 1963), p.618.

Chapter 5

SUMMARY AND CONCLUSIONS

The work carried out during the course of this investigation was aimed at understanding two important interfacial phenomena occurring during welding, namely alloying element vaporization and dissolution of gases at the weld pool surface. The main features of the work and the conclusions are given below.

A theoretical model was developed to predict rates of vaporization and composition change occurring during laser welding. The weld pool temperature distribution was calculated by the numerical solution of the Navier-Stokes equations and the equation of conservation of energy. The heat transfer to the shielding gas and the evaporative heat loss due to vaporization of the alloying elements were taken into account. The computed weld pool temperature distribution was used together with the fundamental principles of gasdynamics and mass transfer for the calculation of vaporization rates. The rates of vaporization due to pressure gradient at the pool surface were determined from the equations of conservation of mass, momentum and translational kinetic energy in the gas phase. In addition, mass transfer rates due to concentration gradient were determined using available mass transfer correlation's among various dimensionless numbers. The effect of plasma on vaporization rates was incorporated based on previous investigations carried out at Penn State and the work undertaken as the part of this work.

The model predictions of vaporization rates and composition change were compared with the experimental observations of various investigations. The rates of vaporization predicted

by the model for pure metals, AISI 201 and AISI 202 steels were in good agreement with the corresponding experimental data. The rates predicted by Langmuir equation were significantly higher than the experimental values. The model predictions of vapor composition for AISI 202 stainless steel was in good agreement with the corresponding experimentally determined values. In addition, the composition change predicted by the model, for the welding of AISI 201 stainless steel with high power conduction mode carbon dioxide laser, were in good agreement with the experimental observations. Independent experimental results on the effect of shielding gas flow rate and the nature of shielding gas on the vaporization rates could be explained on the basis of the model.

The results of the solution of conservation of mass, momentum and energy in the weld pool with and without consideration of evaporative heat loss showed heat loss due to vaporization of the alloying elements significantly decreased the temperatures on the weld pool surface. The role of choice of thermophysical properties on the results of solution of Navier-Stokes equation and equation of conservation of energy were examined. The results indicate that accurate values of thermophysical properties are necessary for realistic simulation of weld pool behavior.

The influence of plasma on vaporization rates was investigated by conducting controlled physical modeling experiments. Experiments were carried out both in the presence and absence of plasma with iron drops under different conditions of pressures. Optical emission spectroscopy was used to characterize the plasma. The results showed that the rates of vaporization in the presence of plasma were significantly lower than when plasma was absent. Under all conditions of experiments the rates of vaporization predicted by Langmuir equation were significantly higher than the experimentally observed rates. In the

behavior was consistent with a decreasing mass transfer rates with pressure. However, in the presence of plasma vaporization rates increased with pressure. The variation in vaporization rate with pressure was qualitatively explained on the basis of changes in electrons kinetic energy and the resulting changes in the magnitude of the space charge.

A two temperature model was developed to understand the dissolution of gases in a metal exposed to plasma. The model assumed that the enhanced solubility under plasma conditions was due to the presence of monatomic gaseous species in the plasma. The model predictions were compared with experimental observations of various investigators to verify the hypothesis. The results indicated that the observed enhanced solubility in plasma can be explained on the basis of the presence of monatomic nitrogen in the plasma.

5.1 Suggestions for Future Work

Heat transfer, fluid flow and alloying element vaporization during welding are quite complex and to model these phenomena, it is important to have trustworthy values of several thermophysical parameters. For example, to predict the temperature profiles on the weld pool surface, values of thermal conductivity and specific heat of both solid and liquid, viscosity of molten metal and temperature coefficient of surface tension are required. Temperature-dependent values of these thermophysical are crucial for realistic simulation of weld pool behavior. In the literature these values are scarce if not non-existent, especially for systems containing plasma. Thus, in addition to the difficulty in developing a rigorous simulation of the highly complex welding process, the lack of appropriate thermophysical data often impedes an in-depth understanding of this process.

Predictions of vaporization rates and composition change in this work were limited to spot welding and welding at low velocities. This was due to the limitation of the fluid flow and heat transfer program which was two-dimensional. A three-dimensional mathematical formulation would give a more accurate predictions than the two-dimensional program.

The effect of plasma on vaporization rate was incorporated on the basis of physical modeling experiments and the vaporization rates were correlated with the characteristics of the plasma. It would be important to test these findings by performing actual welding tests under different conditions.

The dissolution of gases in the weld pool was understood on the basis of a two temperature model. Although the concept of temperature of dissociation in the model provided important insight into the physics of dissolution, it was purely hypothetical. In order to understand the extent of dissolution under various conditions, the characterization of plasma should be carried out and the plasma parameters should be correlated with the solubility of gases.

Appendix A

THERMOPHYSICAL PROPERTIES OF GAS AND VAPOR

A.1   Calculation of Thermal Conductivity, Viscosity and Binary Gaseous Diffusivity

The thermal conductivity of a gas, k_g, at temperature T, is given by [1]:

$$k_g = \frac{1.9891 \times 10^{-4}}{\sigma_g^2 \Omega_k^*(T^*)} \sqrt{\frac{T}{M_g}} \tag{A.1}$$

where k_g is in cal/cm-s-K, σ is the collision diameter in Å, $T^* = T/(\epsilon/k_B)$, where k_B is the Boltzmann constant in erg/molecule-K, ϵ is the intermolecular force parameter in erg/molecule, M_g is the molecular weight of the gas in gm/gm-mole and Ω_k is the slowly varying function of the dimensionless parameter $T/(\epsilon/k_B)$.

The viscosity of a gas, μ_g, at temperature T, is given by [1] :

$$\mu_g = \frac{2.6693 \times 10^{-5}}{\sigma_g^2 \Omega_\mu^*(T^*)} \sqrt{M_g T} \tag{A.2}$$

where μ_g is in gm/cm-s and Ω_μ is again a slowly varying function of the dimensionless parameter $T/(\epsilon/k_B)$.

The binary molecular diffusivity, $D_{A/B}$, of a gas pair A and B, at absolute temperature T is given by [1] :

$$D_{A/B} = \frac{1.8583 \times 10^{-3}}{p\sigma_{A/B}^2\Omega_D(T^*)} \sqrt{\left[\frac{1}{M_A} + \frac{1}{M_B}\right]T^3} \qquad \text{(A.3)}$$

where $D_{A/B}$ is in cm^2/s, p is the pressure in atmosphere, M_i is the molecular weight of the element i, $\sigma_{A/B} = (\sigma_A + \sigma_B)/2$, Ω_D is a slowly varying function of $T/(\epsilon_{A/B}/k_B)$ where

$$\epsilon_{A/B}/k_B = \sqrt{(\epsilon_A/k_B)(\epsilon_B/k_B)} \qquad \text{(A.4)}$$

The pressure p, in the calculation of diffusivity, was taken as 1 atmosphere when the equilibrium vapor pressure of the material was less than the ambient pressure. At temperatures greater than the boiling point of the material, when the equilibrium vapor pressure is greater than 1 atmosphere, p was taken as the average of the equilibrium vapor pressure and the ambient pressure. The data used for the the parameters σ_i and $(\epsilon/k)_i$ are given in Table A.1.

The calculation of thermal conductivity, k_g, viscosity of the gas, μ_g, and the diffusivity of an element i in the shielding gas, $D_{A/B}$, are done at temperature T_{av}, where T_{av} is the average of the ambient temperature and the temperature at the weld pool surface. For computational economy, the calculations were performed once as a function of temperature and equations were fitted to the data obtained. The equations for k_g and μ_g for helium and argon, and $D_{A/B}$ for iron, manganese, chromium and nickel in helium and argon are presented in form of equation in Table A.2. A general purpose Fortran computer program for the calculation of viscosity and thermal conductivity of a gas at any temperature, and binary diffusivity of a gas pair at any temperature and pressure is given at the end of Appendix A.

Table A.1: Data used for the calculation of the thermophysical properties [2,3].

Parameter	σ (A)	ε/k
Iron	2.43	3541.2
Manganese	2.58	2817.9
Chromium	2.46	3738.2
Nickel	2.38	3641.5
Argon	3.418	124.0
Helium	2.576	10.2

Table A.2: Relations used for the calculation of the thermophysical properties in the temperatures range of 1000 K to 3000 K.

Property (units)	Equation
Conductivity of He, k_g (cal /cm-s-K)	$2.8542 \times 10^{-4} + 5.5191 \times 10^{-7} \times T - 3.4712 \times 10^{-11} \times T^2$
Conductivity of Ar, k_g (cal /cm-s-K)	$3.6713 \times 10^{-5} + 6.7597 \times 10^{-8} \times T - 3.9889 \times 10^{-12} \times T^2$
Viscosity of He, μ_g (gm/cm-s)	$2.2029 \times 10^{-4} + 2.2171 \times 10^{-7} \times T$
Viscosity of Ar, μ_g (gm/cm-s)	$2.7373 \times 10^{-4} + 2.7681 \times 10^{-7} \times T$
Diffusivity of Fe (g) in He, $D_{Fe,He}$ (cm^2/s)	$(-2.1360 + 5.4957 \times 10^{-3} \times T + 2.4247 \times 10^{-6} \times T^2)/p$
Diffusivity of Fe (g) in Ar, $D_{Fe,Ar}$ (cm^2/s)	$(-0.61024 + 1.1274 \times 10^{-3} \times T + 6.4892 \times 10^{-7} \times T^2)/p$
Diffusivity of Mn (g) in He, $D_{Mn,He}$ (cm^2/s)	$(-1.6174 + 4.7797 \times 10^{-3} \times T + 2.4582 \times 10^{-6} \times T^2)/p$
Diffusivity of Mn (g) in Ar, $D_{Mn,Ar}$ (cm^2/s)	$(-0.5927 + 1.1469 \times 10^{-3} \times T + 6.1891 \times 10^{-7} \times T^2)/p$
Diffusivity of Cr (g) in He, $D_{Cr,He}$ (cm^2/s)	$(-2.2310 + 5.5302 \times 10^{-3} \times T + 2.3683 \times 10^{-6} \times T^2)/p$
Diffusivity of Cr (g) in Ar, $D_{Cr,Ar}$ (cm^2/s)	$(-0.60579 + 1.1331 \times 10^{-3} \times T + 6.4741 \times 10^{-7} \times T^2)/p$
Diffusivity of Ni (g) in He, $D_{Ni,He}$ (cm^2/s)	$(-2.2184 + 5.6412 \times 10^{-3} \times T + 2.4499 \times 10^{-6} \times T^2)/p$
Diffusivity of Ni (g) in He, $D_{Ni,Ar}$ (cm^2/s)	$(0.60938 + 1.1335 \times 10^{-3} \times T + 6.5149 \times 10^{-7} \times T^2)/p$

*** The equilibrium vapor pressure is calculated from the following relation:

$$p = \sum_{i=1}^{4} x_i \, P_i^0,$$

where i = Fe, Cr, Ni and Mn are the alloying elements, x_i is the mole fraction of element i and P_i^0 is the equilibrium vapor pressure of the pure element.

A.2 References

1. J. O. Hirschfelder, C. F. Curtiss and R. B. Bird, Molecular Theory of Gases and Liquids (John Wiley and Sons, Inc., New York, NY, 1954).

2. R. E. Bird, W. E. Stewart and E. N. Lightfoot, Transport Phenomena (Wiley, New York, NY, 1960).

3. E. T. Turkdogan, Physical Chemistry of High Temperature Technology (Academic Press, New York, 1980).

A.3 Pogram for Calculation of Thermophysical Properties of Gas and Vapor

This Fortran program calculates the thermal conductivity and viscosity of a gas at any temperature and binary diffusivity of a gas pair at any temperature and pressure. The program is given below:

```
       program properties_of_gases
c-----this program calculates the viscosity and thermal conductivity of
c       a gas and binary diffusivity of a gas pair (A/B) at any
c       temperature. and pressure. The intermolecular force parmeters
c       and the collison integral data necessary for calculations are
c       included in. the program for twenty two gases.
c-----definition of important terms in the program-------------------
c       amwt:       molecular weight of gas
c       aoma1:   -   collison integral for calculation of diffusivity
c       aoma2:      collison integral for viscosity and conductivity
c       aktbye1:    temperature/intermolecular force parameter for gas A
c       aktbye2:    temperature/intermolecular force parameter for gas B
c       avgebykt:   temperature/average intermolecular force parameter for A/B
c       ebyk:       intermolecular force parameter
c       igas1:      index for gas A
c       igas2:      index for gas B
c       press:      pressure for calculation
c       sigavg:     average collison diameter for gas pair A/B
c       sig:        collison diameter
c       temp:       tempertaure for calculation
c-----end of definitions, begin program--------------------------
       parameter (noi=2,nop=6,ngas=22)
       character*64 strinp(noi),strpar(nop),output
       dimension valinp(noi),amwt(ngas),sig(ngas),ebyk(ngas),valpar(nop)
       data amwt/2.,4.0026,20.2,39.94,83.8,131.3,28.,32.,28.,44.,30.,
     1 44.,64.,38.,70.9,159.83,253.82,18.,54.93,55.85,51.996,58.7/
       data sig/2.915,2.576,2.789,3.418,3.498,4.055,3.681,3.433,
     1 3.59,3.996,3.47,3.879,4.29,3.653,4.115,4.268,4.982,2.641,2.58,
     1 2.43,2.46,2.38/
       data ebyk/38.,10.2,35.7,124.,225.,229.,91.5,113.,110.,190.,119.,
     1220.,252.,112.,357.,520.,550.,809.,2818.,3541.2,3738,3641.5/
       data strinp/'temperature in K', 'pressure in atmosphere'/
       data valinp/1873.0,1.0/
       data strpar/'Molecular wt. of gas A','Molecular wt. of gas B',
     &'Parameter ebyk of A','Parameter ebyk of B','Sigma of gas A',
     &'Sigma of gas B'/
```

```
          write(*,*)'Type the name of the output file '
          read(*,149)output
149       format(a64)
          open (unit=7,file=output)
5         format(60('-'),/2x,'Selection of binary gas pair'       /,60('-'),/,
          &        '  Hydrogen (1)            Helium (2)',/,
          &        '  Neon (3)                Argon (4)',/,
          &        '  Krypton (5)             Xenon (6)',/,
          &        '  Nitrogen (7)            Oxygen (8)',/,
          &        '  Carbon monoxide (9)     Carbon dioxide (10)',/,
          &        '  Nitrous oxide (11)      Nitrogen dioxide (12)',/,
          &        '  Sulphur dixoide (13)    Flourine (14)',/,
          &        '  Clorine (15)            Bromine (16)',/,
          &        '  Iodine (17)             Water vapor (18)',/,
          &        '  Manganese vapor(19)     Iron vapor (20)',/,
          &        '  Chromium vapor (21)     Nickel vapor (22)',/,
          &        60('-'),/
          &        ' Type indices (in brackets) to identify gases A and B')
89        format(60('-'))
89        format(65('-'))
          write(6,5)
          read(*,*)igas1, igas2
          valpar(1)=amwt(igas1)
          valpar(2)=amwt(igas2)
          valpar(3)=ebyk(igas1)
          valpar(4)=ebyk(igas2)
          valpar(5)=sig(igas1)
          valpar(6)=sig(igas2)
          do 52 iunit=6,7
          write(iunit,129)'Input parameters'
          do 51 i=1,nop
51        write(iunit,69)strpar(i),valpar(i)
52        continue
129       format(65('-'),/20x,a16,/65('-'))
69        format(2x,a50,1pe10.3)
21        write(6,89)
          write(6,109)'Temperature and pressure'
109       format(10x,a40,/,65('-'))
          do 10 i=1,noi
          write(*,59)'Enter',i,'to change',strinp(i),valinp(i)
10        continue
59        format(2x,a5,1x,i1,1x,a9,1x,a22,10x,1pe10.3)
```

```fortran
        noip=noi+1
        write(6,49)'Enter',noip,'if all values are ok'
49      format(2x,a5,1x,i2,1x,a20,/60('-'))
        write(6,39)'Please enter your choice (1 to',noip,'):'
39      format(2x,a30,1x,i2,a2)
        read(*,*)ichange
        if (ichange.eq.noip) go to 30
        write(6,19)'Enter',strinp(ichange),':'
19      format(2x,a5,2x,a60,a2)
        read(5,*)valinp(ichange)
        go to 21
30      continue
        write(7,129)'Input conditions'
        do 54 i=1,noi
54      write(7,69)strinp(i),valinp(i)
        temp=valinp(1)
        press=valinp(2)
c-----calculation of diffusivty of gas A in gas B -----------------
        if (press.lt.1.e-5) go to 20
        avgktbye=temp/sqrt(ebyk(igas1)*ebyk(igas2))
        sigavg=(sig(igas1)+sig(igas2))/2.
        call alpp(avgktbye,aoma1,aoma2)
        delgas=0.001858*sqrt(temp**3)*sqrt(1./amwt(igas1)+1./amwt(igas2))
        delgas=delgas/(press*sigavg**2*aoma2)
        aomadif = aoma2
c----calculation of viscosity and conductivity of gas A----------------
        aktbye1=temp/ebyk(igas1)
        call alpp(aktbye1,aoma1,aoma2)
        amugas1=2.6693e-5*sqrt(amwt(igas1)*temp)/(sig(igas1)**2*aoma1)
        acongas1=1.9891e-4*sqrt(temp/amwt(igas1))/(sig(igas1)**2*aoma1)
        aomagas1 = aoma1
c----calculation of viscosity and conductivity of gas B----------------
        aktbye2=temp/ebyk(igas2)
        call alpp(aktbye2,aoma1,aoma2)
        amugas2=2.6693e-5*sqrt(amwt(igas2)*temp)/(sig(igas2)**2*aoma1)
        acongas2=1.9891e-4*sqrt(temp/amwt(igas2))/(sig(igas2)**2*aoma1)
        aomagas2 = aoma1
c-----write output on the screen and output file---------------------
        do 55 j=6,7
        write(j,99)'Calculated paramters and property values'
        write(j,1)'kT/e for gas A                              ',aktbye1
        write(j,1)'Viscosity/thermal conductivity omega for A  ',aomagas1
        write(j,1)'Viscosity of gas A (gm/cm-s)                ',amugas1
        write(j,1)'Conductivity of gas A (cal/cm-s-K)          ',acongas1
```

```
        write(j,1)'kT/e for gas B                                   ',aktbye2
        write(j,1)'Viscosity/thermal conductivity omega for B  ',aomagas2
        write(j,1)'Viscosity of gas B (gm/cm-s)                 ',amugas2
        write(j,1)'Conductivity of gas B (cal/cm-s-K)           ',acongas2
        write(j,1)'Average kT/e for gas pair A/B                ',avgktbye
        write(j,1)'Binary diffusivity omega for gas pair A/B    ',aomadif
        write(j,1)'Binary diffusivity of gas pair A/B  (cm2/s) ',delgas
        write(j,89)
55      continue
20      continue
99      format(/,65('-'),/5x,a40,/,65('-'))
        write(*,*)'Calculate for different conditons? (for yes type 1)'
        read(*,*)ycont
        if (ycont.gt.0.5.and.ycont.lt.1.5) goto 21
1       format(2x,a43,7x,1pe10.3)
        end
c----subroutine for interpolation to calculate functions for prediction
c    of transport properties of gases at any kT/e. The data are given
c    in Transport Phenomena by Bird, Stewart and Lightfoot, pg. 746.----
c----begin subroutine-------------------------------------------------
        subroutine alpp(xx1,zz1,yy1)
        dimension x(82),y(82),z(82)
        data x/.3,.35,.4,.45,.5,.55,.6,.65,.7,.75,.8,.85,
1       .9,.95,1.,1.05,1.1,1.15,1.2,1.25,1.3,1.35,1.4,1.45,
2       1.5,1.55,1.6,1.65,1.7,1.75,1.8,1.85,1.9,1.95,2.,2.1,
3       2.2,2.3,2.4,2.5,2.6,2.7,2.8,2.9,3.,3.1,3.2,3.3,3.4,
4       3.5,3.6,3.7,3.8,3.9,4.,4.1,4.2,4.3,4.4,4.5,4.6,4.7,
5       4.8,4.9,5.,6.,7.,8.,9.,10.,20.,30.,40.,50.,60.,70.,
6       80.,90.,100.,200.,300.,400./
        data y/2.662,2.476,2.318,2.184,2.066,1.966,1.877,
1       1.798,1.729,1.667,1.612,1.562,1.517,1.476,
2       1.439,1.406,1.375,1.346,1.32,1.296,1.273,1.253,
3       1.233,1.215,1.198,1.182,1.167,1.153,1.14,1.128,
4       1.116,1.105,1.094,1.084,1.075,1.057,1.041,1.026,
5       1.012,.9996,.9878,.9770,.9672,.9576,.949,.9406,
6       .9328,.9256,.9186,.912,.9058,.8998,.8942,.8888,
7       .8836,.8788,.874,.8694,.8652,.861,.8568,.853,.8492,
8       .8456,.8422,.8124,.7896,.7712,.7556,.7424,.664,
9       .6232,.596,.5756,.5596,.5464,.5352,.5256,.513,0.4644,
1       .4630,.4170/
        data z/2.785,2.628,2.492,2.368,2.257,2.156,2.065,
1       1.982,1.908,1.841,1.780,1.725,1.675,1.629,
1       1.587,1.549,1.514,1.482,1.452,1.424,1.399,1.375,
1       1.353,1.333,1.314,1.296,1.279,1.264,1.248,1.234,
```

```
      1  1.221,1.209,1.197,1.186,1.175,1.156,1.138,1.122,
      1  1.107,1.093,1.081,1.069,1.058,1.048,1.039,1.030,
      1  1.022,1.014,1.007,0.9999,0.9932,.9870,.9811,.9755,
      1  .9700,.9649,.9600,.9553,.9507,.9464,.9422,.9382,.9343,
      1  .9305,.9269,.8963,.8727,.8538,.8379,.8242,.7432,
      1  .7005,.6718,.6504,.6335,.6194,.6076,.5973,.5882,0.5320,
      1  0.5016,0.4811/
c----do interpolation in the appropriate region----------------------
         do 10 i=1,82
         inext=i
         if(x(i) .ge. xx1) go to 15
10       continue
15       yy1=y(inext-1)+(xx1-x(inext-1))*(y(inext)-y(inext-1))/
      1  (x(inext)-x(inext-1))
         zz1=z(inext-1)+(xx1-x(inext-1))*(z(inext)-z(inext-1))/
      1  (x(inext)-x(inext-1))
         return
         end
c----end of the program-------------------------------------------
```

A sample output of the program is given in Table A.3

Table A.3 Sample output of the program.

```
-------------------------------------------------------------
                    Input parameters
-------------------------------------------------------------

Molecular wt. of gas A                          3.994E+01
Molecular wt. of gas B                          5.493E+01
Parameter ebyk of A                             1.240E+02
Parameter ebyk of B                             2.818E+03
Sigma of gas A                                  3.418E+00
Sigma of gas B                                  2.580E+00

-------------------------------------------------------------
                    Input conditions
-------------------------------------------------------------

Temperature in K                                1.873E+03
Pressure in atmosphere                          1.000E+00

-------------------------------------------------------------
            Values of thermophysical properties
-------------------------------------------------------------

kT/e for gas A                                  1.510E+01
Viscosity/thermal conductivity omega for A      7.829E-01
Viscosity of gas A (gm/cm-s)                    7.983E-04
Conductivity of gas A (cal/cm-s-K)              1.49E-04
kT/e for gas B                                  6.647E-01
Viscosity/thermal conductivity omega for B      1.960E+00
Viscosity of gas B (gm/cm-s)                    6.56E-04
Conductivity of gas B (cal/cm-s-K)              8.90E-05
Binary Diffusivity omega for gas pair A/B       9.353E-01
Diffusivity of gas A in gas B  (cm2/s)          3.72E+00

-------------------------------------------------------------
```

Appendix B

DERIVATION OF JUMP CONDITIONS ACROSS
KNUDSEN LAYER

The jump conditions across the Knudsen layer are obtained by solving the equations of conservation's of mass, momentum and translational kinetic energy across the Knudsen layer. The details of the solution are given in the following sections.

B.1 Conservation of Mass

The equations of conservation of mass across the Knudsen layer can be written as:

$$\rho_1 \int_0^\infty f_1\xi d\xi = \rho_v \int_{-\infty}^\infty f_3\xi d\xi + \rho_v\beta \int_\infty^0 f_3\xi d\xi \tag{B.1}$$

The left hand side (LHS) of the equation represents the total flux vaporizing at the material surface at temperature T_1. The first term on the right hand side (RHS) represents the flux of the material crossing the Knudsen layer, and hence the net vaporization flux, and the second term represents the flux condensing back on the pool surface. The definitions of the term used in the equations are given in Chapter 3, section 3.1.2.2.

The velocity distribution functions f_1 and f_3 are given by:

$$f_1 = \sqrt{\frac{1}{2\pi RT_l}} \; \exp\left\{ \frac{-\xi^2}{2RT_l} \right\} = a_l e^{-b_l \xi^2} \tag{B.2}$$

$$f_3 = \sqrt{\frac{1}{2\pi RT_v}} \; \exp\left\{ \frac{-(\xi-u)^2}{2RT_v} \right\} = a_v e^{-b_v(\xi-u)^2} \tag{B.3}$$

where $a_i = \sqrt{\dfrac{1}{2\pi RT_i}}$ and $b_i = \dfrac{1}{2RT_i}$, and $i = l$ or v.

Substituting equations (B.2) and (B.3) in equation (B.1) we have:

$$\rho_l a_l \int_0^\infty e^{-b_l \xi^2} \xi \, d\xi = \rho_v a_v \int_{-\infty}^\infty e^{-b_v(\xi-u)^2} \xi d\xi + \rho_v a_v \beta \int_{-\infty}^0 e^{-b_v(\xi-u)^2} \xi d\xi \tag{B.4}$$

or $\qquad I_1 \qquad = \qquad I_2 \qquad + \qquad I_3$

The first term on the LHS of equation (B.4), I_1, can be evaluated from the results given in section B.5 and summarized at the end of the appendix in Table B.1 and is given as:

$$I_1 = \frac{1}{2b_l} \rho_l a_l \tag{B.5}$$

The first term on the RHS of equation (B.4), I_2, can be integrated as follows:

$$I_2 = \rho_v a_v \int_{-\infty}^\infty (\zeta+u) e^{-b_v \zeta^2} d\zeta \qquad \text{where } \zeta = \xi - u \tag{B.6}$$

or $\quad I_2 = \rho_v \, a_v \int\limits_{-\infty}^{\infty} \zeta e^{-b_v \zeta^2} \, d\zeta + \rho_v \, a_v u \int\limits_{-\infty}^{\infty} e^{-b_v \zeta^2} \, d\zeta$ (B.7)

From Table B.1 we have:

$$I_2 = \rho_v \, a_v u \sqrt{\frac{\pi}{b_v}}$$ (B.8)

The second term on the RHS of equation (B.4), I_3, can be evaluated as follows:

$$I_3 = \rho_v \, a_v \, \beta \int\limits_{-\infty}^{0} e^{-b_v(\xi - u)^2} \xi \, d\xi$$ (B.9)

or $\quad I_3 = \rho_v \, a_v \, \beta \int\limits_{-\infty}^{-u} e^{-b_v \eta^2} (\eta + u) \, d\eta \qquad$ where $\eta = \xi - u$ (B.10)

or $\quad I_3 = \rho_v \, a_v \, \beta \int\limits_{-\infty}^{-u} \eta e^{-b_v \eta^2} d\eta + \rho_v \, a_v \, \beta u \int\limits_{-\infty}^{-u} e^{-b_v \eta^2} d\eta$ (B.11)

or $\quad I_3 = \qquad I_4 \qquad + \qquad I_5$

From Table B.1, the first term on the RHS of equation (B.11), I_4, can be written as follows:

or $\quad I_4 = -\frac{\rho_v a_v \beta}{2 b_v} e^{-b_v u^2}$ (B.12)

From Table B.1, the second term on the RHS of equation (B.11), I_5, can be written as follows:

$$I_5 = \frac{\rho_v a_v \beta u}{2} \sqrt{\frac{\pi}{b_v}} \, \mathrm{erfc}(u\sqrt{b_v})$$

(B.13)

Combining equation (B.11), (B.12) and (B.13) we have:

$$I_3 = \rho_v a_v \beta \left\{ -\frac{e^{-b_v u^2}}{2b_v} + \frac{u}{2}\sqrt{\frac{\pi}{b_v}} \mathrm{erfc}(u\sqrt{b_v}) \right\}$$

(B.14)

Combining equations (B.4), (B.5), (B.8) and (B.14) we have:

$$\frac{1}{2b_1}\rho_1 a_1 = \rho_v a_v u \sqrt{\frac{\pi}{b_v}} + \rho_v a_v \beta \left\{ -\frac{e^{-b_v u^2}}{2b_v} + \frac{u}{2}\sqrt{\frac{\pi}{b_v}} \mathrm{erfc}(u\sqrt{b_v}) \right\}$$

(B.15)

Substituting the values of a_i and b_i and putting $u = m\sqrt{2RT_v}$ and rearranging equation (B.15), we have:

$$\rho_v u = \rho_1 \sqrt{\frac{RT_1}{2\pi}} - \beta\rho_v \sqrt{\frac{RT_v}{2\pi}} \left\{ \sqrt{\pi} m \, \mathrm{erfc}(m) - e^{-m^2} \right\}$$

(B.16)

Equation (B.16) represents the conservation of mass across the Knudsen layer. The term on the LHS represents the net vaporization rate at a surface temperature of T_1. The unknowns in the equation are T_v, ρ_v, β and u or m. The density at the pool surface is calculated using ideal gas law.

B.2 Conservation of Momentum

The equations of conservation of momentum across the Knudsen layer can be represented by:

$$\rho_l \int_0^\infty f_1 \xi^2 d\xi = \rho_v \int_{-\infty}^\infty f_3 \xi^2 d\xi + \rho_v \beta \int_\infty^0 f_3 \xi^2 d\xi \tag{B.17}$$

Substituting equations (B.2) and (B.3) in equation (B.17) we have:

$$\rho_l \, a_l \int_0^\infty e^{-b_l \xi^2} \xi^2 \, d\xi = \rho_v \, a_v \int_{-\infty}^\infty e^{-b_v(\xi-u)^2} \xi^2 d\xi + \rho_v \, a_v \, \beta \int_{-\infty}^0 e^{-b_v(\xi-u)^2} \xi^2 d\xi \tag{B.18}$$

or $\qquad I_6 \qquad = \qquad I_7 \qquad + \qquad I_8$

where $a_i = \sqrt{\dfrac{1}{2\pi R T_i}}$ and $b_i = \dfrac{1}{2RT_i}$, and $i = l$ or v.

From Table B.1, the term on the LHS of equation (B.18), I_6, can be written as:

$$I_6 = \frac{\rho_l \, a_l}{4} \sqrt{\frac{\pi}{b_l^3}} \tag{B.19}$$

The first term on the RHS of equation (B.18), I_7, can be integrated as follows:

$$I_7 = \rho_v \, a_v \int_{-\infty}^{\infty} (\zeta+u)^2 e^{-b_v \zeta^2} \, d\zeta \qquad \text{where } \zeta=\xi-u \qquad (B.20)$$

or $$I_7 = \rho_v \, a_v u^2 \int_{-\infty}^{\infty} e^{-b_v \zeta^2} \, d\zeta + 2\rho_v \, a_v u \int_{-\infty}^{\infty} \zeta e^{-b_v \zeta^2} \, d\zeta + \rho_v \, a_v \int_{-\infty}^{\infty} \zeta^2 e^{-b_v \zeta^2} \, d\zeta \quad (B.21)$$

From Table B.1 we have:

$$I_7 = \rho_v \, a_v u^2 \sqrt{\frac{\pi}{b_v}} + \frac{\rho_v \, a_v}{2 b_v} \sqrt{\frac{\pi}{b_v}} \qquad (B.22)$$

The second term on the RHS of equation (B.18), I_8, can be evaluated as follows:

$$I_8 = \beta \rho_v \, a_v \int_{-\infty}^{-u} (\zeta+u)^2 e^{-b_v \zeta^2} \, d\zeta \qquad \text{where } \zeta=\xi-u \qquad (B.23)$$

or $$I_8 = \beta \rho_v \, a_v u^2 \int_{-\infty}^{-u} e^{-b_v \zeta^2} d\zeta + 2\beta \rho_v \, a_v u \int_{-\infty}^{-u} \zeta e^{-b_v \zeta^2} d\zeta + \beta \rho_v \, a_v \int_{-\infty}^{-u} \zeta^2 e^{-b_v \zeta^2} d\zeta \quad (B.24)$$

From Table B.1 we have: .

$$I_8 = \beta \rho_v a_v \left\{ \frac{u^2}{2} \sqrt{\frac{\pi}{b_v}} \, \text{erfc}(u\sqrt{b_v}) - \frac{u}{b_v} e^{-b_v u^2} + \frac{u}{2b_v} e^{-b_v u^2} + \frac{\sqrt{\pi}}{4 b_v \sqrt{b_v}} \text{erfc}(u\sqrt{b_v}) \right\}$$

$$(B.25)$$

Combining equations (B.18), (B.19), (B.22) and (B.25) we have:

$$\frac{\rho_1 a_1}{4}\sqrt{\frac{\pi}{b_1{}^3}} = \rho_v\,a_v u^2\sqrt{\frac{\pi}{b_v}} + \frac{\rho_v\,a_v}{2b_v}\sqrt{\frac{\pi}{b_v}} +$$

$$\beta\rho_v a_v\left\{\frac{u^2}{2}\sqrt{\frac{\pi}{b_v}}\,\text{erfc}(u\sqrt{b_v}) - \frac{u}{b_v}e^{-b_v u^2} + \frac{u}{2b_v}e^{-b_v u^2} + \frac{\sqrt{\pi}}{4b_v\sqrt{b_v}}\text{erfc}(u\sqrt{b_v})\right\}$$

$$(B.26)$$

Substituting the values of a_i and b_i and putting $u = m\sqrt{2RT_v}$, and rearranging equation (B.26), we have:

$$\rho_v(u^2 + RT_v) = \frac{1}{2}\rho_1 RT_1 - \beta\rho_v RT_v\left\{(m^2 + \frac{1}{2})\text{erfc}(m) - \frac{m}{\sqrt{\pi}}e^{-m^2}\right\} \qquad (B.27)$$

Equation (B.27) represents the conservation of momentum across the Knudsen layer. The unknowns in the equation are T_v, ρ_v, β and u or m. The density at the pool surface is calculated using ideal gas law.

B.3 Conservation of Energy Flux

In addition to the translational kinetic energy flux, there is another energy flux component associated with the moving vapor. This energy flux is contributed because of the energy associated with the internal degrees of freedom of the moving vapor and is passively transported by an appropriate mass flux. The energy associated with the internal degrees of freedom per unit mass at temperature T, $e_{int}(T)$, is given by:

$$e_{int}(T) = \frac{(5-3\gamma)}{2(\gamma-1)}RT \qquad (B.28)$$

Adding the energy fluxes due to translational kinetic energy and the internal degrees of freedom, the conservation equation can be written as:

$$\frac{\rho_1}{2}\int_0^\infty f_1\xi^3 d\xi + e_{int}(T_1)\rho_1\int_0^\infty f_1\xi d\xi = \frac{\rho_v}{2}\int_{-\infty}^\infty f_3\xi^3 d\xi + e_{int}(T_v)\rho_v\int_{-\infty}^\infty f_3\xi d\xi) +$$

$$\frac{\rho_v\beta}{2}\int_{-\infty}^0 f_3\xi^3 d\xi + e_{int}(T_v)\,\rho_v\beta\int_{-\infty}^0 f_3\xi d\xi \qquad (B.29)$$

Substituting equations (B.2) and (B.3) in equation (B.29) we have

$$\frac{\rho_1\,a_1}{2}\int_0^\infty e^{-b_1\xi^2}\xi^3\,d\xi + e_{int}(T_1)\rho_1\,a_1\int_0^\infty e^{-b_1\xi^2}\xi\,d\xi =$$

$$\frac{\rho_v\,a_v}{2}\int_{-\infty}^\infty e^{-b_v(\xi-u)^2}\xi^3 d\xi + e_{int}(T_v)\rho_v\,a_v\int_{-\infty}^\infty e^{-b_v(\xi-u)^2}\xi d\xi +$$

$$\frac{\rho_v\,a_v}{2}\beta\int_{-\infty}^0 e^{-b_v(\xi-u)^2}\xi^3 d\xi + e_{int}(T_v)\,\rho_v\,a_v\,\beta\int_{-\infty}^0 e^{-b_v(\xi-u)^2}\xi d\xi \qquad (B.30)$$

From Table B.1 the terms on the LHS of equation (B.30), I_9, can be written as follows:

$$I_9 = \frac{\rho_1\,a_1}{4b_1^2} + e_{int}(T_1)\,\frac{\rho_1\,a_1}{2b_1} \qquad (B.31)$$

The first term on the RHS of equation (B.30), I_{10}, can be evaluated as follows:

$$I_{10} = \frac{\rho_v\,a_v}{2}\,I_{11} \qquad (B.32)$$

where $I_{11} = \int_{-\infty}^{\infty} e^{-b_v\zeta^2} (\zeta+u)^3 d\zeta$ where $\zeta = \xi - u$ (B.33)

or $I_{11} = u^3 \int_{-\infty}^{\infty} e^{-b_v\zeta^2} d\zeta + 3u^2 \int_{-\infty}^{\infty} \zeta e^{-b_v\zeta^2} d\zeta + 3u \int_{-\infty}^{\infty} \zeta^2 e^{-b_v\zeta^2} d\zeta + \int_{-\infty}^{\infty} \zeta^3 e^{-b_v\zeta^2} d\zeta$

(B.34)

From Table B.1 we have:

$$I_{11} = u^3 \sqrt{\frac{\pi}{b_v}} + \frac{1}{2b_v} \sqrt{\frac{\pi}{b_v}}$$ (B.35)

Therefore $I_{10} = \frac{\rho_v a_v}{2} \left\{ u^3 \sqrt{\frac{\pi}{b_v}} + \frac{1}{2b_v} \sqrt{\frac{\pi}{b_v}} \right\}$ (B.36)

The second term on the RHS of equation (B.30), I_{12}, can be written from Table B.1 as follows:

$$I_{12} = e_{int}(T_v)\rho_v a_v u \sqrt{\frac{\pi}{b_v}}$$ (B.37)

The third term on the RHS of equation (B.30), I_{13}, can be evaluated as follows:

$$I_{13} = \frac{\rho_v a_v}{2} \beta I_{14}$$ (B.38)

where
$$I_{14} = \int_{-\infty}^{-u} e^{-b_v \zeta^2}(\xi+u)^3 d\xi \tag{B.39}$$

or
$$I_{14} = u^3 \int_{-\infty}^{-u} e^{-b_v \zeta^2} d\xi + 3u^2 \int_{-\infty}^{-u} e^{-b_v \zeta^2}\xi d\xi +$$

$$3u \int_{-\infty}^{-u} e^{-b_v \zeta^2}\xi^2 d\xi + \int_{-\infty}^{-u} e^{-b_v \zeta^2}\xi^3 d\xi \tag{B.40}$$

From Table B.1 we have:

$$I_{14} = \frac{u^3}{2}\sqrt{\frac{\pi}{b_v}}\,\mathrm{erfc}(u\sqrt{b_v}) - \frac{3u^2}{2b_v}e^{-b_v u^2} + \frac{3u^2}{2b_v}e^{-b_v u^2} + \frac{3u\sqrt{\pi}}{4\sqrt{b_v b_v}}\mathrm{erfc}(u\sqrt{b_v}))$$

$$- \frac{u^2}{2b_v}e^{-b_v u^2} - \frac{1}{2b_v^2}e^{-b_v u^2} \tag{B.41}$$

Substituting (B.41) in equation (B.38) we have:

$$I_{13} = \frac{\rho_v a_v}{2}\beta\left\{\frac{u^3}{2}\sqrt{\frac{\pi}{b_v}}\,\mathrm{erfc}(u\sqrt{b_v}) + \frac{3u\sqrt{\pi}}{4b_v\sqrt{b_v}}\mathrm{erfc}(u\sqrt{b_v})\right\}$$

$$- \frac{\rho_v a_v}{2}\beta\left\{\frac{u^2}{2b_v}e^{-b_v u^2} + \frac{1}{2b_v^2}e^{-b_v u^2}\right\} \tag{B.42}$$

The fourth term on the RHS of equation (B.30), I_{15}, can be integrated with the help of equation (B.14) and is given as follows:

$$I_{15} = e_{int}(T_v)\rho_v a_v \beta \left\{ -\frac{e^{-b_v u^2}}{2b_v} + \frac{u}{2}\sqrt{\frac{\pi}{b_v}} erfc(u\sqrt{b_v}) \right\}$$ (B.43)

Writing in symbolic form, equation (B.30) can be written as:

$$I_9 = I_{10} + I_{12} + I_{13} + I_{14} + I_{15}$$ (B.44)

Substituting the values of the above terms, a_i and b_i and putting $u = m\sqrt{2RT_v}$ and rearranging equation (B.44), we have:

$$\rho_v u\left\{ \frac{3}{2}RT_v + \frac{1}{2}u^2 \right\} = \rho_l\sqrt{\frac{RT_l}{2\pi}}\left\{ RT_l + e_{int}(T_l) \right\}$$

$$-\beta\rho_v RT_v \sqrt{\frac{RT_v}{2\pi}}\left\{ m(m^2+\frac{3}{2})\sqrt{\pi}erfc(m) - (m^2+1)e^{-m^2} \right\}$$

$$-e_{int}(T_v)\left\{ \rho_v u + \beta\rho_v \sqrt{\frac{RT_v}{2\pi}}\left\{ \sqrt{\pi}merfc(m) - e^{-m^2} \right\} \right\}$$ (B.45)

From equation (B.16) we have:

$$\rho_v u\left\{ \frac{3}{2}RT_v + \frac{1}{2}u^2 \right\} = \rho_l\sqrt{\frac{RT_l}{2\pi}}\left\{ RT_l + e_{int}(T_l) - e_{int}(T_v) \right\}$$

$$-\beta\rho_v RT_v \sqrt{\frac{RT_v}{2\pi}}\left\{ m(m^2+\frac{3}{2})\sqrt{\pi}erfc(m) - (m^2+1)e^{-m^2} \right\}$$ (B.46)

Multiplying equation (B.16) with RT_v and adding the result of equation (B.46) and substituting the values of e_{int} we have:

$$\rho_v u\left\{ \frac{5}{2}RT_v + \frac{1}{2}u^2 \right\} = \rho_l\sqrt{\frac{RT_l}{2\pi}}\left\{ RT_l + RT_v + \frac{(5-3\gamma)}{2(\gamma-1)}R(T_l - T_v) \right\}$$

$$- \beta \rho_v R T_v \sqrt{\frac{RT_v}{2\pi}} \left\{ m(m^2+\tfrac{5}{2}) \sqrt{\pi} \operatorname{erfc}(m) - (m^2+2)e^{-m^2} \right\}$$

<div align="right">(B.47)</div>

Approximating $RT_l + RT_v = 2RT_l$ for low values of Mach number we have:

$$\rho_v u \left\{ \frac{5}{2}RT_v + \frac{1}{2}u^2 \right\} = \rho_l \sqrt{\frac{RT_l}{2\pi}} \left\{ 2RT_l + \frac{(5-3\gamma)}{2(\gamma-1)} R(T_l - T_v) \right\}$$

$$- \beta \rho_v R T_v \sqrt{\frac{RT_v}{2\pi}} \left\{ m(m^2+\tfrac{5}{2}) \sqrt{\pi} \operatorname{erfc}(m) - (m^2+2)e^{-m^2} \right\} \quad \text{(B.48)}$$

Equation (B.48) represents the conservation of energy across the Knudsen layer. The unknowns in the equation are T_v, ρ_v, β and u or m. The density at the pool surface is calculated using ideal gas law.

B.4 Jump Conditions Across the Knudsen Layer

The density jump condition can be obtained by equating the value of β from equations (B.16) and (B.27). From (B.16) we have:

$$-\beta = \frac{\rho_v u - \rho_l \sqrt{\frac{RT_l}{2\pi}}}{\rho_v \sqrt{\frac{RT_v}{2\pi}} \left\{ \sqrt{\pi} m \operatorname{erfc}(m) - e^{-m^2} \right\}}$$

<div align="right">(B.49)</div>

From equation (B.27) we:

$$-\beta = \frac{\rho_v(u^2+RT_v) - \frac{1}{2}\rho_l RT_l}{\rho_v RT_v\left\{(m^2 + \frac{1}{2})erfc(m) - \frac{m}{\sqrt{\pi}}e^{-m^2}\right\}} \qquad (B.50)$$

Substituting $u = m\sqrt{2RT_v}$ and equating (B.49) and (B.50) we have:

$$\frac{\rho_v m\sqrt{2RT_v} - \rho_l\sqrt{\frac{RT_l}{2\pi}}}{\rho_v\sqrt{\frac{RT_v}{2\pi}}\left\{\sqrt{\pi}merfc(m) - e^{-m^2}\right\}} = \frac{\rho_v RT_v(2m^2+1) - \frac{1}{2}\rho_l RT_l}{\rho_v RT_v\left\{(m^2 + \frac{1}{2})erfc(m) - \frac{m}{\sqrt{\pi}}e^{-m^2}\right\}} \qquad (B.51)$$

Simplifying equation (B.51) we have:

$$\frac{\rho_v}{\rho_l} = \sqrt{\frac{T_l}{T_v}}\left\{(m^2 + \frac{1}{2})e^{m^2}erfc(m) - \frac{m}{\sqrt{\pi}}\right\} + \frac{1}{2}\sqrt{\frac{T_l}{T_v}}\left\{1 - \sqrt{\pi}me^{m^2}erfc(m)\right\} \qquad (B.52)$$

The equation for β in terms of temperature and density jump conditions can be obtained as follows:

Multiplying equation (B.16) with $\dfrac{e^{m^2}}{2}\dfrac{T_l}{T_v}$ and rearranging we have:

$$\frac{1}{2}\frac{T_l}{T_v}(\sqrt{\pi}me^{m^2}erfc(m) - 1) = \frac{\frac{1}{2}\frac{T_l}{T_v}e^{m^2}\left\{\rho_v u - \rho_l\sqrt{\frac{RT_l}{2\pi}}\right\}}{-\beta\rho_v\sqrt{\frac{RT_v}{2\pi}}} \qquad (B.53)$$

Similarly multiplying equation (B.27) with $e^{m^2} \sqrt{\frac{T_1}{T_v}}$ and rearranging we have:

$$\sqrt{\frac{T_1}{T_v}}\left\{ (m^2 + \tfrac{1}{2})e^{m^2}\text{erfc}(m) - \frac{m}{\sqrt{\pi}}\right\} = \frac{\sqrt{\frac{T_1}{T_v}}\,e^{m^2}\left\{\rho_v(u^2+RT_v) - \tfrac{1}{2}\rho_l RT_l\right\}}{-\beta\rho_v RT_v}$$

(B.54)

Subtracting equation (B.53) from equation (B.54) and making use of equation (B.52) we have:

$$\frac{\rho_v}{\rho_l} = \frac{\sqrt{\frac{T_1}{T_v}}\,e^{m^2}\left\{\rho_v(u^2+RT_v) - \tfrac{1}{2}\rho_l RT_l\right\}}{-\beta\rho_v RT_v} - \frac{\frac{1}{2}\frac{T_1}{T_v}e^{m^2}\left\{\rho_v u - \rho_l\sqrt{\frac{RT_l}{2\pi}}\right\}}{-\beta\rho_v\sqrt{\frac{RT_v}{2\pi}}}$$

(B.55)

Substituting $u = m\sqrt{2RT_v}$ and simplifying we have:

$$-\beta = \left\{(2m^2 + 1) - m\sqrt{\frac{\pi T_1}{T_v}}\right\}e^{m^2}\frac{\rho_l}{\rho_v}\sqrt{\frac{T_1}{T_v}}$$

(B.56)

The temperature jump condition is obtained by substituting the value of $\frac{\rho_l}{\rho_v}$, β and u in equation (B.47) and simplifying. The resultant equation is:

$$\frac{m}{2}\sqrt{\pi\frac{T_1}{T_v}} + 2 = 2\frac{T_1}{T_v} + \frac{(5-3\gamma)T_1}{2(\gamma-1)T_v} - \frac{(5-3\gamma)}{2(\gamma-1)}$$

(B.57)

or $$(2 + \frac{(5-3\gamma)}{2(\gamma-1)})\frac{T_v}{T_1} + \frac{m}{2}\sqrt{\pi\frac{T_v}{T_1}} - 2 - \frac{(5-3\gamma)}{2(\gamma-1)} = 0$$

(B.58)

Taking the roots and neglecting the negative root we have:

$$\frac{T_v}{T_1} = \left\{ \sqrt{1 + \pi\left\{\frac{\gamma - 1}{\gamma + 1}\frac{m}{2}\right\}^2} - \sqrt{\pi\frac{\gamma - 1}{\gamma + 1}\frac{m}{2}} \right\}^2$$

(B.59)

B.5 Selected Integrals

Some of the integrals used in the previous calculations are evaluated here and the results are summarized in Table B.1.

$$I_a = \int xe^{-ax^2}dx$$

(B.60)

or $\quad I_a = \frac{1}{2a}\int e^{-t}dt \qquad$ where $t = ax^2$

(B.61)

or $\quad I_a = -\frac{1}{2a}e^{-t}$

(B.62)

or $\quad I_a = -\frac{1}{2a}e^{-ax^2}$

(B.63)

$$I_b = \int x^2 e^{-ax^2}dx$$

(B.64)

Integrating by parts we have:

$$I_b = x \int xe^{-ax^2}dx - \int \left\{ 1 \int xe^{-ax^2}dx \right\}dx \qquad (B.65)$$

Using equation (B.63) we have:

$$I_b = -\frac{x}{2a}e^{-ax^2} + \frac{1}{2a}\int e^{-ax^2}dx \qquad (B.66)$$

The second term on the RHS can be evaluated by making use of the definition of the error function given in Table B.1.

$$I_c = \int x^3 e^{-ax^2}dx \qquad (B.67)$$

Again integrating by parts we have:

$$I_c = x^2 \int xe^{-ax^2}dx - \int \left\{ 2x \int xe^{-ax^2}dx \right\}dx \qquad (B.68)$$

Using equation (B.63) we have:

$$I_c = -\frac{x^2}{2a}e^{-ax^2} + \frac{1}{a}\int xe^{-ax^2}dx \qquad (B.69)$$

Again using equation (B.63) we have:

$$I_c = -\frac{x^2}{2a}e^{-ax^2} - \frac{1}{2a^2}e^{-ax^2} \qquad (B.70)$$

The results of this section are summarized in Table B.1. All the integrals in solution of the equations of conservation across the Knudsen layer can be calculated by making use of these results taking into account the appropriate limits of the integrals.

Table B.1 Selected integrals and their values

Integral	Value
$\int_{0}^{b} e^{-ax^2} dx$	$\frac{1}{2}\sqrt{\frac{\pi}{a}}\,\mathrm{erf}(b\sqrt{a})$
$\int_{b}^{\infty} e^{-ax^2} dx$	$\frac{1}{2}\sqrt{\frac{\pi}{a}}\,\mathrm{erfc}(b\sqrt{a})$
$\int xe^{-ax^2} dx$	$-\frac{1}{2a}e^{-ax^2}$
$\int x^2 e^{-ax^2} dx$	$-\frac{x}{2a}e^{-ax^2} + \frac{1}{2a}\int e^{-ax^2} dx$
$\int x^3 e^{-ax^2} dx$	$-\frac{x^2}{2a}e^{-ax^2} - \frac{1}{2a^2}e^{-ax^2}$
$\int_{-a}^{-b} f(x)dx$	$-\int_{a}^{b} f(-x)dx$
$\int_{a}^{b} f(x)dx$	$-\int_{b}^{a} f(x)dx$

$\mathrm{erf}(\infty) = 1.0$ $\qquad\qquad$ $\mathrm{erfc}(x) = 1-\mathrm{erf}(x)$

$\mathrm{erf}(0) = 0.0$

$\mathrm{erf}(-\infty) = 0.0$

Appendix C

CALCULATION OF TEMPERATURE, PRESSURE, AND
DENSITY AT VARIOUS LOCATIONS IN THE GAS PHASE

C.1 At the Pool Surface

The pressure at the pool surface, P_1, for a given surface temperature, T_1, is calculated from equation (3.20). The density at the pool surface, ρ_1, is computed from P_1 and T_1 assuming that the vapor behaves like an ideal gas.

C.2 At the Edge of Knudsen Layer

Equation (3.17) to (3.23) are used to calculate the Mach number of the vapor at the edge of Knudsen layer. The Mach number is then used in equation (3.17) and (3.18) to calculate the temperature, T_v, and density, ρ_v, at the edge of Knudsen layer. The pressure at the edge of Knudsen layer, P_v, is equal to the pressure across the contact discontinuity, P_2, and is calculated from equation (3.22).

C.3 Across the Contact Discontinuity

The temperature across the contact discontinuity, T_2, is related to the temperature at the edge of Knudsen layer, T_v, and is given by [1]:

$$\frac{T_2}{T_v} = \frac{M_g}{M_v} \frac{\rho_v}{\rho_g} \tag{C.1}$$

where M_g is the molecular weight of the shielding gas. The pressure across the contact discontinuity, P_2, is calculated by the Rankine-Hugoniot relationship, given by equation (3.22), which relates the pressure in front of and behind the pressure wavefront. The density across the contact discontinuity, ρ_2, is related to the ambient densiy, ρ_g, by the following relation [1]:

$$\frac{\rho_2}{\rho_g} = \frac{(\gamma_g + 1)(\frac{P_2}{P_g}) + (\gamma_g - 1)}{(\gamma_g - 1)(\frac{P_2}{P_g}) + (\gamma_g + 1)} \qquad (C.3)$$

C.4 In the Shielding Gas

The ambient pressure, P_g, is $1 \times 10^5 \, N/m^2$, and the ambient temperature, T_g, is 298 K. The ambient density, ρ_g, is calculated from P_g and T_g, assuming that the shielding gas behaves like an ideal gas.

C.5 Reference

1.   G. Emanuel, Gasdynamics: Theory and Application (AIAA Education Series, NY, 1986).

Appendix D

PROGRAMS FOR SOLUTION OF EQUATIONS OF

CONSERVATIONS IN THE GAS PHASE

The following programs were developed to solve the equations of conservation of mass, momentum and translational kinetic energy in the vapor phase. The details of the equations are given in Chapter 3, section 3.1.2.2.

D.1 Program D.1

This program solves the equations of conservations of mass, momentum and translational kinetic energy in the vapor phase using gasdynamics principles for the evaporation from metals. The constraint on the pressure due to thermodynamic considerations is used to have unique values of Mach number at the edge of Knudsen layer for a given weld pool surface temperature. From the values of the Mach number the vaporization flux due to pressure gradient is calculated. The program is given below:

```
        program  gas_dynamics_puremetals
c-----definitions of important terms in the program------------------
c       alatheat:       latent heat of metal
c       amach:.         mach number
c       amwtme:         molecular weight of the metal
c       amwtgas:        molecular weight of the shielding gas
c       confl:          total flux due to pressure gradient
c       erf:            series approximation of the term: exp(m**2)*erfc(m)
c       erfc:           complimentary error function
c       gamma1:         ratio of specific heats for shielding gas
c       gamma3:         ratio of specific heats for vapor
c       gasr:           gas constant
c       p3ps:           pressure jump conditions across knudsen layer
c       pi:             constant
c       psp:            equilibrium vapor pressure at tsurf
c                       calculated using Clausius-Clapeyron equation
```

```
c        pspl:        pressure at the surface from gasdynamic
c        r3rs:        density jump conditions across knudsen layer
c        resd:        difference between pressure calculated from gas
c                     dynamics and thermodynamics at the pool surface
c        rho3:        density of vapor at the edge of the knudsen layer
c        rs:          density at liquid surface temperature
c        rtemp:       room temperature
c        sped:        velocity of vapor at the edge of knudsen layer
c        spedrt:      speed of sound at room temperature
c        t3ts:        temperature jump conditions across Knudsen layer
c        tboil:       boiling point of metal
c        temp3:       temperature at the edge of knudsen layer
c        tmax:        temperature near which Mach number is close to 1
c        tmelt:       melting point of metal
c        tsurf:       surface temperature on the weld pool
c-----end definitions of terms used in the program-------------------
         parameter (noi=5)
         character*60 filename
         character*60 strinp(noi)
         dimension valinp(noi)
c-----input parameters---------------------------------------------
         data gasr,gamma1,gamma3,rtemp,pi/8.314,1.6667,1.6667,298.0,3.1415/
         data strinp/'molecular weight of shielding gas','molecular weight
        1of metal','latent heat of vaporization (J/gm)','boiling temperatur
        1e (K)','Maximum temp. for calculation (Mach #=1)'/
         data valinp/39.94,55.85,6334.825,3135.0,4800./
c-----modify output filename, if required--------------------------
         filename='output'
         write(*,*)'change the name of the output file (yes: 1, no:0)'
         read(*,*)yescha
         if (yescha.gt.0.5) then
         write(*,*)'type the name of the new output file'
         read(*,69)filename
         endif
69       format(a60)
         open (unit=36,file=filename)
         write(*,79)'input parameters'
79       format(79('-'),/22x,a20)
```

```
11      write(*,129)
129     format(79('-'))
c----modify input parmeters, if required--------------------------
        do 10 i=1,noi
        write(*,89)'Enter',i,'to change',strinp(i),'(',valinp(i),')'
10      continue
        noip=noi+1
        write(*,99)'Enter',noip,'if all values are ok'
89      format(2x,a5,1x,i2,1x,a9,1x,a40,a1,1pe10.3,a1)
99      format(2x,a5,1x,i2,1x,a20,/2x,79('-'))
        write(*,109)'Please enter your choice (1 to',noip,'):'
109     format(2x,a30,1x,i2,a2)
        read(*,*)ichange
        if (ichange.eq.noip) go to 20
        write(*,119)'Enter',strinp(ichange),':'
        read(*,*)valinp(ichange)
        go to 11
119     format(2x,a5,2x,a60,a2)
c-----assign input variables to user friendly names-----------------
20      amwtgas = valinp(1)
        amwtme = valinp(2)
        alatheat = valinp(3)
        tboil = valinp(4)
        tmax = valinp(5)
c----write input parameters in an output file----------------------
        write(36,79)'input parameters'
        write(36,129)
        do 30 i=1,noi
        write(36,139)strinp(i),valinp(i)
30      continue
139     format(2x,a60,2x,e10.4)
        write(36,129)
        write(36,*)'                              program output'
        write(36,129)
        write(36,149)
        write(36,159)
149     format(12x,'Surface Temp.',7x,'Mach #',5x,'Density',6x,'Flux')
159     format(18x,'(K)',20x,'(gm/cm**3)',4x,'(gm/cm**2-s)')
```

```
        write(36,129)
        const=amwtme*alatheat/(gasr*tboil)
        do 40 tsurf=tboil,tmax,100.
        tempterm=1.-tboil/tsurf
c-----Clausius-Clapeyron relation for equilibrium vapor pressure
c       calculation from equation (3.20)----------------------------
        psp=exp(const*tempterm)
c-----begin calculation of mach number-equaions (3.17) to (3.23)--------
21      am=amach*sqrt(gamma3/2.)
        term1=(gamma3-1.)*am/((gamma3+1.)*2.)
c-----temperature jump condition across Kundsen layer, equation (3.17)--
        t3ts=(sqrt(1.+pi*term1*term1)-sqrt(pi)*term1)**2
        tt=1./(1.+0.47047*am)
c-----approximaion of error function term in equation (3.18)------------
        erf=0.34802*tt-0.09588*tt*tt+0.74786*tt*tt*tt
c-----density jump condition across Knudsen layer equation (3.18)-------
        r3rs=sqrt(1./t3ts)*((am**2+0.5)*erf-am/sqrt(pi))
        r3rs=r3rs+0.5*(1./t3ts)*(1-sqrt(pi)*am*erf)
c-----pressure jump condition across Knudsen layer--------------------
        p3ps=r3rs*t3ts
        temp3=tsurf*t3ts
        a3a1=sqrt(gamma3*temp3*amwtgas)/sqrt(gamma1*rtemp*amwtme)
        term2=(gamma1+1.)/4.*amach*a3a1
c-----Rankine Hugoniot Relaionship, equation (3.22)-------------------
        p2p1=1.+gamma1*a3a1*amach*(term2+sqrt(1.+term2*term2))
c-----pressure a pool surface from gasdynamics----------------------
        psp1=p2p1/p3ps
c-----difference between pressures from thermodynamics and gasdynamics--
        resd=abs(psp1/psp-1.)
        amach = amach+0.00005
        if (resd.gt.0.005) go to 21
c-----calculation of mach number over, density a pool surface-(ideal)---
        rs=amwtme*273.*psp/(22400.*tsurf)
c-----density across Knudsen layer-----------------------------------
        rho3=r3rs*rs
c-----speed of sound in vapor at room temperature--------------------
        spedrt=sqrt(1.667*8341*rtemp/amwtme)*100.
c-----speed of sound at the edge of Knudsen layer--------------------
```

```
        sped=spedrt*sqrt(temp3/rtemp)
c-----flux of vapor, equation (3.24)-------------------------------
        confl=rho3*amach*sped
        write(36,169)tsurf,amach,rho3,confl
40      continue
        write(36,129)
169     format(12x,1p,4e13.4)
        end
c-----end of the program-----------------------------------------
```

The outputs of the program for iron and tianium are presented at the end of this appendix in Tables D.1 and D.2, respectively. The plot of Mach number and density of vapor at the edge of Knudsen layer as a function weld pool surface temperature for iron and titanium is preseneted in Figs. 4.7 and 4.8, respectively.

D.2 Program D.2

This program solves the equations of conservation of mass, momentum and translational kinetic energy in the vapor phase for steels using gasdynamics principles developed for alloys in Chapter 3. The constraint on the pressure of the pool surface due to thermodynamic considerations is also taken into account. The output is obtained as a relationship between the pressure and temperature on the pool surface and the Mach number at the edge of the Knudsen layer. The Mach number is used to calculate the vaporization flux due to pressure gradient for the different alloying elements. The program is given below:

```
        program gas_dynamics_alloys
c-----definitions of important terms in the program------------------
c-----terms defined in program 1 are not repeated here---------------
c       amwtmn:    molecular weight of manganese
c       amwtni:    molecular weight of nickel
c       amwtcr:    molecular weight of chromium
c       amfmn:     mole fraction of manganese
```

```
c        amffe:      mole fraction of iron
c        amfni:      mole fraction of chromium
c        amfcr:      mole fraction of nickel
c        amolwt:     average molecular weight of the steel
c        amwtvap:    average molecular weight of vapor at tsurf
c        eqpres:     subroutine to calculate the equilibrium
c                    vapor pressure from equilibrium vapor pressure
c                    temperature relations
c        pmn:    .   partial pressure of manganese
c        pcr:        partial pressure of chromium
c        pni:        partial pressure of nickel
c        totmol:     total number of moles
c        tstar:      temperature at which the equilibrium vapor pressure
c                    for the alloy is one atmosphere, above this temperature
c                    there is driving force for the vapor to move due to
c                    pressure gradient.
c        wtpmn:      initial weight percent of manganese
c        wtpfe:      initial weight percent of iron
c        wtpcr:      initial weight percent of chromium
c        wtpni:      initial weight percent of nickel
c-----end of definitions of terms---------------------------------
         parameter (noi=6)
         character*60 filename
         character*60 strinp(noi)
         dimension valinp(noi)
c-----input parameters-------------------------------------------
         data gasr,gamma1,gamma3,rtemp,pi/8.314,1.6667,1.6667,298.0,3.1415/
         data amwtfe,amwtmn,amwtcr,amwtni/55.85,54.93,51.996,58.70/
         data strinp/'weight pct. of Mn','weight pct. of Cr','weight pct. o
      1f Ni','weight pct. of Ni','molecular weight of shiedling gas','Max
      1imum temp. for calculation (Mach #=1)'/
         data valinp/6.5,17.0,4.25,70.94,4.0026,4000.0/
c-----modify ouput file, if required-----------------------------
         filename='output'
```

```fortran
      write(*,*)'change the name of the output file (yes: 1, no:0)'
      read(*,*)yescha
      if (yescha.gt.0.5) then
      write(*,*)'type the name of the new output file'
      read(*,69)filename
      endif
69    format(a60).
      open (unit=36,file=filename)
      write(*,79)'input parameters'
79    format(79('-'),/22x,a20)
11    write(*,129)
129   format(79('-'))
c----modify input parmeters, if required-----------------------
      do 10 i=1,noi
      write(*,89)'Enter',i,'to change',strinp(i),'(',valinp(i),')'
10    continue
      noip=noi+1
      write(*,99)'Enter',noip,'if all values are ok'
89    format(2x,a5,1x,i2,1x,a9,1x,a40,a1,1pe10.3,a1)
99    format(2x,a5,1x,i2,1x,a20,/2x,79('-'))
      write(*,109)'Please enter your choice (1 to',noip,'):'
109   format(2x,a30,1x,i2,a2)
      read(*,*)ichange
      if (ichange.eq.noip) go to 20
      write(*,119)'Enter',strinp(ichange),':'
      read(*,*)valinp(ichange)
      go to 11
119   format(2x,a5,2x,a60,a2)
c-----assign user friendly names to inpu parameters-------------
20    wtpmn = valinp(1)
      wtpcr = valinp(2)
      wtpni = valinp(3)
      wtpfe = valinp(4)
      amwtgas = valinp(5)
```

```
        tmax = valinp(6)
c----write input parameters in an output file----------------------
        write(36,79)'input parameters'
        write(36,129)
        do 30 i=1,noi
        write(36,139)strinp(i),valinp(i)
30      continue
139     format(2x,a60,2x,e10.4)
        write(36,129)
        write(36,*)'                              program output'
        write(36,129)
        write(36,149)
        write(36,159)
149     format(12x,'Surface Temp.',7x,'Mach #',5x,'Density',6x,'Flux')
159     format(18x,'(K)',20x,'(gm/cm**3)',4x,'(gm/cm**2-s)')
        write(36,129)
c-----star calculaions, composition: weight fraction in mole fraction---
        totmol=wtpfe/amwtfe+wtpmn/amwtmn+wtpcr/amwtcr+wtpni/amwtni
        amfmn=wtpmn/(totmol*amwtmn)
        amfcr=wtpcr/(totmol*amwtcr)
        amfni=wtpni/(totmol*amwtni)
        amffe=wtpfe/(totmol*amwtfe)
c-----find tstar from equilibrium pessures for the given composition----
c-----above tstar there is flow due to pressure gradient---------------
c-----bisection method used: aa & bb are initial guess----------------
        aa=2901.
        bb=4000.
15      tstar=(aa+bb)/2
        call eqpres(aa,pmn,pfe,pni,pcr)
        ptaa=amfmn*pmn+amffe*pfe+amfcr*pcr+amfni*pni-1.
        call eqpres(tstar,pmn,pfe,pni,pcr)
        ptstar=amfmn*pmn+amffe*pfe+amfcr*pcr+amfni*pni-1.
        if ((ptaa*ptstar).lt.0) then
        bb=tstar
```

```
        else
        aa=tstar
        endif
        if (abs(ptstar).lt.0.001) go to 16
        go to 15
16      continue
c-----end tstar calculation----------------------------------------
        do 35 tsurf=tstar+5,3760.,50.
c-----calculate thermodynamic pressure, equation (3.18)---------------
        call eqpres(tsurf,pmn,pfe,pni,pcr)
        psp=amfmn*pmn+pfe*amffe+amfcr*pcr+amfni*pni
c-----calculate average molecular weight of vapor, equation(3.19)-------
        amwtvap=(amffe*pfe*amwtfe+amfmn*pmn*amwtmn
       1+amfcr*pcr*amwtcr+amfni*pni*amwtni)/psp
c-----sound of speed in vapor at room temperature----------------------
        spedrt=sqrt(1.667*8314*rtemp/amwtvap)*100.
c-----begin calculation of mach number, equations (3.17) to (3.23)------
21      am=amach*sqrt(gamma3/2.)
        term1=(gamma3-1.)*am/((gamma3+1.)*2.)
c-----temperature jump condition across Knudsen layer, equation (3.17)--
        t3ts=(sqrt(1.+pi*term1*term1)-sqrt(pi)*term1)**2
        tt=1./(1.+0.47047*am)
        erf=0.34802*tt-0.09588*tt*tt+0.74786*tt*tt*tt
c-----density jump condition across Knudsen layer, equation (3.15)------
        r3rs=sqrt(1./t3ts)*((am**2+0.5)*erf-am/sqrt(pi))
        r3rs=r3rs+0.5*(1./t3ts)*(1-sqrt(pi)*am*erf)
c-----pressure jump condition across Knudsen layer, equation (3.17)----
        p3ps=r3rs*t3ts
c-----temperature at edge of Knudsen layer surface, equation (3.14)---
        temp3=tsurf*t3ts
        a3a1=sqrt(gamma3*temp3*amwtgas)/sqrt(gamma1*rtemp*amwtvap)
        term2=(gamma1+1.)/4.*amach*a3a1
c-----Rankine Hogonoit relation, equation (3.22)----------------------
        p2p1=1.+gamma1*a3a1*amach*(term2+sqrt(1.+term2*term2))
```

```
c-----gasdynamic pressure at pool surface --------------------------
      pspl=p2pl/p3ps
c-----difference between gasdynamic and thermodynamic pressure---------
      resd=abs(pspl/psp-1.)
      amach = amach+0.00005
      if (resd.gt.0.005) go to 21
c-----calculation of mach number over, density at pool surface (ideal)--
      rs=amwtvap*273.*psp/(22400.*tsurf)
c-----density at edge of Knudsen layer------------------------------
      rho3=r3rs*rs
c-----velocity of vapor at edge of  Knudsen layer--------------------
      sped=spedrt*sqrt(temp3/rtemp)
c-----calculate total flux, equation (3.24)----------------------
      confl=rho3*amach*sped
      write(36,169)tsurf,amach,rho3,confl
35    continue
      write(36,129)
169   format(12x,1p,4e13.4)
      end

c-----subroutine to calculate equilibrium vapor pressure --------------
      subroutine eqpres(aa,pmn,pfe,pni,pcr)
c-----thermodynamic equilibrium vapor pressure-temperature relations----
      pmn=10.**(-5.58e-4*aa-1.503e4/aa+12.609)/1.013e5
      pni=10.**(-3519./aa+74.94*alog10(aa)-18.042e-3*aa
     1+15.14e-7*aa*aa-214.297)/1.013e5
      df=86900.-aa*27.78
      pfe=(exp(-df/(1.987*aa)))
      pcr=10.**(-13.505e3/aa+33.658*alog10(aa)-9.290e-3*aa
     1+8.381e-7*aa*aa-87.077)/1.013e5
      return
      end
c-------------end of the program---------------------------------
```

The outputs of the program for AISI 201 steel is presented at the end of the

appendix in Table D.3. The plot of Mach number and density of vapor at the edge of Knudsen layer as a function weld pool surface temperature for AISI 201 stainless steel is preseneted in Fig. 4.27.

Table D.1: Output of program D.1 for pure iron.

input parameters	
molecular weight of shielding gas	.3994E+02
molecular weight of metal	.5585E+02
latent heat of vaporization (J/gm)	.6335E+04
boiling temperature (K)	.3135E+04
Maximum temp. for calculation (Mach #=1)	.4800E+04

program output			
Surface Temp. (K)	Mach #	Density (gm/cm**3)	Flux (gm/cm**2-s)
3.1350E+03	5.0000E-05	2.1712E-04	9.5908E-04
3.2350E+03	6.5201E-02	2.9014E-04	1.6755E+00
3.3350E+03	1.3015E-01	3.7986E-04	4.3879E+00
3.4350E+03	1.9429E-01	4.8865E-04	8.4416E+00
3.5350E+03	2.5789E-01	6.1843E-04	1.4202E+01
3.6350E+03	3.2110E-01	7.7105E-04	2.2073E+01
3.7350E+03	3.8416E-01	9.4804E-04	3.2497E+01
3.8350E+03	4.4717E-01	1.1508E-03	4.5942E+01
3.9350E+03	5.1028E-01	1.3805E-03	6.2899E+01
4.0350E+03	5.7349E-01	1.6382E-03	8.3871E+01
4.1350E+03	6.3690E-01	1.9245E-03	1.0937E+02
4.2350E+03	7.0046E-01	2.2402E-03	1.3991E+02
4.3350E+03	7.6417E-01	2.5858E-03	1.7599E+02
4.4350E+03	8.2808E-01	2.9615E-03	2.1812E+02
4.5350E+03	8.9214E-01	3.3676E-03	2.6679E+02
4.6350E+03	9.5630E-01	3.8044E-03	3.2247E+02
4.7350E+03	1.0205E+00	4.2718E-03	3.8561E+02

Table D.2: Output of program D.1 for pure titanium.

---

input parameters

---

molecular weight of shielding gas	.3994E+02
molecular weight of metal	.4790E+02
latent heat of vaporization (J/gm)	.8820E+04
boiling temperature (K)	.3533E+04
Maximum temp. for calculation (Mach #=1)	.5400E+04

---

program output

Surface Temp. (K)	Mach #	Density (gm/cm**3)	Flux (gm/cm**2-s)
3.5330E+03	5.0000E-05	1.6524E-04	8.3668E-04
3.6330E+03	5.5751E-02	2.1945E-04	1.2423E+00
3.7330E+03	1.1155E-01	2.8623E-04	3.2497E+00
3.8330E+03	1.6700E-01	3.6747E-04	6.2581E+00
3.9330E+03	2.2219E-01	4.6490E-04	1.0552E+01
4.0330E+03	2.7739E-01	5.8012E-04	1.6462E+01
4.1330E+03	3.3280E-01	7.1461E-04	2.4355E+01
4.2330E+03	3.8841E-01	8.6988E-04	3.4626E+01
4.3330E+03	4.4442E-01	1.0471E-03	4.7710E+01
4.4330E+03	5.0083E-01	1.2475E-03	6.4059E+01
4.5330E+03	5.5774E-01	1.4720E-03	8.4151E+01
4.6330E+03	6.1510E-01	1.7216E-03	1.0847E+02
4.7330E+03	6.7291E-01	1.9970E-03	1.3753E+02
4.8330E+03	7.3117E-01	2.2989E-03	1.7182E+02
4.9330E+03	7.8987E-01	2.6279E-03	2.1186E+02
5.0330E+03	8.4898E-01	2.9844E-03	2.5815E+02
5.1330E+03	9.0849E-01	3.3688E-03	3.1120E+02
5.2330E+03	9.6835E-01	3.7815E-03	3.7150E+02
5.3330E+03	1.0285E+00	4.2228E-03	4.3955E+02

Table D.3: Output of program D.1 for AISI 201 stainless steel.

---

input parameters

weight pct. of Mn	.6500E+01
weight pct. of Cr	.1700E+02
weight pct. of Ni	.4250E+01
weight pct. of Fe	.7094E+02
molecular weight of shielding gas	.4003E+01
Maximum emp. for calculation (Mach # =1)	.4000E+04

---

program output

Surface Temp. (K)	Mach #	Density (gm/cm**3)	Flux (gm/cm**2-s)
2.9581E+03	4.6000E-03	2.2836E-04	9.0860E-02
3.0081E+03	6.2451E-02	2.4925E-04	1.3421E+00
3.0581E+03	1.2070E-01	2.7180E-04	2.8188E+00
3.1081E+03	1.7944E-01	2.9614E-04	4.5493E+00
3.1581E+03	2.3874E-01	3.2246E-04	6.5651E+00
3.2081E+03	2.9874E-01	3.5092E-04	8.9036E+00
3.2581E+03	3.5950E-01	3.8177E-04	1.1605E+01
3.3081E+03	4.2126E-01	4.1516E-04	1.4720E+01
3.3581E+03	4.8407E-01	4.5140E-04	1.8301E+01
3.4081E+03	5.4813E-01	4.9077E-04	2.2411E+01
3.4581E+03	6.1360E-01	5.3359E-04	2.7123E+01
3.5081E+03	6.8061E-01	5.8029E-04	3.2523E+01
3.5581E+03	7.4947E-01	6.3126E-04	3.8709E+01
3.6081E+03	8.2043E-01	6.8701E-04	4.5801E+01
3.6581E+03	8.9364E-01	7.4825E-04	5.3935E+01
3.7081E+03	9.6960E-01	8.1559E-04	6.3281E+01
3.7581E+03	1.0486E+00	8.8998E-04	7.4040E+01

Appendix E

PROGRAM FOR THE CALCULATION OF VAPORIZATION RATES

AND COMPOSITION CHANGE

The following program was developed to calculate the total vaporization rates and the vaporization rates of the alloying elements. The program also calculates the composition change of the stainless steel from the gasdynamic principles and from Langmuir equation. The details of the equations are given in Chapter 3, section 3.1.2.2 to 3.1.2.4. The program uses the temperature field and the geometry of the weld pool obtained from the fluid flow and heat transfer program. The program is given below:

E.1 Program E.1

```
        program vaporization_rate
c-----this program calculates the total vaporization rates and the composition
c       change from the temperature field obtained from the fluid flow and heat
c       transfer program -----------------------------------------------
c       afl:          average Langmuir flux between two grid locations
c       alanfl(j,i):  Langmuir flux of the alloying elements, see gdflux(i,j)
c       alsum(i):     vaporization rates of the alloying elements and the total
c                     vaporization rate calculated from the Langmuir equation
c       area:         area on the pool surface between two grid locations
c       delwt(i):     composition change of the alloying elements calculated
c                     using gasdynamic principles
c       delwtl(i):    composition change of the alloying elements calculated
c                     using Langmuir equation
c       density:      density of the material
c       fwtp(i):      final weight percent of the alloying elements calculated
c                     using gasdynamic principles
c       fwtpl(i):     final weight percent of the alloying elements calculated
c                     using Langmuir equation
```

```
c         gdflux(j,i):   gasdynamic flux of the alloying elements, j is the number of
c                        grid points over which the temperature is greater than the
c                        melting point and i=1 for iron, 2 for manganese, 3 for chromium,
c                        4 for nickel and 5 for total vaporization flux
c         jmax:          number of grid points on the pool surface above melting point
c         plfac:         plasma factor in the suppression of the vaporization rate
c         radius(j):     distance on the pool surface,
c         scvel:         scanning velocity of the power source
c         tfl:           average gasdynamic flux between two grid locations
c         tlsum(i):      vaporization rates of the alloying elements and the total
c                        vaporization rate calculated from gasdynamic principles
c         wtp(i):        initial weight percent of the alloying elements
c         wtpcr:         weight percent chromium
c         wtpfe:         weight percent iron
c         wtpmn:         weight percent manganese
c         wtpni:         weight percent nickel
c----begin writing user friendly interface----------------------------
         parameter(nog=2,nof=2,nov=10)
         character*60 filenames(nof),strfile(nof),strnov(nov),grname(nog)
         dimension valnov(nov),im(nog)
         data im/nof,nov/
         data grname/'filenames','other variables'/
         data strfile/'input filename','output filename'/
         data filenames/'datainp','outcc'/
         data strnov/'shielding gas (He: 1, Ar:2)',
        1 'diameter of nozzle (cm)','flow rate of gas (cc/sec)',
        1 'weight pct. of Fe','weight pct. of Mn',
        1 'weight pct. of Cr','weight pct. of Ni',
        1 'plasma factor for composition change','scanning velocity',
        1 'density of the material (gm/cm3)'/
         data valnov/1.0,0.5,550,70.94,6.5,17.0,4.25,0.66,1.524,7.2/
         data amwtfe,amwtmn,amwtcr,amwtni/55.85,54.93,51.996,58.70/
         data gasr,gamma1,gamma3,rtemp,pi/8.314,1.6667,1.6667,298.,3.1415/
         data tmelt/1811.0/
```

```
        data tmelt/1811.0/
        write(6,3)'vaporization rates and composition change'
3       format(2x,79('-'),/12x,a42)
10      write(6,4)
        do 11 i=1,nog
11      write(6,99) 'Enter',i,'to change/view ',gname(i)
        write(6,*)' Enter 3 to start calculations with current values'
99      format(2x,a5,1x,i1,1x,a15,a40)
        write(6,4)
4       format(2x,79('-'))
c-----select a data group to view/change data ---------------------------
        write(*,*) ' Please enter your choice (1 to 3):'
        read(*,*) igroup
        if(igroup.eq.nog+1) go to 51
c-----on screen viewing of parameter values in a selected data group ---------
        write (6,79) gname(igroup)
79      format(2x,79('-'),/15x,a40)
        imax=im(igroup)
21      write(6,4)
        do 40 i=1,imax
        goto(31,32)igroup
31      write(*,30)'Enter',i,'to change',strfile(i),'(',filenames(i),')'
30      format(2x,a5,1x,i1,1x,a9,1x,a29,1x,a1,a8,a1)
        go to 40
32      write(*,59)'Enter',i,'to change',strnov(i),'(',valnov(i),')'
40      continue
        imaxp1=imax+1
        write(6,49)'Enter',imaxp1,'if all values in this group are ok'
49      format(2x,a5,1x,i2,1x,a34,/2x,79('-'))
59      format(2x,a5,1x,i2,1x,a9,1x,a40,a1,1pe10.3,a1)
c-----decide if some of the values need to be changed -----------------------
        write(6,39) 'Please enter your choice (1 to',imaxp1,'):'
39      format(2x,a30,1x,i2,a2)
        read(*,*) ichange
```

```
        if(ichange.eq.imaxp1) go to 10
c-----change parameter value ----------------------------------------
        goto (41,42) igroup
41      write(6,29)'Enter',strfile(ichange),':'
29      format(2x,a5,2x,a20,a2)
        read(5,89)filenames(ichange)
        go to 21
42      write(6,19)'Enter',strnov(ichange),':'
        read(5,*)valnov(ichange)
        go to 21
19      format(2x,a5,2x,a60,a2)
89      format(a60)
51      continue
c-- end data input, assign user friendly names for the variable ----------------
        gastype = valnov(1)
        dianz  = valnov(2)
        flrate = valnov(3)
        wtpfe  = valnov(4)
        wtpmn  = valnov(5)
        wtpcr  = valnov(6)
        wtpni  = valnov(7)
        plfac  = valnov(8)
        scvel  = valnov(9)
        density = valnov(10)
c-----end assignment of user friendly names for variables----------------------
c-----pick molecular weight and room temperature viscosity of the shielding gas---
        if (gastype.lt.1.5) then
        amwtgas = 4.0026
        amuroom = 1.97391e-4
        else
        amwtgas = 39.94
        amuroom = 2.2527e-4
        endif
c-----calculate reynold's number and its function-----------------------------
```

```
            renno=4.*firate*(amwtgas*273.)/(22400.*298.)/(amuroom*pi*dianz)
            fre=2.*sqrt(renno)*sqrt(1.+renno**0.55/200.)
c----calculate composition in mole fraction from weight percent----------------
            totmol=wtpfe/amwtfe+wtpmn/amwtmn+wtpcr/amwtcr+wtpni/amwtni
            amfmn=wtpmn/(totmol*amwtmn)
            amfcr=wtpcr/(totmol*amwtcr)
            amfni=wtpni/(totmol*amwtni)
            amffe=wtpfe/(totmol*amwtfe)
            amolwt=amffe*amwtmn+amfmn*amwtfe+amfcr*amwtcr+amfni*amwtni
c----find tstar for the given composition of steel-------------------------
            aa=2901.
            bb=4000.
110         tstar=(aa+bb)/2
            call  eqpres(aa,pmn,pfe,pni,pcr)
            ptaa=amfmn*pmn+amffe*pfe+amfcr*pcr+amfni*pni-1.
            call  eqpres(tstar,pmn,pfe,pni,pcr)
            pterm=amfmn*pmn+amffe*pfe+amfcr*pcr+amfni*pni-1.
            if ((ptaa*pterm).lt.0) then
            bb=tstar
            else
            aa=tstar
            endif
            if (abs(pterm).lt.0.001) go to 20
            go to 110
20          continue
c----end calculation of tstar--------------------------------------------
                open (unit=11,file='flux')
                open (unit=8,file=filenames(1))
                open (unit=17,file=filenames(2))
                read(8,*)areacs
c-----read location on the pool surface and the corresponding temperature and
c       calculate local vaporization flux (both gasdynamics and Langmuir)------------
                do 440 i=1,100
                read(8,*,end=201)j,radius,tsurf
```

```
      if (tsurf.lt.tmelt) go to 440
      call eqpres(tsurf,pmn,pfe,pni,pcr)
      psp=amfmn*pmn+pfe*amffe+amfcr*pcr+amfni*pni
      if (tsurf.lt.tstar) then
      confl=0.
      go to 101
      endif
c-----pressure gradient driven vaporization flux---------------------------
      amwtvap=(amffe*pfe*amwtfe+amfmn*pmn*amwtmn
     1    +amfcr*pcr*amwtcr+amfni*pni*amwtni)/psp
      spedrt=sqrt(1.667*8314*rtemp/amwtvap)*100.
221   am=amach*sqrt(gamma3/2.)
      term1=(gamma3-1.)*am/((gamma3+1.)*2.)
      t3ts=(sqrt(1.+pi*term1*term1)-sqrt(pi)*term1)**2
      tt=1./(1.+0.47047*am)
      erf=0.34802*tt-0.09588*tt*tt+0.74786*tt*tt*tt
      r3rs=sqrt(1./t3ts)*((am**2+0.5)*erf-am/sqrt(pi))
      r3rs=r3rs+0.5*(1./t3ts)*(1-sqrt(pi)*am*erf)
      p3ps=r3rs*t3ts
      temp3=tsurf*t3ts
      a3a1=sqrt(gamma3*temp3*amwtgas)/sqrt(gamma1*rtemp*amolwt)
      term2=(gamma1+1.)/4.*amach*a3a1
      p2p1=1.+gamma1*a3a1*amach*(term2+sqrt(1.+term2*term2))
      psp1=p2p1/p3ps
      resd=abs(psp1/psp-1.)
      amach = amach+0.00005
      if (resd.gt.0.005) go to 221
      rs=amwtvap*273.*psp/(22400.*tsurf)
      rho3=r3rs*rs
      sped=spedrt*sqrt(temp3/rtemp)
      confl=rho3*amach*sped
      cflfe=amffe*confl*pfe/psp
      cflmn=amfmn*confl*pmn/psp
      cflcr=amfcr*confl*pcr/psp
```

```
        cflni=amfni*confl*pni/psp
c----end calculation of pressure gradient vaporization flux, begin calculation of
c       vaporization flux due to temperature gradient-----------------------
101    prsure=1.
        if (tsurf.gt.tstar) prsure=(psp+1.)/2.
        avtemp=(tsurf+rtemp)/2.
        call gasprop(gastype,avtemp,prsure,visgas,dfegas,dmngas,
      1 dcrgas,dnigas)
        dengas=amwtgas*273.*prsure/(22400.*avtemp)
        akinvis=visgas/dengas
C--------------------iron------------------------------------------
        scno=akinvis/dfegas
        shno=fre*scno**0.42*0.48271            .
        amasco=shno*dfegas/dianz
        diffe=amasco*psp*amwtfe*amffe/(82.0594*tsurf)
C------------------manganese-------------------------------------
        scno=akinvis/dmngas
        shno=fre*scno**0.42*0.48271
        amasco=shno*dmngas/dianz
        difmn=amasco*psp*amwtmn*amfmn/(82.0594*tsurf)
C----------------chromium--------------------------------------
        scno=akinvis/dcrgas
        shno=fre*scno**0.42*0.48271
        amasco=shno*dcrgas/dianz
        difcr=amasco*psp*amwtcr*amfcr/(82.0594*tsurf)
c----------------nickel--------------------------------------
        scno=akinvis/dnigas
        shno=fre*scno**0.42*0.48271
        amasco=shno*dnigas/dianz
        difni=amasco*psp*amwtni*amfni/(82.0594*tsurf)
c----calculate total gasdynamic vaporization flux (pressure gradient +
c       concentration gradient)----------------------------------
        totdif=diffe+difmn+difcr+difni
        totgd=totdif+confl
```

```
          totfe=cflfe+diffe
          totmn=cflmn+difmn
          totcr=cflcr+difcr
          totni=cflni+difni
c-----calculate local vaporization flux from Langmuir equation----------------
          alanmn=44.34*pmn*amfmn*sqrt(amwtmn/tsurf)
          alanfe=44.34*pfe*amffe*sqrt(amwtfe/tsurf)
          alancr=44.34*pcr*amfcr*sqrt(amwtcr/tsurf)
          alanni=44.34*pni*amfni*sqrt(amwtni/tsurf)
          totlan=alanmn+alanfe+alancr+alanni
          write(11,999)tsurf,radius,totfe,alanfe,totmn,alanmn
        1 ,totcr,alancr,totni,alanni,totgd,totlan
c----write the local vaporization flux of the alloying elements calculated from
c      gasdynamics and the Langmuir equation in a file------------------------
999       format(12e15.5)
440       continue
201       continue
          close (11)
          rewind (11)
c----call subroutine to integrate the local vaporization fluxes for calculation
c      of total vaporization rates and the composition change from both gasdynamic
c      principles and Langmuir equation----------------------------------------
          call totflux(11,areacs,plfac,scvel,density,
        1 wtpmn,wtpfe,wtpcr,wtpni)
          end
c-----integrate the local flux to calculate the total vaporization rates----------
c      the vaporization fluxes written in an output file ('flux') in the main
c      program are reread in this subroutine in a different format, in an array
c      form, to facilitate the computation----------------------------------
          subroutine totflux(iunit,areacs,plfac,scvel,density,
        1 wtpmn,wtpfe,wtpcr,wtpni)
          parameter(nj=100)
          dimension radius(nj),gdflux(nj,5),alanfl(nj,5),alsum(5),
        1 tlsum(5),wtp(4),fwtp(4),fwtpl(4),delwtl(4),delwt(4)
```

```
             character*64 flux
             wtp(1) = wtpfe
             wtp(2) = wtpmn
             wtp(3) = wtpcr
             wtp(4) = wtpni
             open (unit=11,file='flux')
             jmax=0
c-----read the local temperature, distance and vaporization fluxes at the pool
c      surface until the end of the file is reached------------------------
             do 10 j=1,nj
             read(iunit,*,end=200)temp,radius(j),gdflux(j,1),alanfl(j,1),
           1 gdflux(j,2),alanfl(j,2),gdflux(j,3),alanfl(j,3),gdflux(j,4),
           1 alanfl(j,4),gdflux(j,5),alanfl(j,5)
             jmax=jmax+1
10           continue
200          continue
c-----do integration over the pool surface to calculate the vaporization rates---
             do 30 i=1,5
             alsum(i)=0.0
             tlsum(i)=0.0
             do 20 j=jmax,2,-1
             area=-3.1415927*(radius(j)**2-radius(j-1)**2)
             afl=(alanfl(j,i)+alanfl(j-1,i))/2.
             tfl=(gdflux(j,i)+gdflux(j-1,i))/2.
             alrate=afl*area
             tlrate=tfl*area
             alsum(i)=alsum(i)+alrate
             tlsum(i)=tlsum(i)+tlrate
20           continue
30           continue
c-----calculate the composition change from the vaporization rates, area of cross
c      section of the pool, plasma factor, scanning velocity and initial wt. pct.--
c-----calculate weight percent change from gasdynamic principles----------------
             do 11 i=1,4
```

```
          anum = 2.0*scvel*areacs*density*wtp(i)/100.0-tlsum(i)*plfac
          denom = 2.0*scvel*areacs*density-tlsum(5)*plfac
          fwtp(i)=anum/denom*100.0
          delwt(i) = fwtp(i)-wtp(i)
11        continue
c-----calculate weight percent change from Langmuir equation --------------------
          do 12 i=1,4
          anum = 2.0*scvel*areacs*density*wtp(i)/100.0-alsum(i)
          denom = 2.0*scvel*areacs*density-alsum(5)
          fwtpl(i)=anum/denom*100.0
          delwtl(i) = fwtpl(i)-wtp(i)
12        continue
c----write the output in an output file----------------------------------------
          write(17,99)
99        format(86('-'),/42x,'Iron',8x,'Manganese',3x,'Chromium',4x
          1 ,'Nickel'/86('-'))
          write(17,98)(wtp(i),i=1,4)
98        format(2x,'Initial Wt. Pct.',20x,4(2x,e10.4))
          write(17,97)(tlsum(i),i=1,4)
97        format(2x,'Gasdynamic Vaporization Rate (gms/s)',
          14(2x,e10.4))
          write(17,96)(alsum(i),i=1,4)
96        format(2x,'Langmuir Vaporization Rate (gms/s)',2x,
          14(2x,e10.4))
          write(17,95)(fwtp(i),i=1,4)
95        format(2x,'Gasdynamic Final Wt. Pct',12x,4(2x,e10.4))
          write(17,94)(fwtpl(i),i=1,4)
94        format(2x,'Langmuir Final Wt. Pct',14x,4(2x,e10.4))
          write(17,93)(delwt(i),i=1,4)
93        format(2x,'Gasdynamic Wt. Pct. Change',10x,4(2x,e10.4))
          write(17,92)(delwtl(i),i=1,4)
92        format(2x,'Langmuir Wt. Pct. Change',12x,4(2x,e10.4))
          write(17,91)
91        format(86('-'))
```

```
      return
      end
c-----subroutine to calculate the viscosity of the shielding gas and diffusivity
c        of the alloying elements in the shielding gas. the relations are given in
c        Appendix A----------------------------------------------------
      subroutine gasprop(gastype,t,prsure,visgas,dfegas,dmngas,
     1 dcrgas,dnigas)
      if (gastype.lt.1.5) then
      visgas = 2.2029e-4 + 2.2171e-7*t
      dfegas = -2.1360+5.4957e-3*t+2.4247e-6*t**2/prsure
      dmngas = -1.6174+4.7797e-3*t+2.4582e-6*t**2/prsure
      dcrgas = -2.2310+5.5302e-3*t+2.3683e-6*t**2/prsure
      dnigas = -2.2184+5.6412e-3*t+2.4499e-6*t**2/prsure
      else
      visgas = 2.7373e-4 + 2.7681e-7*t
      dfegas = -0.61024+1.1274e-3*t+6.4892e-7*t**2/prsure
      dmngas = -0.59274+1.1469e-3*t+6.1891e-7*t**2/prsure
      dcrgas = -0.60579+1.1331e-3*t+6.4741e-7*t**2/prsure
      dnigas = -0.60938+1.1335e-3*t+6.5149-7*t**2/prsure
      endif
      return
      end
c----subroutine for equilibrium vapor pressure calculation--------------
      subroutine eqpres(aa,pmn,pfe,pni,pcr)
      pmn=10.**(-5.58e-4*aa-1.503e4/aa+12.609)/1.013e5
      pni=10.**(-3519./aa+74.94*alog10(aa)-18.042e-3*aa
     1          +15.14e-7*aa*aa-214.297)/1.013e5
      df=86900.-aa*27.78
      pfe=(exp(-df/(1.987*aa)))
      pcr=10.**(-13.505e3/aa+33.658*alog10(aa)-9.290e-3*aa
     1      +8.381e-7*aa*aa-87.077)/1.013e5
      return
      end
c----end of the program----------------------------------------------
```

The output of the program for laser welding of AISI 201 stainless steel
with a laser power of 2000 Watts in helium environment is given in Table E.1.

Table E.1: Output of program E.1 for AISI 201 stainless steel welded with a laser power of 2000 Watts.

	Iron	Manganese	Chromium	Nickel
Initial Wt. Pct.	.7094E+02	.6500E+01	.1700E+02	.4250E+01
Gasdynamic Vaporization Rate (gms/s)	.3406E-02	.2442E-02	.1974E-02	.1701E-03
Langmuir Vaporization Rate (gms/s)	.6698E-02	.1134E-01	.4154E-02	.3083E-03
Gasdynamic Final Wt. Pct	.7161E+02	.5933E+01	.1682E+02	.4300E+01
Langmuir Final Wt. Pct	.7542E+02	.1719E+01	.1684E+02	.4564E+01
Gasdynamic Wt. Pct. Change	.6675E+00	-.5669E+00	-.1815E+00	.4999E-01
Langmuir Wt. Pct. Change	.4484E+01	-.4781E+01	-.1591E+00	.3136E+00

Appendix F

EQUILIBRIUM VAPOR PRESSURE DATA

The equilibrium vapor pressures of the various vaporizing species, viz., Mn, Cr, Ni, and Fe over the respective pure liquids, at temperature T (K), expressed in atmospheres were calculated using the following equations:

$$\log P^0{}_{Mn} = (-5.58 \times 10^{-4}T - 1.503 \times 10^4/T + 12.609)/1.013 \times 10^5 \qquad \text{(Reference 1)}$$

$$\log P^0{}_{Ni} = (-3.519 \times 10^3/T + 74.94 \log T - 18.042 \times 10^{-3} T + 15.14 \times 10^{-7}T^2$$
$$-214.297)/1.013 \times 10^5 \qquad \text{(Reference 2)}$$

$$\log P^0{}_{Cr} = (-13.505 \times 10^3/T + 33.658 \log T - 9.29 \times 10^{-3} T + 8.381 \times 10^{-7}T^2$$
$$- 87.077)/1.013 \times 10^5 \qquad \text{(Reference 2)}$$

$$\ln P^0{}_{Fe(l)} = -4.3734 \times 10^4/T + 13.98 \qquad \text{(Reference 3)}$$

$$\ln P^0{}_{Fe(s)} = (-21080/T - 2.14 \log T + 16.89)/760.0 \qquad \text{(Reference 4)}$$

References

1. R. Hultergen, P. D. Desai, D. T. Hawkins, M. Gleiser,K. K. Kelly and D. D. Wagman, Selected Values of the Thermodynamic Properties of the Elements, (ASM Inetrnatinal, Materials Park, Ohio, 1973).

2. R. E. Honig, D. A. Kramer, Physicochemical Measurements in Metals Research, vol. 4, (Interscience Publishers, NY, 1970).

3. E. T. Turkdogan, Physical Chemistry of High Temperature Technology, (Academic Press, 1980).

4. Smithells Metals Reference Book, 6th Edition, Ed. E. A. Brandes, (Butterworths and Co. , London, 1983).

Vita

Kamlesh Mundra was born in Ajmer, India, on 9 August 1963. After completion of his high school education in 1982, he entered Indian Institute of Technology, Kanpur, India and graduated with a Bachelor of Technology degree in Metallurgy in 1986. He then joined Indian Institute of Science, Bangalore, India to pursue graduate studies in Metallurgy, leading to a Master of Engineering degree in 1988. In 1989 he joined The Pennsylvania State University to continue his graduate studies leading to the Doctor of Philosophy in Metals Science and Engineering. He was the student winner in the poster session competition in the 73 and 74 American Welding Society annual conventions. He is the member of American Welding Society, American Society for Metals and Tau Beta Pi. He is a co-author of the following publications.

(1) K. Mundra and T. DebRoy, "Calculation of Weld Metal Composition Change in High Power Conduction Mode Carbon Dioxide Laser Welding of Stainless Steels", Metallurgical Transactions B, 1993, Vol. 24B, pp. 145-155.

(2) K. Mundra and T. DebRoy, "Towards Understanding Alloying Element Vaporization During Laser Beam Welding of Stainless Steels", Welding Journal Research Supplement, 1993, Vol. 72(1), pp. 1s-9s.

(3) K. Mundra, T. DebRoy, T. Zacharia and S. A. David, " Role of Thermophysical Properties in Weld Pool Modeling", Welding Journal Research Supplement, 1992, Vol. 71(9), pp. 313s-320s.

(4) T. DebRoy, S. Basu and K. Mundra, "Probing Laser Induced Metal Vaporization by Gas Dynamics and Liquid Pool Transport Phenomena", Journal of Applied Physics, 1991, Vol. 70(3), pp. 1313-1319.

(5) K. Mundra and T. DebRoy, "Modeling of Weld Metal Composition Change During Laser Welding of Stainless Steels", International Trends in Welding Science and Technology, Eds. S. A. David and J. M Vitek, (ASM International, Materials Park, OH, 1993), pp. 75-79.

(6) S. S. Babu, S. A. David, J. M. Vitek, K. Mundra and T. DebRoy, "Development of Macro- and Microstructures of Low Alloy Steel Welds - Inclusion Formation", Submitted to Materials Science and Technology.